JPRS-JST-91-007
14 FEBRUARY 1991

JPRS Report

Science &
Technology

Japan

27TH AIRCRAFT SYMPOSIUM,
PART 3

DTIC QUALITY INSPECTED 3

19980515 177

SCIENCE & TECHNOLOGY
JAPAN

27TH AIRCRAFT SYMPOSIUM, PART 3

CONTENTS

Effect of Piping Interference Removal Device in Wind Tunnel Tests of STOL Model Plane

906C0041A Tokyo HIKOKI SHINPOJIUMU in Japanese Oct 89 pp 184-187

[Article by Hitoshi Takahashi and Teruomi Nakatani, National Aerospace Laboratory; and Takashi Inoue, Kawasaki Heavy Industries]

[Text] 1. Introduction

A model engine that operates with high-pressure air was used in the wind tunnel test of the STOL experimental plane "Asuka," which was researched and developed at the National Aerospace Laboratory. High-pressure air (20 atmospheres maximum) was supplied to the model engine through the pressure piping mounted within the wind tunnel. The flow of high-pressure air through this pressure piping interferes with the wind tunnel balance and an excessive force (piping interference force) is generated. There have been attempts to reduce this piping interference force by using high-pressure rubber hose. However, this led to other problems. For example, hose rigidity increased, interference increased, there was a deterioration in reproducibility due to the hysteresis phenomenon, zero drift occurred, and asymmetry appeared during sideslip when pressure was placed on the rubber hose. Therefore, we developed an air joint (piping interference removal device) based on the air-bearing principle as a system to replace the conventional rubber hose system.[1]. We conducted a wind tunnel test to confirm the effectiveness of this system, checked the reproducibility of the data thus obtained and conducted a comparative analysis of the new system against the conventional rubber hose system. This paper reports on this system since it has been confirmed that it will withstand practical use. In addition, since the detailed structure and functions of the piping interference removal device have already been reported, these will be explained simply here.[2,3]

2. Piping Interference Removal Device

The piping interference removal system developed at the National Aerospace Laboratory consists of a pressure supply device, an air-bearing joint, and a strut piping device. The air-bearing joint shown in Figure 1 is the heart of the piping interference removal device. It comprises an air supply adaptor, a bearing base, an outer eccentric floating shaft, an inner eccentric floating shaft, an output bearing, and a bellows. The degree of freedom for movement in

(Asuka) Total plane model side
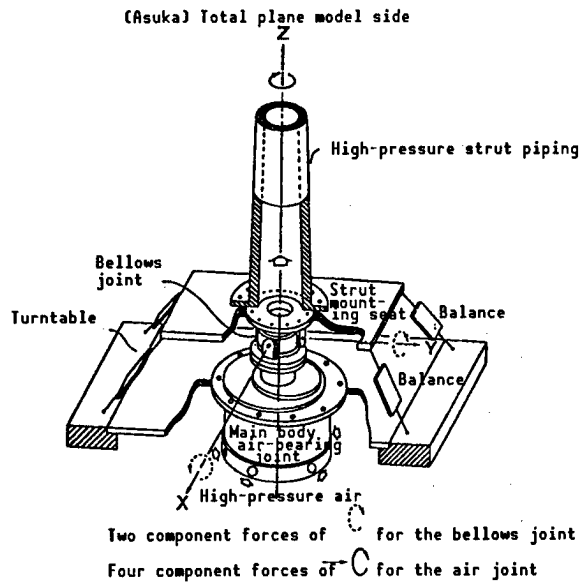
Figure 1.

three directions and for rotation of one direction by the eccentric air-bearing joint and the degree of freedom for rotation in two directions by the bellows are permissible. This configuration makes it possible to eliminate the interference caused by the six component forces placed on the model.

3. Static Load Test of Piping Interference Removal Device and Rubber Hose Interference Test

A static load was placed on the piping interference removal device (herein-after called the device) installed within the balance of the large, low-speed wind tunnel at the National Aerospace Laboratory and the interference force of the six component forces was measured. As a result, it was found that all component forces were within the error of the balance accuracy. Next, the six component interference forces were measured when a pressure (original pressure) of 6 kg/cm^2~18 kg/cm^2 was applied by reciprocating sweeping to this device. It was determined that all six component interference forces were basically within the balance accuracy and it was determined that the other five interference forces, excluding lift, had no relation to the original pressure as designed. However, since it became clear that each interference force showed a change and that they lacked reproducibility when the original pressure was less than 10 kg/cm^2, it was decided that the subsequent total plane wind tunnel test would be conducted at the original pressure of 11 kg/cm^2. Because of the reaction effect generated by the blind on the lift component, the interference force fluctuates with increases in the original pressure. Nevertheless, this effect is eliminated at zero-point correction by conducting a wind tunnel test under a fixed original pressure.

Meanwhile, the interference force for all of the six component forces fluctuates against the original pressure when the rubber hose is used, the fluctuation changes every time the attachment method or testing order differs and there is also the possibility of fluctuation in the same testing order. Therefore, this device was developed as a means of replacing the rubber hose method and for removing the piping interference effect.

2

When the wind tunnel test model was mounted on this device, it was found that the interference force was small and that reproducibility was good. Moreover, it became clear that fluctuation during the α and β sweeps could be removed by static tare and that fluctuation due to changes in the original pressure could be removed by zero-point correction. Therefore, piping interference correction has not been made in the wind tunnel test since then.

4. Effect of Piping Interference Removal Device

A total STOL plane model was attached to this device and a wind tunnel test was conducted to check the effect. The wind tunnel used in this test was the large, low-speed wind tunnel of the National Aerospace Laboratory. Tests were conducted on the following three items:

     (1) α, β continuous sweep reproducibility
     (2) Original pressure change reproducibility
     (3) Comparison with previous wind tunnel test results

4.1 α, β Continuous Sweep Reproducibility Test

In the conventional rubber hose method, the rubber hose riding on the turn-table of the wind tunnel would be dragged when the model was made to sideslip (β sweep). Zero-point transfer also occurred and problems with data reproducibility and accuracy arose when it was alternately conducted with incident angle change (α sweep). Therefore, improvement of data reproducibility when alternately repeating the α and β sweeps was promoted by using this device. The test was conducted on a STOL L/D form, $C_J = 1.0$ in the following order: $\alpha \rightarrow \beta \rightarrow \alpha \rightarrow \beta$ sweep. The results of the test are shown in Figure 2. Although a slight difference was recognized at a large angle of incidence, it was judged that reproducibility was sufficient.

4.2 Original Pressure Change Reproducibility Test

The presence of interference force changes was checked by alternately repeating the test when the original pressure was high and low. These tests were conducted in the same manner as described in Section 4.1 with the original pressure set at 11 kg/cm^2, 17 kg/cm^2, and 11 kg/cm^2, and reproducibility was compared. The effect of original pressure change was recognized at the same level as that shown in Figure 2, but it was judged to be within a range that would not present problems in terms of basic characteristic acquisition.

4.3 Comparison With Previous Wind Tunnel Tests

We checked reproducibility from points that could be considered to be related to the structure and function of this device as described in Sections 4.1 and 4.2. After determining that it could be used effectively, we conducted a reproducibility check test in the same form as described above to confirm the effect of this device.
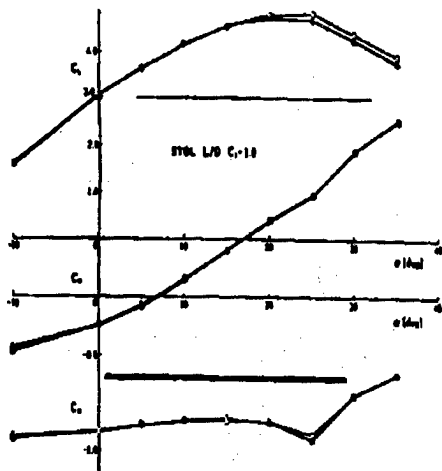
α, β continuous sweep
reproducibility
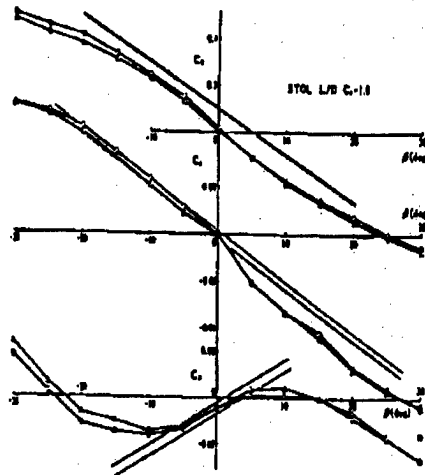
α, β continuous sweep
reproducibility

Figure 2.

The comparable forms with the previous data are as follows:

(1) STOL T/O AEO Without tail
(2) STOL T/O AEO Total plane
(3) STOL L/D AEO Without tail
(4) STOL L/D AEO Total plane

Moreover, there is a slight difference in VG of all forms.

As a comparative example of these forms, the results of the STOL T/O, AEO, total plane form are shown in Figure 3 (α sweep) and Figure 4 (β sweep). Since it is a system in which the engine thrust is changed under a fixed original pressure and since the engine thrust is changed by changing the original pressure in the conventional rubber hose system, there are times when the BCL value (leading edge, aileron) differs slightly between the two systems.

In observing the three longitudinal component forces, a difference is observed near stalling for C_L and C_D but overall it appears that they coincide fairly well. However, when C_m uses this device, an unevenness becomes conspicuous and the value differs sharply. Although it is not well understood why there is no great difference in C_L and C_D and why this phenomenon occurs in C_m only, the following may be the reasons:

(1) Piping interference (problem of air joint)
(2) Noise of measurement system, nonconformity of device (C_m system only)
(3) Balance system (C_m system only)

With the exception of one segment, there is practically no difference in the trend of the aerodynamic coefficient for the three horizontal component forces and it is believed that it coincides well when considering the difference of model improvement and VG form.

4
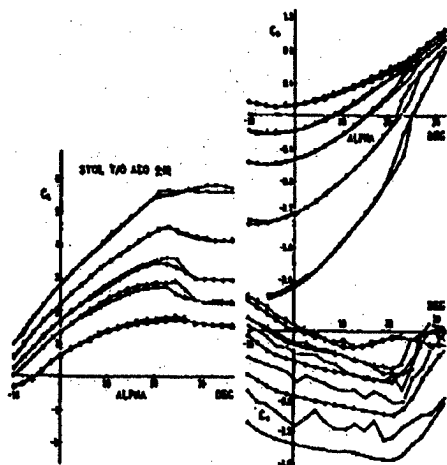
Figure 3.

Figure 4.

62
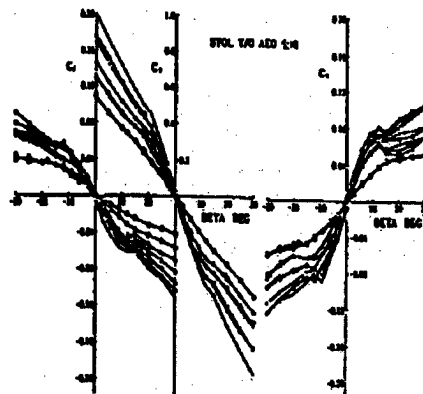
	CJ1	CJO	CJOL	CJIL	CJAL
O	0.000	0.000	0.0000	0.0000	0.0000
Δ	0.560	0.515	0.0000	0.0000	0.0127
●	1.105	1.040	0.0000	0.0000	0.0123
■	2.023	1.927	0.0000	0.0000	0.0225
o	3.382	3.144	0.0001	0.0000	0.0378

A3.2

	CJ1	CJO	CJOL	CJIL	CJAL
O	0.000	0.000	0.0000	0.0000	0.0000
Δ	0.543	0.498	0.0000	0.0000	0.0064
⊕	1.054	0.989	0.0000	0.0000	0.0012
⊗	1.974	1.881	0.0000	0.0000	0.0239
o	3.229	3,093	0.0000	0.0000	0.0389

62

	CJ1	CJO		
o	0.000	0.000 · 3.275 3.138		
Δ	0.563	0.518		
●	1.115	1.050		
x	2.027	1.931		

A3.2

	CJ1	CJO
o	0.000	0.000
Δ	0.500	0.500
⊕	1.044	0.961
⊗	1.963	1.888

5. Conclusion

We have developed a noncontact air joint (piping interference removal device) system as a system to replace the conventional rubber hose system to reduce the interference to the balance by the pressure piping in the wind tunnel test of the motive power provided model using high-pressure air. We have conducted functional and effect tests on the new system. Reproducibility was assessed primarily using forms comparable with data obtained by the conventional rubber hose system in the effect test. The results demonstrated that there was no great difference in the aerodynamic coefficient trend, the reproducibility was superior, and that the device was viable. Moreover, studying the advantages and disadvantages of this device indicate the following:

(1) Improved points

1) The piping interference is small.
2) Piping interference correction is unnecessary.
3) Continuous repetition of α and β sweeps is possible.
4) Bilateral symmetry (especially $C_J = 0$) has improved during β sweep.
5) The change for C_J of the stalling point position of C_L has become smooth.

5

(2) Problem points

1) Skill is necessary for installation.
2) It is easily affected by environmental conditions (humidity, dust, and oil).
3) The bellows joint is short, flexural rigidity becomes great and testing is not possible when the original pressure is low.
4) Since the floating shaft of the joint is all stainless steel, the force of inertia is great, standby is necessary for data collection after the model attitude angle setting, and the data are apt to become dispersed when the waiting time setting is unsuitable.

References

1. Nakatani and Hayashi, Patent Right Acquisition (Eccentric Fluid Coupling, Patent No. 1416296).

2. Takahashi, Nakatani, Iba, et al., 1988 Precision Engineering Society Lecture Conference.

3. Takahashi, Nakatani, Uchikawa, et al., "Total STOL Plane Model Wind Tunnel Test (Engine Nacelle Length Effect)," 26th Aircraft Symposium 1D7.

Effects of Engine Nacelle Length During Wind Tunnel Test of Total STOL Plane Model

[Article by Hitoshi Takahashi and Teruomi Nakatani, National Aerospace Laboratory; and Takashi Inoue, Kawasaki Heavy Industries]

[Text] 1. Introduction

A wind tunnel test has been conducted on a model of the STOL experiment plane "Asuka," which has been developed at the National Aerospace Laboratory. This model is 8 percent the size of the actual plane. The reduced ratio of 8 percent was derived from the ratio between the fan diameter of the FJR engine mounted on the actual plane and the fan diameter of the simulated engine mounted on the wind tunnel test model. However, the length of this simulated engine is longer than 8 percent of the actual plane engine. Therefore, it was necessary to correct for the difference in engine length for the data obtained during the wind tunnel test.

We have prepared an engine nacelle (flow-through nacelle) that has the same shape as that for the actual plane as well as a model follow-through nacelle (Figure 1) in order to assess the necessary correction level for this engine length difference. We have conducted wind tunnel tests using various forms and have made comparative studies based on the results corrected by the conventional correction method. We will report here on these results.

2. Correction for Nacelle Length Difference of Actual Plane and Model[1]

Since the simulated engine is relatively longer than the actual plane engine, as shown in Figure 1, the aerodynamic force working on the nacelle must be taken into account in calculating the aerodynamic force on the actual plane from the aerodynamic data obtained from the wind tunnel test. Correction for the nacelle length difference between the model and the actual plane is done by calculating the aerodynamic load working in the engine fan face position. In addition, a correction that takes into account the difference in the angle of incidence for the air intake (model 0°, actual plane 4°) of the model engine and the actual engine has also been added. The aerodynamic load for the nacelle has been calculated from the measured values for nacelle pressure distribution obtained in the wind tunnel test and by analyzing the nacelle

7

Model follow-through nacelle
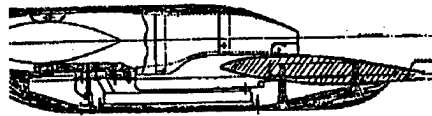
Actual plane-type follow-through nacelle

Figure 1.

Nacelle load
moment control
point
(Actual plane E/C
fan face surface)

Model supporting point

Model type
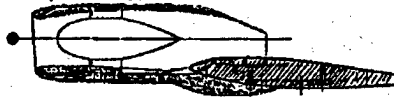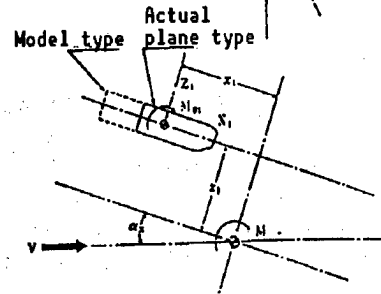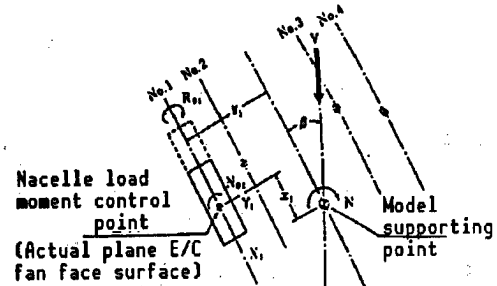
Actual plane type

Six component forces correction by
intake position difference

Figure 2.

intake surrounding flow for the actual plane and the model corresponding to the nacelle effective angle of incidence. The nacelle effective angle of incidence here is the sum of the angle of incidence of the airframe, the upwash angle from the main wing (obtained by numerical analysis), and the upwash angle by the fuselage (similarly obtained by numerical analysis). As shown in Figure 2, correction is made for the six component forces by using the calculated effective angle of incidence centered around the nacelle aerodynamic load and intake of both the actual plane and the model.

The six component forces (per engine unit) working on the model supporting points shown for the wind tunnel stability axes are as follows:

$$C_{L1} = C_{z1}\cos\alpha_N - C_{x1}\sin\alpha_N$$

$$C_{D1} = C_{z1}\sin\alpha_N + C_{x1}\cos\alpha_N$$

$$C_{m1} = C_{m01} + C_{z1}\frac{x_1}{\bar{c}} + C_{x1}\frac{z_1}{\bar{c}}$$

$$C_{y1} = C_{y1}$$

$$C_{l1} = C_{L1}\frac{y_1}{b} + C_{y1}(\frac{x_1}{b}\sin\alpha_N + \frac{z_1}{b}\cos\alpha_N)$$
$$+ C_{l01}\cos\alpha_N + C_{n01}\sin\alpha_N$$

$$C_{n1} = -C_{D1}\frac{y_1}{b} + C_{y1}(-\frac{z_1}{b}\sin\alpha_N + \frac{x_1}{b}\cos\alpha_N)$$
$$- C_{l01}\sin\alpha_N + C_{n01}\cos\alpha_N$$

8

The sum of the four engine units, respectively, becomes:

$$C_L = \Sigma C_{Li}, \quad C_D = \Sigma C_{Di}, \quad C_m = \Sigma C_{mi}, \quad C_y = \Sigma C_{yi}, \quad C_l = \Sigma C_{li},$$
$$C_n = \Sigma C_{ni}$$

The six component forces are obtained from the nacelle aerodynamic load of the model and the actual plane, and the difference for each component force becomes the correction amount caused by the nacelle length difference.

3. Wind Tunnel Test Results

3.1 Windmill Simulation Effect

A drag object (central body) equivalent to the windmill drag was attached in the interior of the flow-through nacelle (Figure 1) to replicate the windmill condition of the simulated engine. We compared the case where $C_J = 0$ (windmill condition) for the simulated engine and the corresponding case for the model flow-through nacelle. We conducted tests on the STOL T/O and STOL L/D forms. A portion of the test results are shown in Figure 3.

RUN No. 201 0 model-type   RUN No. 211 0 model-type
flow through.   flow through.
Windmill simulation.   Windmill simulation.
Total plane T/O condition.   Total plane L/D condition.
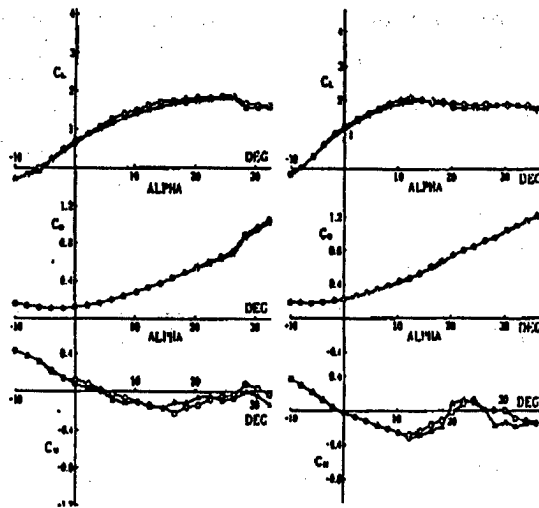
Figure 3.

Arranging these compared results shows:

(1) α sweep

- C_L is greater for the flow-through nacelle.
- C_D is smaller for the flow-through nacelle for small α and C_D is larger for the flow-through nacelle for large α.
- For C_m, α in which the flow-through nacelle demonstrates head lift is slightly larger.

9
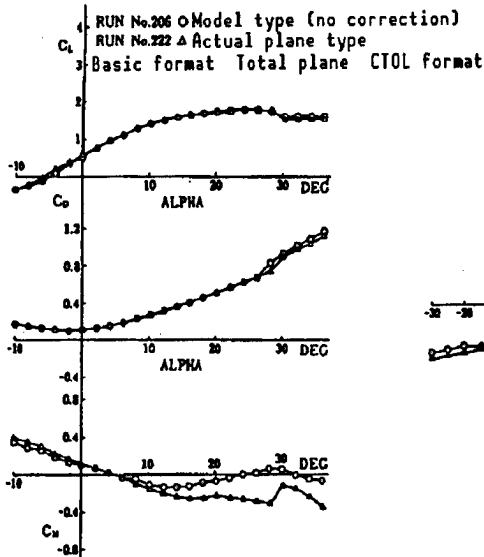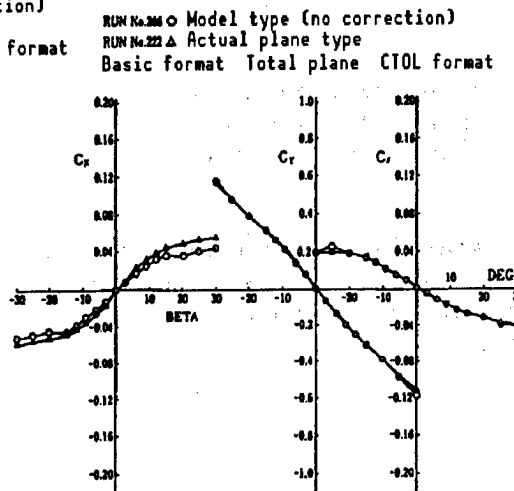
Figure 4.

Figure 5.

(2) β sweep

- C_y has a greater absolute value for the flow–through nacelle.
- There is practically no difference between C_l and C_n.

Moreover, these windmill effects were taken into consideration when analyzing the data of the flow–through nacelle.

3.2 Nacelle Form Effect and Nacelle Form Correction Effect

A wind tunnel test was conducted in various flap configurations for cruising, CTOL, STOL T/O, go–round, and L/O. The object was to compare data on the aerodynamic performance, focusing on the nacelle length difference between the actual plane and the model.

3.2.1 Effect of Nacelle Form

Examples of comparisons of the data for the actual plane–type flow–through nacelle and data for the model flow–through nacelle without a correction for nacelle form to check the change of the six component forces depending on the difference in nacelle length are shown in Figures 4 and 5. Moreover, a comparison of the results for the various flap forms makes it possible to arrange the six component forces as follows:

(1) α sweep

(a) C_L

- C_L of the actual plane–type nacelle is larger for small α.
- There is no difference between both sets of values in the α area excluding those for small α and large α.
- α becoming C_{LMAX} is larger by 2~4 percent for the actual plane type.

10

- When exceeding α is becoming C_{LMAX}, C_L of the model type becomes larger.

(b) C_D
- The actual plane type is smaller in large α.
- There is practically no difference between both in the α area excluding small α and large α.

(c) C_m
- α is greater for the actual plane type when C_m changes to plus.
- $C_{m\alpha}$ is greater for the actual plane type.
- Both the minimum and maximum values of C_m are larger for the actual plane type.

(2) β sweep

(a) C_Y
- $|C_Y|$ of the model type is larger in large $|\beta|$.
- There is no difference between both in the β area excluding $|\beta|$.

(b) C_1
- $|C_1|$ of the model type is larger in large $|\beta|$.
- There is no difference between both in the β area excluding large $|\beta|$.

(c) C_n
- C_n of the actual plane type is larger in the total plane form while $C_{n\beta}$ is larger in the actual plane type.

3.2.2 Nacelle Form Correction Effect

Examples of results of a data comparison of the actual plane-type flow-through nacelle and the model flow-through nacelle provided with a nacelle form correction to study the adequacy of nacelle form correction are shown in Figures 6 and 7. The results can be summarized as follows:

(1) α sweep

(a) C_L and C_D
- Correction is too great for C_L and C_D.

(b) C_m
- $C_{m\alpha}$ is practically identical.
- The difference between the maximum value and minimum value of C_m has decreased considerably.

(2) β sweep

(a) Correction of C_Y is too great.
(b) There is no difference in C_1.
(c) Correction for C_n is proper and the two almost coincide.

11
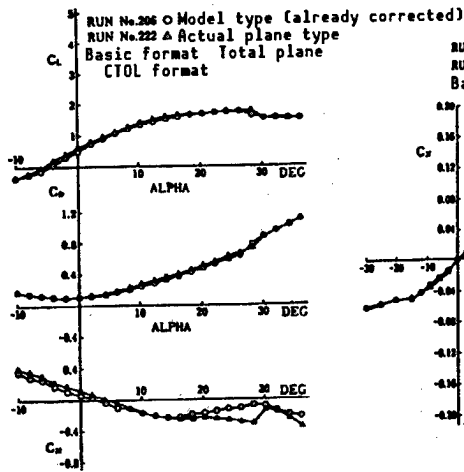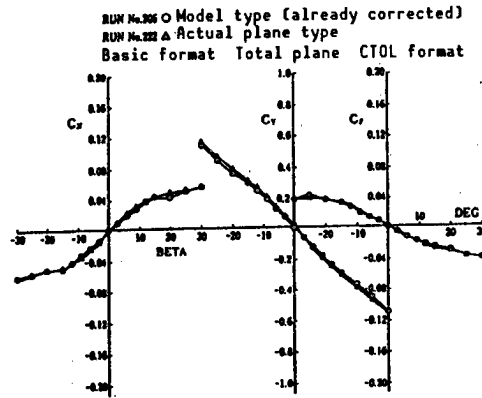
Figure 6.   Figure 7.

4. Conclusion

Actual plane-type and model flow-through nacelles were prepared and wind tunnel tests were conducted on them to study the adequacy of data correction for the difference in length between the actual plane and the model engine nacelle. However, only the case where $C_J = 0$ only was used due to restrictions on the simulated engine. As a result the following conclusions were obtained:

(1) Correction was too great for the force data.
(2) Moment data correction is quite good.

References

1.   NALTM-452, 1981, pp 52-53.

Laminar Flow Control Test of Three-Dimensional Swept-Back Wing

[Article by Yoji Ishida, Masayoshi Noguchi, Shigeo Kenba, Osamu Nonaka, and Hideo Hoshino, National Aerospace Laboratory]

[Text] 1. Introduction

Laminar flow control (LFC) technology aims at maintaining the boundary layer on a wing surface in a laminar flow by suction and at sharply reducing the frictional resistance. Research on LFC technology has been actively conducted primarily in the United States in recent years for the purpose of putting this technology to practical use.[1] Research on this technology has not been pursued as actively in Japan up to now. However, considering the effect of the application of LFC technology to the air transport system, there is an urgent need for Japan to develop its own LFC technology. To date, we have conducted LFC tests on wings with simple shapes (two-dimensional wing,[2] infinite yawing wing,[3] etc.). We have recently conducted an LFC test on a three-dimensional swept-back wing close to the shape of that of an actual plane and have been able to demonstrate a sharp reduction in resistance. This article will describe the results of that experiment.

2. Experiment

2.1 Model and Measurement System

Figure 1 is a schematic diagram of the model three-dimensional swept-back wing used in this test. The half wing width is 2.2 m, the leading edge sweep-angle is 26.5 dielectric anisotropy, the taper ratio is 0.58, and an area 950~1,650 mm from the span in the Y direction is a suction surface. The suction surface from near the leading edge up to 25 percent of the chord length is a porous surface and the area from 25 percent of the chord length up to 80 percent of the chord length is a multigroove surface. The surface downstream from 80 percent of the chord length is a nonsuction surface. Static pressure holes were provided in two places—Y = 950 mm and Y = 1,650 mm—to measure the static pressure of the wing. Figure 2 shows the internal structure of the suction blade. There is an independent small plenum chamber directly under the surface skin and there is a large collection duct that collects from 4~5 of these plenum chambers. Both the plenum chamber and the collection duct are

13
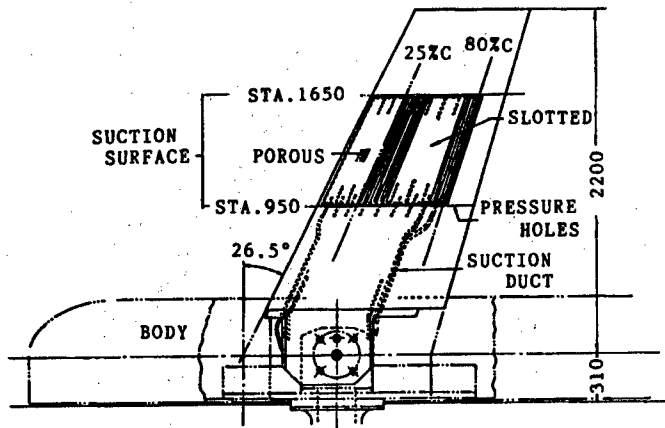
Figure 1. Schematic Diagram of Test Model

connected with the metering hole. there is a total of nine collection ducts. Suction is created by a vacuum pump through the suction duct allotted to each collection duct. The suction flow rate is measured by a float-type flow meter and the flow rate can be adjusted by a needle valve (Figure 3). Suction is created by the upper surface only.

2.2 Results of Experiment

We measured conduct on the wing surface static pressure distribution C_f, the static wake pressure and the total pressure distribution. Measurements were conducted when there was no suction. We also sought to identify a suction distribution (Figure 6) capable of maintaining laminar flow up to 90 percent of the chord length point at wind velocities of 30, 40, 50, and 55 m/s, respectively, and we used various conditions with incidence angles of 0° and 1° and wind velocities from 30-60 m/s (5 m/s interval).

2.2.1 Wing Static Pressure Distribution

The static pressure distributions for STA. 950 and STA. 1,650 at a wind velocity of 50 m/s and an angle of incidence of 0° are shown in Figure 4. The two static pressure distributions are virtually identical and the similarity of the span direction is good. Moreover, although omitted in the drawing, the difference attributable to wind velocity is also extremely small.

2.2.2 Natural Transition Point

The transition point of the boundary layer in the nonsuction surface was measured by the China-Clay method. The results are shown in Figure 5. The transition of the wing root (circled mark) is slightly faster than that of the wing tip (triangle mark), but there is no great difference. It is estimated that the transition point on the suction surface is positioned in the middle of both parts.

14
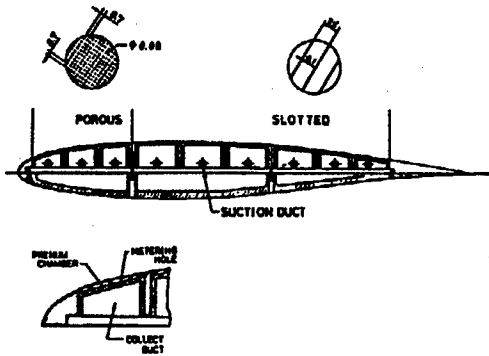
Figure 2. Internal Structure of
Suction Blade
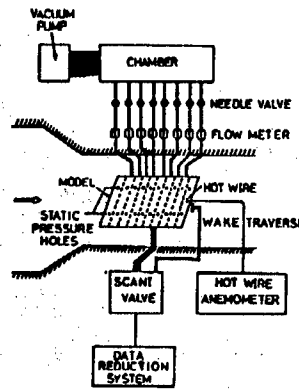
Figure 3. Suction and Suction Measur-
ing System
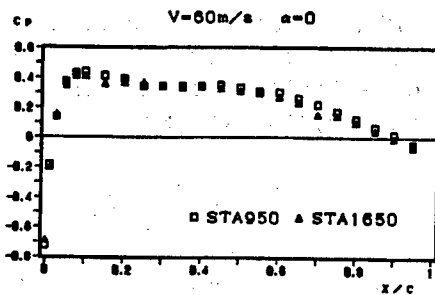
Figure 4. Wing Static Pressure
Distribution
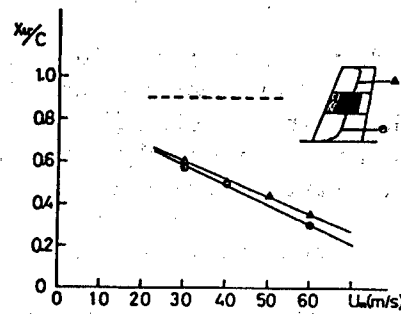
Figure 5. Transition Point (China-
Clay Method)

2.2.3 Suction Speed

We tried to delay the transition point estimated in Figure 5 up to the 90 percent chord length by suction. The necessary suction distributions at wind velocities of 30, 40, 50, and 55 m/s, respectively, are shown in Figure 6. The amount of suction is the value of the cm/s order. Characteristically, the amount of suction near the leading edge becomes large when the flow is three-dimensional.

2.2.4 Measurement of Drag

We carried out a wake traverse within the central cross section of the suction area and obtained the wake drag to assess how much the drag was reduced by the suction shown in Figure 6. Figure 7 shows the results thus obtained (angle of incidence 0°). It is known that the drag becomes less than one-half in the Reynolds number range, which has an effect during suction as compared to when there is no suction (circled mark). However, an accurate evaluation cannot be obtained unless the power required for suction is taken into account.

15
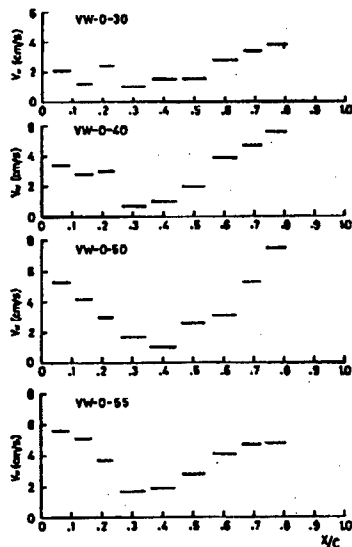
Figure 6. Suction Speed for Maintaining Laminar Flow Up to 90 Percent of Chord Length
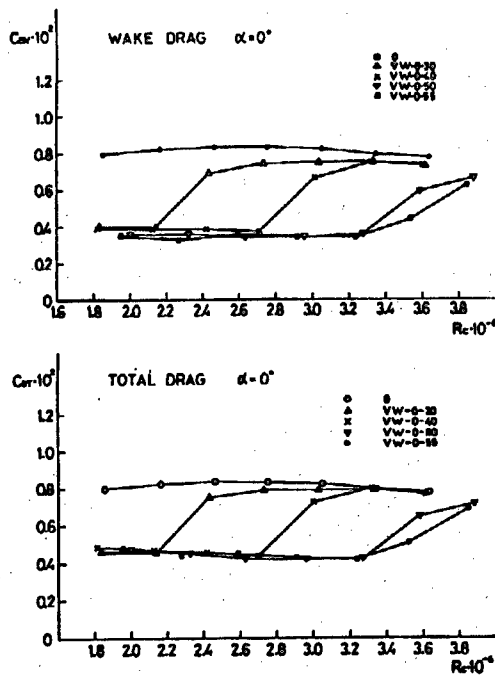
Figure 7. Wake Drag When Applying the Suction Speed Shown in Figure 6 (upper)
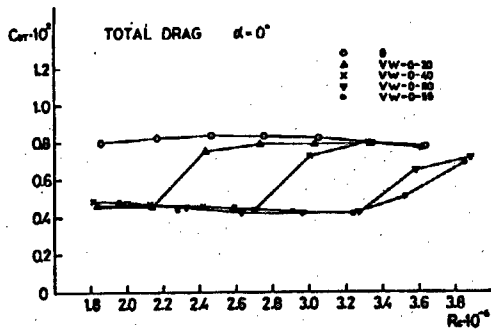
Figure 8. Total Drag Coefficient When Applying the Suction Speed Shown in Figure 6 (lower)

C_{Deq} or "equivalent drag," which means that the power required for suction has been converted into drag, consists of a term in proportion to the suction flow rate coefficient and a term in proportion to the integral of the product of suction speed and surface pressure. The total drag, C_{DT}, which adds drag to the wake drag, is shown in Figure 8. It is known that a further sharp reduction in drag occurs even when the suction power is taken into consideration.

The results shown in Figure 8 follow virtually a single line when plotted against the converted flow rate $C_Q \cdot 10^7 \sqrt{Rc}$ (Figure 9). It is known that the drag suddenly decreases when the converted flow rate exceeds a value of 3. The drag reduction factor far surpasses 40 percent in this case (Figure 10). It has been demonstrated that such a great drag reduction is achievable by maintaining the laminar flow up to the 90 percent chord length point.

In addition to the optimum suction mode described above, studies also have been made on the drag reduction effect when suction is applied near the leading edge or near the trailing edge only. The former consistently produces a drag reduction of about 14 percent up to 1 wind velocity of 55 m/s; however, the latter had absolutely no effect on drag reduction even during strong suction. Details of this phenomenon will be explained at the Lecture Meeting of the 27th Aircraft Symposium.

16
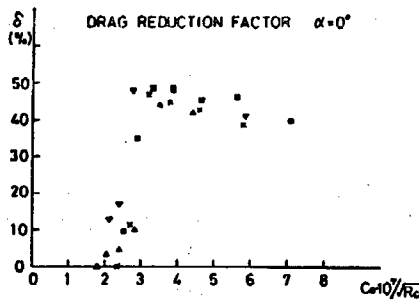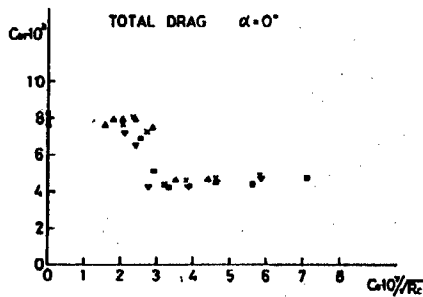
Figure 9. Diagram Plotting Total   Figure 10. Drag Reduction Factor
          Drag Coefficient Against
          Converted Flow Rate

3. Conclusion

A suction surface consisting of a porous surface and a multigroove surface was provided for an actual plane form three-dimensional swept-back wing and a laminar flow control test was conducted. A 90 percent chord length laminar flow was realized up to a Reynolds number of 3.8 (10^6) and to a wind velocity of about 57 m/s by adjusting the amount of suction. As a result, a sharp total drag reduction exceeding 40 percent was achieved even when the amount of power required for suction was taken into consideration.

Suction in the leading edge range is extremely important in the case of a three-dimensional wing and, generally, the higher the Reynolds number, the greater the amount of suction necessary. This demand is extremely critical and, when suction is insufficient, even by a very small amount, realization of a laminar flow is not possible.

References

1.   Harris, C.D., Harvey, W.D., and Brooks, Jr., C.W., "The NASA Langley Laminar Flow Control Experiment on a Swept, Supercritical Airfoil-Design Overview," NASA TP-2809, 1988.

2.   Ishida, Y. and Noguchi, M., "Experimental Research on Low-Speed, Two-Dimensional Laminar Flow Control Wing by Suction From Porous Surface," National Aerospace Laboratory Report, TR-967, 1988.

3.   Ishida, Y., "Experimental Research on Laminar Flow Control Wing at Low Speed," 1987 Research Announcement Meeting of National Aerospace Laboratory.

Electrostatic Breakdown of Electronic Equipment

[Article by Nobuai Naito, Japan Air Systems Co.]

[Text] 1. Introduction

In recent years, computers and communication and navigational equipment and instruments that have adopted many semiconductor devices and whose performance has been dramatically improved by the remarkable progress of electronic technologies have also been introduced in large numbers into aircraft. ICs (integrated circuits) and LSIs (large-scale integrated circuits), especially those that use MOS (metal oxide semiconductors) are being widely used and the realization of higher levels of integration and lower electricity consumption are being promoted. Although these semiconductor devices are indispensable for miniaturizing and reducing the weight of electronic equipment and instruments, they also suffer from significant defects in that they are extremely sensitive to the level of static electricity that the human body constantly possesses, they are subject to damage, their functions deteriorate and sometimes they can be fractured by contact with objects charged with static electricity or just by approaching a static electric field even without making direct contact. Electronic equipment and instruments incorporating these semiconductor devices are subject to the influence of static electricity through their external terminals or connectors. There have been many cases where the problems of electronic equipment and instruments were caused by the influence of static electricity. Initially, they are manifest as potential troubles; they then become nonconformities in which reproducibility is hard to achieve and inquiry is difficult. Thus they can pose serious threat to the reliability of an entire system that uses such electronic equipment and instruments.

Since the number of so-called high technology aircraft that use many pieces of high-performance electronic equipment and instruments incorporating electronic parts that are sensitive to static electricity will continue to increase in the future, special care is required in handling them.

This article will describe the effects of static electricity on electronic parts, equipment, and instruments together with the countermeasures adopted by aviation companies.

18

2. Mechanisms of Static Electricity Discharge and Static Electricity Fracture Generation

When the distance between objects electrified with different types of static electricity of more than a sufficient amount is small, the electric charge is discharged through the air and a current flows between the two objects, even when they are not connected with a conductor. Static electricity is discharged practically unnoticed from the human body when the voltage is less than about 10,000 volts. The relationship between humidity and a human body charged with static electricity in daily life is shown in Table 1. Static electricity of about 10,000 volts is generated daily on workers engaged in the maintenance of an aircraft and this leads to recognizing anew the importance of static electricity prevention measures in aircraft maintenance.

Table 1. Relationship Between Humidity and the Size of a Static Electricity Charge Carried by the Human Body

Cause of static electricity generation	Generated static electricity voltage (Volts)	
	Humidity 10~20%	Humidity 65~90%
Walking on carpet	35,000	1,500
Walking on vinyl floor	12,000	250
Working at bench	6,000	100
Part replacement work and taking paper sheets in and out of a vinyl envelope	7,000	600
Working while sitting on a chair with a polyurethane seat cushion	18,000	1,500

Electronic parts, thin film resistors, bipolar, and junction devices using MOS sensitive to static electricity are subject to damage of the oxidized electrode layer and junction parts by the high voltage of static electricity or discharge current and a functional deterioration of stalling is generated.

A protective circuit for static electricity is generally incorporated by the parts manufacturers in these devices, but since the amount of static electricity varies widely depending on the generating conditions, it is virtually impossible to adopt protective measures for static electricity at all levels. An example of an IC from an OP AMP that was actually damaged by the discharge of static electricity is shown in Figure 1. A classification of electronic parts sensitive to static electricity by the static electricity pressure proof level is shown in Table 2.

(Magnified 20 times)   (Magnified 200 times)

(Magnified 1,000 times)   (Magnified 5,000 times)
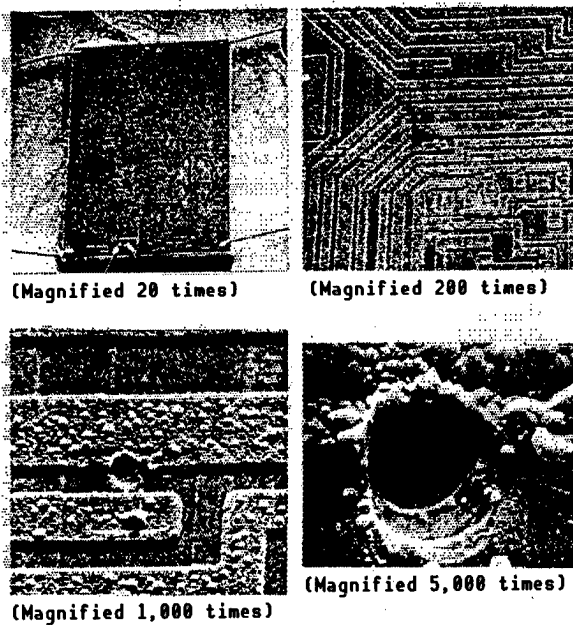
Figure 1. Damaged Area About 6 Microns in Diameter on IC From
OP AMP Caused by Static Electricity Discharge
(► indicates the damaged part.)

3. Static Electricity Comprehensive Measures

In providing static electricity fracture prevention measures for electronic
equipment and instruments, it must be emphasized that such measures will be
worthless if such measures are provided for one section only. A comprehensive
and continuous scheme must be provided from the production and assembly
process of parts, equipment, and instruments by production manufacturers up to
end users, and this must include inspection services at customs clearance in
case of import/export products.

For aircraft companies, measures to prevent static electricity fracture begin
with acceptance of electronic equipment and instruments and electronic parts
that are sensitive to static electricity. They include storage, handling,
installation on the airframe, airframe maintenance and continue up through the
maintenance of equipment and instruments removed from the aircraft.

(1) Establishment of Awareness

The most important and basic element in the execution of comprehensive
measures is to establish awareness. There can be no success unless a correct
cognition and understanding of the problem points involving static electricity
can be established. Learning how static electricity affects electronic parts;
elaborating an identification method that can be used for electronic parts,
and electronic equipment or instruments using such parts; and establishing,
standardizing, and thoroughly vetting basic operations are important for all
aspects of handling parts, equipment, and instruments sensitive to static
electricity.

20

Table 2. Classification by Static Electricity Pressure Proof Level

Classification	Electronic parts
1A. Extremely low pressure proof level (0~170 V)	• MOS (metal oxide semiconductor) devices without protective circuit • Microwave semiconductor • SAW (surface acoustic wave) device • JFET (junction field effect transistor) • Microcircuit using LSI (large-scale integrated) • Silicon on sapphire • Gallium on arsenic compound
1B. Comparatively low pressure proof level (170~1,000 V)	• CMOS (complementary metal-oxide semiconductor) device • Bipolar transistor • ECL (emitter coupled logic) • SCR (silicon control rectifier) • Film-shaped thin resistor • Hybrid using parts of 1B classification
2. Medium pressure proof level (1,000~4,000 V)	• MOS device with protective circuit • Schottky device • Precision resistance network (RZ type) • TTL (transistor transistor logic) microcircuit • OP AMP using MOS capacity • LSI • Hybrid using parts of classification 2
3. Comparatively high pressure proof level (More than 4,000 V)	• Zener diode • Power rectifier • Power diode

(2) Educational Training

The objective cannot be achieved when only some sections conduct educational training on static electricity measures. It is necessary to conduct educational training that is consonant with different workshop environments, continuously and not sporadically, within an overall framework that includes design, manufacture, assembly, inspection, packing, storage, shipping for the manufacturers, acceptance, inspection, transportation, storage, and installation on and removal from airframes, repair and inspection and, moreover, handling during customs inspection in the case of import/export products for users. Educational training by aviation companies is necessary not only for those engaged in aircraft maintenance but also for parts maintenance workers in the maintenance shop and workers engaged in the acceptance, storage, and handling of parts. In addition, education should not be temporary and it is necessary that cautions on static electricity also be established in maintenance manuals, operating procedures, etc. Further, improving awareness and

21

standardizing operations for electronic equipment and instruments, and parts sensitive to static electricity should be promoted routinely.

(3) Identification (Warning labels)

When handling parts sensitive to static electricity, it is necessary to put it in a static electricity shield bag to prevent static electricity fracture and to paste a warning label like that shown in Figure 2 on the bag to show that it contains parts sensitive to static electricity. Moreover, together with pasting a warning label and taking similar steps to identify electronic equipment and instruments that use parts sensitive to static electricity, it is necessary to call attention on handling. This warning label consists of a yellow base so that the meaning can be grasped at a glance, a standard symbol in block, and a written handling precaution. It is necessary for workers handling parts sensitive to static electricity to understand the meaning of this type of warning label and to take special care when working. It is also necessary for aviation companies to show clearly in their maintenance manuals, operation procedures, etc., which pieces of electronic equipment and instruments and parts are sensitive to static electricity and to instruct employees engaged in maintenance work to paste a warning label on relevant parts that do not have labels.

A standard label marked "RS 471" is used in civil aviation in the United States.

(4) Storage of Parts Sensitive to Static Electricity

The important thing when storing parts that are susceptible to the effects of static electricity is to store them as they are in the static electricity shield bag when these parts have been shipped from the parts production manufacturers. The static electricity shield bag prevents the generation of static electricity within the bag as well as preventing the intrusion of static electricity from the exterior. The bag is transparent to allow inspection of its content without having to take it out of the bag.

An example of the structure of the static electricity shield bag is shown in Figure 3. A static electricity shield bag that contains parts should, as a general rule, not be opened in places other than a workbench provided with measures to protect against static electricity. This is because parts can become charged with static electricity and subjected to its influence merely by conveying the parts even when there is no contact with their conductive elements.

(5) Working Environment of Maintenance Shop

The level of humidity within the maintenance shop is an important factor in the generation of static electricity. A humidity level of 40-60 percent is generally ideal, but the generation of static electricity cannot be completely prevented even by maintaining humidity in this range. The environment within the maintenance shop is generally air-conditioned and it is necessary in this case to pay attention as the humidity frequently becomes low. Since dust becomes the generation source of static electricity, dust control is also

MIL-STD-129

JEDEC/EIA Standard RS471

(Joint Electronic Device Engineering Council / Electronic Industries Association)

Caution
Contents
Static-Sensitive
Handling
Precautions Required
Contents _____

Caution
Static-Sensitive
Devices
Handle Only at
Static-Safe Work
Stations
Reusable Container
Do Not Destroy

Figure 2. Examples of Warning Labels

4. Wear resistant coating

1. Polyethylene film   2. Polyester film   3. Conductive metal (nickel) layer
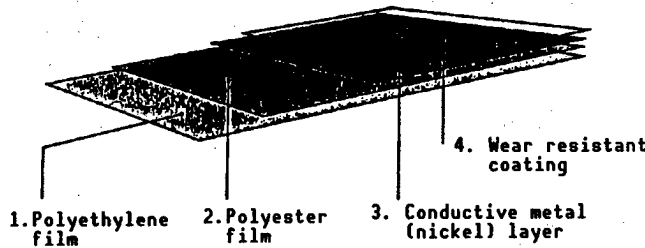
- Nonelectrification property (resistivity 10^{13} Ω/sq)
- Heat sealing possible
- Tear resistant
- Great dielectric strength

- Highly tension resistant
- Excels in dimensional stability
- Great dielectric strength
- Resistance to breakdown is great

- Resistivity 10^{2} Ω/sq
- Continued conductivity
- Transparent (light transmittance 40%)

Figure 3. Example of Static Electricity Shield Bag

important. It is especially important to note that air ionization prevents the electrification of insulating materials and prevents dust adhesion. Moreover, since floors can easily be a source of static electricity as many people, carts, etc., move across them, an electroconductive floor material capable of releasing static electricity safely, surely, and yet promptly is necessary. A new fiber possessing a self-discharging property recently has been developed. When such a fiber is used in workclothes, etc., the static electricity generated on the human body and workclothes will always be discharged into the air so that neither the body of the worker nor his clothes will become charged with a high potential of static electricity. It is believed that this will be effective in preventing damage to electronic equipment and instruments by the direct discharge of static electricity.

```
Wrist strap (current
limiting resistance
┌─1 MΩ incorporated)            Conductive work board
○─/\/\/─┐                    ┌─ ⁻(Max 10⁸ Ω)

    ┌──/\/\/──┐    ═══════════════════════════════
(5M 1Ω~1M 1Ω)
                    ║                            ║
                    ║                            ║
(5M 1Ω~1M 1Ω)
    ┌──/\/\/──┐    ═══════════════════════════════
    ═══════════════════════════════════════════════
    ┴
          └─Floor      └────Conductive floor mat
```
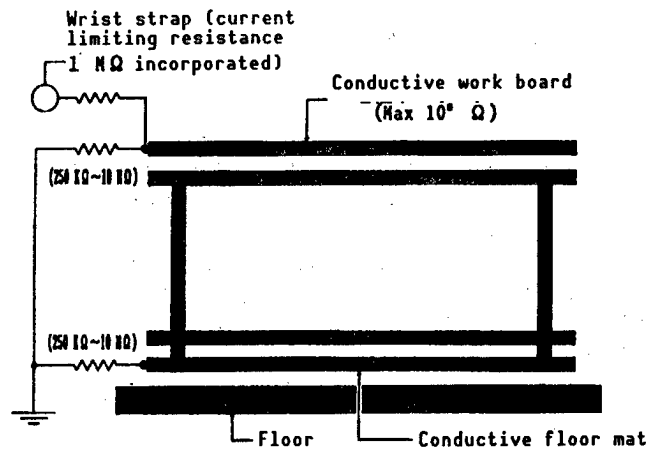
Figure 4. Workbench

(6) Work Table

It is necessary that a work table where parts, equipment, and instruments sensitive to static electricity are handled be provided with the correct parts and is properly grounded, as shown in Figure 4. In particular, a wrist strap worn on the worker's wrist is important for promptly releasing charged static electricity from the human body. Moreover, it is necessary to check periodically to ensure that the electroconductive workboard on the work table surface is always clean and that a correct electrical characteristic is maintained.

(7) Working Environment for Maintenance Within Aircraft

Electronic equipment and instruments mounted on aircraft are also occasionally subject to the effects of lightning, in addition to sudden changes of temperature, humidity, atmospheric pressure, etc. These are used in extremely severe environments compared to most ordinary electronic equipment and instruments. There are also cases when the replacement of electronic equipment and instruments must be done outdoors. This is also sometimes true for maintenance work. The principal measure that can be taken to protect against static electricity that can be used in such an environment at the present stage is to make workers aware that there must be no direct contact with the external terminals or connectors of electronic equipment and instruments that incorporate parts sensitive to static electricity. However, since it is certain that the number of aircraft using electronic equipment and instruments sensitive to static electricity will only increase in the future, measures to protect against static electricity during aircraft maintenance work is a big topic for the future.

(8) Handling During Customs

It is necessary to give special attention to handling procedures during customs clearance when importing and exporting electronic parts and electronic equipment and instruments that incorporate electronic parts sensitive to static electricity. It is necessary for the customs persons concerned to understand the problems of static electricity correctly. It is also necessary to explain patiently to them that electronic parts, equipment, and instruments are subject to damage by improper handling.

24

(9) Trouble Diagnosis for Electronic Equipment and Instruments Subject to Static Electricity Fracture

Since the functional nonconformity of electronic equipment and instruments affected by static electricity fracture lacks reproducibility, as mentioned above, and since there are many cases when diagnosing the trouble is difficult, a great emphasis is placed on the reliability of the system. When aviation companies conduct maintenance work on electronic equipment, instruments, and parts where there is a possibility of suffering static electricity fracture, it is important for maintaining the reliability of the system that the parts maintenance department and airframe maintenance department keep in close contact with each other and exchange data on past positive maintenance achievements.

4. Recent Trends

The refining and diversification of semiconductor devices have continued to progress and these devices have become even more susceptible to the influence of static electricity. In addition, many pieces of electronic equipment and instruments that have been made of solid state components and digitized by using such parts have been mounted in aircraft and these aircraft have appeared as high technology planes.

When these aircraft encounter thunder during flight or when lightning occurs in their vicinity, discrepancies caused by damage to parts sensitive to static electricity in the interior of electronic equipment and instruments can cause malfunctions of the systems using this equipment and instruments. Deteriorated functions have been reported in the United States recently. These discrepancies have been noted to affect computer logic, automatic control of engine thrust, and automatic flight control. Composite materials are becoming widely used in airframes and since they are nonconductive materials, they are also susceptible to the effects of thunder. It is standard practice for each manufacturer of aircraft, electronic equipment, and instruments to apply a preventive measure against thunder in the design process; however, this cannot be said to be perfect.

Therefore, the U.S. Federal Aviation Agency (FAA) is seeking to adopt a new regulation on measures to protect against the effects of thunder. This regulation, which would apply to new airframes, would require the use of an electronic system based on advanced technology.

5. Conclusion

It will be impossible to achieve the objective unless measures to protect against static electricity are universally applied. It is also necessary that these measures be applied continuously at all levels of the company to maintain the reliability of the system. However, the most important thing is to conduct operations that are fundamentally sound. It must also be acknowledged that it takes time to gain an accurate knowledge of those parts that are sensitive to static electricity and to realize sufficiently that practically all static electricity fractures are attributable to human causes.

References

1. "Guidance for Electrostatic-Sensitive Device Utilization and Protection," ARINC (Aeronautical Radio, Inc.) Project Paper 606.

2. Proposed Rules: "Protecting Electrical and Electronic Systems Against Lightning," FEDERAL REGISTER, U.S. FAA, Vol 54 No 102.

Issues Related to Subsonic Passenger Plane Technologies

906C0041E Tokyo HIKOKI SHINPOJIUMU in Japanese Oct 89 pp 312-313

[Article by Tsuruo Choyo, Japan Aircraft Development Association]

[Text] It is the dream of engineers who design passenger planes to develop a new type of passenger plane by using epochal technologies and thereby conquer the global passenger plane market.

The story of how the following aircraft competed in the world market fires the imagination of engineers even now. However, in the realm of subsonic jet passenger planes designed for short and medium distances, there is no strong demand for high speed from the user's side when considering the block flight time. Further, since it is impeded technically by the sound barrier, by the compressibility of air, high speeds do not become a big topic for this type of passenger plane.

> Boeing 247 and Douglas DC-3
> Douglas DC-4, DC-6, DC-7, and Lockheed Constellation
> Boeing 707 and Douglas DC-8
> Douglas DC-10 and Lockheed L-1011

Comfort, cost, appeal to passengers, safety improvements, etc., become relevant when speed, which is the greatest advantage of aircraft compared to other means of transportation, does not greatly exceed the speed of conventional means. However, this does not mean that the passengers and airline companies are greatly dissatisfied by or have problems with current aircraft.

In comparison with other means of transportation, aircraft are more comfortable, safer, and economical. There are not necessarily more bankruptcies among airline companies than among other types of businesses. It has been said that statistically the accident rate per flight distance is not reflective of a great safety record. Although people say they are afraid of flying, the number of nonurgent and unnecessary sightseeing tourists is skyrocketing yearly. Historically, the number of passengers decreased sharply after an aircraft accident and a long time was required for recovery, but in recent years, such decreases have been small and recovery has been fast.

27

Nevertheless, sales competition among passenger plane manufacturers is extremely severe. It cannot be said that an aircraft will sell just because it is cheap or when, to use a broad term, it is a slightly "profitable aircraft." Aircraft preferred by passengers, aircraft preferred by pilots, and aircraft with a good profit margin will sell. The technical question is how can such an aircraft be made.

This situation is not much different from the development competition among manufacturers of general merchandise. It may be said that the technical and design topics for subsonic and transonic passenger planes are the same as those for a color TV. Although a fuss has been made over high-resolution TV, the common people do not necessarily look forward to the starting of high-resolution TV broadcasts. This is because they would have to purchase and replace equipment that is expensive and they refrain from burdening the large sum listening charges which is compulsorily collected. The common people will not be troubled by not seeing the high-resolution TV.

There is currently a complete set of jet passenger planes. These planes range from the 100-seat class up to the 520-seat class. This situation is virtually the same as that for color TV. Both TV and aircraft manufacturers had exerted efforts to expand the range from ultralarge sizes down to lower-end sizes. Each also encountered difficulties in their own ways and the issue has been how to find a gap in this fully packed market system. However, although there may be a slot (gap) referred to as, "It is good neither for one thing nor another" in the conventional merchandise system, the slot will be crushed by the conventional products and its merchandizing will be a failure unless the slot has a sufficient existing value in terms of its aim, performance, and cost against other conventional merchandise. In any event, passenger plane manufacturers around the world are seeking to sell new airframes by discovering new slots together with improving conventional planes and exerting efforts to secure a share of the market. At the same time, they are continuing to devote a huge amount of resources in basic technical research and development. The question is whether there is a project or not, and the research base has not changed. The principal areas of research are:

Improving aerodynamic efficiency: Improving MXL/D
Improving structural efficiency : Weight reduction
Improving passenger comfort
Improving the social environment, such as noise reduction, etc.

When the time comes, the results of this research and technical development will be integrated and a product developed. One approach is to develop an innovative passenger plane by freely using innovative technologies abundantly. Other approaches involve developing an airframe that represents an evolution of current airframes or developing an airframe whose technical level is in the improvement range although it was developed from scratch to take full advantage of up-to-date technologies. Deciding which approach to follow depends greatly on the decision of the designers and engineers. No matter which route is chosen, a sufficient existing value cannot be exhibited against a competitive plane unless such basic technical research and development has been carried out.

Both the Boeing 737 that has improved the present plane and the Airbus A320 that has utilized new technologies have succeeded; however, the 737, which was considered to have achieved a revolutionary performance difference by actively adopting technological innovation, has yet to be a commercial success.

The Japan Aircraft Development Association, with the aid of MITI, is conducting research in the following areas:

- R&D of a new type of plane in concert with Boeing—YXX
- Potentiality investigation of international joint development of 75-seat plane

There is a recognition that this corresponds to efforts to discovering slots, efforts to prepare slots, and efforts to expanding the periphery, as described above. Since my intention is to announce the contents, to the extent possible, of concrete research examples such as research on aerodynamics, structure, and productivity improvement, etc., within permissible limits and also in the 27th Aircraft Symposium, it will be appreciated if those informed on this matter will examine and make comments on this subject. Based on these valued opinions, we hope to make our future research more effective.

Investigation of Civilian Transport Plane YSX 75

906C0041F Tokyo HIKOKI SHINPOJIUMU in Japanese Oct 89 pp 326-329

[Article by Shinichi Nakagawa, Mitsubishi Heavy Industries]

[Text] **1. Market Environment for 60~100 Seat Plane**

Planes of this class fell between the cheap turboprop planes with less than 60 seats and jet planes with more than 100 seats. However, the operating cost per seat of planes in this latter category became cheap and, therefore, 60~100-seat planes were not able to gain a big share of the market. Sales of the F-28 were limited to few planes and the DC-9 and Boeing 737 were made into large planes at an early stage. There were only 600~700 jet planes in this division that were ever operated (Figures 1.1 and 1.2).

Since planes of this size were generally used for comparatively short-distance operations, it was difficult to take full advantage of the high speed of expensive jet planes in competition with the cheap turboprop planes. Although slightly too large, these latter planes were able to compete with large jet planes because of their cheap operating cost per seat. Thus, intermediate planes could not penetrate the market for economic reasons. An examination of the ASK distribution shows that planes of less than 100 seats play only a supplementary role; however, when planes of this class can advance into the present market of more than 100 seats, there is a great latent demand (Figure 1.3).

Investigation on Airline Companies

Visits were made to airline companies in Japan, the United States, Europe, and the Asian and Pacific areas in 1987 and 1988 to investigate opinions regarding the future trends in the demand for planes of this class. Opinions fell into two broad groups. One group expressed a desire for planes of 75~100 seats, citing the necessity for delicate servicing, given the increase of passengers, airport confusion, and liberalization. The other group doubted that this class of planes would be necessary, arguing that the economical development of such planes would be difficult. The realization of an economical high-speed plane is the key.

30
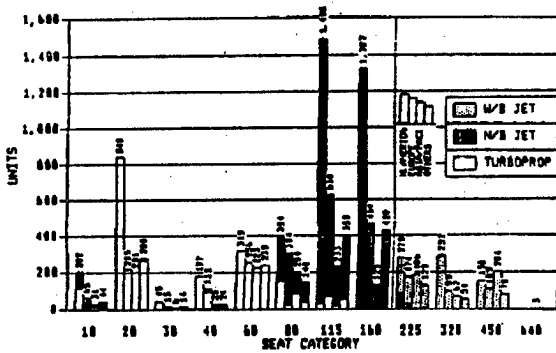
Figure 1.1 Actual Fleet—1987
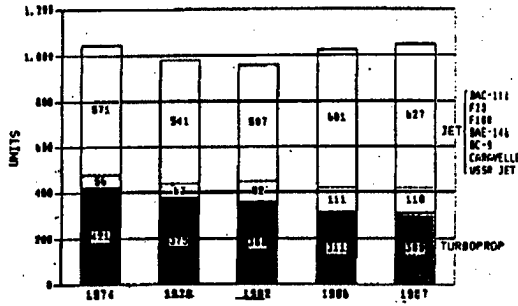
Figure 1.2 60~99 Seater Aircraft Fleet History
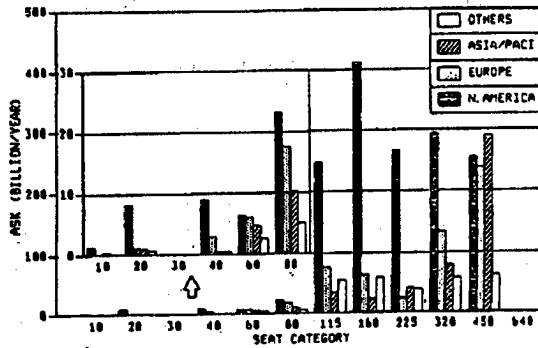
Figure 1. 3. ASK Distribution—1988

2. Conditions in Various Foreign Countries and Development of Competitive Planes

Both foreign aircraft and engine manufacturers have the same understanding of the market environment. There are projects (Figure 2.1) besides the YSX 75 and many of these are based on the concept of joint development among many countries.

3. Image of Airframe Specifications

The specifications of the airframe were established based on the results of the investigation mentioned above. The conceptual design included the following:

Number of seats   :   75 seats   An aft fuselage extension to provide for
                                              90~100 seats is also being considered.
Speed   :   Cruising speed M = 0.75 (economical cruising)
Cruising distance: 1,500 NM
Take off and land-
ing performance   :   1,500 M   1,400 M also considered domestically
Type   :   Can be converted subsequently to turboprop engine
Price   : $12~14 million

31

Type of aircraft	No. of seats	Developer	Development projects and present status	Characteristics/others
MPC 75	Standard 76 seats	•Joint development MBB (West Germany)/CATIC (China) •Lockheed (U.S.) Japanese participation in joint development sought	•Development scheduled 1991 •Initial delivery in 1995 or 1996 •Establishment of MPC Aircraft Co. • [illegible]	•Newly sold •Propfan engine mounted
ATRA90	93~130 seats	•JPTN (Indonesia)/Boeing (U.S.)/MBB West Germany)/Fokker (Holland) joint development	•Design work in suspension •Propfan engine trends, market trends being narrowed down	•Newly sold •Propfan engine mounted
RJ	Standard 48 seats	•Canadair (Canada)	•Initial delivery in second quarter 1992 •G/A March 1989	•Determination of large jet plane, Challenger 601 •Orders for 116/20 Jun 89
Shorts FJX	Standard 44 seats	•Shorts(England) •Participation of MBB (West Germany) in joint development project sought	•Initial delivery 1993 under initial project •G/A in second quarter 1989 under initial project	•Newly sold •Development discontinued following buyout of Shorts by Bombadier Co.
ATR92	80~100 seats	•Joint development among Aerospatiale (France), Aeritalia (Italy), Casa (Spain)	•Research stage •G/A scheduled 1991 •Initial delivery 1994–1995 •Engine not yet selected	•Possibility of Aerospatiale's AS100 airframe, Aeritalia's VMA becoming ATR92 great •Newly sold
EMB145	45~48 seats	•Embraer (Brazil)	•Launched Jun 89 (initial flight 24 Jun 89) •Initial delivery spring 92 •Mounted engines CFE738, ALF–302, RB/AllisonRB 380	•Searching for financial partner • [illegible]

Figure 2. Development Trends of Competitive Aircraft

```
Engine                   : Turbolan (or ProPlan)
Pax                      : 75 (5 abreast, 32 in pitch)
Design image             : 1,500 nm
Max operating altitude
  cabin pressure         : 35,000 ft./7.48 psi
Max cruise speed/
  altitude               : 0.82 Mach/35,000 ft.
Max operating speed      : 340 kt.CAS/0.82 Mach
Balanced field length    : 1,500 m (Max T/O weight, ISA, sea level)
Landing field length     : 1,500 m (Max L/D weight, ISA, sea level,
                             dry runway)

En route climb limit
  altitude               : 16,000 ft.
                             (1,000 nm mission weight, ISA·10°C)
Initial cruise altitude
  capability             : 35,000 ft. (Max T/O weight)
Max payload              : 17,250 lbs. (Full Pax. 230 lbs./pax.)
```

Requisition sheet for Option 1 (high-speed steering aircraft)

```
Engine                   : Turbolan (or ProPlan)
Pax                      : 75 (5 abreast, 32 in pitch)
Design image             : 1,000 nm
Max operating altitude
  cabin pressure         : 35,000 ft./7.46 psi
Max cruise speed/
  altitude               : 0.72 Mach/35,000 ft.
Max operating speed      : 320 kt.CAS/0.72 Mach
Balanced field length    : 1,200 m (Max T/O weight, ISA, sea level)
                         : 1,200 m (350 nm mission, ISA·20°C, sea
                             level)
Landing field length     : 1,200 m (Max L/D weight, ISA, sea level,
                             wet runway)
En route climb limit
  altitude               : 16,000 ft.
                             (1,000 nm mission weight, ISA·10°C)
Initial cruise altitude
  capability             : 35,000 ft. (Max T/O weight)
Max payload              : 17,250 lbs. (Full Pax. 230 lbs./pax.)
```

Requisition sheet for Option 2 (STOL steering aircraft)
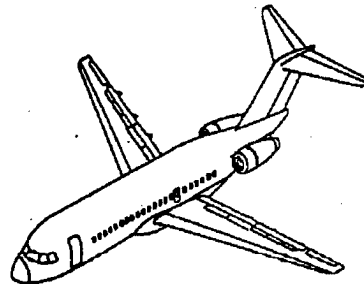
Figure 3.1 [Drawing and Specifications]

The specifications are shown in Figure 3.1. Option 1 refers to those with a take-off and landing distance of 1,500 m while Option 2 is for a STOL of 1,200 m.
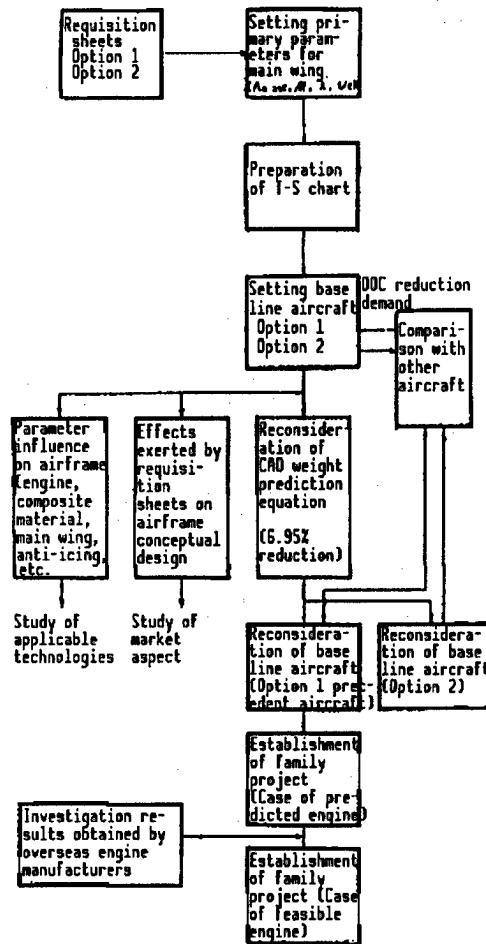
Figure 4.1 Flow of Conceptual Design Work for YSX 75

4. Conceptual Design

A conceptual design that satisfies the above specifications was prepared using CAD (computer aided design) (Figure 4.1). The type of main wing selected for this plane is shown in Figure 4.2 The layout of the passenger cabin is shown in Figure 4.3 and the flight pattern used to determine the design cruising distance is shown in Figure 4.4.
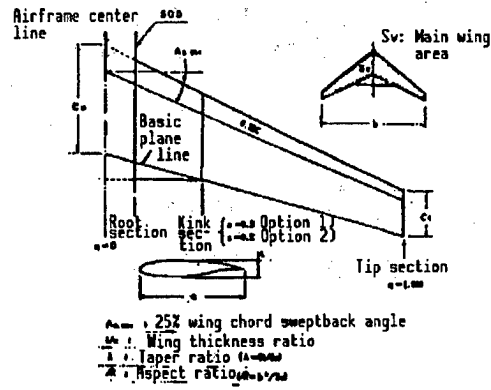
Figure 4.2 List of Principal Parameters for Main Wing

G: Galley
L: Lavatory
S: Stowage
A: Attendant sheet
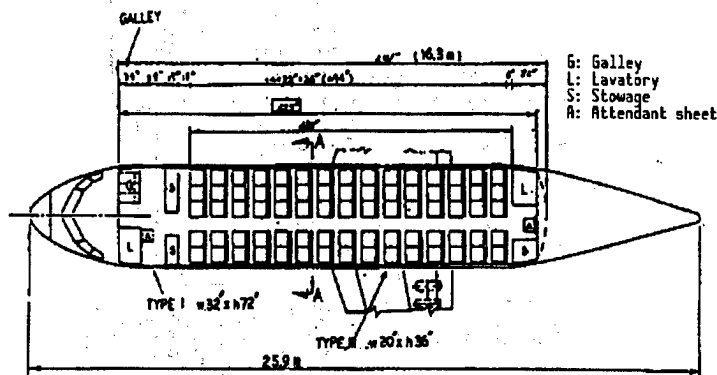
Figure 4.3 Layout of Passenger Cabin
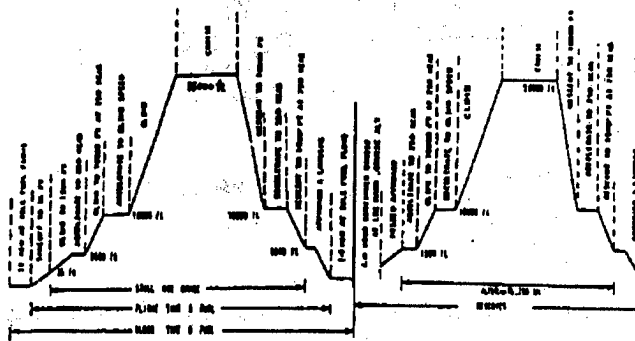
Figure 4.4 Flight Pattern for Designed Cruising Distance
Notes: (1) 1,500 nm Option 1 designed cruising distance (windless)
　　　 (2) 1,000 nm Option 2 designed cruising distance (windless)

35
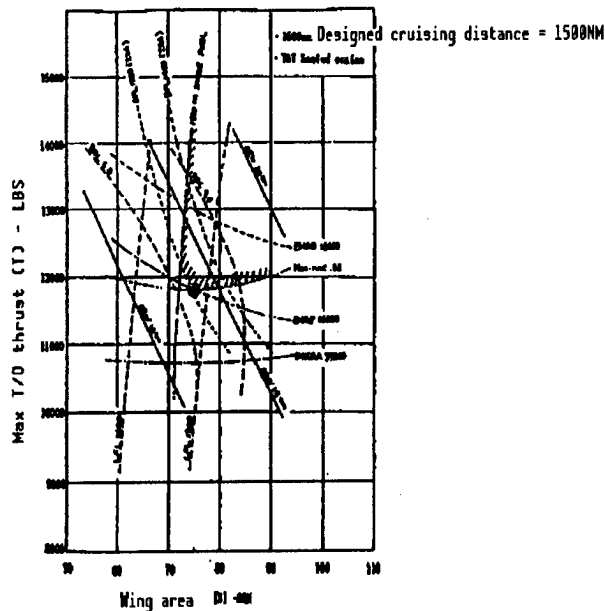
DEV: Operating weight empty (ton)
BFL: Take-off runway length (at maximum take-off weight, ISA) (m)
LFL: Landing field length (at maximum landing weight, DRY)
INICRA 35000: Initial cruising altitude: 35,000 ft.
ENRB 16000: Engine-starting/stopping ascending limit: 16,000 ft.
             (Main wing leading edge anti-icing bleed air extraction)
ENRP 16000: Engine-starting/stopping ascending limit: 16,000 ft.
             (Not dependent on main wing leading edge anti-icing bleed
             air technique)
H_{CR}-MAX.82: Maximum cruising speed: Mach 0.82 (300 nm cruising range,
             80% road factor, cruising intermediate point weight)
1500 nm RANGE FUEL: Necessary main wing area for loading fuel
                     necessary for 1,500 nm cruising range)
DOC: Direct cruising cost for 1,500 nm range

Figure 4.5 Option 1 T-S Chart

The baseline plane mentioned here is an airframe that has been designed
based on the existing low by-pass ratio engine performance. The design
technique used was the T-S diagram shown in Figure 4.5 and the optimum
combination of the maximum T/O output and main wing area satisfying the
demanded specifications was obtained by this diagram.

The effects of the engine, the high-lift device, the materials used
(composite materials), the main wing leading edge anti-icing system, and the
engine mounting system against the established base line plane were studied
and evaluated. The conceptual design was promoted by using the process of
incorporating economy improvement measures and seeking other improvements.

Two examples of factors that have a significant effect will be introduced.

36

(1) Effect of Engine

The design cruising distance of 1,500 NM is a comparatively long distance for a plane of the 75 seat class. The relation between the fuel necessary to fly this distance and the fuel tank capacity in the main wing becomes a principal factor in determining the main wing area.

Specifications

Total length:	31.2 m
Total width:	23.8 m
Total height:	8.4 m
Fuselage diameter:	3.3 mϕ
Main wing area	63 m^2 (swept-back angle 21°, aspect ratio 9)
Operating weight empty:	16.6 tons
No. of seats:	75 (5 abreast, 32" pitch)
Pressurization of passenger cabin: 7.46 psi	
Underfloor luggage room capacity: 400 ft^3	
Engine:	2 turbofans (maximum thrust 11,800 lbs.)

Performance parameters

Designed cruising distance: 1,500 NM (alternate: 200 NM)
Maximum cruising speed: 491 kt TAS/0.82 M (altitude 26,000 ft.,
                          weight 27.4 tons)
Approach speed: 123 kt TAS (maximum landing weight)
Plane take-off runway length: 1,480 m (ISA)
                          1,640 m (ISA + 20°C) (maximum take-off
                                        weight for both)
Landing field length: 1,320 m (FAR, DRY, maximum landing weight)
Initial cruising altitude: 35,000 ft. (ISA, weight 28.8 tons)
Engine-starting/stopping ascending altitude: 16,000 ft (ISA + 10°C,
                          weight 28.1 tons)

Restricted items

Maximum operation speed:	340 kt CAS/0.82 m
Maximum take-off weight:	33.0 tons
Maximum landing weight:	27.8 tons
Maximum zero fuel weight:	24.4 tons
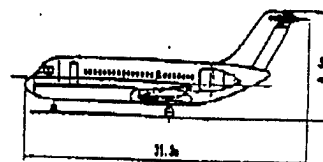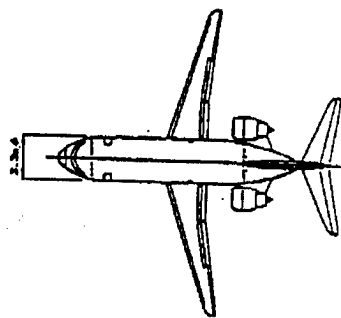
Figure 4.6 Option 1 (X4331M) Principal
          Specifications and List of
          Performance Parameters

(2) Main Wing Leading Edge Anti-Icing System

The effective thrust of the engine drops when conducting anti-icing by bleed air extraction. It is very disadvantageous economically by comparison to anti-icing systems that do not use the bleed air technique.

About 10 types of airframes were designed. The performance and economy of these airframes were compared with those of other planes. A line drawing of the airframe that was left as the candidate airframe is shown in Figure 4.6. A comparison of this airframe with other airframes is shown in Figures 4.7 and 4.8.

[illegible]
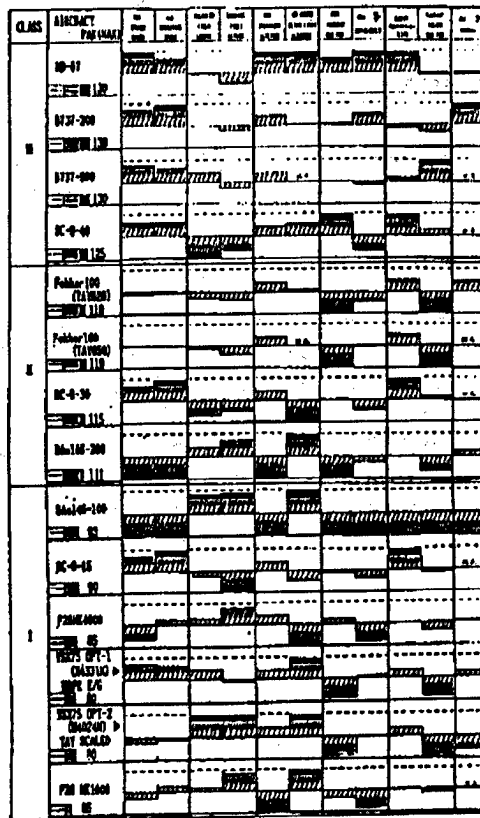
Color coding has divided 100 points into six.

Figure 4.7 Overall Comparison of Various Types of Aircraft

Consideration of Family Plane

A planning drawing based on a study of the potentiality of a family plane using the airframe mentioned above as the base is shown in Figure 4.9. The results will vary greatly, however, depending on the engine that will be designed initially for the 75 seat plane and the kinds of engines that may appear in the future. The assumption made on engines with the possibility of realization at the end of 1989 will be shown here.

38

Figure 4.8 Option 1 (X4331M) DOC Comparison

Figure 4.9 Family Aircraft Project (Case of feasible engine)

5. Topics

Studies up to 1989 have been made on the application of composite materials to main structures, anti-icing not dependant on extraction, high by-pass ratio engine, etc., assuming their adoptability. The adoption or rejection of these ideas will have a great effect on the basic components of the airframe. Also, considerable R&D will be necessary before these concepts can be adopted. In addition, it is necessary to study and design an airframe based on the engine data close to the market demand that is both economic and feasible.

Marketability of Supersonic Transport Planes

[Article by Hiroshi Mizuno, Japan Aircraft Development Association]

[Text] 1. Introduction

There is a supersonic airplane known as the "Concorde." Development of the Concorde began in 1962 and it entered into service in 1976 after an elapse of 13 years. However, it had entered into service in limited lines characterized by extremely high passenger fares. Thus, despite national subsidies by France and England to cover the enormous development costs, the project was terminated after the production of only 14 planes. This article will explore the potential of a supersonic transport (SST) plane that will be commercially profitable to airline operators and aircraft manufacturers, and with a fare acceptable to many passengers. The discussion will focus on the specifications for such a plane and on potential demand, which can be enhanced by incorporating the technical progress achieved over a period of close to 30 years. It goes without saying that much will depend on the presupposed technical level. It is assumed that its commission in service will be in the period from 2005 to 2010. Issues relating to technical progress that are utilized up to that point will be left to subsequent speakers.

2. Air Passenger Demand

It is believed that the growth of air transport has been supported by fare reduction, which in turn was made possible by the global development of economic activities together with the progress of aircraft technologies. The increase of passenger demand in the future based on current trends will be about 4 percent annually. This will result in an increase of 2.6 times the present level by the year 2010. Since the increase in the number of long-distance travelers is high, the increase in this category will be 5 percent for passenger kilometers and 4.2 times the number by 2010. The Asia and Pacific area, which is among the markets reflecting a high economic growth, will become a market matching that of the United States and Europe (Figure 1).
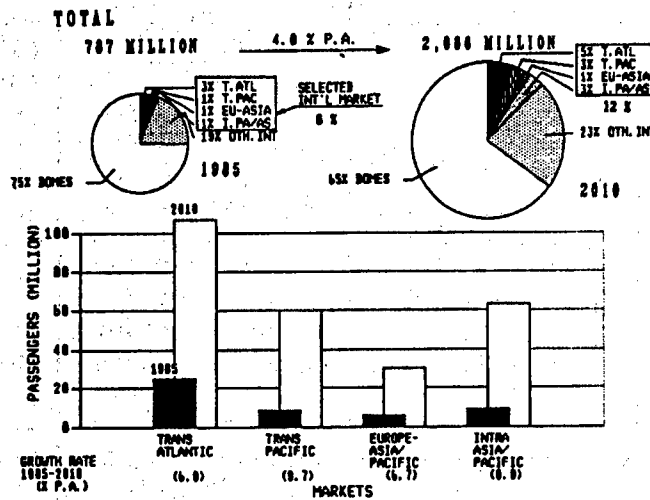
Figure 1. Selected International Market
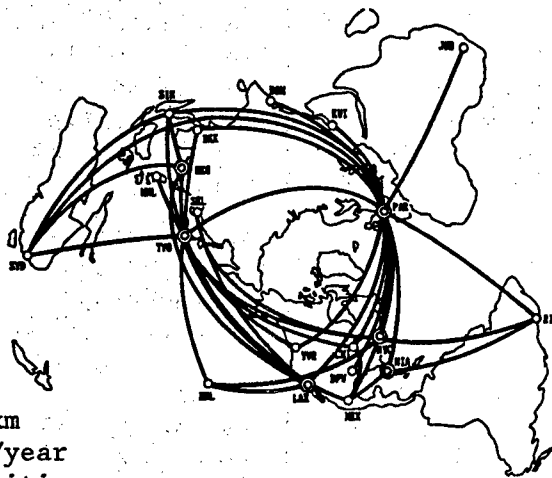
Longer than 2,000 km
Over 1 million pax/year
20 representative cities,
 38 routes
167 million pax,
 1,146 billion rpk.
(8% pax, 26% rpk of total
 market in 2010)

Figure 2. Possible SST/HST Network in 2010

This report is based on a study of 38 routes between 20 representative cities around the world that are suited for the operation of SSTs with a distance greater than 2,000 km and an estimated passenger volume of more than 1 million annually (Figure 2). Roughly speaking, the route network consists of a three-pole structure centered around North America, Europe, and several Asia/Pacific areas. The number of passengers for the route network represents 8 percent and the passenger kilometers 26 percent of the projected total volume of air traffic in the year of 2010.
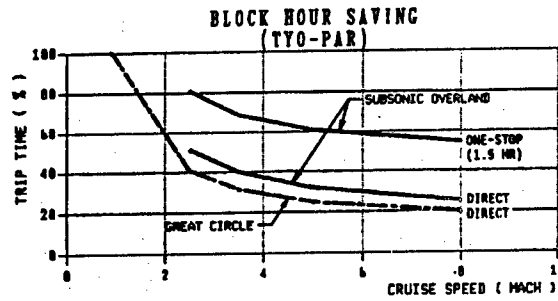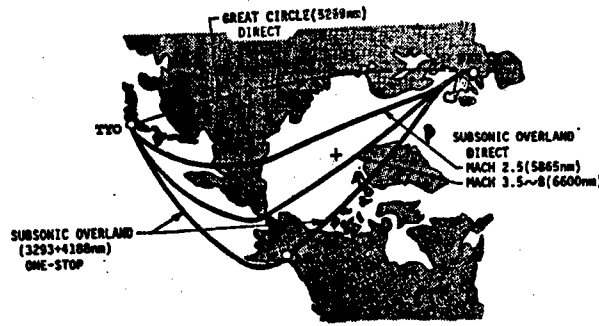
Figure 3. Sample Analysis of Route Between Tokyo and Paris
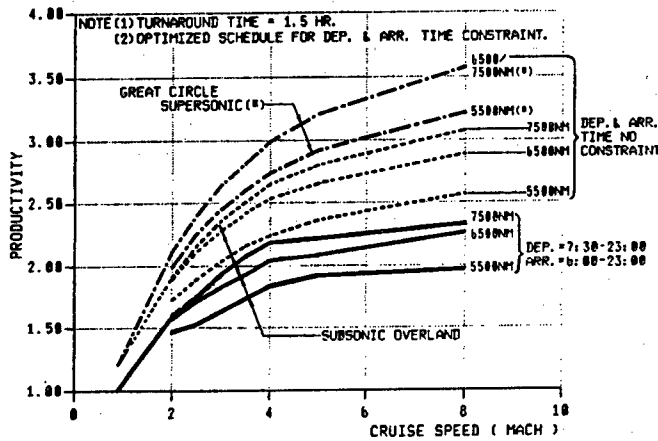
Figure 4. SST/HST Productivity (Optimized schedule)

3. Route Analysis and Productivity of Equipment and Materials

When considering the time required for the take-off and landing, ascending, descending, acceleration, and deceleration of SSTs cruising at high speed at high altitudes, it follows that the longer the route, the greater the advantage. However, this does not necessarily mean that traveling time is inversely proportional to cruising speed. Moreover, half of the total of 38 routes contain a portion of land under the great-circle course and this raises the problem of sonic boom. The permissible limit is said to be 0.5~1 PSF, but because the probability of achieving this limit at the present stage is small, a roundabout way or subsonic flight has been assumed. A sample analysis for the route between Tokyo and Paris is shown in Figure 3. Two options are available. One is to pass through the skies over Siberia at subsonic speed or to make a detour over the Bering Strait at high speed.

42

Oil supply becomes important in the case where the cruising distance becomes insufficient and the advantage of high speed is lost. The time required for oil supply and maintenance is uniformly assumed to be 1.5 hours here; however, productivity further deteriorates in a high-speed plane that has to be cooled after landing. In addition, the adaptation of airport noise to the present ICAO standard is also a major topic. Midnight and early morning departures and arrivals are still limited in many airports, even for the newest subsonic planes. Departures and arrivals in this time zone also may be inconvenient for general passengers. Optimization of the operating sche-dule for this global network while avoiding these midnight and early morning departures and arrivals was attempted, but there is still a significant deterioration in the operational efficiency of high-speed planes, i.e., productivity suffers considerably. This problem is demonstrated in Figure 4 and the importance of cruising performance can also be clearly seen here. The productivity of an M=3 airframe of 7,500 nautical miles is equivalent to that of an M=6~8 airframe of 500 nautical miles.

4. Economy and Necessary Number of SSTs

Figure 5 contains an estimate of the direct operating cost (DOC) of super-sonic planes (300 seats) based on the presently used 747 plane. The airframe cost was handled here as a variable and the cost of all airplanes has been assumed to be the same as for the 747. The competitive opponent is the advanced subsonic plane with an M=0.9 airframe. While crew costs and depreciation costs decrease for ultrasonic planes by virtue of their high speed and high conductivity, the fuel cost is because of the high speed and additional weight. Moreover, the high unit cost of high temperature stable fuel for more than M=3 pushes up this cost. The gross weight of the M=3.5 airplane exceeds 1 million pounds and whether it can be used at current airports is doubtful, but this is ignored here. The ratio of the total operating cost (TOC) that includes the uniform indirect operating cost (IOC=2/3 the 747 DOC) per seat to this DOC against the subsonic plane shown as the variable of the airplane cost is the top right diagram in Figure 6. This TOC is regarded as the fare and the passenger share of this is shown in the top left diagram of Figure 6. Explanations of the derivation of this curve will be kept for another occasion. Economy class passengers are sensi-tive to the fare and when the average fare becomes 1.67 times, the passenger share is reduced to one-third share mainly composed of business passengers. The number of necessary planes corresponding to the airplane price as shown in the lower right diagram of Figure 6 is obtained in this manner.

5. Development and Production Costs and Number of Planes Required

It cannot be said, of course, that there is an accurate estimate of the development and production costs. There are, however, estimates of $15 billion for the development cost of an M=2 airplane and $150 million as the average production cost of a mass production run of 400 airplanes; $30 billion as the development cost of an M=3.5 airplane and $270 million as the average production cost of a mass production run of 400 airplanes. This compares to a development cost of $4 billion and an average production cost of $65 million for a mass production run of 400 planes for the 747 airplane.
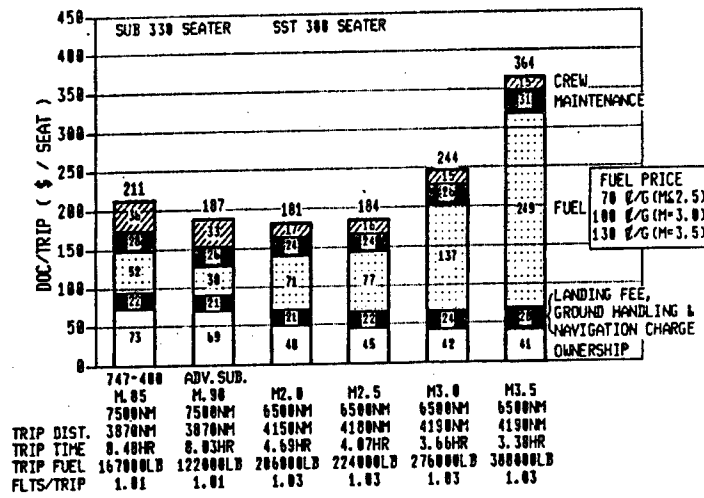
Figure 5. SST/HST DOC Per Trip
(Constant A/P price = $102 M; spares = $13 M)
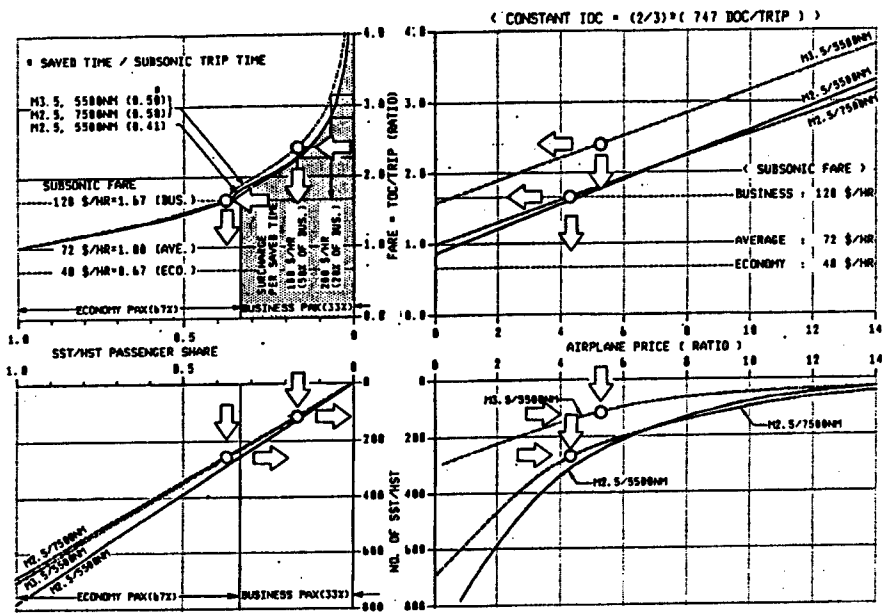
Figure 6. Airplane Price Vs. Number of SST/HST

When the number of mass produced airplanes is small, the development cost allotted per plane and the mass production average cost will also increase, and the price per airplane will rise. The relationship between airplane price and cost is shown in Figure 7. The intersecting points in the diagram give the maximum demand in terms of the number of planes. This holds true at about 600 planes for the M=2 airplane and also at 120 planes for the M=3.5 airplane. However, there are indications that the latter may not hold true and that there may be a slight estimation error. The maximum demand for airplanes of various specifications is shown in Figure 8, but these are not necessarily in proportion to the passenger share. Maximum values are about 75 percent and the average fare shows an increase of about 15 percent over that of subsonic

44

AIRPLANE PRICE (RATIO)
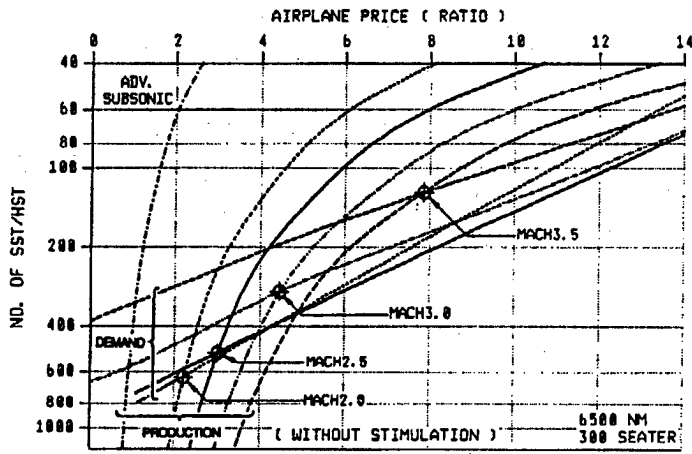
Figure 7. Relationship Between Airplane Price and Cost
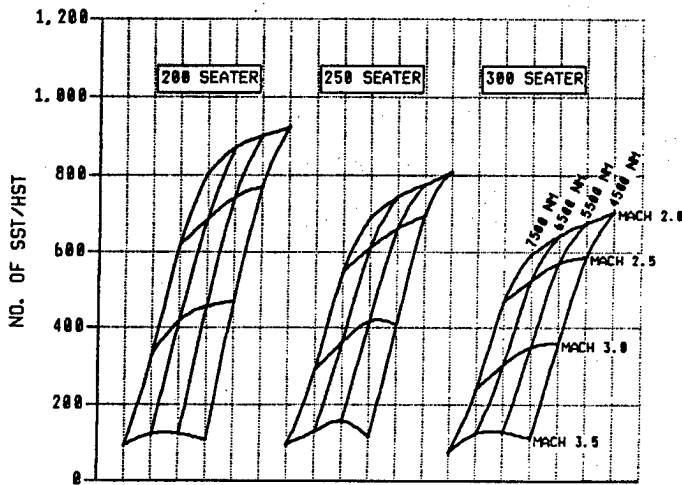
Figure 8. Maximum Number of SST/HST

planes with 250~300 seats, M=2~2.5 airframes and a cruising distance of about 6,500 nautical miles. Explanations of the passenger induction ratio will also be kept for another occasion.

Airframe Project for Supersonic Transport Planes

[Article by Toshio Hanai and Hikaru Takami, Mitsubishi Heavy Industries]

[Text] 1. Introduction

Given the sharp increase in demand for aircraft transport and the desire of passengers for shorter flight times, together with the remarkable develop-ment of the world economy as represented by the Pacific area, R&D has been started in Japan, the United States, and major European countries aimed at the realization of a second-generation supersonic transport plane (SST).

Studies will be made on the specifications for the second-generation SST. We will discuss these specifications together with technical issues related to creating an airframe suitable for market demands.

2. Specifications and Technical Topics for SST

It can be considered that the following capture the expectations (demands) on the operator's side for the second-generation SST.

- A cruising distance of more than 6,500 nm.
- Travel time shortened to less than one-half.
- Operating cost equal to that of subsonic planes.
- Accommodate more than 300 passengers.
- Environmentally acceptable.
- Turnaround time shortened.

These are the main parameters for the number of passengers, cruising speed, and range. Together they form the basic specifications from the operator's perspective for creating a new SST. A capacity as great as possible is demanded from the viewpoint of transportation capacity and economy. Currently, a passenger capacity of about 250~300 persons is being studied. A reduction of travel time by more than one-half is demanded and a Mach number greater than 2 is necessary for the cruising speed. However, when the Mach number becomes extremely great, i.e., more than 6, the productivity (annual passenger transport distance per plane) improvement becomes extremely small and is not realistic. With regard to range, a minimum range of 4,500 nm is necessary for

necessary for the plane to be able to cross the Pacific Ocean and since
there is a strong demand for nonstop service to the East Coast of the United
States, a range of more than 6,500 nm has also become an object of study.
The specifications for study have been established as follows:

- Number of passengers: 200~300
- Cruising speed: Mach 2~5
- Cruising range: 4,500~7,500 nm

Table 1. Envisioned Technical Levels for Supersonic Transport Planes

	Technical field	Technical items	
SST (M=2~3.5)	Technical level	1995-type certificate acquisition	2005-2010-type certificate acquisition
	Aerodynamic	Same as Concorde	Natural laminar flow Camper optimization/ vortex flap Area rule
	Structure material	General areas: Aluminum alloy FRP High temperature areas: Titanium alloy	General areas: Heat-resistant FRP Improved Al alloy High temperature areas: Heat-resistant titanium alloy
	Propulsion	Variable cycle engine JP fuel	Improved variable cycle engine JP fuel
HST (M=4~5)	Technical level	2005-2010-type certificate acquisition	2020-2010-type certificate acquisition
	Aerodynamic	Natural laminar flow Camper optimization/ vortex flap Area rule	Natural laminar flow Camper optimization/ vortex flap Area rule Blended wing-body
	Structure material	General areas: Superalloy Heat-resistant titanium alloy High temperature areas: Heat-resistant titanium alloy	General areas: C/C composite High temperature areas: C/C composite
	Propulsion	Turboram Liquefied methane	Improved turboram Liquefied methane

ADVANCED TECHNOLOGY IMPACT

300 PASSENGERS
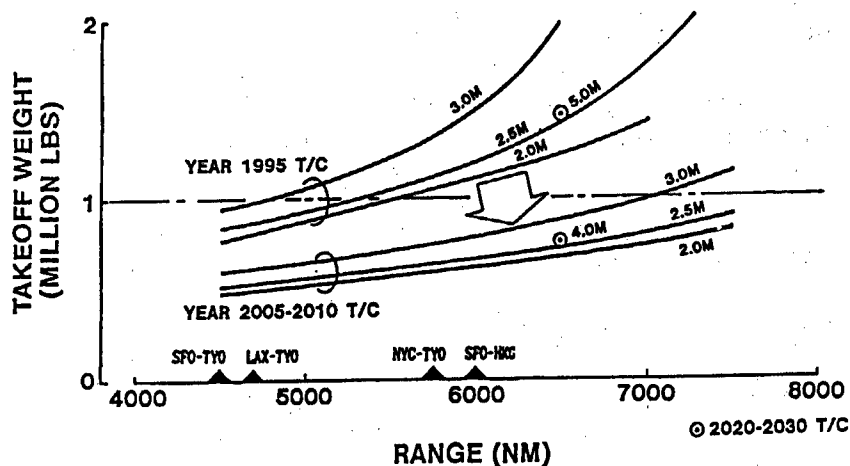
Figure 1. Effects of Advanced Technology on SST
Airframe Scale

A program for delineating the airframe specifications has been prepared, based on a study of the specifications. The specifications were made into parameters, the technical level was envisioned, and the airframe scale (weight, size, etc.) was obtained as a result. The two levels of the 1995 T/C acquisition level and 2005-2010 T/C acquisition level were used as the technical levels for the SST (M=2~3.5) shown in Table 1. Two levels of the 2005-2010 T/C acquisition level and 2020-2030 T/C acquisition level were used as technical levels for HST (M=4~5) shown in Table 1.

As an example of the study results, the effect of the technical level exerted on the airframe scale (take-off weight) in the case of 300 passengers with the cruising speed as the parameter is shown in Figure 1. The airframe scale generally increases as the number of passengers increases, as the cruising range becomes longer, and as the cruising speed becomes higher. Since there is a desire to make the airframe scale (take-off weight) less than that of the Boeing 747 (about 870,000 lbs.) from the viewpoint of using existing airport facilities without having to make significant improvements, it is believed that a take-off weight of less than 1 million lbs. is the guideline. When applying this standard, a maximum cruising distance of only 5,500 nm is available at a cruising speed of Mach 2, using the assumptions for the 1995 T/C. Thus, it would be possible to fly from Tokyo to the west coast of the United States, but flying nonstop to the east coast would be impossible. At the same time, however, technological innovation should have a marked effect when it comes to the airframes created from 2005-2010 T/C and it should be possible to achieve sufficient cruising performance while reducing the size of the airframe. With regard to the case where the cruising is in the range of Mach 4-5, it has been indicated that an airframe can be created, based on the assumptions for the 2020-2030 T/C, capable of carrying 300 passengers with a

cruising distance of 6,500 nm. However, the airframe scale is not realistic for the technical level of the 2005-2010 T/C assumptions. It would be very difficult to realize such an airframe in this timeframe.

This demonstrates that further progress in various technical fields is necessary to develop an SST that can satisfy the demands of the operators.

The technological innovation necessary for the airframe for the 2005-2010 T/C acquisition (M=2~3.5) can be summarized as follows:

▷ Aerodynamic

- Frictional resistance reduction by supersonic laminar flow
- Zero lift resistance reduction by supersonic area rule
- Induction resistance reduction by optimum camber

The assumed technological innovation will reduce resistance by about 20 percent.

▷ Structure·Material

- Structural weight reduction by the use of heat-resistant composite materials
- Structural weight reduction by the use of heat-resistant titanium materials

The assumed level of technological innovation differs depending on the Mach number, but there will be a weight reduction of 15~25 percent.

▷ Engine

- Improvement of specific fuel consumption in the subsonic and supersonic ranges by VEC
- Improvement of thrust weight ratio through the adoption of heat-resistant, lightweight materials

The assumed technological innovation will increase the thrust-to-weight-ratio by 10 percent and reduce SFC by 5 percent.

Figure 2 presents a comparison between a set of sample airframe specifications derived from an analytical study and those of the Boeing 747. The new SST would have a total length of about 91 m, a total width of about 39 m, and a take-off weight of about 730,000 lbs. It will carry 300 passengers. It will fly at a speed of Mach 2.5 with a cruising range of 6,500 nm. It was assumed that the lift-drag (L/D) ratio at cruising speed is 8.8 and that the SFC of the engine is 1.36.

Since the specification study mentioned above is only for the initial stage, it will be necessary to take into account future improvements, such as greater precision, and the effects of adopting such improvements on the surrounding environment. This includes airport noise, sonic boom, and engine exhaust.

	Boeing 747	New SST
No. of passengers	366	300
Cruising speed (km/h) (Mach speed)	1,000 (0.85)	2,700 (2.5)
Cruising distance (km)	10,000~ 14,000	12,000
Total length (m)	70.7	91.3
Wing width (m)	59.6	39.4
Wing area (m^2)	511	962
Weight (tons)	380	330
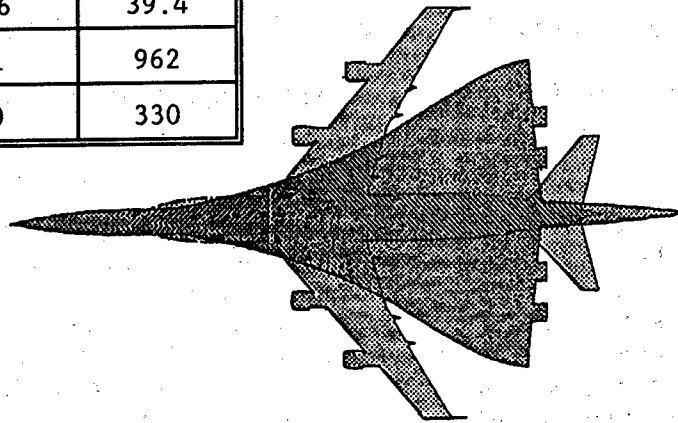
Example of SST Airframe Specifications

3. Conclusion

This article has presented the specifications for an SST that will be capable of competing economically with subsonic passenger planes and has described the major technical R&D topics necessary for its development. It is necessary to begin R&D on these technical topics now if a second generation SST is to be available by the beginning of the 21st century. Moreover, it is said that an international joint development effort will be necessary to develop such a plane. We also believe that it will be necessary for Japan to promote relevant R&D at an early period so that it can independently make an international contribution.

This report has been based primarily on the activity of the Supersonic Transport Plane Development Trend Investigation Committee of the Japan Aerospace Industry Association.

Aerodynamic Technology for Supersonic Transport Planes

906C0041I Tokyo HIKOKI SHINPOJIUMU in Japanese Oct 89 pp 342-345

[Article by Takashi Uchida and Kenji Yoshida, Kawasaki Heavy Industries]

[Text] 1. Introduction

Twenty years already have elapsed since the maiden flight of the Concorde. Over the past decade many new subsonic airplanes have appeared, but there have been no new supersonic transport planes (SSTs). The first generation of SSTs, such as the Concorde, have demonstrated the technical potentialities of SSTs, they have also left behind many questions with regard to economy and sociality (environmental adaptability). It can be said that there has been a considerable international accumulation of technical information on supersonic flights at speeds of less than Mach 3 through R&D on the Concorde and on military planes. Therefore, the next step up would be to develop the next generation of SSTs (Mach number greater than 3) as far as aerodynamic technology is concerned. Today, when the technical possibilities have already been demonstrated, the objects of the development efforts of the next generation of SSTs should be a high level of economy and wide social acceptance around the world. This report will describe the relationships between economy, social acceptability, and aerodynamic technology, and will present topics related to design technology.

2. Effects of Aerodynamic Technology on Economy

Transport efficiency (η) is considered by making economy one of the indexes, as expressed in equation (a):

$$\eta = \underbrace{\frac{Onerous\ weight\ x\ distance}{fuel\ weight}}_{} \propto \frac{\overbrace{(Cruising\ Mach\ No.\ x\frac{Lift}{Resistance})}^{}}{Aerodynamic\ efficiency}$$

$$\underbrace{(\frac{Onerous\ weight}{Total\ equipped\ weight})}_{Structural\ efficiency}\ \underbrace{(\frac{1}{Specific\ fuel\ consumption})}_{Engine\ efficiency} \tag{a}$$

Aerodynamic efficiency must be improved to promote overall SST efficiency. It is necessary that the aerodynamic efficiency of the next generation of SSTs exceed the existing aerodynamic efficiency of about 17 for subsonic passenger

51
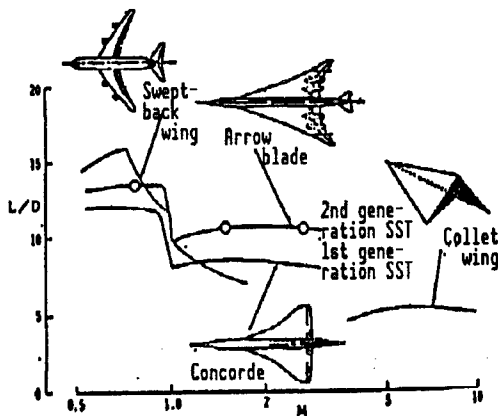
Figure 1. Drag Ratio Mach Number[1]
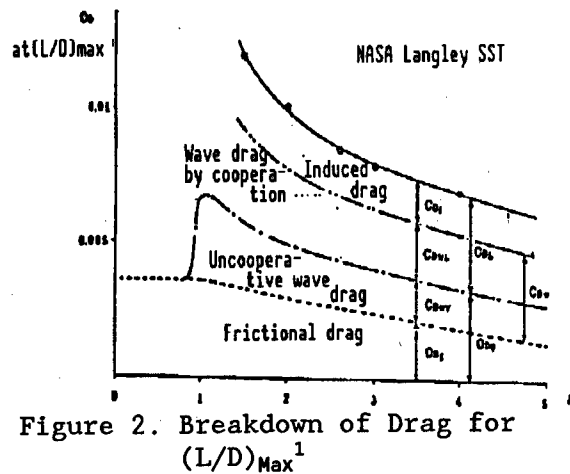
Figure 2. Breakdown of Drag for $(L/D)_{Max}$[1]

planes. The aerodynamic efficiency of the Concorde is about 14 (Figure 1), while an efficiency rating of about 25 is demanded for the new generation of SSTs.[1] Further, since lift is the weight at cruising, aerodynamic efficiency improvement technology also involves the technology of drag reduction and improving cruising velocity.

(1) Drag Reduction Technology

The drag of supersonic planes can be roughly expressed by the following equation (b):

$$D = \underbrace{\frac{C_f qS}{}}_{Frictional\ drag} + \underbrace{\frac{k_1 \frac{L^2}{qSA}}{}}_{Inductional\ drag} +$$

$$\underbrace{k_2 \frac{M^2-1}{2} \frac{L^2}{qSA}(\frac{b}{1})^2}_{Wave\ drag\ by\ lift} + \underbrace{k_3 qS_v(\frac{d}{1})^2}_{Wave\ drag\ by\ volume}$$

(b)

where:
- q : Dynamic pressure
- C_f: Frictional coefficient
- L : Lift
- M : Mach number
- S : Standard area
- A : Aspect ratio of wing
- b : Wing width
- d : Diameter of equivalent body of revolution
- 1 : Airframe length
- S_v: Cross section of equivalent body of revolution

The wave drags peculiar to supersonic planes and not associated with subsonic planes are shown in the last two terms on the right side of equation (b). Examples of various drag components are shown in Figure 2. All components are of about the same size. Incidentally, cruising takes place at (L/D) ₋ maximum. As can be seen from Figure 2, it is a lift by the zero lift drag ₋ lift when it is $(L/D)_{max}$. Thus reducing the zero lift drag is important for drag reduction.

52
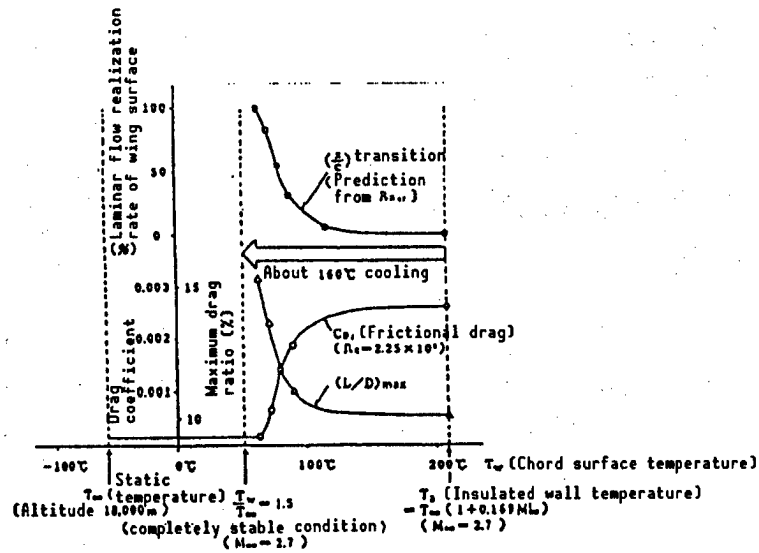
Figure 3. Realization of Laminar Flow by Wall Surface Cooling[1]

The following can be cited as zero lift drag reduction technologies:
- (1) Achieving laminar flow of the boundary layer
- (2) Turbulent boundary layer control
- (3) Refinement of airframe shape

Moreover, for drags based on lift:
- (4) Optimization of wing plane shape
- (5) Optimization of camber and twist distribution
- (6) Optimization of leading edge suction[1]

(2) Outline of Drag Reduction Technology

(2.1) Laminar flow of the boundary layer:

The following techniques can be used to produce laminar flow of the boundary layer:

- (1) Realization of natural laminar flow (NLF) by adjustment of the shape
- (2) Laminar flow control (LFC) by suction of boundary layer
- (3) LFC by wall surface cooling (Figure 3)

Since LFC requires a motive power, it is necessary to approach this problem from the viewpoint of overall system efficiency. Moreover, a sonic boom (to be mentioned later) cannot be avoided. Thus, when subsonic cruising over land is necessary, a contrivance for achieving laminar flow in both assumed areas, subsonic and supersonic, may be demanded.

(2.2) Turbulence boundary layer control:

Currently, there are no sound methods for controlling the turbulence boundary layer. However, it will be necessary to seek to develop a device capable of checking the turbulence frictional drag itself.

53
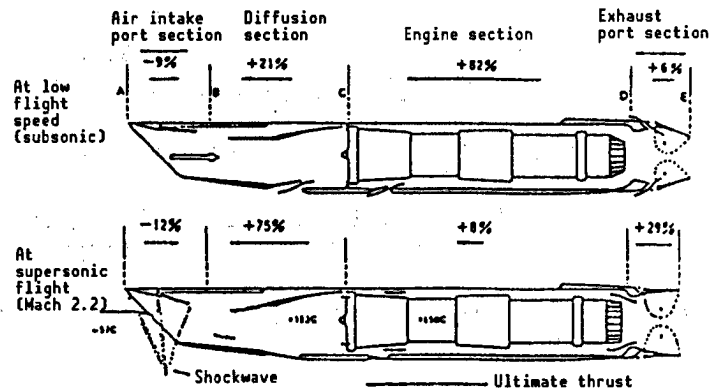
Figure 4. Thrust Distribution of Concorde's Olympus Engine[3]

(2.3) Refinement of airframe shape

The following must be studied as ways to reduce wave drag.

> (1) An airframe shape that becomes a smooth and slender equivalent body of revolution
> (2) A blended wing body
> (3) An efficient air intake

The air intake in particular plays an important role in propulsion system thrust (Figure 4).

(2.4) Optimization of wing plane shape:

It is generally better to make the cross section change in the flow direction small to reduce the wave drag. To achieve this, the leading edge of the swept-back angle must be large while the wing thickness ratio becomes small to achieve the necessary wing shape. However, the wing root must be sufficiently thick to ensure structural soundness and a long chord is required. Therefore, the delta wing inevitably becomes the standard shape of the wing. In addition, the delta wing has an advantage in terms of longitudinal stability as the movement centered around the wind pressure remains small as velocity increases or decreases. An alternative shape is the arrow wing. This shape maintains the basic characteristics of the delta wing and acts to reduce induction drag by increasing the aspect ratio (Figure 5). However, the arrow wing has a strong tendency to pitch up and has poor high angle of incidence characteristics. Flutter measures are also an important topic but, it is felt that active control technology (ACT) will play an important role in resolving this problem.
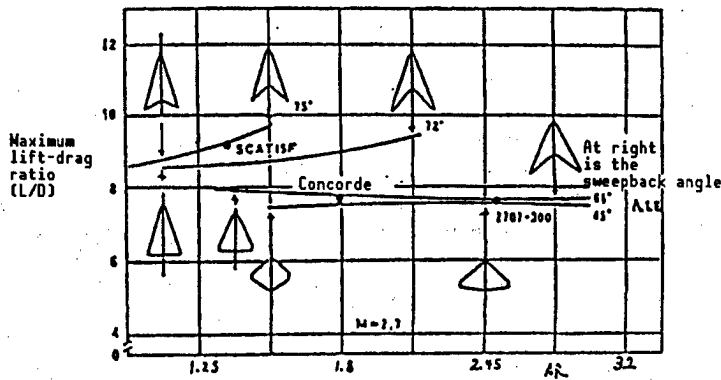
Figure 5. Maximum Lift Drag Ratio of Arrow Wing[1]
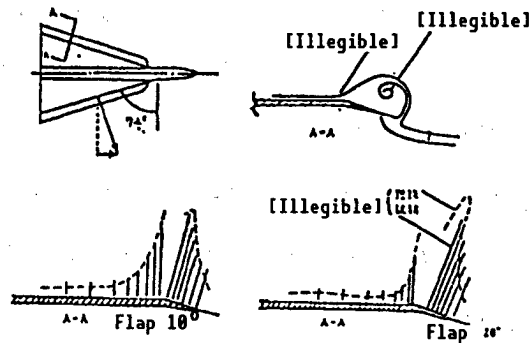
Figure 6. Principle of Vortex Flap[1]

(2.5) Optimization of camber and twist distribution:

Camber has more influence on wave drag than lift. The twist distribution is closely related to the wing width direction load distribution and, in its turn, to induction drag. A lift drag ratio improvement of about 1 is possible by optimizing a warped wing that combines these two shapes.

(2.6) Optimization of leading edge suction:

The subsonic leading wing edge generates a large negative pressure in the neighborhood of the leading edge and this pressure generates the components of thrust and lift. It may be possible to maximize the thrust component by devising the appropriate leading edge shape. Vortex flap technology aimed at stabilizing the vortex generated on the leading edge is also promising for a thin wing with a small leading edge radius (Figure 6).

(3) High Lift Device

Although the stalling angle of incidence for the low aspect ratio wing is great, a high degree of lift must be obtained at a low angle of incidence because of such limitations as leg length, tail skidding angle, pilot's angular range of the view, etc. Thus, it is necessary either to make the wing area large or to equip it with a high lift device. The former was adopted for the first generation SSTs and there are many that have adopted the latter in

55
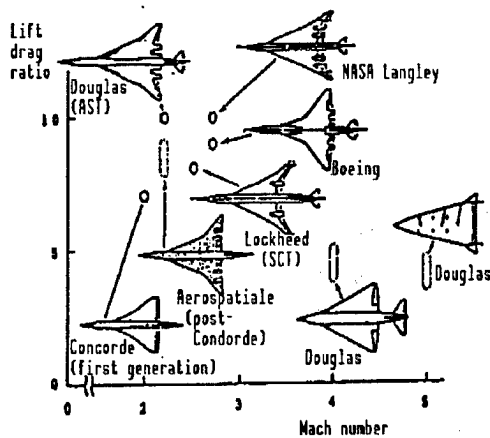
Figure 7. Plan for Second Generation SST
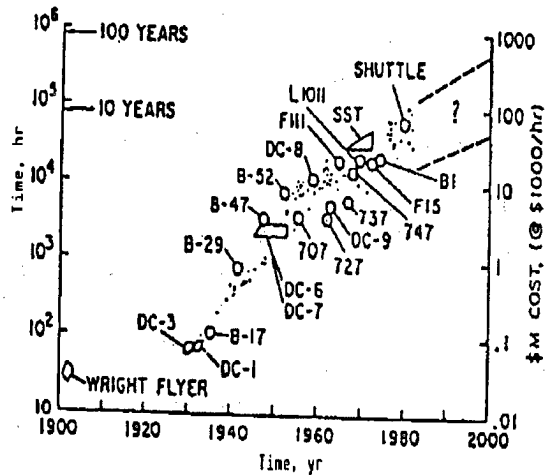
Figure 8. Wind Tunnel Testing Time and Expenditures Required for Airframe Development

the plans for the next generation of SSTs (Figure 7). A high lift has been obtained in the Concorde by utilizing the leading edge separation vortex. Application of the vortex flap mentioned above will be a promising topic for future study.

3. Social Acceptability and Aerodynamic Technology

The noise problem is very important from the standpoint of social acceptability (environmental adaptability) and the design of a quiet airframe is an important task for aerodynamic technology. The engine and the sonic boom peculiar to supersonic planes are the main sources of noise.

(1) Engine Noise Reduction Technologies:

Technologies to reduce engine noise can be classified into two broad groups: airframe technology and engine technology. The following are related to airframe technology:

1) Reducing the requirement for engine thrust
2) Seeking new engine arrangements (for example, placing the engine on the upper surface of the main wing)
3) Improving the flying system

The following are related to engine technology:

1) Reducing exhaust speed
2) Annular core nozzle
3) Noise suppressor nozzle
4) Thermal acoustic shield
5) Sonic inlet
6) High performance suction material

56

The FAR/PART 36 STAGE II is currently the noise standard for SSTs. However, a STAGE III equivalent to that of subsonic planes or a standard in conformity with that is expected to be applied in the future and further efforts on R&D will be necessary to meet it.

(2) Sonic Boom Reduction Technology:

There is no control standard at present for sonic boom, but the many research results obtained up to now indicate that the intensity of the sonic boom must be less than 1 lb/ft^2 (0.0005 atmospheric pressure) in order to be socially acceptable. When this demand cannot be satisfied, supersonic flights over land will not be permitted, and airlines will be compelled to conduct subsonic flights. This will be a severe restriction on operations. Sonic boom is caused because the pressure variation field produced by the airframe is not diffused and becomes localized in supersonic planes. By contrast, the pressure variation field of subsonic planes spreads and diffuses over the entire space. Since the pressure field supporting the airframe weight is transmitted directly to a limited part of the earth's surface, it s necessary to make the airframe light. Moreover, an optimum airframe shape must be provided as the pressure distribution of the airframe bottom surface determines the waveform of the sonic boom. The relationship between airframe shape and sonic boom is ascertainable by the Whitham theory.[2] The following may be considered as methods to reduce sonic boom:

    1) Optimization of flight altitude and speed
    2) Reducing airframe weight
    3) Optimization of airframe shape
    4) Optimization of operational system

4. Aerodynamic Design Tools

(1) Wind Tunnel Facility:

The wind tunnel test is the key to current and future aerodynamic design. It is necessary to create a testing environment that in terms of Mach number, Reynolds number, and thermal characteristics is similar to actual flight environments. This is accomplished using a wind tunnel. However, there is no wind tunnel that is capable of realizing all of these environments at the same time and it is believed that the construction of such a wind tunnel will be difficult in the future also. Therefore, the effective utilization of existing wind tunnels and wind tunnels to be constructed in the future must be promoted. The wind tunnel testing time required in the development of aircraft is shown in Figure 8. This trend suggests that an enormous amount of testing time will be required for the development of the next generation SST. How this problem will be resolved is an important topic for SST development.

(2) Computerized Wind Tunnel:

The development of computers has progressed rapidly in recent years. Concurrent with this development, computation aerodynamics (CFD) have also expanded rapidly. Although there are several restrictions on CFD now, it is believed that these restrictions will be cleared away in the future. The strongest

point for CFD is that it is able to handle actual flight environments that are difficult to reproduce in a wind tunnel facility. Moreover, it is able to simulate handling according to the terminal numbers of the computer and in this regard it is just like a wind tunnel. However, it goes without saying that the presence of a high-performance computer is the premise. It is believed that in time CFD will perform an important role at the same level as wind tunnel testing.

5. Conclusion

Enhancing performance is the primary task for aerodynamic technology in developing the next-generation SST. To obtain an optimal aircraft shape, many design techniques and means must be developed. It will be necessary to set out the development plan clearly.

References

1. SST/HST Development Trend Investigation, Japan Aerospace Industry Association, March 1988.

2. Whitham, G.B., PROC. ROY. SOC., 1950.

3. Sanuki, M., AIR WORLD, April 1989.

4. Chapman, D.R., et al., ASTRO. AND AERO., April 1975.

Structure, Materials for Supersonic Transport Planes

[Article by Kenichiro Shirakine and Yorihide Tsutsumi, Fuji Heavy Industries]

[Text] 1. Introduction

The structure of a supersonic transport plane (SST) is exposed repeatedly for long periods to a high-temperature environment caused by aerodynamic heating. Although the Mach number, i.e., the maximum momentary surface temperature, is low in comparison to such craft as the space shuttle, the duration of the heating period is long and the environment against the structure is severe. At the same time, the key to the materialization of an SST is weight reduction. In particular, reducing the weight of the structural elements, which account for more than one-half of the total airframe weight, is extremely important. Therefore, it is no exaggeration to say that the airframe scale to be realized is determined according to the practical application of lightweight heat-resistant materials and the development of a heat-resistant structure using these materials. This article will describe the present status of and problems associated with the development of structures and materials for SSTs whose air speed ranges from Mach 2 to about Mach 6.

2. Structural Design Requirements for SST

The airframe surface temperature produced by aerodynamic heating is affected by a number of factors, including velocity and airframe shape, but there is currently no established analytical method for obtaining an accurate temperature. The problems involved in estimating aerodynamic heating and temperature using data from various publications, etc., are illustrated in Figure 1. The following is a list of design requirements peculiar to supersonic planes. These requirements should be considered during the structural design process to ensure that the airframe can withstand these temperatures.

- High temperature strength and rigidity of structural members.

- Providing thermal protection and cooling systems for structural members.

59
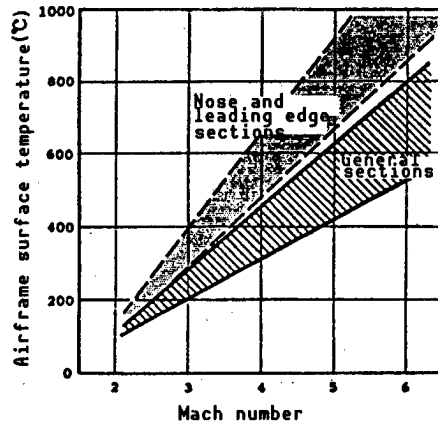
Figure 1. Airframe Surface Temperature Produced
by Aerodynamic Heating

• Temperature difference among structural members or thermal stress
  among different materials

• Protection against thermal shock caused by sudden temperature changes
  and against thermal fatigue caused by repeated thermal shocks

• Heat insulation between the passenger cabin interior and the airframe
  surface, and a pressure cabin structure capable of withstanding high
  temperatures

• Heat insulation between the cryogenic fuel tank (in the case of
  liquid fuel) and airframe surface, and the high-pressure tank
  structure

3. Present Status and Development Trends of Heat-Resistant Structural Materials

It is said that the usable temperatures of materials that have traditionally
been used as aircraft structural materials are roughly 150°C for aluminum
alloy, 350°C for titanium alloy, and 150°C for epoxy resin system composite
materials. However, in observing actual examples of the practical application
of materials in supersonic planes, we find that aluminum alloy is used for the
Concorde, which has a velocity of less than Mach 2.2, while titanium alloy is
the main material used in the SR-71 reconnaissance plane, which is a Mach 3
aircraft. Inconel superalloy is used in the X-15 experimental plane of the
Mach 6 aircraft. However, it is necessary to create an airframe suitable for
a cruising distance and a number of passengers that will be economically
viable over the international routes for supersonic transport planes that are
expected to be developed in the future. Weight reduction by putting new heat-
resistant materials to practical use is an extremely important part of this
challenge. The temperature characteristics in terms of specific intensity and
specific rigidity of various materials are shown in Figure 2. Many of these
materials possess qualities that make them still suitable for practical
application.

60
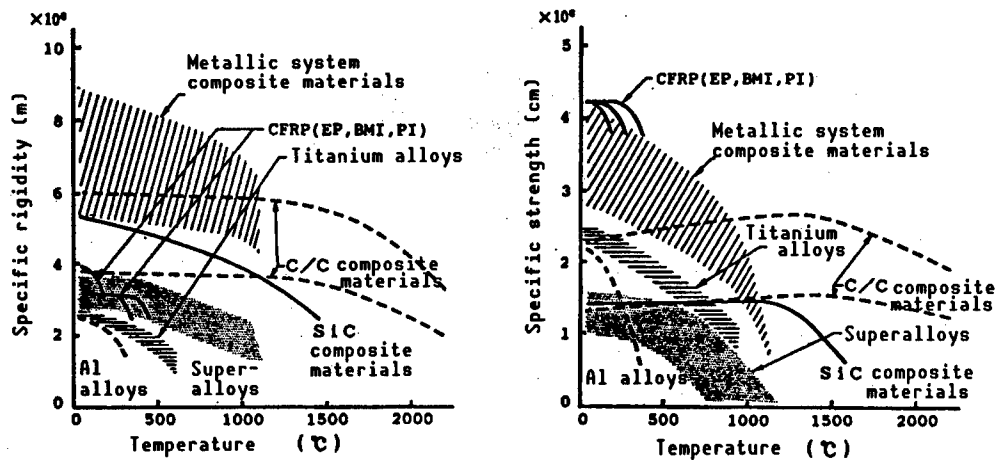
Figure 2. Temperature Characteristics of Structural Materials

Research and development of powder alloys using a rapid solidification process has been promoted for improving the material's heat-resistant property. It is anticipated that an iron-cerium-aluminum alloy will be able to resist temperatures up to 300°C and that RSR titanium will be able to resist temperatures up to 700°C. However, large-scale material production of these powder alloys will be difficult given the present level of production technology.

A superalloy is an alloy with nickel or cobalt as the base. These materials are capable of resisting temperatures up to about 600°C and have been used in jet engines. However, since their specific gravity is great and the materials are rare and expensive, it is believed that they are only partially suitable for use as structural materials. Research on improving heat-resistant properties is being promoted also for superalloys primarily in terms of material production technologies such as unidirectional solidification, single crystals, eutectic crystals, etc.

In addition to aluminum matrix composite materials, which are capable of resisting temperatures up to about 300°C, various metallic system composite materials are the subject of practical application research for military planes in the United States. Titanium matrix composite materials with a heat-resistant level of about 600°C, and titanium aluminate and superalloy matrix composite materials with a heat-resistant level of about 1,100°C are still in the research stage at the laboratory level. Many aspects of these metallic system composite materials remain to be explored, including production technology for such materials and parts forming technology.

Bismalemide and polyimide system composite materials, which are highly heat resistant, have emerged from among resin system composite materials. It is anticipated that they can be used as materials for supersonic planes. The bismalemide system composite material has a heat-resistant potential of about 250°C. Since there is not much difference in workability between it and conventional epoxy, it is being studied for application in the next U.S. fighter plane and it can be said that it is entering the practical use stage.

61

Polyimide system composite materials, meanwhile, have a heat-resistant potential of about 350°C, but there is still room for improvement in terms of its workability.

Carbon-carbon (C-C) composite materials and silicon carbide (SiC) composite materials both have excellent heat resistance. C-C composites are the most heat-resistant materials currently known. They are capable of resisting temperatures up to 1,600°C. However, since there is a drop in strength caused by oxidation beginning about 650°C, the development of an oxidation-resistant coating method is currently being explored. The heat resistance of SiC composite materials is slightly lower than that of C-C composites, but there is no problem in terms of oxidation. However, there is a problem peculiar to ceramics in that its toughness is low.

4. Trends in Heat-Resistant Structural Design

Representative concepts for heat-resistant structures include hot structure, thermal protection system (TPS), and active cooling structure. The hot structure is basically the same concept as that of conventional structures. Although it is the simplest structure, it does require a lightweight heat-resistant material capable of withstanding surface temperature of the airframe. It also requires a heat insulation layer for the inner side of the structural members and the development of a lightweight adiabatic structure is also important.

By contrast, the thermal protection system concept involves covering the outside of the structural members with a thermal protection material and keeping the temperature of the structural members low. The weight of thermal protection material increases the overall weight, but there is the advantage that conventional materials can be used for the structural members. This concept is potentially applicable to a comparatively wide range of design conditions by changing the shape and composition of the thermal protection materials. Two examples, the multiwall TPS and the stand-off TPS, are shown in Figure 3.

The active cooling structure concept involves actively cooling the structural members with a cooling liquid, etc., to keep the temperature of the structural members low. An example of an active cooling structure is shown in Figure 4. Structural temperature is lowered by passing the cooling liquid through pipes that have been spread throughout the structure. The cooling liquid itself is cooled by passing it through a heat exchanger with the liquid fuel. The system can become complicated, but since conventional materials can be used and since there is no residual heat in the structure, it is effective for extended exposure to heat.

Which material will be used and which structural mode will be adopted for the structure of a supersonic transport plane depends greatly on the heat-resistant characteristics of the materials that have been put to practical use in developing the airframe. Moreover, both airframe cost and airframe weight are important in the case of civilian transport planes. Application also becomes restricted for high-performance materials that have been put to practical use when the material cost is expensive or the airframe production cost becomes high because the fabrication method is complicated and difficult.
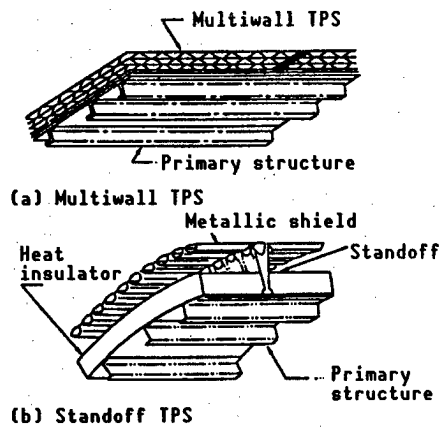
Figure 3. Examples of Thermal Protection System Structures
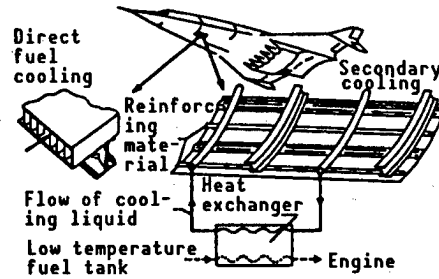
Figure 4. Example of Active Cooling Structure

Not only is it possible to achieve a drastic reduction of fabrication costs but weight reduction has also become possible by using titanium alloys and new fabrication technologies such as SPF/DB (superplastic fabrication/diffusion welding). These new technologies have contributed greatly to the realization of the Mach 3 class airframe. However, a new class of heat-resistant materials has become necessary for the Mach 5 class airframes. Such materials will require many developments in large-sized parts fabrication technology and technological renovation has also become an important problem.

The airframe that will appear at the beginning of the 21st century has been conceived and the structures and materials that are promising candidates for this airframe are shown in Table 1 [not reproduced]. It will be necessary to obtain the optimum solution by exchanging studies on airframe development.

5. Conclusion

This article has summarized research studies conducted in 1987 and 1988 by the Japan Aerospace Industry Association, which were sponsored by MITI. A further substantial reduction in weight is indispensable for the supersonic transport planes that are expected to be developed in the near future. This creates many technical problems in the structure and material fields, but it can also be said to be an extremely interesting area for aircraft design engineers.

References

1.   Stone, J.E. and Kock, L.G., "Hypersonic Airframe Structure Technology Need and Flight Test Requirements," NASA CR, 3130.

2.   AEROSPACE AMERICA, October 1987.

3.   "Integrated Hypersonic Vehicle Design and Related Technologies," UCLA Short Course.

Study of Supersonic Transport Plane Engine Performance

906C0041K Tokyo HIKOKI SHINPOJIUMU in Japanese Oct 89 pp 350-353

[Article by Shichikei Sugiyama, National Aerospace Laboratory; and Hiroyuki Miyagi and Kanji Itahara, Ishikawajima-Harima Heavy Industries Co., Ltd.]

[Text] 1. Introduction

There are great expectations regarding the realization of the next generation of supersonic transport planes (SSTs) and their contribution to the rapid progress of international aviation. There are several problems that we cannot ignore and pass by in the development of SSTs. In particular, airport noise at take-off is an important problem. The variable cycle engine (VCE) is looked on as an engine with the potential to conquer this problem. The VCE is able to change the by-pass ratio according to the flying speed by changing the shape of various engine parts. Thus, a significant reduction of specific fuel consumption and noise can be achieved in comparison to fixed-shape engines. Since it is considered impossible for conventional fixed-shape engines to satisfy the requirements for supersonic plane engines, studies have been made on the steady-state characteristics of VCEs and on the effects on the engine of the operation of the variable elements.

2. Load Performance of Steady-State Parts

(1) Engine Cycle

According to the cycle parametric study of an engine cruising at supersonic speed, both specific impulse and specific fuel consumption deteriorate as the by-pass ratio becomes larger, given the current level of state element technology. As the level of element technology improves, however, the reduction of specific fuel consumption by high by-passing will become possible and a by-pass ratio in the neighborhood of 0.5-1.0 will be the optimum cycle.[1] In this research, the cruising speed was set at Mach 2.5. Some important points regarding engine design are shown in Table 1. These values were selected after taking into consideration low fuel consumption at cruising speed, etc. Moreover, the engine shown in Figure 1 has four variable elements: the fan stator blade, the flow pressure turbine nozzle, the back by-pass injector, and the thrust nozzle.
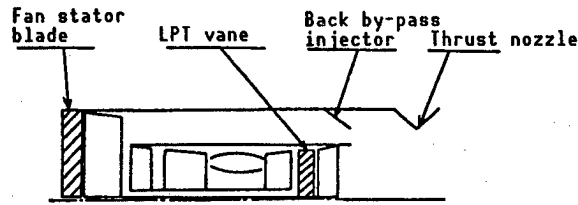
Figure 1. Variable Cycle Engine

Table 1. Engine Design Parameters

Mach number	2.5
Altitude	60,000 ft.
Turbine inlet temperature	1,750°C
By-pass ratio	1.0
Total pressure ratio	14.7

(2) Performance of Fixed-Shape Engine

The main cause of airport noise that become the problem for supersonic planes is jet noise. It is generally said that the jet noise is equivalent to jet speed x10^8. It is essential, therefore, to lower this speed.

The partial load characteristic on earth was obtained for the engine that had been established in the cycle study and the jet exhaust speed in the fixed-shape engine was obtained. The effect of changing the by-pass ratio and jet exhaust speed relative to the Mach numbers is shown in Figure 2. Although an afterburner was not used, the exhaust speed for the ground-based test reached 640 m/s and the control value of FAR 36 STAGE 3[2] for present subsonic planes could not be satisfied.

(3) Noise Reduction by VCE

The fan flow rate can be increased and the exhaust speed can be reduced while maintaining a fixed level of thrust through the application of VCE. The relationship between thrust and exhaust speed and between thrust and air flow rate when VCE was applied in a ground-based test is shown in Figure 3. When the thrust nozzle is opened, the thrust decreases slightly, but the overall air flow rate increases and the jet exhaust speed can be reduced. When the fan stator blade is opened, the air flow rate further increases and the thrust can be maintained at an almost constant level. The back by-pass injector is necessary to prevent choking of the by-pass duct pursuant to opening the thrust nozzle and fan stator blade.

65
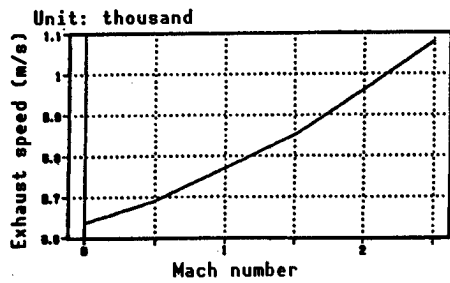
Figure 2(a). Relationship Between
Exhaust Speed and Mach Number
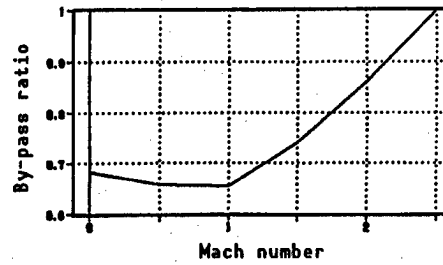
Figure 2(b). Relationship Between
By-Pass Ratio and Mach Number
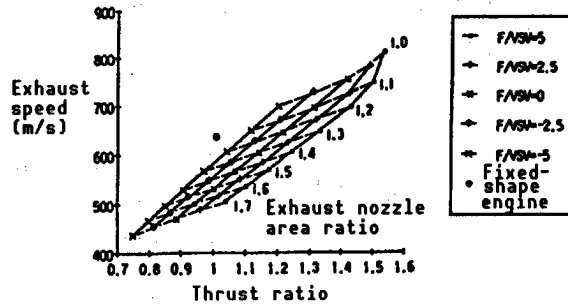
Figure 3(a). Relationship Between Exhaust Speed and Thrust Ratio
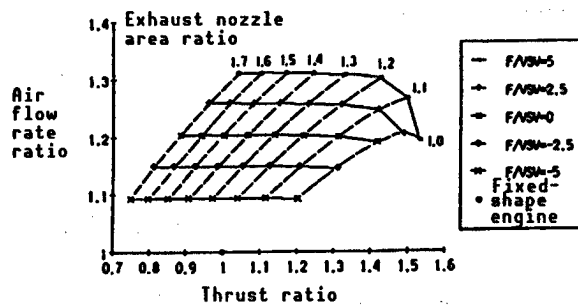
Figure 3(b). Relationship Between Air Flow Rate and Thrust Ratio

The relationship between thrust and the by-pass ratio is shown in Figure 4. The by-pass ratio can be increased by opening the thrust nozzle. The facts described above demonstrate that there is a potential for lowering the jet exhaust speed and reducing the airport noise through the application of VCE.

3. Dynamic Characteristics of VCE

It is important for actual operations to understand the effects exerted by the operation of the variable elements on the VCE. In this research, a VCE simulation model was prepared and the dynamic characteristics of the engine accompanying the step variation of the variable elements were studied.
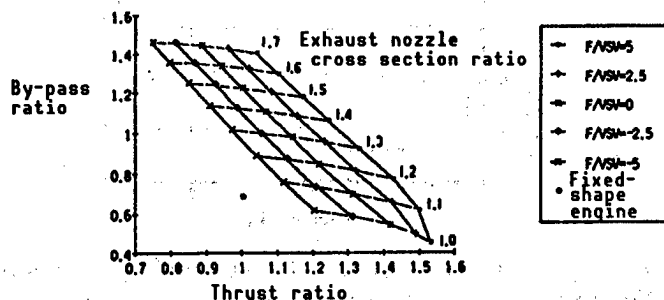
Figure 4. Relationship Between By-Pass Ratio and Thrust Ratio
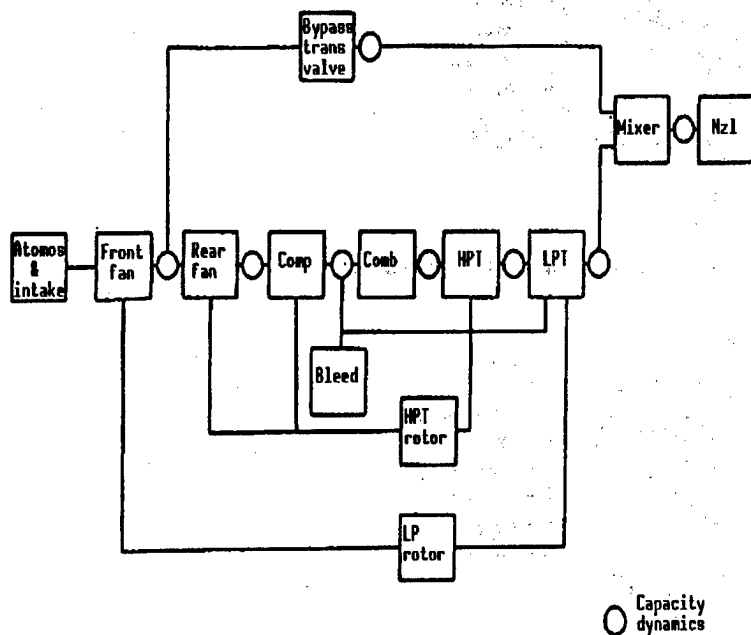
Figure 5. Simulation Model

(1) Simulation Model

Figure 5 is schematic diagram of the simulation model. The model is a system designed to obtain the engine dynamic characteristics from the element characteristics. The model is based on rotor dynamics and capacity dynamics.

(2) Simulation Results

The simulation results of the compressor effect against the step variation of the by-pass injector are shown in Figures 6 and 7. In Figure 6, time represented on the horizontal axis while by-pass injector area, pressure ratio (on map) and corrected air flow are plotted on the vertical axis.

In Figure 7, the corrected flow rate is depicted on the horizontal axis, while the pressure ratio is depicted on the horizontal axis. It shows the transfer of the operating point on the map of the compressor.

4. Conclusion

The following conclusions were obtained by calculating the steady-state partial load performance and unsteady performance of the VCE which is looked on as the next-generation supersonic plane engine:

(1) It has been ascertained that noise reduction at take-off is not possible with conventional fixed-shape engines but that it becomes possible by varying the thrust nozzle, fan stator blade, and back by-pass injector.
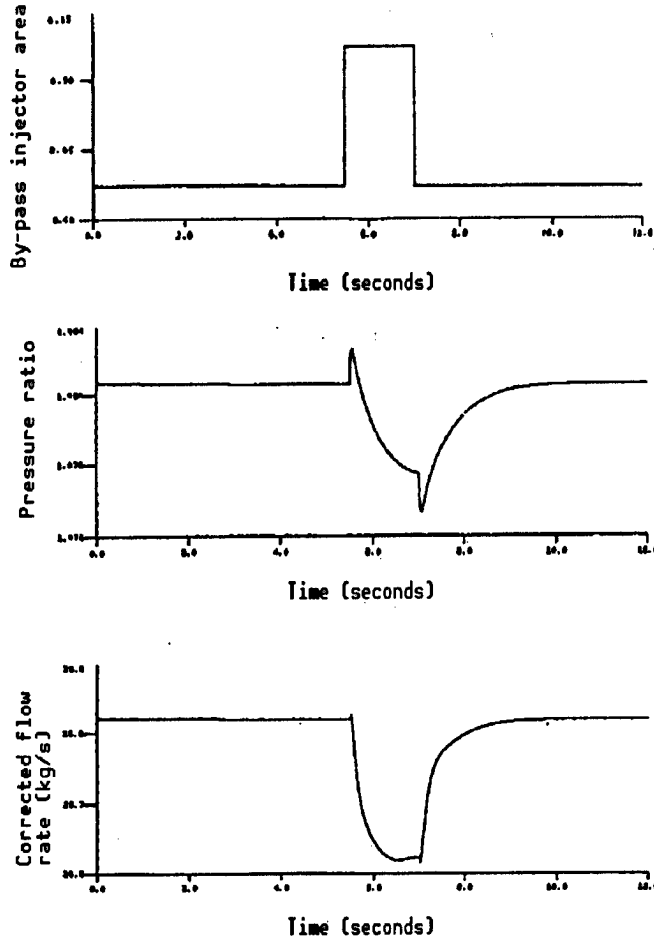
Figure 6. Example of Behavior When Changing the By—Pass
Injector Area in Stepped Condition
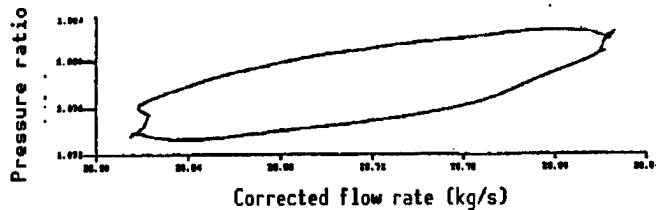
Figure 7. Behavior on Compressor P—Q Chart Corresponding to Step Response

(2) It became clear from the simulation results that the effect exerted by the
by—pass side variable elements on the core side was great. This indicates that
the VCE is a system with a strong mutual interference and that it is necessary
to ensure sufficient consideration of control design.

5. Concluding Remark

The compressor effect against the step variation of the by—pass injector was
simulated as the first step in studying the unsteady characteristics of the
VCE. Since the addition and reduction of fuel and the control of variable
parts are conducted simultaneously in more than two places, these responses

68

overlap and mutually interfere in an actual VCE, and, sometimes, the entire engine falls into an unstable operation condition. It is necessary to conduct further simulations that will focus on engine control in order to gain a better understanding of this phenomenon.

References

1. Tamaki, Itahara, and Harada, "Parametric Study of Engine Cycle for Supersonic Planes," Manuscripts from 29th Lecture Meeting on Aviation Prime Engines, February 1989.

2. Smith, M.J.T., et al., "Future Supersonic Transport Noise Lessons From the Past," AIAA-88-2989, 1988.

Aerodynamics of Supersonic Transport Planes: Parametric Study of Main Wing Shape by Wind Tunnel Test

[Article by Kenji Yoshida, Kawasaki Heavy Industries]

[Text] 1. Introduction

The development of the next-generation SST has followed a distinctive path in recent years.[1,2] The greatest focal point in the aerodynamic design of SSTs has been on the problem of how to reduce drag during supersonic cruising. The possibility of achieving a lift-drag ratio of about 10 at Mach 2.2 has recently been reported in SST research in the United States. This represents epochal progress given that the lift-drag ratio of the Concorde is about 7. The progress of drag reduction technology can be cited as reason that such a value has become possible. The drag reduction technology of today is summarized in Figure 1.

It is regrettable that we do not now have a sufficient accumulation on these up-to-date technologies. Therefore, based on the background described above, we first of all confirmed the effects of various technologies and, then, initiated basic research on the aerodynamic shape of the SST with the aim of its optimization. Among the various technologies examined, this paper focuses on the effects of the shape of the main wing plane and the shape of the airfoil leading edge as the first stage, and reports on the results of a study conducted using wind tunnel tests and theoretical analyses to understand their effects.

2. Outline of Wind Tunnel Test

This test was conducted using velocities up to Mach 1.4 at our Kawasaki three-dimensional transonic wind tunnel.

(1) Objectives

The following are the objectives of the investigation:

1) Effect of arrow wing[3]
2) Effect of leading edge radius
3) Effect of vortex flap[4]

Friction drag reduction

O Natural laminar flow
- Subsonic leading-edge
- Laminar flow airfoil

O Laminar flow control
- Suction
- Wall cooling

O Turbulent flow drag reduction
- Riblet

Lift dependent Drag reduction

O Wing planform
- Arrow wing

O Warp

O Vortex Flap

O Area rule
- Supersonic

O Blended wing-body

Wave drag reduction
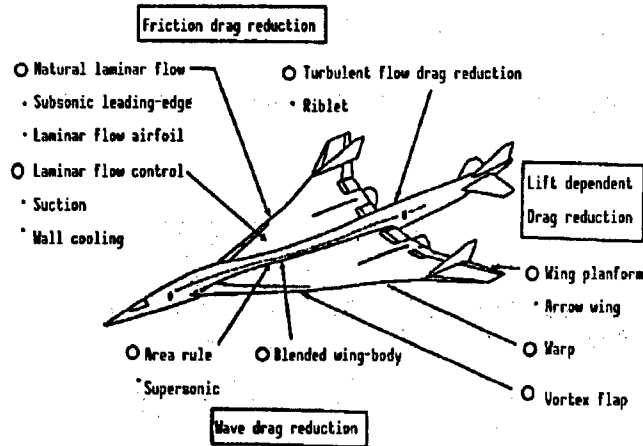
Figure 1. Various Drag Reduction Measures

DELTA

Main wing area S

Main wing V value

BASIC (BS)

p = 0.5   s/ℓ = 0.3635   τ = 0.0288

OGEE

BASIC (BS)

p = 0.4755   s/ℓ = 0.3448   τ = 0.0277

ARROW

BASIC (BS)
τ = 0.0292

MODIFIED WEDGE (MW)
τ = 0.0268

20 deg. VORTEX FLAP (VF)
τ = 0.0268
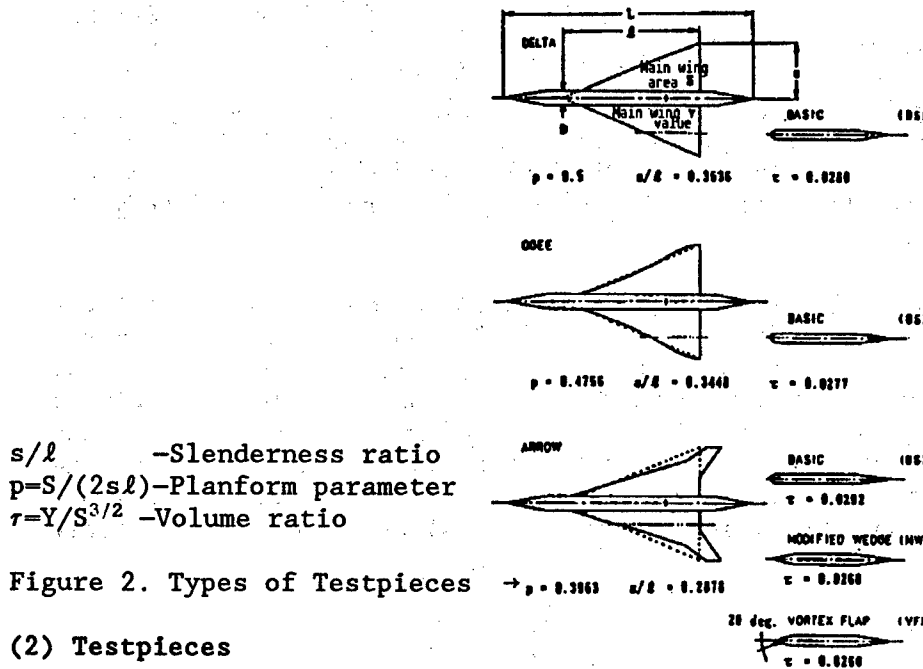
s/ℓ   —Slenderness ratio
$p=S/(2s\ell)$—Planform parameter
$\tau=V/S^{3/2}$ —Volume ratio

Figure 2. Types of Testpieces   p = 0.3963   s/ℓ = 0.2878

(2) Testpieces

See Figure 2 for schematic drawings of the testpieces. Figure 3 [not reproduced] is a photograph of one of the testpieces in the wind tunnel.

    1) Main Wing: Plane shape—There are three main wings: the delta wing, the ogee wing, and the arrow wing. However, the aspect ratio is the same (A = 1.45). The main wing area is S = 0.11 m² and the wing width is b = 0.4 m.

    Leading edge shape—There are three shapes: the arrow shape (only oval shape and mentioned as BS), wedge shape (MW), and vortex flap shape (VF).

71

2) Fuselage: The middle body part has a "Kamaboko" shape: the front
tip and rear end part have a pointed shape, as shown in
Figure 3 [not reproduced]. The body length is L = 1 m,
height is H = 0.05 m, and depth is D = 0.05 m.

3) Testing form: Form of wing and fuselage only by staying support
(see Figure 3 [not reproduced]).

4) Wind tunnel testing: M = 0.3~1.4, α = −4°~8°.

5) Study item: Mach number characteristic of C_D (especially supersonic
area).

3. Test Results and Considerations

3.1 Effects of Plane Shapes

(1) Zero Lift Drag (C_{DO})

1) It became clear from the wind tunnel test results that C_{DO} became
larger in the following order: arrow < ogee < delta in the supersonic
area and the difference of each shape became smaller with the increase
in the Mach number.

2) A drag calculation equation[2,5] based on the linear theory and
statistical data was used, and the relevant condition for each parameter
was checked by examining the wind tunnel test results. The following
results were obtained:

(i) The arrow wing certainly became smaller than the delta wing in
the supersonic area. This was due primarily to the reduction of
wave drag (C_{DT}) attributable to the main wing volume. The greatest
factor was the reduction of the fineness ratio, s/l, and the plane
shape parameter, p. These parameters characterize the plane shape
(Figure 2) and the fact that the p and s/l of the main wing becom-
ing small means that the main wing becomes long and slender. Since
the more slender the object, the smaller the physical disturbance
to the main flow. Thus, it can be inferred that C_{DO} becomes small.

(ii) The difference in C_{DO} between the arrow wing and the delta
wing shows virtually no change against increases of the Mach
number in the supersonic area. This differs from the wind tunnel
test results. It is believed that the reason for this lies in the
fact that the wave drag of the fuselage is not dependent on the
Mach number and is assumed to be fixed in this calculation equa-
tion. Thus, a reconsideration of the calculation equation is
necessary. More detailed information concerning pressure distribu-
tion, wind tunnel tests where M > 1.4, etc., are necessary, and
these will certainly be the subject of future research.

72
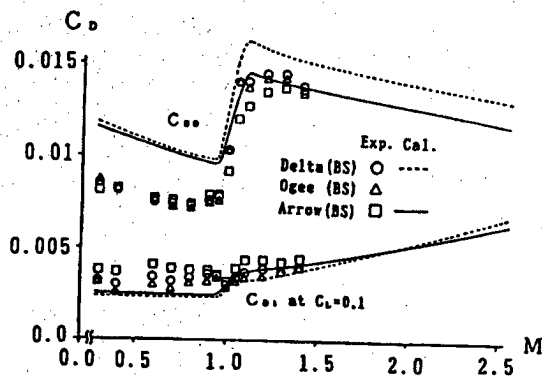
Figure 4. Effects of Plane Shapes

(2) Induced Drag (C_{Di})

1) It becomes clear from the wind tunnel test results as shown in Figure 4 that C_{Di} becomes larger in following order: ogee < delta < arrow in the supersonic area and that the difference of each shape becomes smaller with the increase of the Mach number. Moreover, a large change in the induced drag is not observed against the change from subsonic to supersonic.

2) The following result was obtained from the calculation result using the drag calculation equation.

• The arrow wing is certainly larger than the delta wing in the supersonic area in the same range as that of the wind tunnel test. However, this trend becomes reversed when M > 2. This is due to the p and s/l reduction of the arrow wing acting to reduce wave drag (C_{DL}) pursuant to lift generation. This is undoubtedly the arrow wing effect.[3] The physical reason is the same as in the case of C_{DT} and it can be understood from the fact that the disturbance (pressure variation) to the exterior pursuant to the lift generation of the main wing becomes small when it becomes long and slender. The breakdown of the induced drag by the calculation equation is shown in Figure 5. It can be seen from the drawing that the p and s/l reduction achieved by making the wing an arrow shape reduces the increase rate of C_{DL} against the Mach number. Although there is a difference in the absolute values when comparing the calculation values and experiment values in Figure 4, it coincides quite well in the supersonic area for the difference of the arrow and delta wings. Therefore, it can be considered that the relevant condition in the calculation equation is satisfactory for now.

3.2 Effects of Leading Edge Shape

(1) Zero Lift Drag (C_{DO})

1) The wind tunnel results shown in Figure 6 show that C_{DO} becomes larger in the following order: MW < VF < BS in the supersonic area and the difference of each shape becomes larger with the increase of the Mach number. The difference between MW and BS is especially great.

73
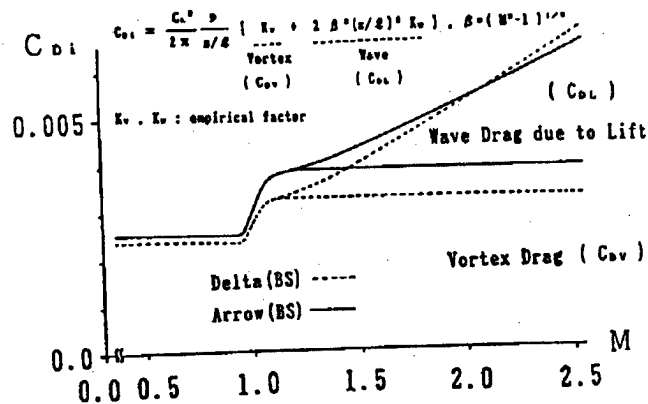
Figure 5. Breakdown of Induced Drag by Linear Theory
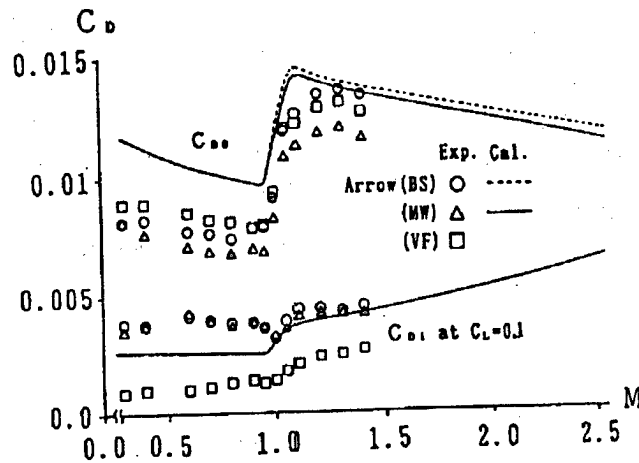
Figure 6. Effects of Leading Edge Shapes

2) The following result has been obtained from the calculation using the drag calculation equation.

• MW becomes significantly smaller than Bs in the supersonic area.

This can be tentatively understood by the fact that the relevant area decreases in comparison to an oval when the leading edge becomes pointed as in MW, reduction of the main wing volume as a whole occurs, and C_{DT} becomes small. However, it is believed that a reconsideration of the calculation equation is necessary as it is insufficient relative to the quantitative value, as also indicated by the drawing.

On the other hand, a calculation cannot be made on VF as the increase and decrease of drag by vortex lift cannot be handled in this calculation equation. Since VF generally does not generate even a thrust component in the $C_L = 0$ condition, i.e., the condition where there is no vortex lift, it becomes an obstacle for the air current and only generates additional drag. It can be considered that the reason why VF, given the same volume and leading edge radius as MW, did not become much

74

smaller than BS in comparison to the C_{D0} of MW, which decreases far more than BS in the supersonic area, is due to this.

(2) Induced Drag (C_{Di})

1) It becomes clear from the wind tunnel results shown in Figure 6 that C_{Di} becomes larger in the order of VF < MW < BS in the supersonic area, that the difference between MW and BS is small but the value of VF is about one-half of BS, that the difference between VF and BS becomes smaller with the increase of the Mach number, and that VF does not show a great change against the change from subsonic to supersonic.

2) Similarly, the following result has been obtained from the calculation result by the drag calculation equation.

- C_{Di} becomes larger with the increase of the Mach number in the supersonic area of MW.

This trend coincides with the experiment and the value is also quite close. However, the difference with other shapes is reflected only by the volume and leading edge radius in this calculation equation. Also, since these parameters were not contained in C_{Di}, the differences for each shape could not be discovered. Moreover, the reason why the VF value is small in the wind tunnel test is undoubtedly the VF effect and is due to the thrust component of the suction force by the leading edge separation vortex.

4. Conclusion

The effectiveness of the arrow wing was first confirmed from the study made on the main wing plane shape through the wind tunnel tests and theoretical analyses. The effectiveness of the vortex flap was confirmed next from the study made on the leading edge shape. However, the effect of a round leading edge on leading edge thrust could not be determined.

This wind tunnel was capable of supporting tests only up to Mach 1.4, but since the nonlinearity of the aerodynamic characteristics—as in the case of near transonic speeds—is originally weak at supersonic speeds, it should also be highly effective in linear theory. Therefore, there is a way to determine the effect of each reduction technology by using this wind tunnel. This is to determine the absolute value first by wind tunnel tests up to M = 1.4, extrapolating the results for velocities greater than Mach 1.4, calculating the difference, and conducting an evaluation for velocities near the design point (M = 2~3). It also can be said that the real value of this wind tunnel test lies in such an approach.

In the future, we look forward to exploring the combination of main wing torsion and camber distribution (also called warp shape) and area rule effect as other reduction technologies. We also plan to conduct parametric studies using wind tunnel tests and to reassess the equation used for drag calculation in aerodynamic design based on the results we have obtained.

References

1. Japan Aerospace Industry Association, 1987 SST/HST Development Trend Investigation Report, 1988.

2. Japan Aerospace Industry Association, Supersonic Transport Plane Development Trend Investigation Report for 1988, 1988.

3. Wright, Bruckmann, and Rodovich, J. AIRCRAFT, Vol 15 No 12, 1978, p 829.

4. Covell and Wood, AIAA Paper No 87-2475, 1987.

5. Kuchemann, AERODYNAMIC DESIGN OF AIRCRAFT, 1978.

Automation of Assembly by Robots

[Article by Akehiro Mizutani, Fuji Heavy Industries]

[Text] 1. Introduction

The automation of industry in Japan has made remarkable progress in recent years and examples of manless plants operating continuously for 24 hours can be seen in a number of places. Although automation has progressed in the machining field in the production of aircraft, assembly works remain heavily dependent on manual operations by skilled workers.

Spurred by the adoption of composite material structures for aircraft, Fuji Heavy Industries began to explore assembly automation technology for the purpose of stabilizing quality and shortening working hours. This article reports on the application of drilling robots to composite material structural assemblies, which is a portion of the results of the Fuji Heavy Industries' study.

2. Application of Drilling Robots

The intermediate training aircraft (hereinafter called T-4) of the Japanese Air Self-Defense Force was the first domestically produced plane to use a carbon fiber reinforced composite material (CFRP) in the primary structure. Fuji Heavy Industries was in charge of manufacturing the CFRP structural members for the vertical tail, etc., of this training aircraft. Figure 1 shows the robot drilling sections of the T-4 vertical tail, horizontal tail, and flap that our company was in charge of manufacturing. Since CFRP is physically hard in comparison to aluminum alloy, its machinability is inferior and the following various problems occur during assembly drilling work:

(1) Since the hardness of CFRP is high, machining efficiency is reduced and drilling time increases.
(2) Delamination between layers occurs.
(3) Drill wear is severe.
(4) The working environment becomes bad due to dust generation.
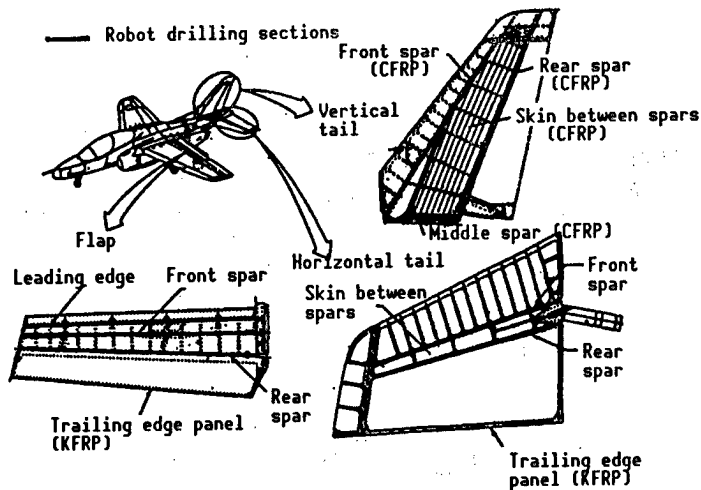
Figure 1. Robot Drilling Sections in T-4 Training Aircraft

To solve these problems, it was necessary to develop a drilling method that could be conducted at a fixed feed rate, where the driller could maintain the drilling posture for a long period, and where the presence of dust would not affect the worker. Since this drilling method would replace workers, it was also necessary to consider the cost effectiveness of the equipment being introduced. The development of a practical drilling system that used robots and the associated equipment cost was cheap and was approached from this perspective.

3. Outline of System

An outline of the robot drilling system that we developed and introduced is shown in Figure 2. This system consists of a program section, which was established in the technical department, and a machining section, which was established in the assembly workshop.

The program section conducts the off-line teaching work which prepares the program of the robot by using the graphic terminal. The term off-line teaching means conducting a teaching operation by using the computer graphic function of the three-dimensional CAD system (CATIA in this system) and moving the robot on the picture plane. This has the advantage of not having to occupy the machining section for a long period for the teaching of assembly parts as in the on-line system.

A program that has been prepared off-line is input to the robot and the machining section conducts compensation work with the actual machine and performs the drilling work. The machining section consists of the main robot body, a drilling head, an automatic tool replacement device, and a dust collector.

(1) Main Robot Body

A six-axis robot with a working range of 1.4 m x 3.8 m x 1.6 m is placed on a 7 m traveling device and the movement of the five drilling members is made possible. The main specifications of the robot are shown in Table 1.

78
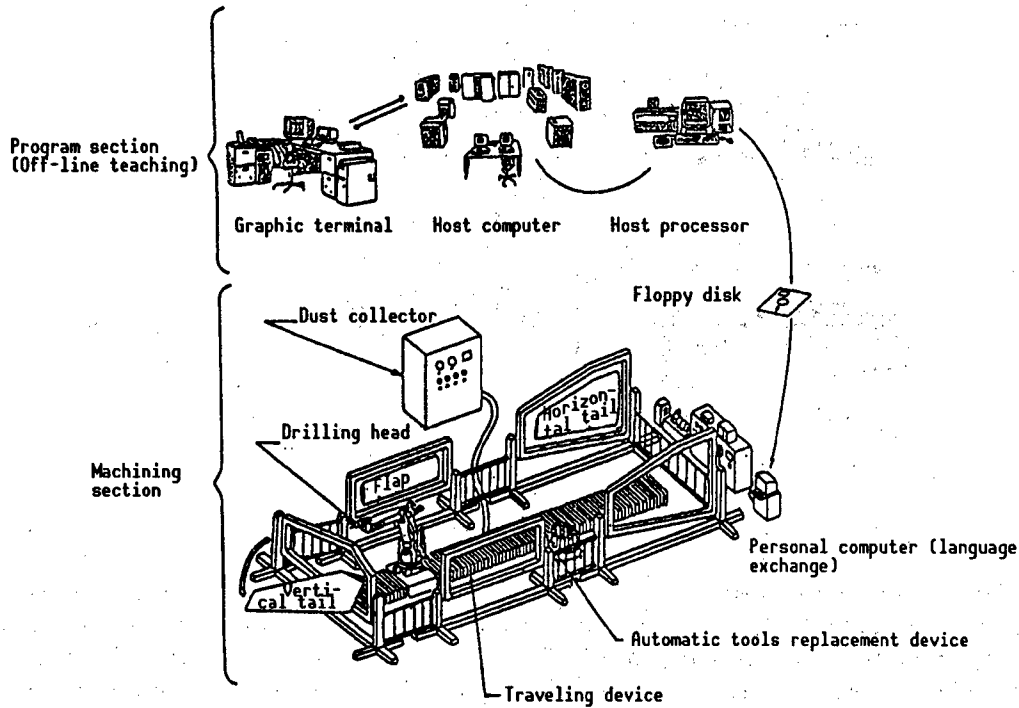
Figure 2. Outline of Robot Drilling System
for T-4 Training Aircraft

Table 1. Main Robot Specifications

Item	Specification
Structure	Vertical joint type
Degree of freedom	6 + 1 (traveling shaft)
Portable weight	70 kg
Position repeatability precision	0.5 mm

(2) Drilling Head

The drilling head is provided with a function for grasping the drill holder, a function for feeding the drill at a fixed rate, and a compensation function for absorbing the program error and dust collecting port. The combinations of the drill rotation frequency and feed rate are stored in advance as the drilling conditions and these are made so that they can be taken out according to the program. A diagram of the drilling head is shown in Figure 3.

Attachment (Fixing part to robot arms)

Dust collecting hose

Robot

Work

Drilling plate

Drill

Nosepiece

Error correction device

Inserting cylinder

Feed cylinder

Hydraulic motor
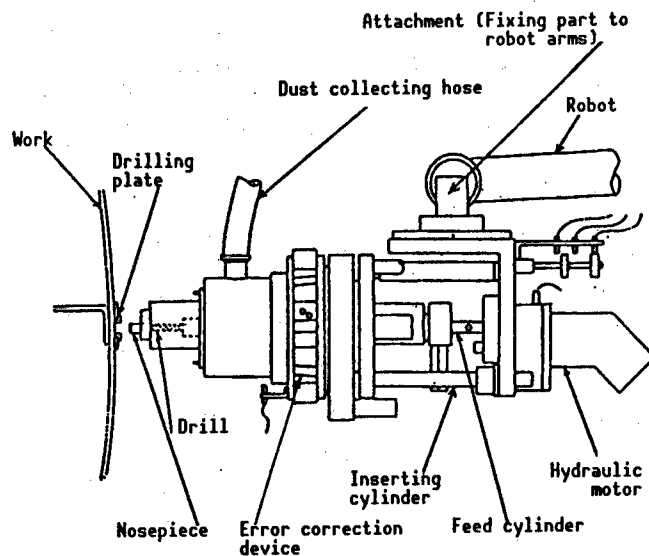
Figure 3. Drilling Head
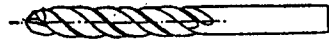
Figure 4. Double Angle Drill[1]

(3) Automatic Tool Replacement Device

This device automatically replaces different drills according to the program in accordance with the CFRP hole diameter. It also serves as a drill supplying device for automatically replacing a drill with the next drill when the prescribed number of drillings is reached. The drill is attached to the drill holder. Up to a maximum of 12 drill holders can be simultaneously set to the replacing device.

(4) Dust Collector

It collects dust and chips generated during drilling by negative pressure and a dust collection port is provided on the head section. The main dust collector body has been positioned outdoors to facilitate chip disposal.

4. Drilling Technology of Composite Materials

(1) Development of Drill

Conventional drilling techniques by workers involved the use of a backup to prevent delamination during CFRP drilling. However, a drill capable of conducting drilling without a backup became necessary for robot drilling. The CFRP drill that is used in this system today is a double angle drill developed by Fuji Heavy Industries, and the accuracy of the drilling diameter, durability, and delamination prevention effect have all been improved in comparison to those of conventional drills. The appearance of the double angle drill is shown in Figure 4.

(2) Development of Drilling head

The drilling head has been designed to be compact and lightweight to enable the robot to preserve the functions described above. Moreover, it was necessary to set the actuation timing of each drilling device properly to conduct the drilling work securely and efficiently. The optimum actuation timing was set through experiments. In particular, the working time of the error correction device in automatic drilling was taken into consideration so that it matched the insertion timing of the nose to the drilling plate.

(3) Drilling Conditions

Experiments have clearly demonstrated that it is necessary to change the drilling conditions in combination with the type of materials. The practical drilling conditions obtained from drilling experiments are shown in Table 2.

Table 2. Drilling Conditions

	CFRP-CFRP	CFRP-Al	KFRP-Al
Rotation frequency (rpm)	1,200	1,500	1,150
Feed rate (mm/sec)	1.3	1.0	1.6

5. Effects of Adopting Robot Drilling Technology

The automatic drilling of CFRP structures was realized by the drilling system and drilling conditions that have been described above. A comparison of drilling by robot and conventional manual drilling is shown in Table 3. Drill holding during drilling has become secure, drilling quality has been improved by maintaining a fixed feed rate, and drill life has been extended by about 70 percent over manual drilling. Moreover, working time has been reduced by about 30 percent.

Table 3. Comparison of Human and Automated Drilling

Item	Worker	
	Robot	Generation to slight degree
Drilling time	1	0.7
Drill life	1	1.7
Rate of delamination	1	0.1
Dust generation	No generation	None

6. Future Topics

Robot drilling has become operational by acquiring the application outlook in the T-4 production, and it is believed that the solution of the following future topics is necessary:

(1) The accuracy of robots programmed by off-line teaching was worse than initial expectations and compensation by using the actual machine structure became necessary. Thus it is necessary to promote the improvement of the matching accuracy of the off-line data and robot action.

(2) Establishment of a depth control method is necessary for the simultaneous conduct of countersinking work.

7. Conclusion

Drilling work occupies an important position in the assembly process. It is believed that the automation of CFRP drilling is very useful in improving product quality and shortening working time. It is felt that in the future it will be necessary not only to drill the outer plates and beams, but to drill the beams and ribs, and to devise methods for the automatic attachment of nut plates, etc., in stages. It will also be necessary to expand the mechanization and automation ratios of assembly works. With regard to developments overseas, there is some information about R&D and practical applications by the Boeing Co., McDonnell, and other companies. We wish to promote automation technologies in Japan so that we will not fall behind the United States and the European countries.

References

1.   Patent Application, Tokukai 1988-306812.

Development of Flat Panel Display for Aircraft

[Article by Tomoyuki Udagawa, Masao Fujii, Noboru Atsubayashi, Yoichiro Kurihara, Masaaki Imamura, and Akeyoshi Shinkawa, Yokogawa Hokushin Electric Corp.]

[Text] 1. Details of Development

With the emergence of large, high-performance aircraft in recent years, integrated electronic indicators with CRT displays are being installed to reduce the workload of pilots, eliminate redundancy, and improve the cockpit.

For the last five years our company has been promoting the development of a color liquid crystal display (LCD) system using a liquid crystal panel as the aircraft display device for the next generation of aircraft. We have developed systems that measure 3 x 3 inches, 4 x 4 inches, and 5 x 5 inches. We recently were able to install the 5 x 5-inch system in the flight simulator of the National Aerospace Laboratory and had the opportunity to conduct various evaluations.

This report will describe the flat panel display (FPD) system, including the picture drawing processing section, and will discuss the present status of LCD panels, focusing primarily on the 5 x 5-inch model.

2. Development Conditions of LCD Panel

Table 1 shows the development conditions of LCD panels. Many STN-type LCD panels are used for the display panel of general laptop computers, primarily for cost reasons. But there is also a development effort centered around the TFT-TN panel, which offers superior reliability and the highest contrast among displays designed for aircraft use.

The display theory of the TN liquid crystal display is shown in Figure 1, and an example of the structure of a TFT active matrix liquid crystal color display is shown in Figure 2.
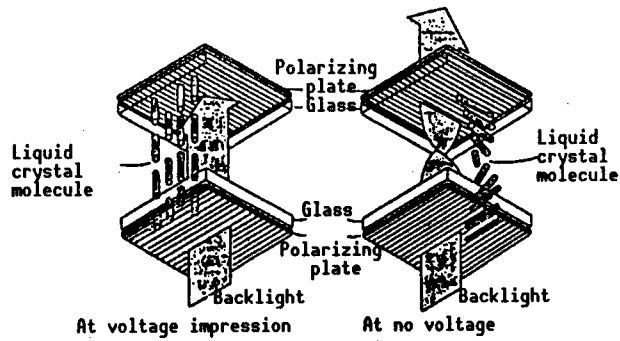
Figure 1. Operation Theory for TN Liquid Crystal Display
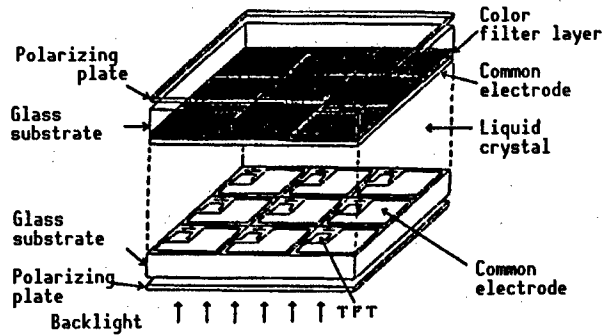
Figure 2. Example of TFT Liquid Crystal Display Structure

Table 1. Development Conditions for LCD Panel System

	TFT—TN system	STN	GH system	Phase transi-tion type	Ferro-electrics
Contrast	20~100	15	10	5	10
Angle of visibility	Δ	Δ	Δ	o	o
Colorization	●	o	o	x	o
Resolution	0.12~0.3	0.2~0.4	0.2~0.4	Used in fixed pattern	0.4
Response speed	20~80 ms	150 ms	70~150 ms	10~40 ms	15 μs
Temperature range	−10~80°C	−10~80°C	−10~80°C	−10~80°C	−20~66°C
Character-istics	High contrast High speed response	Lower cost than TFT—TN	Low cost	Wide angle of visi-bility	Storage property Wide angle visibility High speed response

3. Comparison With CRT

Comparison of the performance characteristics of the aircraft CRT and the FDP we installed in the simulator, together with the performance characteristics of a model installed in an actual plane which followed a parallel development path, is shown in Table 2.

Table 2. Performance Comparison of CRT and LCD for Aircraft

	CRT (5 inch size)	LCD flat panel display	
		Simulator-mounted device	Actual plane-mounted device
Resolution	0.18 mm/dot	0.16x0.14 mm/dot	0.14x0.14 mm/dot
Display color	Full color	Multicolor	Full color
Contrast (in daylight)	2:1	5:1	10:1
Light intensity	200 Ft-L	150 Ft-L	150 Ft-L
Angle of visibility	Hori-zontal more than ±60° Verti-cal more than ±60°	Hori-zontal +50° -50° Verti-cal +45° - 0°	Hori-zontal +60° -60° Verti-cal +50° -10°
Refresh rate	60 Hz	70 Hz	60 Hz (video mix)
External shape (depth)	318 mm	160 mm	100 mm
Weight	6 kg	3.8 kg	More than 3 kg
Vibration-proof	2 G	5 G	5 G
Operation environment temperature	-54~55°C	0~40°C	-54~55°C (However, with heater)

The LCD is known for being thin, lightweight, and requiring little electrical power. Further, in addition to its visibility and anti-vibration property in daylight, it is a device that is superior in terms of maintenance requirements.
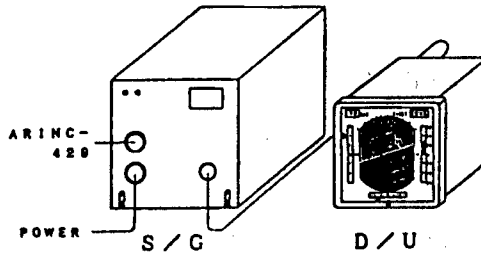
Figure 3. FDP System
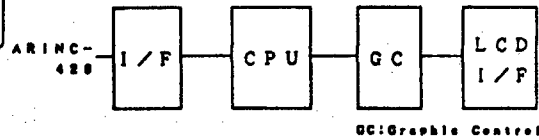
Figure 4. S/G Block Diagram

(1) Picture drawing with RGB as a set

(2) Picture drawing by controlling RGB individually
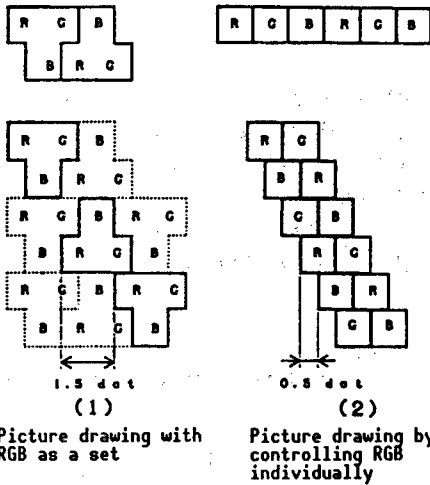
Figure 5. Difference of Display According to Pixel Handling Method
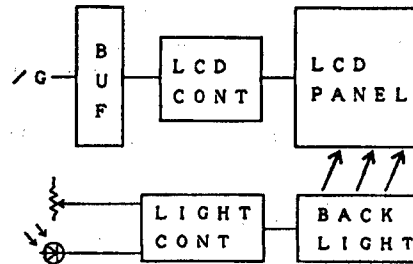
Figure 6. D/U Block Diagram

4. Outline of FPD System

The connection sequence of the FPD system is shown in Figure 3. Picture drawing processing is conducted with the symbol generator (S/G) based on the data from external buses such as an ARINC-429, etc. Its configuration is such that the display is made on an LCD by the display unit (D/U).

(1) Structure of S/G

A block diagram of the S/G is shown in Figure 4. The primary differences between the S/G for CRT and S/G for LCD are that the CRT is capable of making mixed displays of vector scan and raster scan, whereas the LCD is capable of raster scan only. Also, in contrast to the CRT which is able to handle simultaneously a set of RGB as one color dot, a jagged condition (condition appearing like stairs) becomes conspicuous as shown in Figure 5(1) when an LCD handles a similar pixel.

The S/G for LCD which is being developed by our company now has taken these points into consideration, and, by providing the functions described below, it

86

has been made so that detailed animation display can be conducted smoothly for only the raster scan:

- Division of picture plane and shortening of picture drawing time by a parallel picture drawing process.

- Synthesis of picture plane by window circuit.

- Load reduction of picture drawing process circuit by hardware modifications to provide smearing out function.

- Detailed picture drawing process based on the independent control of each RGB pixel (Figure 5(2)).

(2) Structure of D/U

A block diagram of the D/U is shown in Figure 6. Various backlight methods are being studied, as shown in Table 3. However, Yokogawa Hokushin Electric Corp. is presently using a fluorescent lamp for such reasons as the wavelength of each RGB color, luminous efficiency, etc. Although it is generally said that the luminous intensity of the fluorescent lamp is difficult to control in comparison with other light sources, our company has made light intensity of a wide range possible by means of a circuit-like device.

Table 3. Performance Comparison of Backlight Devices

Condition	Evaluation		
	Fluorescent lamp	ELs	Electric bulbs
1. Light source color is white (6,500 K)	⊙	o	Δ
2. Brightness	⊙	x	Δ
3. Low consumption of electric power	⊙	⊙	Δ
4. Life is more than 2,000 hours	⊙	x	x
5. It is not thick (thin light source)	Δ	⊙	Δ
6. Dimmer is possible	o	o	⊙
7. Usable in temperature of −40°C~85°C	Δ*	⊙	⊙
8. Highly resistant to vibration	o	⊙	Δ

Note: Δ*: Heater necessary

87
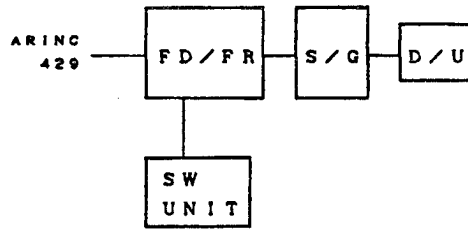
Figure 7. System Mounted on Flight Simulator

The adjustment of light intensity is controlled by a signal from the external light sensor in addition to the volume positioned at the front and is made to change automatically according to the external brightness. Moreover, a design that has also taken into consideration the adaptation time of human eyes has been provided.

A diffusion plate is built in between the LCS and the backlight, and the uniformalization of light intensity has been promoted. In addition to this, a built-in heater has been provided on the back of the LCD and display at low temperature has been made possible.

5. Simulator Equipped System

A block diagram of the system mounted on the flight simulator is shown in Figure 7.

The ARINC-429 data bus has one entry port into the FD/FR unit, and, after conducting operations, picture drawing processing is made by S/G and is displayed by D/U. Moreover, it is made so that the selection of the display format, etc., is possible by the SW unit attached to the pedestal board of the cockpit.

6. Future Policy

The evaluation test we conducted using a simulator has confirmed that LCDs are suitable as general-purpose indicators for aircraft.

Together with promoting further miniaturization and improved performance through a high level of circuit integration, the addition of superpositioned display functions with the external video signals, etc., in the future, we also plan to pursue related developments, such as enhancing environmental resistance and improving reliability.

References

1.   NIKKEI ELECTRONICS, 2 Jan 84.

Simulator Evaluation Tests of Liquid Crystal Flat Display

[Article by Hiroyasu Kawahara, Kaoru Wakairo, and Akira Watanabe, National Aerospace Laboratory; Tomoyuli Udagawa, Kengo Takeda, and Noboru Shobayashi, Yokogawa Hokushin Electric Corp.]

[Text] 1. Introduction

The instruments used on the newest large passenger jet planes are changing from the conventional electromechanical system flight instruments to integrated flight instruments. Airplanes like the B-767 and B-747-400 have already entered service with such integrated instrument and have accumulated positive achievements. Moreover, similar developments are being eagerly promoted for the A-320 and MD-11, which will enter into service in the near future as developmental planes. Most of the integrated instruments installed in these airplanes are either 8-inch CRT displays or liquid crystal flat panel displays (LCDs). LCDs have several advantages in comparison to CRTs, although they are still in the development stage. However, it is believed that the introduction of LCDs will be inevitable in the future.

The National Aerospace Laboratory has long been engaged in research on electronic integrated instruments and has compiled research results on hardware, display formats, etc.[1,2]

Evaluation tests have been conducted with a flight simulator on the function, performance, display format, etc., of an LCD made by Yokogawa Hokushin Electric Corp. This report will outline steps required before LCDs can be installed in actual planes. Moreover, it is planned to use a liquid crystal display in conjunction with the technical research related to the experimental STOL plane "Asuka" conducted by the National Aerospace Laboratory.

2. Outline of Liquid Crystal Display

Please refer to the work by T. Udagawa, et al., cited in the references (to be announced at preliminary lecture) for details regarding LCDs.
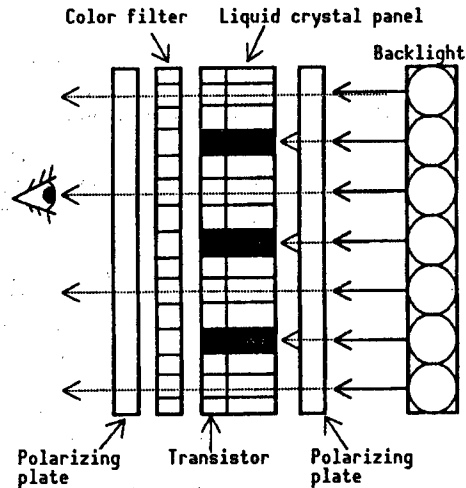
Figure 1. Conceptual Diagram of Liquid Crystal Display

2.1 Characteristics (Comparison With CRT)

The following are the principal characteristics of an LCD as compared to a CRT.

(1) It is compact and lightweight.
(2) It does not require high voltage.
(3) It excels in visibility against backlight.
(4) It saves energy.
(5) It is free of deflection strain and color shifts.
(6) The color tone is uniform when light intensity is stepped down.
(7) It does not require an explosion-proof structure.

2.2 Structure

A conceptual diagram of the structure is shown in Figure 1. The basic composition consists of the following elements:

(1) Liquid crystal panel
(2) Color filter
(3) Deflection plate
(4) Backlight

The basic operation principle is that a transistor is provided for each pixel of the liquid crystal panel and the liquid crystal shutter opens and closes (deflects) according to the ON and OFF signal from the transistor. The color filter has been arranged so there is a corresponding RGB for each pixel of the liquid crystal panel. The color pixels take on colors and become observable by the light of the backlight (many fluorescent lamps) which passes through the panel corresponding to the opening of the shutter.

2.3 Performance

The performance of the LCD used in this evaluation test is shown in Table 1.

Table 1. Performance of Liquid Crystal Display

	Item	Performance/Standard
1	Display area	Vertical 125.3 mm x Horizontal 122.9 mm
2	Display color	16-color simultaneous display from 256 colors
3	Resolution (minimum)	Vertical 0.145 mm x Horizontal 0.16 mm
4	Contrast	More than 10
5	Light intensity control	0.5~80 Ft.L
6	Angle of visibility	Left and right 60°
7	Refresh rate	80 Hz
8	Data update rate	40 Hz/20 Hz
9	Power source/electricity consumption	AC 115V/400 Hz/70 W

3. Display Format

As noted above the display format that was the object of this evaluation test is a display format based on the format developed for the technical research of the STOL experimental plane "Asuka." It displays speed, altitude, and elevation rate centered around the attitude indicator. The display format for the evaluation object is shown in Figure 2.
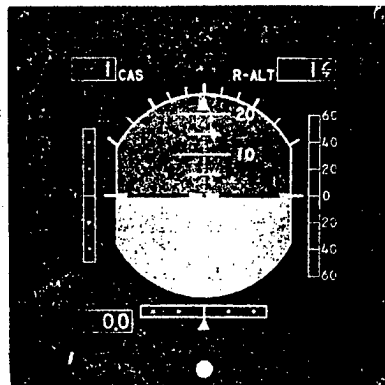
Figure 2. Display Format

91
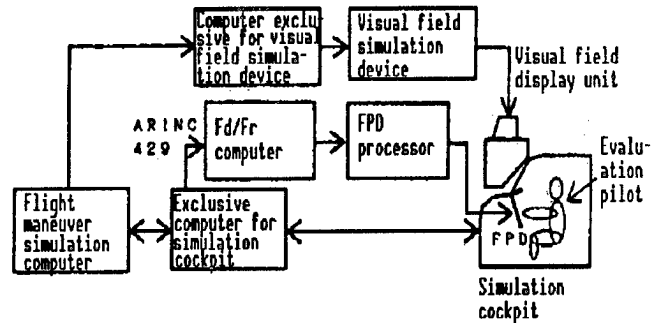
Figure 3. Block Diagram of Flight Simulation Test

4. Simulator Evaluation Tests

4.1 Test Objective

The objective of the test is to mount the LCD now under development on the hardware and software (display format) of the flight simulator and to have the pilot determine whether or not it possesses the functions and performance required of an integrated aviation instrument.

4.2 Testing Facility

(1) Flight Simulator Facility

For our experiment we used the general—purpose flight simulator facility of the National Aerospace Laboratory.[4] The equipment used in the evaluation tests is described below. Figure 3 is a block diagram of the simulation test.

(a) Simulated cockpit: The attitude indictor (ADI) of the captain's seat instrument panel was removed and a 5—inch LCD was installed. Therefore, the conventional speed indicator, altimeter, elevation rate meter, etc., were left in their original positions. The display processor was set in the space beside the electric rack in the back part of the cockpit. A photograph of the cockpit with the LCD installed is shown in Figure 4 [not reproduced].

(b) Flight motion simulation computer: An MV/20000 computer made by Nippon Data General Co. was used as the main computer and an S/250 computer was used as the simulated cockpit exclusive computer. Coupling of the flight motion simulation computer and the display processor was effected by an ARINC 429 and the data transfer rate was set at 25 times/second.

(c) Flight motion model: The STOL take—off and landing forms of the experimental STOL plane "Asuka" were used.

4.3 Evaluation Pilot

The evaluation tests were conducted by a total of 23 evaluation pilots: two research pilots from the National Aerospace Laboratory, 12 test pilots from aircraft manufacturers, and nine test pilots from airline service companies.

92

4.4 Evaluation Tests

Tests were conducted for normal take-off (STOL take-off form), ascending, form change, air work, approach (STOL landing form) and landing, and evaluation points and comments were entered in the evaluation sheet.

4.5 Evaluation Items and Comments Entry Sheet

Evaluation points and comments on the following evaluation items were entered on the evaluation sheet:

(1) Size and thickness of the symbols, lines, and numerical figures.
(2) Color tone of the symbols, lines, and numerical figures.
(3) Motion smoothness of the symbols, lines, and numerical figures.
(4) Reading ease of the symbols, lines, and numerical figures.
(5) Functions and performance of hardware.

Items (1) to (4) are evaluations of the display format, while item (5) is an evaluation of the hardware. An example of the evaluation comment sheet is shown in Figure 5.

(Concerning symbol, line, size, and thickness of numerical figures)

	Item	1	2	3	4	5	6	7	Comments
1	Horizontal line								
2	Airframe symbol								
3	Pitch radar								
4	Bank angle scale								
5	Bank angle pointer								
6	G/S, LOC scale								
7	G/S, LOC pointer								
8	Ascending rate scale								
9	Ascending rate pointer								
10	CAS display								
11	Altitude display								
12	GA, V_1, V_R, V_2 display								

Remarks: 1: Superior   4: Satisfactory   7: Improvement required
   • Insert the o mark in the corresponding blank space and the comments in the comment column.

Figure 5. Example of Evaluation Comment Sheet

Item	Evaluation						
	1	2	3	4	5	6	7
1 Horizontal line	●	●● ■		●● ■■■■		●	
2 Airframe signal	●	●●		● ▪	●●● ■	●●● ■	■▪
3 Pitch scale	● ■	●●	■	●●● ■■■■	●●●		● ■■■
4 Bank angle scale	●● ■■	●		●●●●● ■	■■	●	●
5 Bank angle pointer	●● ■	●● ■	■	●●●●● ■	▪		●
6 G/S, LOC scale	●●● ■	●		●●●●● ■▪	■	■	●
7 G/S, LOC pointer	●●● ■	●		●●●● ■	● ■		● ■■
8 Ascending rate scale	●●●● ■	●		●●●● ■■■■	●● ■		●●● ■■■
9 Ascending rate pointer	●●●●	●		●● ■■■	●●	■■	● ■■■
10 Speed display	●●●● ■	●● ■■	●	●● ■■■■	●	■	■
11 Altitude display	●●●● ■	●● ■		● ●●● ■■	■■	■	■
12 G_A, V_1, V_2, V_R display	●● ▪	● ■		● ●●●● ■		■	■

●■ : 5 pilots   ● : Aircraft manufacturer
● ■ : Single pilot   ■ : Airline company

Figure 6. Example of Evaluation Results (Symbol, line,
size, and thickness of numerical figures)

5. Test Results and Studies

The evaluation point results for evaluation items (1), (2), and (5) are shown in Figures 6, 7, and 8. Each of the drawings has been plotted commonly by classifying separately the pilots of the aircraft manufacturers and the pilots of the airline companies.

5.1 'Size and Thickness' of Symbols, Lines, and Numerical Figures

Figure 6 indicates that there are problems in the pitch scale, airframe symbol, elevation rate scale, elevation rate pointer, etc.

Some of the complaints were that the line on the pitch scale was too narrow, the display became jagged in a small bank angle, the dot for each 1° should be made a short horizontal line, etc. Another problem involved changes in symbol shape, as shown below, to indicate the raising and lowering of the landing gear.

94

	Item	Evaluation						
		1	2	3	4	5	6	7
1	Background (top part)	●●●● ■■■	●●		●●●● ■■			
2	Background (bottom part)	● ■	●●		●●●● ■■■	● ■■■■		●● ■■
3	Horizontal line	●●●	●●		●●●● ■■	■■		● ■
4	Airframe symbol	●●	●●		●●	■■	●	●● ■■■■
5	Pitch scale	●●●	●● ■	■	●●●●	■		●
6	Bank angle scale	●●●	●●	■	●●●● ■■■■			●
7	Bank angle pointer	●●	●●●	■	●●●	●	■	● ■
8	GS, LOC scale	●●●	●● ■		●●●● ■	■■		
9	GS, LOC pointer	●●●●	●●		●● ■	● ■■■	■■■	● ■■
10	Ascending rate scale	●●●●	■	■	●●●● ■■■	■	■■	●
11	Ascending rate pointer	●●●●	●		●●● ■■	■	■■■	● ■■
12	Speed display	●●●● ■	●	■■	●■■			
13	Altitude display	●●●● ■	●	■■	●■■ ■			
14	GA,V₁,V₂,V₃ display	●●	●		●■■ ■■■			■

●■ : 5 pilots   ● : Aircraft manufacturer
● ■ : Single pilot   ■ : Airline company

Figure 7. Example of Evaluation Results (Symbol, line, and color tone of figures)

	Item	Evaluation						
		1	2	3	4	5	6	7
1	Size of picture plane	● ■	●●	● ■	●●●● ■■■■	● ■■		
2	Picture plane resolution	●● ■■	●●	●●●	●●●● ■■■	● ■	■■■	●
3	Picture plane brightness	●●●● ■■	●● ●●	●	●● ■		■	●● ■
4	Light intensity adjusting range	●●● ■■■	●	■	●●●● ■■■■	●	■	●●●●
5	Backlight appearance	●● ■■■■	● ■■	●●● ■■	●●● ■			
6	Type of coloring	●	●	●●	●● ●	●	● ■■	■
7	Do missing pixels bother you?	●●●		■	●●●● ■	● ■		

	Angle of visibility (left and right directions)		Ideal angle	Max. visible angle
8		Aircraft manufacturer	5 5. 7˚	6 5. 0˚
		Airline company	5 0. 0˚	8 2. 8˚

●■ : 5 pilots   ● : Aircraft manufacturer
● ■ : Single pilot   ■ : Airline company

Figure 8. Evaluation Result Example (Functions and performances of hardware)

It was difficult for the pilots to make the distinction when the top and bottom became reversed.
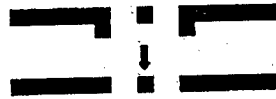
Moreover, it became clear that a hollow shape was better than a solid shape as shown below.
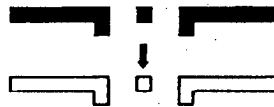
Next, the initial scale on the elevation rate display was set at ±6,000 ft/min. However, because the indicated value could not be made out, the display was programmed to automatically change over to a scale of ±3,000 ft/min at altitudes above 4,500 ft and to a scale of 1,500 ft/min at altitudes less than 4,500 ft. In any event, it was pointed out that it was difficult to read the indicated value accurately. The display gain was too high at the scale of ±1,500 ft and altitude maintenance in the neighborhood of a "zero" elevation rate was difficult. It is also understood that it would be preferable for all to conform to the SAE ARP.[5]

5.2 'Color Tone' of Symbols, Lines, and Numerical Figures

Figure 7 indicates that there were problems on the bottom part of the background, airframe symbol, G/S, LOC pointer, and elevation rate pointer.

Amber was selected as the color for the bottom part of the background. The generation of neutral tints, however, was difficult because of the nature of the hardware. Vertical stripes entered and a sense of incompatibility was generated as the pitch scale consisted of horizontal lines. Since it should be basically uniform, it will be necessary to improve the hardware.

The airframe symbol was painted out in black. However, as pointed out above, a hollowed light color is better. We believe that the best way to improve the G/S, LOC pointer, and elevation rate pointer is to conform to the shape and color tone of the SAE ARP.

5.3 'Movement Smoothness' of Symbols, Lines, and Numerical Figures

The discontinuity of the signal was visually recognized clearly upon checking the data transfer cycle between the flight maneuver computer and the display processor at 20 Hz initially. Therefore, the continuity of the signal was confirmed by changing the cycle to 25 Hz. Although this is merely a difference of 5 Hz, it nonetheless has a delicate effect.

Although it could be judged that movement smoothness was generally achieved, up to the last digit is displayed for the purpose of promoting altitude display precision on a digital display. It was found that digit movement was too fast and that this had an effect on reading ease.

96

5.4 'Reading Ease' of Symbols, Lines, and Numerical Figures

We believe that the overall results for shape, size, color tone, and smoothness are linked to reading ease. The fact that it is difficult to read the airframe symbol, pitch scale, elevation rate scale and pointer, altitude display, etc., also has been demonstrated by previous evaluation results. We believe that, by taking these results into account, the LCD can be made into an easily readable instrument by reviewing the digital display system, conducting an overall reevaluation of the display format, and reexamining the color tone including the neutral tints.

5.5 Functions and Performance of Hardware

The evaluation results of the hardware are shown in Figure 8.

(1) Picture plane size: The liquid crystal display used for this test was the 5-inch type (vertical 125.3 mm x horizontal 122.9 mm). It is of sufficient size when used as an EADI, but the 8-inch size is better when used as EFIS.

(2) Picture plane resolution: The smallest dot is 0.16 mm, the white line is 0.32 mm, and there are no particular problems. However, the establishment of a technology for eliminating the jagged appearance of oblique lines is necessary.

(3) Picture plane brightness: It lacks uniformity across the entire picture plane. The presence of darker patches is not desirable.

(4) Light intensity adjustment range: A flicker appeared in the neighborhood of the minimum light intensity. The light intensity has to be reduced for night flights and thus such a flicker is not acceptable. It should be possible continuously to adjust the light intensity all the way down to the minimum intensity. However, there is little loss of color tone when the light intensity is reduced, as occurs in a CRT.

(5) Visibility against backlight: It was confirmed that there was sufficient visibility against a powerful backlight (sunlight assumed).

(6) Types of colors: Many more colors, including the generation of neutral tints, are necessary.

(7) Missing pixels: The yield of a liquid crystal display panel depends on the number of missing pixels. Against a total number of 600,000 pixels, the absence of 20 pixels or less is allowed at present. It has been determined that there is virtually nothing to worry about with regard to missing pixels as long as they do not concentrate in one place.

(8) Angle of visibility: The only defect of the liquid crystal display is that visibleness from oblique directions is inferior. Sufficient visibility has been obtained in the normal operating range of pilots. The angle needed to observe the left seat EADI from the right side of the cockpit of a large jet plane is about 60° as shown in Figure 9. The maximum visible angle of display obtained in this evaluation test is 58.4°, although this is considered
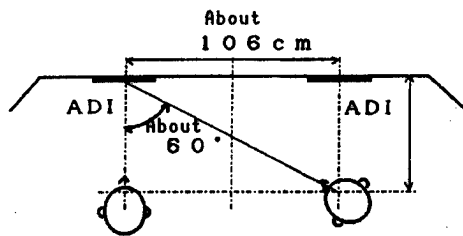
Figure 9. Facing Angle of Captain Seat ADI From Co-Pilot
Seat (Case of large transport planes)

sufficient for the present level of performance, securing a wider angle is
desired.

6. Conclusion

6.1 Display Format

There is room for repair and improvement on the digital display for such
elements as the pitch scale, airframe symbol, elevation rate indication,
altitude indication, etc. It is believed that the best policy is to conform to
the SAE ARP both for color tone and the shape of each symbol.

6.2 Hardware

It is considered necessary as future technical tasks to establish a multicolor
display technology including neutral tints, a light intensity adjustment
function for low light intensity, a jagged condition elimination technology,
a large picture plane for a wide angle of visibility, etc.

References

1.   Okabe, M., et al., "Research and Trial Manufacture of Integrated
      Aviation Instruments," National Aerospace Laboratory Report, TR–608, Apr
      80.

2.   Kawahara, H., et al., "Flight Simulation Evaluation Test of Multi-
      function Display Device," National Aerospace Laboratory Report, TM–596,
      Oct 88.

3.   Udagawa, T., et al., "Development of Aircraft Flat Panel Display,"
      Preprinted manuscripts for 27th Aircraft Symposium, Oct 89.

4.   Kawahara, H., et al., "Flight Simulation Test Facility: Composition,
      Functions, and Performance of Simulated Cockpit Device," National
      Aerospace Laboratory Report, TM–577, Nov 87.

5.   SAE: Recommended Aerospace Practice, ARP–4102/7, Nov 87.

Aircraft-Mounted Optical Data Bus (3): Bus Control Software, Performance Evaluation Test

[Article by Mitsumi Mayanagi, Minoru Takizawa, Tadao Uchida, and Hajime Yoishi, National Aerospace Laboratory; Yoshio Suemitsu and Toshiyuki Morita, Nippon Electric Co.; and Junzo Kodama, Sanwa Electronics Co.]

[Text] 1. Introduction

Research on an optical data bus has been in progress in various countries for some 10 years,[1] but such a device has not been put to practical use for an aircraft. This is attributable to the reliability problem of optical fiber technology.

To solve this problem, the National Aerospace Laboratory (NAL) has been conducting elemental research on a fly by light (F&L) device. NAL's goal is to create an optical flight control system, which it hopes to link with the research on future technologies for the STOL plane.[2-5] Previous reports have dealt with the trial manufacture and development and the environmental testing of an aircraft—mounted optical data bus. This report will describe the bus control software and performance evaluation test. The objectives of this research are to ensure the reliability of the optical data bus and to demonstrate its practicality. Therefore, considerations have been made so that the objectives could be achieved in the development of bus control software. In addition, the establishment of reliability standards on earth and tests difficult to conduct on planes were conducted prior to the flight tests used in the performance evaluation test.

2. Total Configuration of Bus Control Software

This bus control software consists primarily of a central processing unit (BC), input terminal equipment (RT1) control software, and output terminal equipment (RT2) control software (Figure 1). Each set of software consists of a main body and a terminal (PC). The main body is an 8086 assembly language program, writing is done on a ROM within the CPU board of each piece of equipment. Bus control processing, input/output signal processing, etc., are conducted. For the PC, writing is done on a floppy disk using the basic language program. Actuation is made on a personal computer and it is used for the conversational processing with the main body.

Bus control software

Input terminal equipment control software | Central processing unit control software | Output terminal equipment control software

PC. — Main body (for each)

Conversation processing | Main body IF. | PC. IF. | Input/output processing | Bus control processing (RT)

Discrete input signal processing
Discrete output signal processing
ARINC input signal processing
ARINC output signal processing

Conversation processing | Main body IF. | PC. IF. | Input/output processing | Bus control processing (BC)

Discrete input signal processing
Discrete output signal processing
Analog input signal processing
Bus control processing, selection, setting
Display of bus transmission test results

Channel selection
Frame cycle setting
Bus data transmission control
Wrap around check

Conversation processing | Main body IF. | PC. IF. | Input/output processing | Bus control processing (RT)

Discrete input signal processing
Discrete output signal processing
Analog input signal processing
Analog output signal processing
ARINC output signal processing

Figure 1. Overall Configuration of Optical Data
Bus Control Software

3. Bus Data Transmission and Input/Output Signals

The data transmission order of bus, as shown in Table 1, is conducted in the order of (1) through (12). The transmission of odd numbers—(1), (3), and up to (11)—and the transmission of even numbers—(2), (4), and up to (12)—use the same data corresponding to each. The computation of the error rate is made by judging the existence of errors when comparing the same data. Moreover, the BC also has incorporated the transmission data between RT1 and RT2. The number of messages per frame is 72, the number of transmission words is 2,406, the transmission time of the bus is 51.24 m sec, the read/write time of the memory is 16.94 m sec, the rewrite time of the memory is 16.86 m sec, the wrap around check time is 16.27 m sec and the time for the others is 17 m sec. Where possible, functions are overlapped and the minimum cycles per frame is made up of 110 m sec.

There are three types of input/output signals for each piece of equipment: discrete input/output (DI/DO) signals, ARINC input/output (ARI/ARO) signals, and analog input/output (AI/AO) signals. The hardware links among these signals are shown in Figure 2.

100

Table 1. Data Transmission Within One Frame Cycle and Time Necessary for Wrap Around Check Processing (Unit: m sec)

Or-der	Trans-mission direc-tion	Number of transmitted words	Trans-mission time	Memory read/ write time	Memory rewrite time	Check time
1	BC →RT1	CW(2W)+DW(11W)+SW(2W)	0.34	0.088	0.17	0
2	RT1→BC	Transmission of above for wrap around	0.34	0.088	0	0.17
3	BC →RT2	CW(2W)+DW(11W)+SW(2W)	0.34	0.088	0.17	0
4	RT2→BC	Transmission of above for wrap around	0.34	0.088	0	0.17
5	RT1→RT2	CW(2W)+DW(4W)+SW(2W)	0.20	0.032	0.08	0
6	RT2→BC	Transmission of above for wrap around	0.20	0.032	0	0.09
7	RT1→RT2	(CW(2W)+DW(32W)+SW (2W)) x 16	12.22	4.096	8.19	0
8	RT2→RT1	Transmission of above for wrap around	12.22	4.096	0	7.85
9	RT1→RT2	(CW(2W)+DW(32W)+SW (2W)) x 16	12.22	4.096	8.19	0
10	RT2→BC	Transmission of above for wrap around	12.22	4.096	0	7.85
11	RT2→RT1	CW(2W)+DW(9W)+SW(2W)	0.30	0.072	0.14	0
12	RT1→BC	Transmission of above for wrap around	0.30	0.072	0	0.14
	Total	2,406 W	51.24	16.944	16.86	16.27

* 1 frame cycle = Transmission + Memory read/write + Memory rewrite + Wrap
around check + Others
= 51.24 + 16.94 + 16.86 + 16.27 + 17.00
= 118.31 (ms) ⟶ 110 (ms)
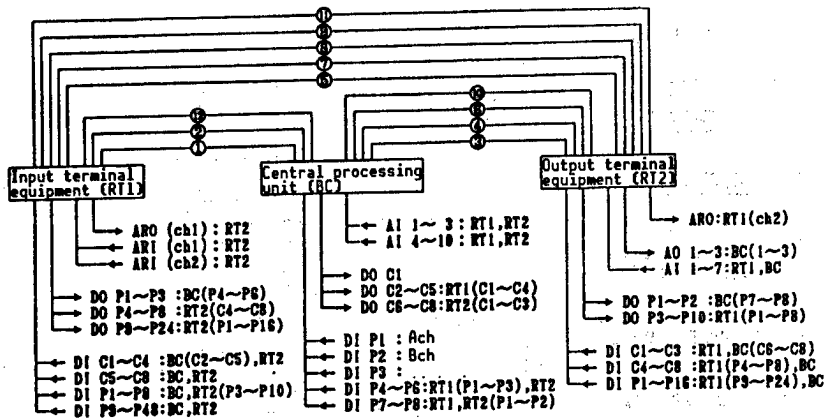
Figure 2. Input/Output Signal Processing of Data Bus
Transmission for Main Body of Various Equipment

4. Bus Control Software for Each Piece of Equipment

Figure 3 is a flowchart of the bus control software for the bus controller. Each step on the left side loop of Figure 2 is conducted in order by the power on of this software. In other words, after automatically conducting the initial setting, the real time timer setting and the input/output signal processing of the DI, DO, AI, etc., it looks for an interrupt command from the PC or programmable interval timer (PIT). It returns and conducts input/output signal processing when there is no interrupt and then repeats the procedure of looking for an interrupt command from the PC or PIT. When there is an interrupt command from the PC, it proceeds to the bottom of the loop and stops the bus transmission. It then performs selection of transmission starting, setting of frame cycle, display of error information, etc. Finally, it returns to the initially set step and conducts the various steps for reactuating the bus transmission. When there is an interrupt from the PIT, it proceeds to the selection of the transmission channel and conducts bus transmission by the central loop when light (A) and electricity (B) have been set. Upon completion, it returns to the loop at interrupt and repeats input/output signal processing. It proceeds to the right side loop when the selection of the transmission channel has been set to both A and B, and it performs data transmission alternately by both A and B channels.

Flowcharts for bus control software of the input/output terminal equipment shown in Figures 4 and 5, respectively, are similar to the bus control software of the bus controller with the exception of the setting of the wrap around (WA) checking transmission data when the bus transmission demand is a judgment reception of either RX or TX. The transmission data for (1) and (2) and the wrap around check program are shown in Figure 6.

102
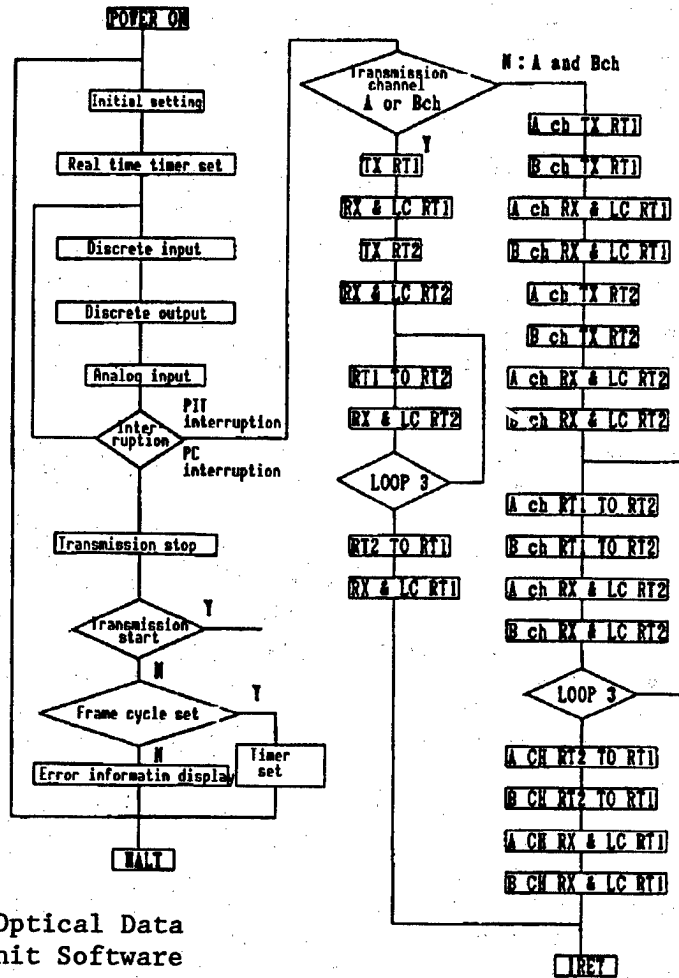
Figure 3. Flowchart of Optical Data
Bus Control Unit Software
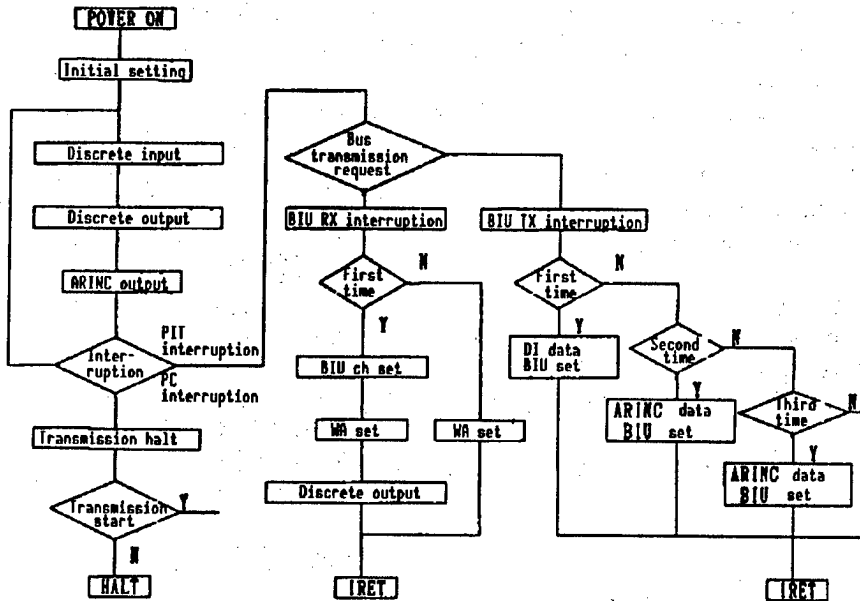
Figure 4. Flowchart of Optical Data Bus Input Terminal Equipment Software

103
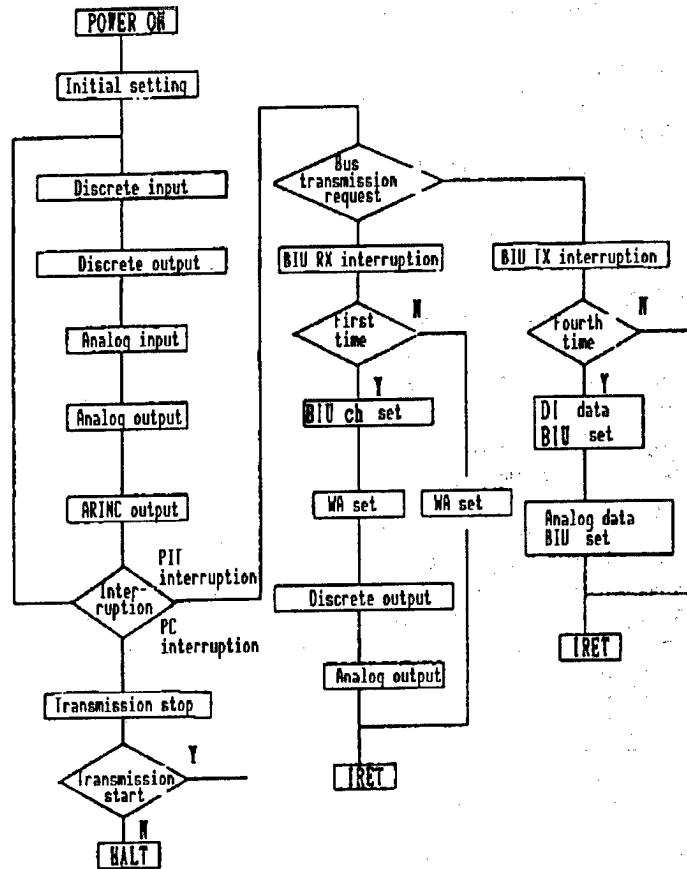
Figure 5. Flowchart of Optical Data Bus Output Terminal Equipment Software

```
              MOV          S1,0
              MOV          D1,8
              MOV          CX,11
    CHA_510:
              MOV          AX,ES:DBOB[D1]
              COM          BIU_DATA[S1],AX
              JNZ          CHA_520
              ADD          S1,2
              ADD          D1,2
              LOOP         CHA_510
              JMP          CHA_530
    CHA_520:
              MOV          BX,2006H
              CALL         BIU_ERR
    CHA_530:
```

Figure 6. Wrap Around Check Program
(Comparison of (1) and (2) transmission data)

5. Performance Evaluation Test

Explanations will be made here on the measurement of the most important bit error rate, which shows the bus reliability quantitatively in the performance evaluation test. This is calculated from the generation frequency of bit errors and bus actuating time written in the nonvolatile memory of the bus controller.

Table 2. Evaluation Test Results (Measured values of error rate for optical transmission)

Test No.	Working time	No. of frames passed	Total No. of messages	Total No. of bits	Error rate	
					Message	Bit
1	601 m	327,818	23,602,896	1.57×10^{10}	$\leq 4.23 \times 10^{-8}$	$\leq 6.34 \times 10^{-11}$
2	607 m	331,090	23,838,480	1.59×10^{10}	$\leq 4.19 \times 10^{-8}$	$\leq 6.27 \times 10^{-11}$
3	623 m	339,818	24,466,896	1.63×10^{10}	$\leq 4.08 \times 10^{-8}$	$\leq 6.11 \times 10^{-11}$
4	607 m	331,090	23,838,480	1.59×10^{10}	$\leq 4.19 \times 10^{-8}$	$\leq 6.27 \times 10^{-11}$
5	610 m	332,727	23,956,344	1.60×10^{10}	$\leq 4.17 \times 10^{-8}$	$\leq 6.24 \times 10^{-11}$
6	621 m	338,727	24,388,344	1.62×10^{10}	$\leq 4.10 \times 10^{-8}$	$\leq 6.13 \times 10^{-11}$
7	612 m	333,818	24,034,896	1.60×10^{10}	$\leq 4.16 \times 10^{-8}$	$\leq 6.22 \times 10^{-11}$
8	601 m	327,818	23,602,896	1.57×10^{10}	$\leq 4.23 \times 10^{-8}$	$\leq 6.34 \times 10^{-11}$
9	604 m	329,454	23,720,688	1.58×10^{10}	$\leq 4.21 \times 10^{-8}$	$\leq 6.30 \times 10^{-11}$
10	620 m	338,181	24,349,032	1.62×10^{10}	$\leq 4.10 \times 10^{-8}$	$\leq 6.14 \times 10^{-11}$

The values shown in Table 2 have been obtained as test results. However, these values are not those derived from error generation but are those that have been compulsorily stopped from the restriction of testing time and they become of smaller values when the testing time is extended. Moreover, according to the bus standard,[6,7] the prescribed value of the message error rate is less than 10^{-6} and the prescribed value of the bit error rate is less than 10^{-12}. Therefore, the former is sufficiently satisfied but the latter is an unsatisfactory value due to the shortage of testing time. However, when the test was continuously conducted for a period of 26 days and no error was generated, there is the possibility of satisfying the latter condition as the bit error rate becomes less than 10^{-12}.

6. Conclusion

Research and development on an optical data bus has been undertaken as a link to future technologies for STOL planes. Although work on an optical data bus has been under way for many years, the flight tests described in the following article have progressed smoothly and it is expected that they will be completed during this fiscal year.

There were no special technical problems and the data necessary for demonstrating the reliability of the bus were available thanks to the recent development and performance evaluation test of bus control software.

The development of a flight control loop system incorporating the optical data bus for further promoting the reliability and practicability of the optical data bus, demonstration by means of flight experiments with actual planes, and the realization of a high level of performance through high-speed bus transmission to take full advantage of its optical merits remain future topics.

References

1. Mayanagi, "Flight Control System Optical Technology," JAPAN AEROSPACE SOCIETY JOURNAL, Oct 84.

2. Mayanagi, et al., "Aircraft-Mounted Optical Data Bus (1): Trial Manufacture and Development," Lecture manuscripts for 26th Aircraft Symposium, Oct 88.

3. Takizawa, et al., "Aircraft-Mounted Optical Data Bus (2): Environmental Tests," Lecture manuscripts for 26th Aircraft Symposium, Oct 88.

4. Mayanagi, et al., "R&D on Optical Fiber Data Bus for Aircraft: (I) System Configuration and Basic Design, (II) Bus Control," Lecture manuscripts for 20th Aircraft Symposium, Nov 82.

5. Ibid., "R&D on Optical Fiber Data Bus for Aircraft: (IV) Optical Data Bus Characteristics Evaluation Test," Lecture manuscripts for 21st Aircraft Symposium, Nov 83.

6. MIL-STD-1553 A and B, Aircraft Internal Time Division Command/Response Multiplex Data Bus, 1975, 1978.

7. Proposed DOD-STD-1773, Fiber Optics: Mechanization of an Aircraft Internal Time Division Command/Response Multiplex Data Bus, Apr 85.

Aircraft-Mounted Data Bus (4): Flight Data

[Article by Tadao Uchida, Mitsumi Mayanagi, Minoru Takizawa, Toshiharu Inagaki, Koki Hozumi, and Kazutoshi Ishikawa, National Aerospace Laboratory]

[Text] 1. Introduction

The National Aerospace Laboratory has been promoting the development of elementary technologies and basic experiments on these technologies ever since 1980 for the realization of a fly-by-light flight control system for future STOL planes. An optical encoder, star coupler, optical data bus, etc., can be listed among the elementary technologies that have been developed.

We have conducted a flight test with our experimental plane, a Dornier DO228-200 (Photograph 1 [not reproduced]). This was an extension of the laboratory tests of the optical data bus. This report will focus on the results of this testing.

Main Specifications of Dornier Experimental Plane

Type	:	DORNIER 228-200
Engine	:	715 shp x 2
Total length	:	15.7 m
Total width	:	17.0 m
Total height	:	4.9 m
Wing area	:	32.0 m^2
Maximum take-off weight	:	5,700 kg
Maximum cruising velocity:		370 km/h (at sea level)

2. Test Objectives

The test objectives were to operate the optical data bus system in an actual flight test environment, to check its functions and performance, and to establish its reliability. In parallel with these objectives, a method for mounting optical fiber cables on aircraft and a corresponding handling method are also topics that should be considered.
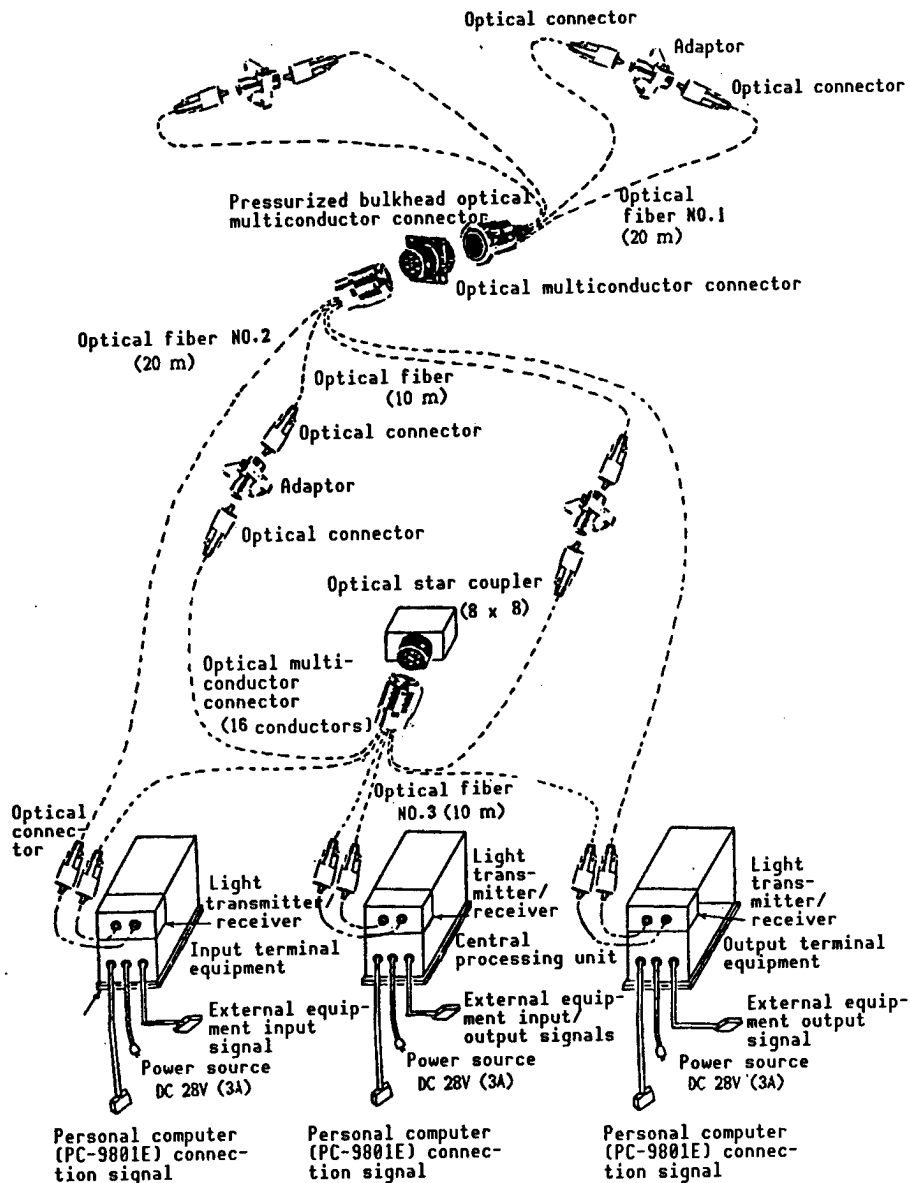
Figure 1. Configuration of Optical Data Bus as Mounted

Each environmental level of this test is gentle in comparison to the environmental resistance tests conducted on earth. However, this test is relevant in that it represents an operation in an actual flight environment, which is a complex environment.

3. Testpiece and Functions

The optical data bus (Figure 1), which is the testpiece, consists of the central processing unit (bus controller), which is the main component; input terminal equipment; output terminal equipment; optical fiber cables connecting the various pieces of equipment; single conductor connectors; adaptors; optical multiconductor connectors, including those for pressurized bulkheads; and
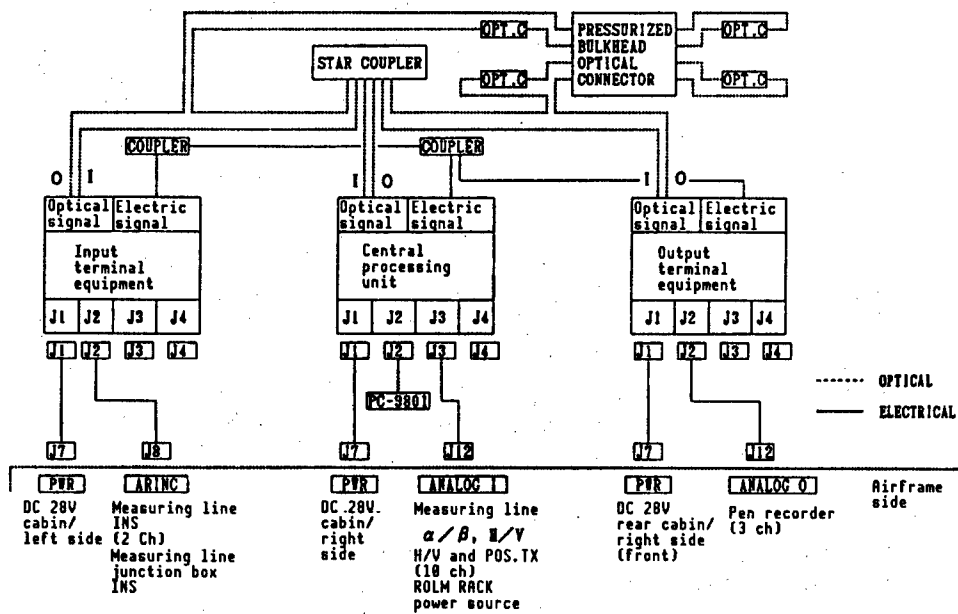
Figure 2. Configuration of Optical Data Bus System
and Coupling With Airframe Side

the star coupler. The central processing unit serves as the data bus con-
troller in the optical data bus. The input/output terminal equipment responds
to the instructions of the central processing unit and perform the functions
of signal format conversion (A/D, D/A, serial/parallel, etc.), conversion of
the data format to MIL-STD-1553B, etc. The functions of the optical trans-
mission cables, etc., are self-evident, while the function of the star coupler
is to distribute and couple optical signals. When this optical data bus has
been systematized for fly-by-light, additional functions such as flight
control rule computation for the central processing unit, and signal process-
ing, and a subcontroller role for input/output terminal equipment can be
provided. A functional block diagram including the connections with the
airframe side sensor and the power source is shown in Figure 2. This optical
data bus has an electronic data bus as a standby in case of trouble.

4. Testing Method

The optical data bus system shown in Figure 1 was mounted on the experimental
plane in our laboratory (Photograph 2 [not reproduced]). Figure 2 shows how
the connections with the power source and signals in the airframe side were
made. In this test, signals covering some 50 different types of positions,
attitudes, etc., from the altimeter, pitot pressure speed meter, α meter, β
meter, and INS were input as signal sources into the optical data bus system.
Signal formats consisted of analog signals, discrete signals and ARINC
signals. These signals are exchanged between the bus controller and the
input/output terminal equipment or between the input and output terminal
equipment. Signal wrap around is performed, mutual signals are compared, and
the transmission error was counted. The analog data were recorded on the pen
recorder from the output terminal equipment to monitoring the test.

This data bus system operates from the moment the power source in the plane is turned on before take-off until the power source is turned off after landing. The generation frequency of error data for this entire period was recorded.

There were many cases when the test flight mission was not a specially assigned flight motion and was conducted in parallel with other tests. In such cases the test flight consisted of an ordinary take-off and landing, together with standard turn and maneuvering motions. To date, 10 test flights have been conducted with a total flight test time of 988 minutes. The main flight records were maximum speed of about 180 KT, an altitude of about 9,500 ft, and a maximum turn and bank angle of about 60°. The air temperature and atmospheric pressure at take-off were recorded as part of the overall meteorological conditions during the test. The high and low ranges of these two factors were from 31~18° and about 30.03~29.72 in·Hg, respectively.

5. Test Results

Transmission errors were nil for all tests conducted to date. Measuring the error rate against the total number of messages and total number of bits in the transmission signal for the various flight tests produced the results shown in Table 1. For reference, the percentage against the total time is also shown.

Table 1. Flight Test Results (Measured values of error rate for optical transmission)

Test No.	Working time	No. of frames passed	Total No. of messages	Total No. of bits	Error rate	
					Message	Bit
1	115 m	62,727	4,516,344	3.01×10^9	$\leq 2.21 \times 10{-}7$	$\leq 3.31 \times 10^{10}$
2	121 m	66,000	4,752,000	3.17×10^9	$\leq 2.10 \times 10{-}7$	$\leq 3.14 \times 10^{10}$
3	118 m	64,363	4,634,136	3.09×10^9	$\leq 2.15 \times 10{-}7$	$\leq 3.22 \times 10^{10}$
4	82 m	44,727	3,220,344	2.15×10^9	$\leq 3.10 \times 10{-}7$	$\leq 4.64 \times 10^{10}$
5	94 m	51,272	3,691,584	2.46×10^9	$\leq 2.70 \times 10{-}7$	$\leq 4.05 \times 10^{10}$
6	94 m	51,272	3,691,584	2.46×10^9	$\leq 2.70 \times 10{-}7$	$\leq 4.05 \times 10^{10}$
7	112 m	61,090	4,398,480	2.93×10^9	$\leq 2.27 \times 10{-}7$	$\leq 3.40 \times 10^{10}$
8	94 m	51,272	3,691,584	2.46×10^9	$\leq 2.70 \times 10{-}7$	$\leq 4.05 \times 10^{10}$
9	72 m	39,272	2,827,584	1.88×10^9	$\leq 3.53 \times 10{-}7$	$\leq 5.29 \times 10^{10}$
10	86 m	46,909	3,377,448	2.25×10^9	$\leq 2.96 \times 10{-}7$	$\leq 4.43 \times 10^{10}$
Total	988 m	538,904	38,801,088	2.59×10^{10}	$\leq 2.58 \times 10^{-8}$	$\leq 3.87 \times 10^{-11}$

1 message = 337 words x 20 bits

A message error rate of less than 10^{-6} and a bit error rate of less than 10^{-12} are required according to the bus standard (MIL-STD 1553). This standard has been adequately satisfied for the former but not for the latter. It is absolutely impossible to satisfy the standard for the latter in a single flight test and it is believed that it should be applied to the total testing time. Moreover, the analog output of the bus (recorded by the pen recorder) monitored during the flight was also normal. There was no evidence of nonconformity as prudent attention was paid to handling.

6. Conclusion

Confirmation of the operation of optical transmission elements, together with the functions and reliability of the optical data bus, was conducted through these tests. We plan to promote experiments aimed at enhancing the practicality of flight-by-light and to increase the number of future flight hours.
In conclusion, we wish to note the cooperation received from Yoshio Suemitsu and other members of Nippon Electric Co. in the execution of these tests.

References

1. MIL-STD-1553B: Aircraft Internal Time Division Command/Response Multiplex Data Bus, 1978.

2. Proposed DOD-STD-1773: Fiber Optics Mechanization of an Aircraft Internal Time Division Command/Response Multiplex Data Bus, Apr 85.

3. Mayanagi, et al., "Aircraft-Mounted Optical Data Bus (1): Trial Manufacture and Development," 26th Aircraft Symposium, Oct 88, and "Aircraft-Mounted Optical Data Bus (3): Bus Control Software and Performance Evaluation Test," 27th Aircraft Symposium, Oct 89.

4. Takizawa, et al., "Aircraft-Mounted Optical Data Bus (2): Environmental Tests," 26th Aircraft Symposium, Oct 88.

Verification of Hypersonic Flow by Numerical Simulation of Spaceplane
Environment

[Article by Yukimitsu Yamamoto, National Aerospace Laboratory; and Osahiko
Arakawa and Ryuji Yoshida, Mitsubishi Heavy Industries]

[Text] 1. Introduction

Research on space shuttles, i.e., the so-called spaceplanes, as a new space
transport system for the 21st century is being actively promoted both
domestically and abroad. Hypersonic aerodynamic technology has emerged as one
of the most important research factors. It contains many thermal aerodynamic
topics that are not relevant to conventional aircraft design technology, such
as the problems of large incident angle aerodynamic characteristics, severe
aerodynamic integration technology with scramjet engines during ascent, etc.
To help understand these problems, a series of hypersonic wind tunnel tests
have been conducted in the National Aerospace Laboratory. Meanwhile, the
advent of supercomputers has dramatically expanded our capacity for the
analysis of numerical fluid mechanics and computational fluid dynamics (CFD).
Supercomputers have reached the stage where they can serve as powerful means
for designing spaceplanes. The hypersonic aerodynamic and aerodynamic heating
characteristics of the spaceplane environment have been investigated in detail
by numerical simulation using the Navier-Stokes equation, and the results were
verified through a comparison with the wind tunnel test results. This article
reports on these results.

2. Numerical Analysis Method

The basic equation used for the numerical analysis is the three-dimensional
thin layer approximation Navier-Stokes equation. The numerical analysis method
involves flow rate separation total variation diminishing (TVD) windward
difference calculus[1,2,3] and it has a secondary precision by the extrapolation
of the MUSCL type. The time direction integral is the implicit approximate
factorization (IAF) method,[4] but approximation of diagnolizing, etc., have not
been made.

A three-dimensional hyperbolic partial differential equation[5] was used for the
lattice forming method. This method is capable of preparing lattices that

intersect with the object surface perpendicularly and has the advantage that lattice formation is easy in ranges having three-dimensional indentations. Moreover, lattices were also prepared for areas including the wake area further behind than the main wing trailing edge in this numerical analysis to make the large incident angle calculation possible. However, the base flow calculation has been omitted and the fuselage part has been extended as is up to the wake area. The computation lattice is recomposed by linear interpolation from the basic lattice mentioned above. In other words, since the outer side of the shockwave surrounding the airframe is characterized by a uniform hypersonic flow, it is desirable from the point of effective use of lattices to conform the outer side boundary of the lattice to the shockwave as much as possible. Therefore, the outer side boundary of the lattice for each angle of incidence is made to conform to the shape of the shockwave in advance. Moreover, lattices are concentrated in the neighborhood of the object surface to capture the viscosity effect. For boundary conditions, the pressure gradient in the perpendicular direction to the object surface and each velocity distribution were set at zero and an isothermal wall was imagined for obtaining aerodynamic heating. A uniform flow condition was provided in the outer side boundary plane of the lattice and a runoff condition by extrapolation was provided to the downstream boundary in the back of the object. The conditions of the numerical computation were set at Mach 7, a Reynolds number of 4.4×10^6 which makes the entire length the standard, a uniform flow temperature of 67 K, and an object surface temperature of 300 K. These conditions almost coincide with the uniform flow conditions of the hypersonic wind tunnel of the National Aerospace Laboratory. Moreover, Baldwin-Lomax algebraic random number model[6] has been adopted in this computation.

3. Comparison of Pressure Distribution Characteristics

This section will focus on a comparison of the space shuttle zero degree configuration pressure distribution test and the numerical simulation results. The configuration as shown in the diagram in Figure 1 consists of a fuselage, a double delta wing, and two vertical tails. The main wing profile is NACA-0005. There are four sets of comparison objects. The three symmetric cases of incident angles (α) are 0°, 10°, and 20°, while the asymmetric incident angle is 20° and the sideslip (β) angle is 5°. An extremely superior coincidence has been obtained from $\alpha = 0°$ and up to a large angle of incidence of 50° for the comparison of the aerodynamic coefficient results.[2] The positions and numbers of pressure holes on the upper and lower surfaces of the spaceplane pressure test model are shown in Figure 1. The pressure distribution comparison results when incident angle is 20° and the sideslip angle is 5° are shown in Figure 2. "ETA" in the drawing expresses the dimensionless length X/L along the object axis measured from the head tip of each cross section, the Y axis is the span direction coordinate and it has been made dimensionless by the maximum width W within each cross section. C_p on the X axis is the pressure coefficient, which is defined as $C_p = (P-P_\infty)/(0.5\rho_\infty U_\infty^2)$. The pressure distribution determined by computation is expressed by a solid line for the upper airframe surface and by a dotted line for the lower surface. The pressure distribution of the windward side sideslip is shown on the left side, the pressure distribution of the leeward side sideslip is shown on the right side in the drawing, and cross section configurations have been drawn in on the bottom part. As can be seen from the series of drawings, the numerical computation

113
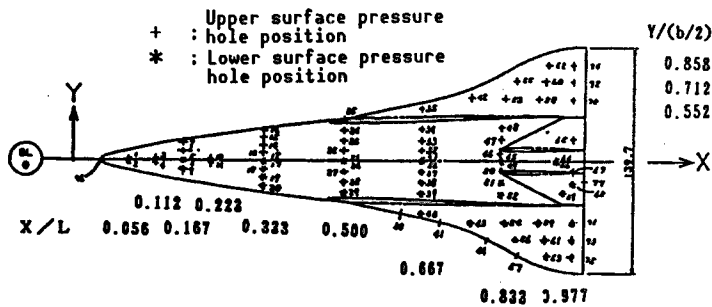
Figure 1. Number and Position of Pressure Holes for
Hypersonic Wind Tunnel Pressure Test Model

results are all pressure hole positions. The values derived by computation are
virtually equal to the experiment values and the reliability of the pressure
results of this analysis has been demonstrated. It is not possible in this
article, for reasons of space, to discuss the asymmetric computation case.
However, the computation results showed a superior coincidence with experi-
mentally derived values through each angle of incidence and it was ascertained
that numerical simulation plays an important role in determining the pressure
characteristics of spaceplanes.

Figure 3 shows the oil flow in the asymmetric case. The separation line of the
windward side sideslip of the main wind upper surface nears the fuselage side
surface, the separation line of the leeward side sideslip drifts inversely
toward the main wing leading edge side, and the separation line on the
fuselage upper surface joins with this.

4. Verification of Aerodynamic Heating Characteristics

Analysis of the hypersonic aerodynamic heating characteristics of spaceplanes
is extremely important in designing thermal protection and a heat-resistant
structure. Research in this field has conventionally centered around an
analysis of the obtuse configuration surrounding the head part. However, in a
spaceplane the main wing leading edge experiences high aerodynamic heating
because of the repressing effect, and the interference between the shockwave
generated by the leading edge and the shockwave from the head part sometimes
cause a local aerodynamic heating peak that sharply exceeds the value at the
head part stagnation point.[7] In addition, the aerodynamic heating of this area
is greatly affected by the main wing sweepback angle, the radius of curvature
of the leading edge of the wing and the attitude angle of the airframe. The
aerodynamic heating characteristics of the main wing leading edge surroundings
will be parametrically investigated by numerical simulation in this section
and the results of these effects, which have been studied in detail, will be
presented.

Three types of airframe configurations with different main wing sweepback
angles were taken up and the profile was changed from NACA0005 to NACA0010 to
facilitate the analysis of the leading edge surroundings. Moreover, the cross
sectional direction lattice point distribution of the main wing leading edge
was improved at 10° intervals and the precision of the analysis was improved.

114
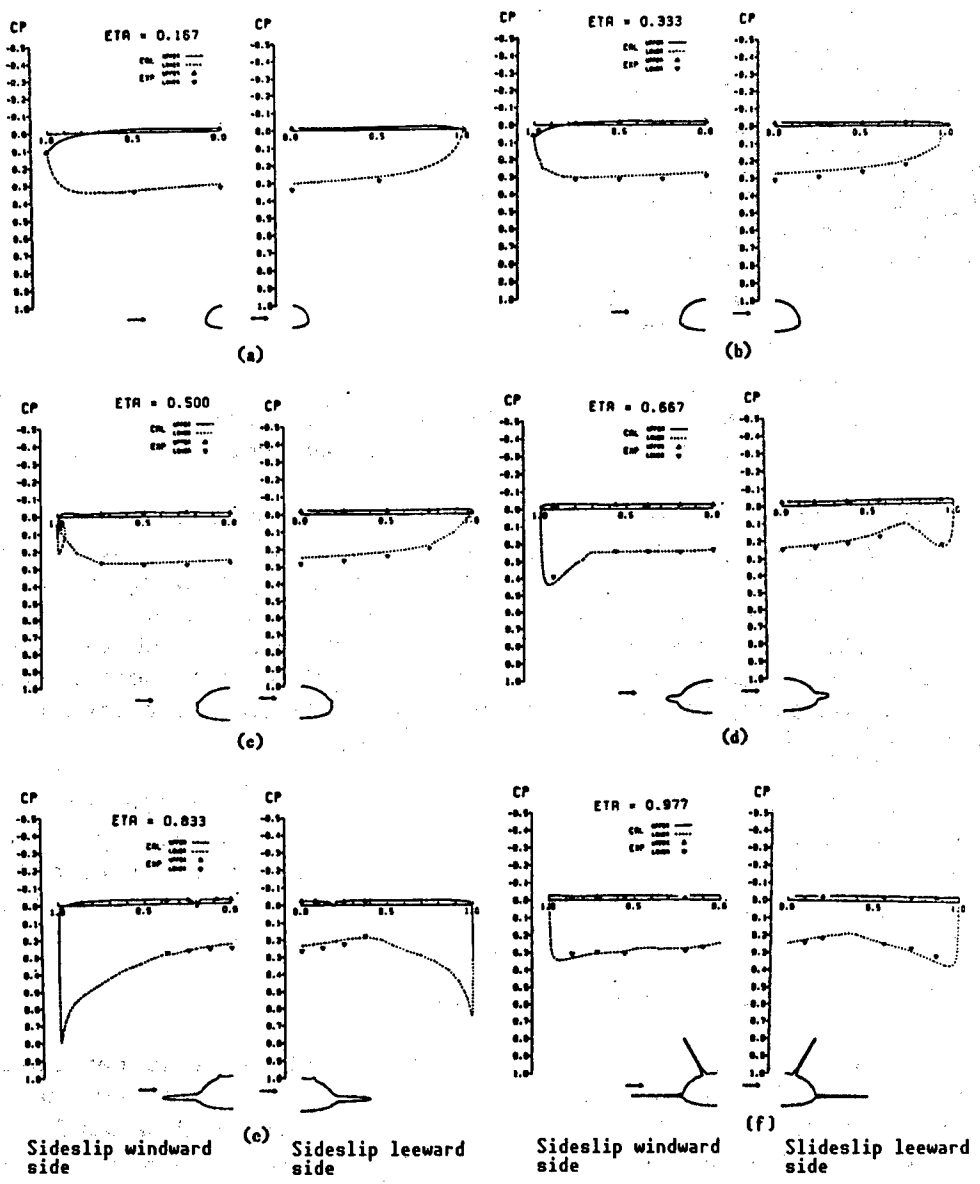
Figure 2. Comparison With Experimental Values of Spaceplane Cross Section Pressure Distribution Where Angle of Incidence Is 20° and Sideslip Angle Is 5° ($M_\infty = 7.0$, $Re_\infty = 4.4 \times 10^6$)


Windward side upper surface sideslip

Leeward side upper surface sideslip
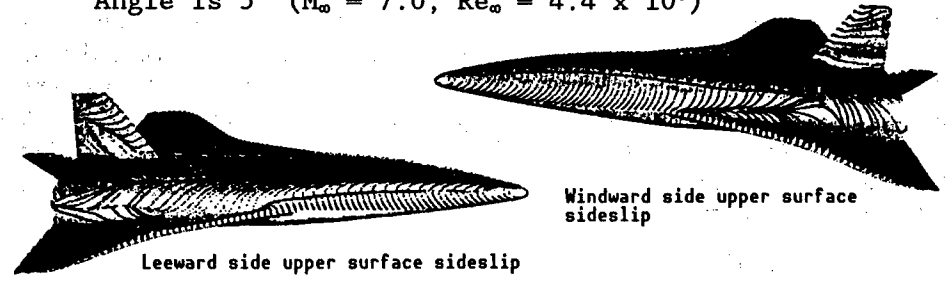
Figure 3. Oil Flow in Asymmetric Case
($M_\infty = 7.0$ $Re_\infty = 4.4 \times 10^6$, $\alpha = 20°$, $\beta = 5°$)

115

The study of the aerodynamic heating characteristics of the tip fin attached to the main wing tip also can be listed as another feature of this analysis. The main purpose of the tip fin is to maintain directional stability at a high angle of incidence and experiments on this point have also been conducted.[8,9] An analysis was also conducted on the incident angle side subjected to severe aerodynamic heating by taking into consideration the case when this concept is reflected in the configuration design of spaceplanes. Numerical computation was conducted on those cases where the angle of incidence (α) was 0°, 10°, and 20° for each configuration. The number of lattice points for the parametric computation was about 330,000 points with a main flow direction of 91 points, a circumferential direction of 73 points, and a vertical direction to object of 50 points. Among these, the main flow direction for 21 calculation cross sections was assigned for the computation of the wake area.

The three types of airframe configurations taken up in this section have a common fuselage and vertical tail for each configuration and the upper and lower cross sections of the fuselage, respectively, consists of different oval cross sections. The SPH001 is the same as the zero degree configuration, with the exception that the profile is NACA0010 and the SPH002, in contrast to this, has a main wing sweepback angle of 45° and a configuration in which a tip fin is attached to the main wing tip. The tip fin is slanted 30° to the outer side and the sweepback angle is 45°, the same as the main wing. With the exception of the strake part, SPH003 has the same tip fin as SPH002 at the main wing sweep-back angle of 53°. The hypersonic aerodynamic heating test is conducted by the phase change coating method and by the temperature measuring method using infrared radiation.[10] A comparison with these test results has been made with the SPH002 configuration as the representative example. The outer side shockwave configuration at an angle of incidence of 20° for the SPH002 surroundings is shown in Figure 4. That the state that the shockwave generates in the tip fin surroundings penetrates the shockwave from the head section is clear. The surface aerodynamic heating chart at an angle of incidence of 0° for the SPH002 configuration and heating distribution along the symmetric line of the fuselage with a top and bottom angle of incidence of 0°, 10°, and 20° and the main wing leading edge are shown in Figure 5. The aerodynamic heating is made dimensionless at the maximum value of the head section. The maximum value of local aerodynamic heating along the leading wing edge at an angle of incidence of 0° appears at the tip fin root. The aerodynamic heating peak of the tip fin root decreases at an angle of incidence of 10°, and the maximum value moves to the upper part of the tip fin leading edge. Despite the fact that a sharp pressure peak generates at the root of the main wing, aerodynamic heating does not increase much. This is because the radius of curvature of the leading edge at the root of the main wing is extremely large in comparison to that of the tip fin root, and it is known that the radius of curvature of the leading edge exerts a great effect on heating. Both sets of angles of incidence have also plotted for the experimental values in the peak neighborhood and this has shown superior coincidence. The aerodynamic heating along the tip fin decreases and shows a flat distribution at an angle of incidence of 20°.

116
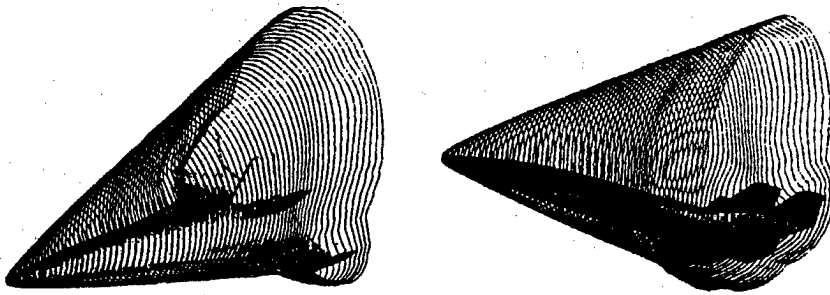
Figure 4. Outer Side Shockwave Shape of SPH002 Environment
(M_∞ = 7.0, Re_∞ = 4.4 x 10^6, α = 20°)

a) Aerodynamic heating chart (α = 0°)
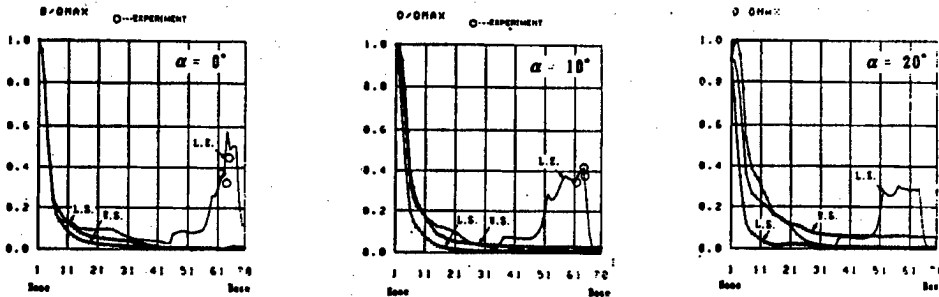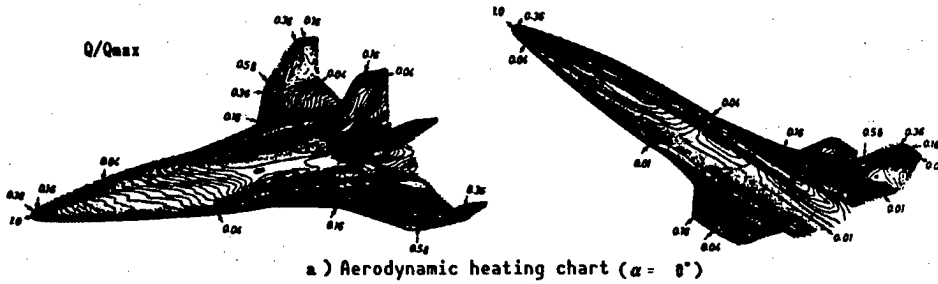
(b) Comparison with experimental values of surface aerodynamic heating distribution along
the fuselage upper and lower symmetric lines and main wing leading edge

Figure 5. Aerodynamic Heating Distribution of SPH002 Surroundings
(M_∞ = 7.0, Re_∞ = 4.4 x 10^6)

Numerical calculations

a) SPH001 form belly surface

Numerical calculations

b) SPH002 form back
   surface

Experimentally derived
data

Experimentally derived
data
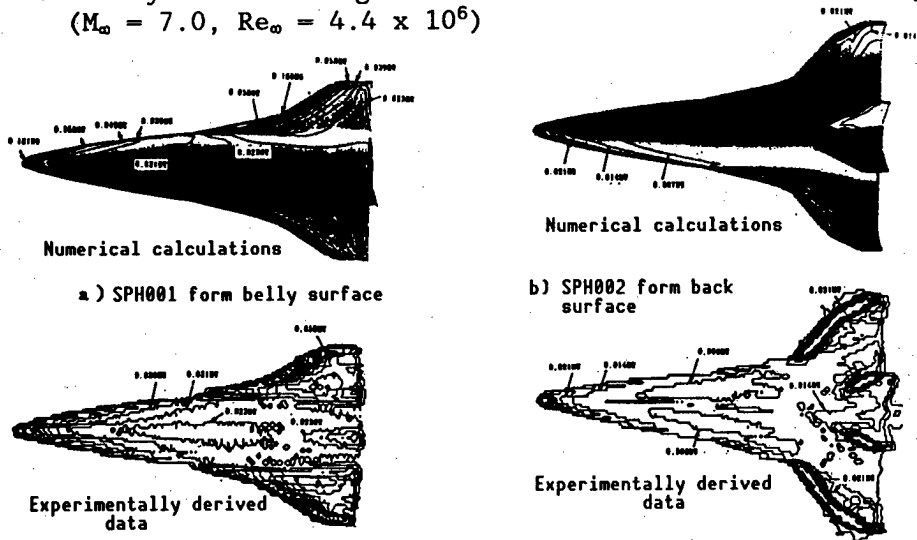
Figure 6. Comparison With Experimentally Derived Values of
Space Shuttle Surface Aerodynamic Heating Distribution
(M_∞ = 7.0, Re_∞ = 4.4 x 10^6, α = 10°)

117

Meanwhile, the dimensionalized stagnation point of aerodynamic heating at an angle of incidence of 0° shows the value of 0.866 MW by numerical computation, which is about one-half that of the experimental value of 1.77 MW. It is believed that the reason for this difference is because the radius of curvature of the head section of the spaceplane model is extremely small (about 2 mm). Thus, the inflow depth of heat becomes large in comparison to the radius of curvature and the supposition of semi-infinite unidimensional thermal conduction does not hold true. This fact also applies to the main wing leading edge, which has a small radius of curvature. A more rigorous analysis of internal thermal conduction is necessary to make a quantitative comparison.

Finally, the results of a comparison of the experimentally derived values and surface aerodynamic heating distribution are shown in Figure 6. Both the computation and experimental values in the drawing are the actual aerodynamic heating of the loop side of SPH001 (angle of incidence 10°). The considerable degree of coincidence demonstrates that the calculated values for semi-infinite unidimensional thermal conduction were upheld by the experiment.

5. Conclusion

We investigated hypersonic aerodynamic and aerodynamic heating characteristics in detail by conducting a numerical analysis of the spaceplane's zero degree configuration surroundings using the Navier-Stokes equation. Verification of these calculations was conducted through a comparison with the experimentally derived results of the hypersonic wind tunnel of the National Aerospace Laboratory. The comparison showed a superior coincidence of values for the aerodynamic coefficient up to a large angle of incidence and the results were virtually coincident in all areas for pressure distribution. Although there were quantitative differences for the aerodynamic heating characteristics, an extremely superior coincidence was seen from the qualitative heating distribution that was made dimensionless along the main wing leading edge for the three types of configurations. An improvement in the analytical precision of the experimental results for the head section and wing leading edge can be expected in the future. A sufficient coincidence was also obtained quantitatively for aerodynamic heating distribution in other areas. However, it is difficult to gain an accurate understanding of the three-dimensional shockwave interference pattern of the main wing leading edge surroundings given the number of lattice points used in the numerical analysis, and it will become necessary to conduct large-scale computations in the future.

We believe that from the series of analyses described above we were able to show the reliability, practicability, and effectiveness of using numerical simulation in the aerodynamic design of spaceplanes. it will be important in the future to promote analyses in fields where experiments are difficult, such as the evaluation of actual gas effects at higher velocities, the application of CFD to engine integrated configurations, etc.

118

References

1. Yamamoto, Y., AIAA Paper 88-2615.

2. Ibid., 89-1699.

3. Yamamoto, Y., Araki, H., and Yoshida, R., AIAA Paper 89-1699.

4. Beam, R.J. and Warming, R.F., AIAA J., Vol 16 No 4, 1978, pp 393-402.

5. Steger, J.I. and Rizk, Y.M., NASA TM-86753.

6. Baldwin, B.S. and Lomax, H., AIAA Paper 78-257.

7. Keyes, J.W. and Hains, F.D., NASA TN D-7139.

8. Wittliff, C.E., AIAA Paper 84-1752.

9. Wells, W.L., MacConchie, I.O., Helms III, V.T., and Raney, D., AIAA Paper 85-0974.

10. Inoue and Yamamoto, "Hypersonic Aerodynamic Heating of Spaceplanes," Japan Aerospace Society, 20th Annual Lecture Meeting, 1989.

Application of Composite Materials in Aircraft

906C3829A Tokyo HIKOKI SHINPOJIUMU in Japanese Oct 89 pp 414-417

[Article by Yuujirou Yoshida, Fuji Heavy Industries]

[Text] **1. Introduction**

Because of their excellent mechanical properties, composite materials are increasingly being used in the manufacture of aircraft. This is an area where, until recently, aluminum alloys had been predominantly used. While their full-fledged adoption in passenger plane components is as yet rarely seen, they are widely used in military and commercial planes. In this article, I will present an outline of the problems involved in using such materials together with an assessment of their future prospects. The article will focus primarily on the raw-material technology sector, drawing on an investigation entitled "The Possibility of Applying Composite Materials in Aircraft (Research and Investigation on the Trends of the Next-Generation of Composite Materials—Part II)." This study was carried out by the Institute for Research and Investigation of Next-Generation Metals and Composite Materials in FY 1988. The study was commissioned by the Japan Machine Industry Association.

2. Current Use of Composite Materials in Passenger Planes

Since many studies have been published on the application of composite materials in airplanes, only the most current information is presented here. Among all passenger planes owned by private airlines, the one in which composite materials are most heavily used is the Air Bus A320. The sites of application are shown in Figure 1. Of these, the use of composite materials in the vertical tail fin is remarkable as this marks the first time they have been so used in mass produced civil passenger planes, although they have been used for over 15 years in this role in military planes, including the F-15 and the F-16. The material in question is an intermediate-temperature thermosetting resin, FIBERDUX 913, made by Chiba-Geigie. This innovative change appears to be a bold one. The application of composite materials in the Air Bus A320 is made aggressively, totaling some 15 percent by weight. In addition to the vertical tail fin, composite materials are used in the horizontal tail fins, ailerons, spoilers, etc.

120
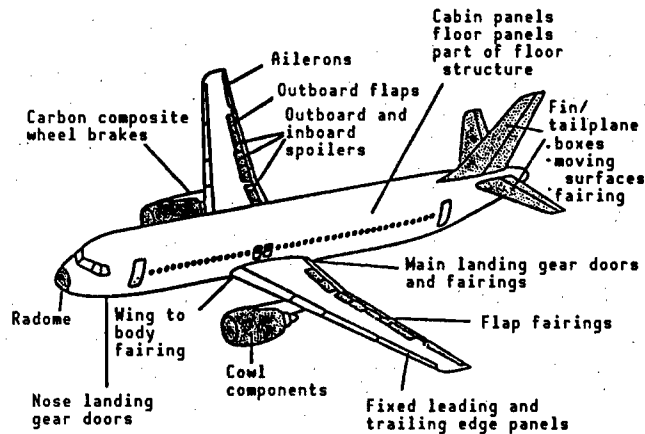
Figure 1. Sites of Application of Composite Materials
in the Air Bus A320

In the ATR 72 (maiden flight in the summer of 1988), the application of
composite materials is extended to even the external surface of the main wing,
a primary structure. A reduction in weight of some 30 percent has been
accomplished for this plane by replacing the metals normally used in beam
structures and spar webs by a carbon-carbon composite, although the plane
remains unchanged structurally.

3. Problems Involved in Composite Materials in Connection With Requirements for Aircraft Design

Requirements for materials are basically different for different types of
aircraft. Table 1 presents target values for subsonic civil aircraft. The
major mechanical properties required for the material (carbon fiber-reinforced
epoxy-type composite material in this case) were calculated on the basis of a
requirement for a 35 percent weight reduction in the plane's structure. An
examination of the properties of composite materials presently available in
comparison with the above target levels shows that the target levels have
already been attained for some individual items, but that no material can yet
pass all target levels. Improvements in both the matrix and the reinforcement
fibers will be necessary to achieve the target levels.

(1) Carbon Fibers

Any improvement in a material's tensile modulus depends solely on improving
the properties of the carbon fibers. The use of fibers with high modulus of
elasticity will improve the tensile modulus, but will degrade other proper-
ties. The development of a high-modulus, high-strength fiber is therefore to
be desired. Improvement in terms of fiber qualities is also necessary for
obtaining better values in the compression strain of holed or perforated
objects. At present, the compression characteristics of holed objects cannot
be improved as desired even with use of high-strength intermediate-modulus
carbon fibers. It is not yet known whether the problem lies in the matrix or
in the fiber, but research aimed at improving the compression strength of the
carbon fibers together with the interface conditions with the matrix is
underway.

121

Table 1. Targets for Improvement of Materials[*]

	Need for improvement	Present level	Target for improvement	Reference
Tensile fracture strain	1.2 times	1.30 %	1.56 %	UD material, 0° direction
Modulus of elasticity	1.7 times	130 MPa	221 MPa	UD material, 0° direction
Compression strain after impact	1.2 times	0.35 %	0.42 %	0, ±45, 90° materials, 1500 lb-in/in
Compression strain for perforated objects	1.2 times	0.69 %	0.83 %	0, ±45, 90° materials

Key: UD: unidirectional
*: The data presented are for carbon fiber-reinforced composite materials of the epoxy type.

(2) Matrix

Many problems are involved n the matrixes that are currently the subject of investigation. These matrixes include epoxy (EP), bis-maleimide (BMI), thermo-plastic resin (TP), and fiber-reinforced metals (FRM). Table 2 presents the major technological problems involved and the measures being taken to solve them. Nevertheless, these problems will not be solved without substantial amounts of research and development.

(a) EP: The major problems to be confronted are how to impart higher functions to the materials and how to render them more amenable to processing and molding. As for functions, materials that can meet requirements for both high toughness and high resistance to wetness and heat need to be developed. EP alone may not be able to meet these requirements, and development of a variant between the EP and BMI, or TP, or another resin is expected. Good amenability to molding is also extremely important. It is necessary to focus on the problem of moldability from the very beginning of the development of a material. Good moldability directly affects the quality of the product, the quantity of production, and also manufacturing costs, because in recent years there has been a steady growth in the introduction of automated molding processes.

(b) BMI: This material is superior to EP in terms of resistance to heat, but poorer than EP in toughness. The method of molding is based on that for EP. This material, therefore, could prove to be a very attractive material provid-ing it is possible to improve its toughness. In cases where BMI is used because of its resistance to heat, it is a prospective material for use in supersonic civil passenger planes (M = 2.0~2.5) rather than in subsonic aircraft.

Table 2. Major Technological Problems for Different Materials and Relevant Methods of Solution

Material	Technological problems	Method of solution
Composites involving epoxy and bis-maleimide resins	1. Improving heat resistance 2. Improving toughness and resistance to impact 3. Easier molding: improving tack, drape, and exposure time	• Developing and improving new epoxy and bis-maleimide types of matrixes • Developing and improving technologies for controlling the interface with the reinforced fiber • Improving prepreg manufacturing technologies • Increasing the quality of reinforcement fibers
Thermo-plastic composites	1. Improving toughness 2. Improving resistance to humidity, chemicals, and heat 3. Easy molding (molding at low temperatures) 4. Easy secondary molding	• Developing and improving new thermoplastic matrix polymers • Developing technologies for controlling the interface with reinforcing fibers • Developing technologies for prepreg manufacture • Developing plate materials for thermal molding
Metallic composites	1. Developing raw materials that are large and long in size • Supplying appropriate preform materials • Developing improved materials for molding and processing • Developing improved materials for welding	• Developing production facilities for materials of intermediate and large sizes • Executing research and development aimed at actual practical objects

(c) TP: TP is an attractive material in that its toughness is very high in comparison with that for EP. In addition, it may be easy to mold. Many types of TP with diverse characteristics have been developed and the most promising among them will be selected after intensive research on their application has been carried out. The technological problems involved in the use of TP are improving its resistance against heat, and improving its compression strength and resistance to the effects of oil and weather. The establishment of molding and processing technologies for aircraft components and structural elements is also necessary. It is quite possible that TP can be adopted for use in major

structural elements, thus surplanting EP. This is assuming that the target levels for the quality of the material can be attained and that a low-cost molding and processing technology can be developed.

(d) FRM: Of the properties of FRMs shown in Table 3, their heat resistance must be the one on which to base their application if their properties are to be utilized at all. Research on the application of FRM lags 10 years or more behind that for fiber-reinforced plastic (FRP). Perhaps most importantly, no research has yet been initiated on mass production technology for aircraft. In other words, the phase of basic assessment of this raw material has just ended, while technologies for raw materials, designs, molding and processing, etc., for structural components and for large structural elements have yet to be developed. It is also conceivable that research could be conducted on applications not for an entire fuselage but for limited parts of an aircraft. This is particularly true for subsonic civil aircraft; since molding FRM requires an extremely high level of technology compared to that for FRP. Supersonic civil passenger aircraft, in contrast, will become a target for full-scale research.

Table 3. Advantages of FRM

Advantage of FRMs over FRP	Advantages of FRMs over metals
(1) High (per-volume) specific strength (2) Superior high-temperature characteristics (3) High strength in the transverse direction (4) High modulus of elasticity in the transverse direction (5) Free from deterioration resulting from vapor absorption (6) High electric conductivity (7) High thermal conductivity (8) Limited damage resulting from radioactivity (9) Limited gas generation	(1) High specific strength (2) High specific elastic modulus (3) High fatigue limit (4) Superior wear resistance (5) Superior high-temperature characteristics: high strength, low creep, superior creep-fracture characteristics (6) Low thermal expansion coefficient (7) Higher resistance against laser exposure (8) Superior vibration decay

4. Time of Possible Application of Individual Materials and Reduction in Cost

Composite materials may possibly find broad applications as structural elements in civilian passenger planes, providing the technological problems discussed above can be solved. Table 4 shows possible structural sites for the application of individual composite materials and the prospective time for their application.

Table 4. Prospective Time for Application of Different Materials in Different Structures

Structure	Composites applied	Prospective time of application*	Major sites of application
Wing	Epoxy resin composites Bis-maleimide composites	5-10 years	• Inboard and outboard wings (spar web) and spar, outboard • Central wing (spar web) spar, outboard, rib
		Establishment of technology in a short time is possible	• Trailing edge panels • Spoilers and flappers
	Thermoplastic composites	In about 5 years	• Fixed leading edge panels, slat rib
	Metal composites	In 10-15 years	• Leading edge of slats
Fuselage	Epoxy composites Bis-maleimide composites	In 5-10 years	• General part of pressurization cabin in aft fuselage
		In about 3 years	• Floor
Tail wing	Epoxy composites Bis-maleimide composites	In about 3 years	• Horizontal tail plane (general part, central wing) • Vertical tail plane (general part, fixtures)
		Establishment of technology in a short time is possible	• Rudders, elevators
	Thermoplastic composites	In about 5 years	• Leading and trailing edge panel ribs
	Metal composites	In 10-15 years	• Leading edge panel of the horizontal tail plane

*Periods necessary from the time of the start of development of a composite material with use of a new or existing raw material through buildup of design data, through development of molding and processing technologies including technologies for automated processes, and through the development of a quality control system, among other things, up until the time when the start of the development of an aircraft frame to which the relevant materials and structural designs are applicable becomes possible.

125

The target for EP is an advance in application from the main body of the tail to the wing and the fuselage structures. Allowing for the present technological levels where the vertical tail plane is mass produced and also the predicted speed of material development in the years to come, the development of relevant technologies will require some 3 years for the tail plane structure, 5 to 10 for the spar web structure of the wing, and 10 for the fuselage structure. The same figures may conceivably apply to the prospects for the application of BMI.

TP has yet to find any application in aircraft on a mass production scale. Data from application tests need to be accumulated for structural elements and for actual components. An estimate based on the current fact-and-tendency investigation indicates that some 5 years will be necessary for the application of the material in the ribs and in the fixed leading edge panels, but such applications may possibly come a little earlier in terms of technology given the present level of development exhibited at the sample fair this spring.

Estimation of the time of application for FRM is difficult. Application in slats and in the leading-edge panel of the tail plane, as shown in the table, was determined on the basis of the material's resistance to impact and heat, but aggressive research pushing beyond the level of what is required for structural elements needs to be executed in order to solve the problems involved in the technologies and facilities for molding and processing the material.

Another important problem for determining the time of application is that of cost. One indispensable condition for expanding the application of composite materials in civilian aircraft in the years to come is a reduction in the cost of manufacture of the material (cost of material, cost for component processing, cost for assembly, etc.) down to a level equivalent to or below that for metals, though an actual materialization of low cost for composite materials needs to make an assessment of the total cost, including the cost for maintenance, in actual operation. There is no prospect for the reduction of the cost of the material to a level that compares with that of metals, but assembly costs have definite prospects for being reduced. The key issue for the future, therefore, is to reduce processing costs. It may be essential, by breaking from the conventional concept of metals, to select materials and structural modes more amenable to molding (simplification of structure, unit structure for higher efficiency, etc., for the latter) from the very stage of designing, and also to apply automated production technology to the extent possible.

Application of Composite Materials in Aircraft Engines

[Article by Shin-ichi Ouhama, Aero-Space Industry Headquarters and Ishikawajima-Harima Heavy Industries]

[Text] 1. Introduction

In general, composite materials consist of fibers that exhibit a high degree of strength and a high modulus of elasticity at high temperatures and a matrix that acts to bind these fibers. Materials to be used in aircraft engines must have a high specific strength, or a high ratio of strength to density, in order to reduce the weight of the engines. A fiber-reinforced composite material wherein a high strength fiber reinforces a low-density matrix could be an ideal material.

This article describes the research and investigation on this subject carried out by the Committee for the Investigation of Future Technologies of Composite Materials in 1987.

2. Composite Materials Applicable for Use in Aircraft Engines

Table 1 presents the composite materials that may be suitable for use in aircraft engines. Of these, fiber-reinforced plastics (FRPs) are widely available as industrial materials and are already being applied in aircraft engines, although to a limited extent. They are beginning to be used more widely, thanks to the advent of heat-resistant FRPs and the development of heat-resistant matrix resins. The current goal is to find composites that can withstand temperatures of 370°C and above.

Other composite materials such as fiber-reinforced metal (FRM), fiber-reinforced superalloy (FRS), fiber-reinforced ceramics (FRC), and carbon-carbon composites (C/C) have been around longer than FRP but have yet to find actual areas of application; it is out of the question, however, that research and development of these advanced composite materials will be accelerated henceforth.

Table 1. Composite Materials Adapted for Use in Aircraft Engines[1]

| Category	Name	Fiber	Matrix	Density g/cm³ (approx)	Range of tolerable temperature upper limit °C	Feature (specific strengths are for unidirectional mater.)
Fiber-reinforced resin composite materials	FRP (epoxy)	Glass (G) Carbon (C) Kevlar (K)	Epoxy resin	1.5	120	Light weight, high strength, high rigidity Specific strength at around 100 km
	Heat-resistant FRP (polyimide)	Carbon (C)	Polyimide resin	1.5	250	High-temperature version of the material described above
	Advanced heat-resistant FRP	Carbon (C)		1.5~1.7	400	Still higher temperature version of the above two materials
Fiber-reinforced metal composite materials	Al series FRM	SiC Carbon (C)	Al alloy Heat-resistant Al alloy	2.7	450	Specific strength at around 50 km
	Ti series FRM	SiC	Ti alloy	4	600	Specific strength at around 40 km
	Advanced FRM	SiC	Heat-resistant Ti alloy Intermetallic compounds	3.4~4	800	Specific strength at around 25 km
Super heat-resistant composite materials	FRS	Metals with high melting points	MCrAlY Intermetallic compounds Alloy with high melting point	8~12.5	1200 1400	Ni-alloy substitutes with improved temperature toleranc
	FRC	SiC C	Si_3N_4,SiC, glass	2.5~3	1500 1800	Specific strength at around 40 km Ceramics with improved toughness
	C/C	C	C	1.7~2	2000	Super heat-resistant, light weight, high strength, high rigid. Spec. st. over 40 km
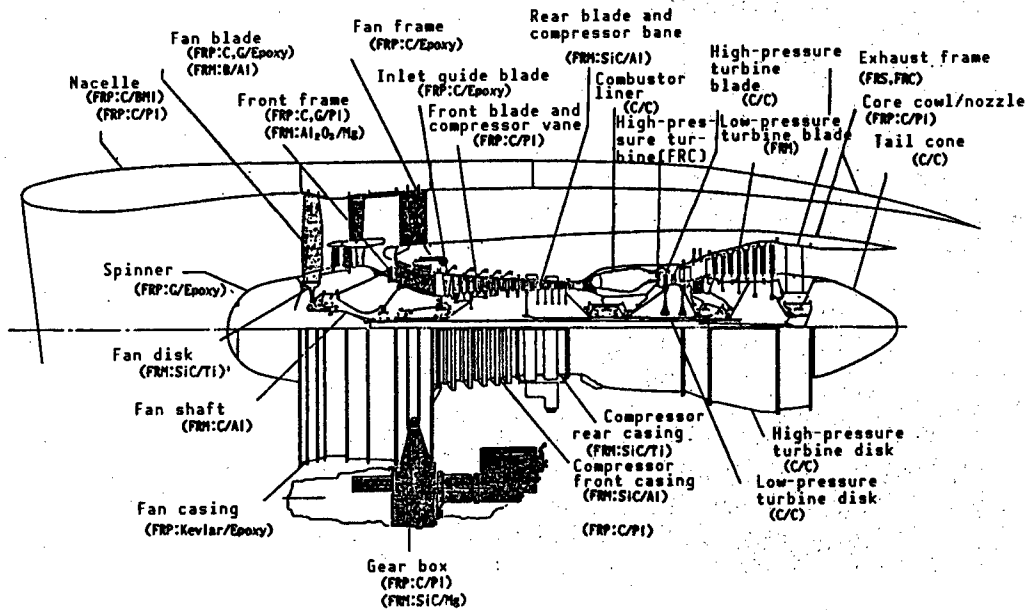
Figure 1. Prospective Composite Materials for Application in Turbofan Engines[1]

Figure 1 identifies composite materials that may in the future be used in the major components of turbofan jet engines. Figure 2 presents time that will probably be required before these composite materials find practical applications.

2000

Surface temperature of material (℃)

Combustor/turbine section

C/C

1500

F R C

Crystal controlled superalloy

(DS) (SC) (ODS) F R S

1000

(Turbofan Compressor)

Advanced
FRM

500

F R M

Ti alloy

Advanced heat-
resistant FRP

Heat resistant FRM

Aℓ alloy FRP

1980   1990   2000   2010   2020

Approximate year of practical application
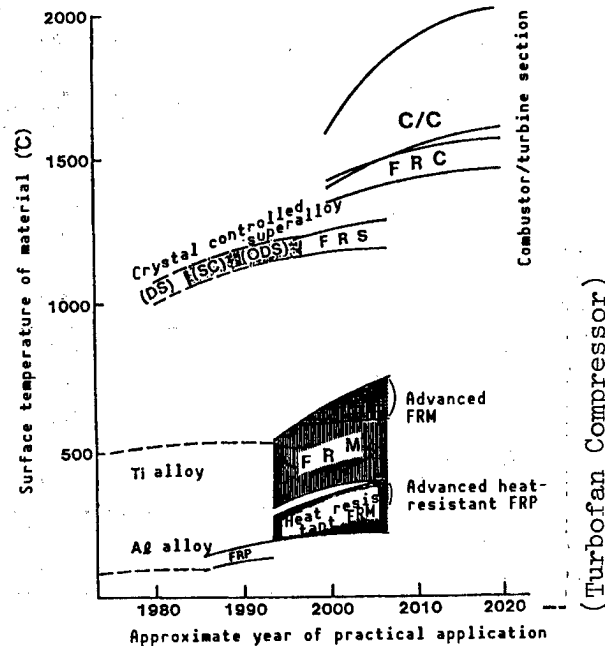
Figure 2. Prospects for Practical Application of
Composite Materials in Airplane Engines[1]

3. Advantages in Using Composite Materials

The first advantage in using composite materials in aircraft engines is weight reduction. The reductions in engine weight that can be achieved through the application of different composite materials are presented in Table 2.

For fan-compressors, the simple substitution of a composite for a conventional material primarily with the aim of reducing weight makes it possible to achieve a weight reduction amounting to about 20 percent of the total weight of the turbofan engine. If a composite material with a high specific strength is used in the moving blade of the turbofan, which in turn reduces the weight of the moving blade, it makes it possible to reduce the strength of the disk that bears the centrifugal force of the blade and, further, to reduce the weight of the axle system. In addition, it is expected that this will be to the advantage of the containment of the fan-compressor case.

Moreover, the application of composite materials in the rotating part of the machine makes it possible to increase the rotating speed of the fan-compressor and thereby improve the efficiency of the fan and increase the pressure ratio of the compressor.

The use of FRS FRC, and C/C, whose resistance to heat far surpasses that of conventional metals, will make it possible for the temperatures at the turbine inlets to be increased from the present 1,400°C to 1,700°C and above if applied to the high temperature parts of the turbine. This could possibly lead to an epochal advance in the capacity and efficiency of future engines. These advanced composite materials, which are super-resistant to adverse environmental effects, will also be available as useful materials for the fuselage

129

Table 2. Prospects for Reducing Weight of Turbofan Engines by Application of Composite Materials[1]

Figures in ( ) are values for reduced weight expressed in %

Engine elements	Current weight*	Weight reduction first 10 yrs	Weight reduction second 10 yrs	Weight reduction after 20 yrs	Components where composite materials can be applied
Static sections of fan and high pressure compressor	209.3	122.6 (59)			Fan case Fan frame Front frame Rear compressor case Front compressor case
Rotational sections of fan and relevant flow passage	110.7	53.9 (49)			Spinner, outer vane Fan blade (moving 1st, 2nd stages) Vane (1st, 2nd stages) Disk (1st, 2nd stages)
Rotational sections of high pressure compressor and its flow passages	67.3	22.4 (33)	6.2 (9)		Inlet guide blades, spool Compressor blade (moving) 1st–12th stages Compressor vane (static) 1st stage to OGV Disk, 1st, 2nd, 7th stages
Combustor	43.7			31.6 (72)	Liner Case
Turbine	169.4		40.0 (24)	62.4 (37)	Blade (moving) of high and low pressure Vane (static) of high and low pressure High pressure turbine disk, 1st, 2nd stages Low pressure turbine casing
Exhaust	20.0		5.0 (25)		Exhaust frame Tail cone
Others	459.6	15.0 (3)			Gear box Spares
Entire engine	1080.0	213.9 (20)	51.2 (5)	94.0 (9)	[continued]

130

		213.9 (20)	265.1 (24)	359.1 (33)	
Cumulative reduced weight Nacelle	693.0	381.0 (55)			Inlet, fan cowling Main structures, USB nozzle, Core cowling Core nozzle, Lower door
Total	1773.0	594.9 (34)	51.2 (3)	94.0 (5)	
Cumulative reduced weight		594.9 (34)	646.1 (36)	740.1 (42)	

* Current weight of the components to which composite materials are to be applied in the coming years.

and the engines of the coming supersonic and hypersonic transports (SST/HST) and space planes.

4. Technological Problems Confronting the Application of Composite Materials

There are more technological problems confronting the application of composite materials in aircraft engines. These include a technology for designing structures made of heterotrophic materials, a technology for molding and processing composites into engine components, devising means to improve the resistance to impact either of composite materials or of any materials by turning them into composites, technologies to improve the resistance of composites to weather and erosion, nondestructive testing technology, technologies for a quality control system, and technologies for engine demonstration and endurance tests.

The imposing developmental problems involved include the materialization of an advanced heat—resistant FRP by developing a new heat—resistant resin, creating an advanced heat—resistant FRM by developing a new matrix metal such as an intermetallic compound, and creating an advanced composite material that will be superresistant to adverse environmental effects.

Figure 3 presents prospective time frames for the application of different composite materials in engines.

In proceeding with practical applications for these composites, it is necessary for the researcher to be well acquainted with the environments in which the specific components are to be used and with the stress conditions to which these components will be subjected and to work out an optimal design for structure and material on that basis (tailoring). It is, therefore, essential that structure designers and material technologists work together in intimate cooperation.

Major engine components	Years 1985 1990 2000 2010 2015
Fan blades (moving)	Ti alloy → FRP/FRM
Fan casing Fan frame Front frame	Ti alloy → FRP
Fan disk	Ti alloy → FRM
Compressor vanes and blades	Ti, Ni alloy → FRP/FRM
Compressor casing	Ti alloy → FRP/FRM
Combustor liner	Ni, cobalt alloy → FRC or C/C
Combustor casing	Ni alloy → C/C
Turbine nozzle	Ni, cobalt alloy → FRS, FRC, C/C
Turbine disk	Ni alloy → C/C
Turbine blade (moving)	Ni alloy → C/C
Exhaust frame	Ni alloy → FRS
Tail cone	Ni alloy → C/C
Nacelle	Al alloy → FRP
Gear box	Al alloy → FRM

Figure 3. Projected Times for the Application of
Composite Materials in Aircraft Engines[1]

5. Conclusion

The composite materials discussed above must henceforth play a very important part in improving the performance and reducing the weight of aircraft engines. It is expected, in particular, that demands for composite materials with higher heat resistance will grow more intense. Although research and development on these materials will take a very long time, starting from basic research on materials through application research to demonstration tests, it must be pushed along steadily but aggressively. Progress and development in materials as a result of research and development on these materials probably will contribute greatly to the advance of aircraft engines in the future.

References

1. Japan Machine Industry Association and the Institute for Research and Development of Future Metals and Composite Materials, "Research and Investigation of Future Technologies on Composite Materials for FY 1987 —Part 2," 1988.

Advanced Composite Materials for Aerospace Industry

[Article by Nobuo Takeda, Advanced Science and Technology Research Center, Tokyo University]

[Text] 1. Introduction

CFRP and other advanced composite materials offer a number of advantages, such as light weight, high strength, high rigidity, dimensional stability, freedom of design, and ease of molding in one body. Because of these advantages, they are now providing many of the materials used in the aerospace industry and are serving as various types of primary and secondary structural materials. This paper presents an outline of the present state of advanced composite materials for use in the aerospace industry (mainly for CFRP) and describes the problems involved and current research trends.

2. Higher Quality (Primarily in terms of strength) of Structural Materials; High Strength, High Rigidity, and High Elongation Are the Objective

The use of carbon fibers for reinforcement produces a notable improvement in the performance of composite materials. The trends in research and development may be grouped into three categories, as shown in Figure 1: 1) high strength and high elongation (for application in the primary structural elements of aircraft); 2) high rigidity (for application in space structural elements); and 3) an intermediate level between the two with a balance between strength and elastic modulus.

Second, the resins used as the matrix must also feature high performance (interface strength, elongation, strength, rigidity, and resistance to heat and moisture) if the high performance potential of CF is to be fully displayed. According to R. Ishikawa,[1] present research and development efforts can be grouped into three categories (Figure 2):

(1) The development of resins that are super-resistant to heat, represented by polyimide. The goal of this research is to overcome the lack of moldability of resins of this type. PABI, Larc, PMR, etc., have been developed in the West, and materials equivalent or superior to these also have been developed in

133

Japan under the Jisedai Project (Research and Development of Basic Technologies for Future Industry) sponsored by MITI. The possibility of finding practical applications for these materials is growing.

(2) Development of an epoxy resin with a high elongation capacity. The goal of this effort is to develop materials with a high degree of toughness. Attempts have also been made to develop elastomer and thermoplastic resins, to improve hardeners, etc. The problem here is how to balance the property of toughness with those of resistance to heat and resistance to moisture.

(3) Development of thermoplastic resins that are resistant to heat, represented by PEEK (polyether ether keton). These plastics are noteworthy because of their good bonding capacity, the ease with which they can be manufactured and repaired, etc. This is in addition to their high degree of elongation and toughness. The problem here is improving its resistance to heat.
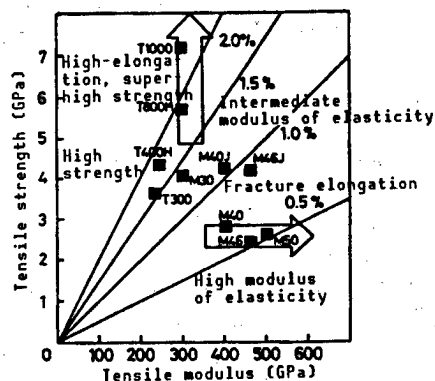
Figure 1. Trends in the Development of Carbon Fibers
(From the catalogs of the Toray Co.)
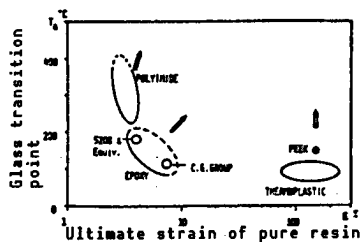
Figure 2. Plot of Heat Resistance Vs. Fracture Elongation in Resins[1]
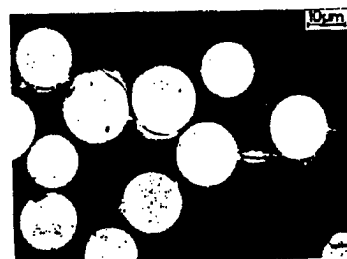
Figure 3. Cracks Formed in Layers of Glass FRPs in the 90° Direction in an Impact Fracture

3. Transverse Crack (90° Layer Crack)

Composite materials reinforced with long fibers are frequently used as laminates, but cracks are liable to appear in the resin or at the interface between the resin and the fibers when the fibers are not oriented in the direction of the stress (Figure 3). In actual design work, a critical strain

134

capable of producing a 90° layer crack often becomes the most important factor (Figure 4). Improving the toughness of these resins is essential for raising the value for the limiting strain.
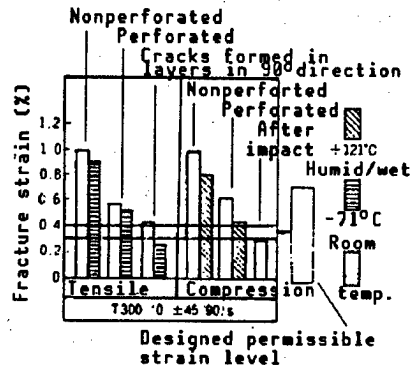

Figure 4. Fracture Strain of Carbon Fiber Reinforced
Plastics Under Different Conditions[2]

4. Interlayer Fracture Toughness G_{IC}, G_{IIC}

The interlayer fracture of laminates represents an important fracture mode unique to fiber-reinforced composites. Recent research results have largely established the methods for measuring interlayer fracture toughness. These consist of Mode I, Mode II and a mixed mode, as shown in Figure 5. Interlayer fracture toughness can be improved by toughening the resin, as described in the previous section (Figure 6), but can be further enhanced by a stitching process wherein the laminate is sewn with a fiber in the traverse (90°) direction or by the use of a three-dimensional fabric.
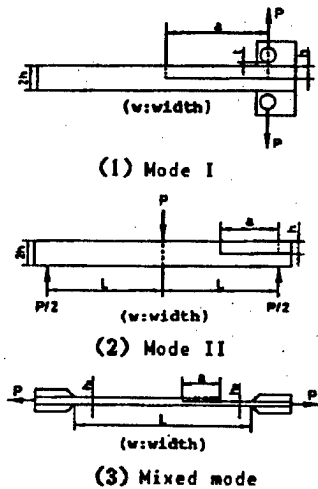
Figure 5. Testing of Interlayer (Interlaminar) Fracture Toughness
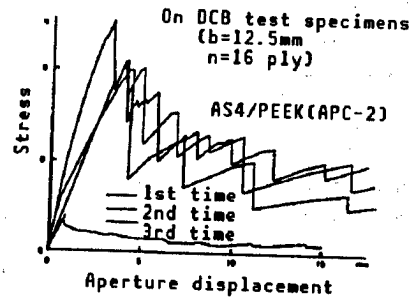
Figure 6. Plot of Stress Vs. Strain in Mode I Test for Interlayer Fracture Toughness[3] (Interlaminar fracture toughness)

135

5. Intralayer Fracture Toughness G_{Ic}, G_{IIc}

Since composite materials are both heterotropic and heterogeneous, a theoretical analysis of fractures within a layer encounters a number of extreme difficulties, and the application of fracture mechanics will not necessarily be successful. The growth direction of cracks in a laminate, for example, differs markedly depending on the manner in which it was laminated (Figure 7). Intralayer fracture toughness can conceivably be raised by 1) using resins with greater elongation and toughness, 2) hybridization by adding aramide or glass fibers, and 3) the use of crack arresters (Figure 8).
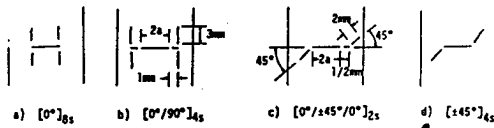
Figure 7. Modes of Fractures Dependent on Lamination Structures[4]
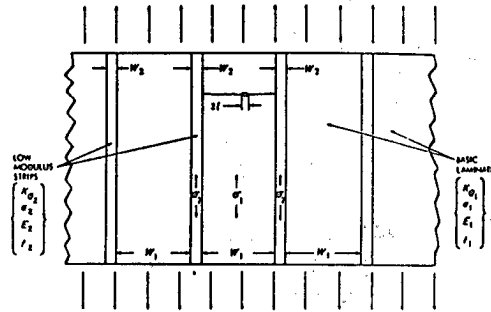
Figure 8. Concept of Crack Arrestors[5]

6. Impact Characteristics

Because CFRP lacks toughness in relation to impact stress—which is a major deficiency of this plastic—the impact characteristics become a major factor in designing the structure of a composite board (Figure 4).[6] In the development of fan blades made of CFRP in the 1960s, the problem of foreign object impact damage (FOD) brought the project to a standstill. Further, the application of composite materials in the primary structural elements of aircraft demands that the compression–after–impact (CAI) characteristics be improved (Figure 9). Measures to counteract the problem include the toughening of the resins, stitching, three–dimensional fabrics, etc. (Figure 10).
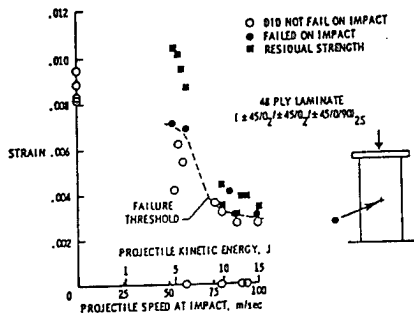
Figure 9. Compression After Impact (CAI) for CFRP Laminates[7]
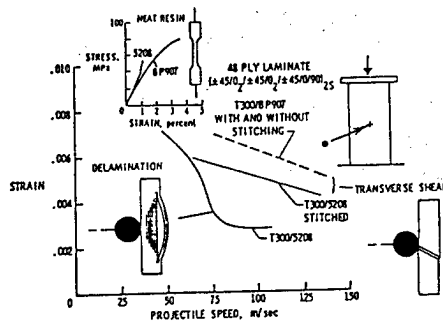
Figure 10. Effects of Improved Toughness of Resins and Stitching on the CAI Characteristic[7]

7. Fatigue Characteristics

Unidirectionally oriented reinforced materials generally have high strength in the running direction of the fibers and thus also have good fatigue character- istics. The damage mechanism in multilayer laminates, in turn, usually follow the pattern of transverse crack→delamination→fiber breakage (Figure 11). Once again it is necessary to underscore the importance of high-quality resins. For example, a CFRP using PEEK as the matrix develops far fewer transverse cracks than one using epoxy resin (Figure 12).
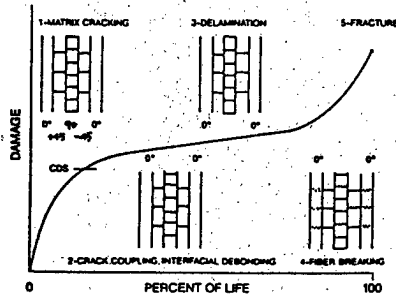

Figure 11. Process of Fatigue Damage in Multilayer Laminates[8]
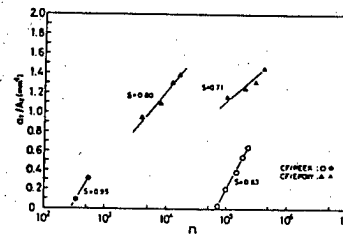
Figure 12. Relationship of Transverse Crack Density (a_T/A_T) to the Number of Repetitions in the Fatigue Test (n)[9]

A_T: Area of observation

a_T: Total length of transverse cracks in the observed area

s : Amplitude of stress waves/static strength

Stress ratio: R = 0

8. Strength at High Temperatures

As noted in Section 2, the development of resins that are both easy to mold and display superior strength characteristics at high temperatures is highly desired. Potential ways to achieve this goal include improving the heat resistance of epoxy resins, improving the molding amenability of polyimide, and developing new heat-resistant resins.

9. Properties Under Wet Conditions

Composite materials made from a resin with a high degree of toughness frequently exhibit inferior strength when wet. A number of superior resin qualities in addition to toughening the material is necessary to produce a composite that has not only the superior CAI characteristics referred to above but also superior compression-in-hot-wet-condition (CHW) characteristics (Figure 13).
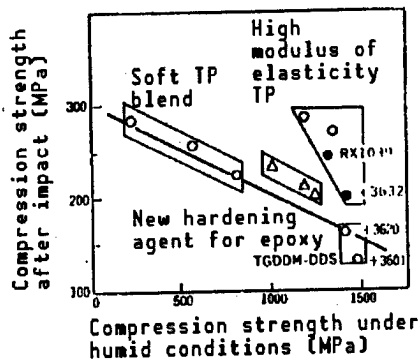
Figure 13. CAI Characteristics and CHW Characteristics[2]
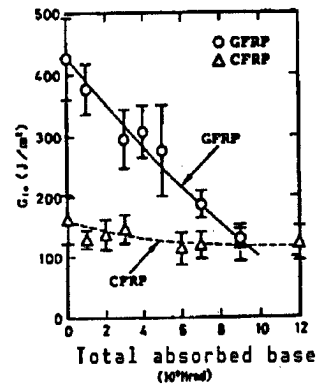
Figure 14. Dependence of Mode I Interlayer Fracture Toughness on Total Absorbed Dose From an Electron Beam[10]

10. Resistance to Radiation

In the area of nuclear fusion reactors, CFRPs could potentially be applied in materials related to superconducting magnets, such as electric insulation materials, heat insulation materials, liquefied-helium containers, heat-insulating support materials, etc. The research activities involved here consist primarily of neutrons and X-rays. In addition, CFRPs have already been put to use in large-size space structures. Radiation in the space environment consists primarily of ultraviolet rays, positrons, electrons, X-rays, and oxygen in an elementary state. It has been noted that an assessment of interlayer fracture toughness, as well as that of strength, is important in assessing the resistance to radiation of a composite (Figure 14).

11. Nondestructive Test Technologies

Modes of the internal damage suffered by composites are diverse and no single method is capable of eliciting sufficient information. Various methods such as those using X-rays, ultrasonic C scan (Figure 15), AE, AU, dynamic viscoelasticity (Figure 16), etc., need to be combined for accurate identification of the specific damage mode.

12. Molding Technologies

Research on molding technologies has been expanding recently. Notable problems being addressed include shortening the molding cycle, automating molding processes, monitoring the hardening process (dielectric characteristics, electrical conductance) and determination of optimal molding conditions.

13. Reduction of Cost

Industrial production of pitch-type carbon fibers is being promoted by oil and steel makers, among others, with an aim to producing a high modulus fiber in quantity production at low cost. They hope to be able to apply such fibers for architectural purposes and as a substitute for asbestos. Notable among the
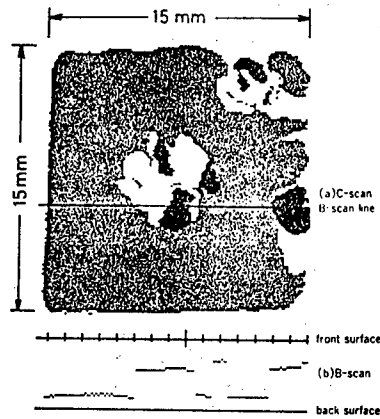
Figure 15. Reflection-Type Supersonic Wave
Picture of a Glass Fiber-Reinforced,
Injection-Molded Board Which Has
Suffered Impact Stresses With Resulting
Internal Layer Separation[22]
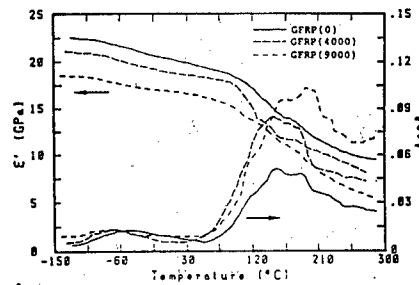
Figure 16. Dynamic Viscoelasticity
of a GFRP Exposed to an
Electron Beam[12]

questions involved are the low strength of the product, its low elongation and its insufficient agreement with the matrix (lower interlayer shearing strength).

Table 1. Advantages of Each of the Two Bonding Methods[13]

Advantages of mechanical bonding	Advantages of adhesive bonding
• Ease with which the materials can be tested, assembled, and disassembled. • Limited values for variances in bonding strength and thus a high level of reliability is possible. • High resistance to peeling (separation) is expected. • Strength and creep strength at high temperatures are enhanced. • No special surface treatment and hardening time is necessary. • Does not become brittle or lose its strength against impact force at low temperatures.	• No stress concentration, no cuts in the fibers and no reduction in the cross sectional area that supports stresses occur as the result of drilling. • High specific strength at the portion of adhesion and hence a reduction of weight is possible. • The number of components drops. • Rapid and smooth finishing and tight sealing or airtightness are possible. • Possibility of lower costs (large-area bonding, bonding made simultaneously with molding). • A high degree of resistance to corrosion (electrical and chemical) is expected.

14. Joining and Reparation

Bonding the composite with an adhesive is favored over mechanical joining in terms of structural efficiency, though the latter method is often the method of choice (Table 1). The resultant product has a fairly high level of strength, but lacks reliability. Thus, it is generally used only in secondary structural materials.

References

1. Ishikawa, R., JOURNAL OF THE JAPAN AEROSPACE SCIENCE SOCIETY, Vol 32 No 370, 1984, p 612.

2. Ueda, A., KOGYO ZAIRYO, Vol 34 No 10, 1986, p 30.

3. Ishikawa, R., JOURNAL OF THE JAPAN AEROSPACE SCIENCE SOCIETY, Vol 13 No 2, 1987, p 63.

4. Yeow, Y.T., Morris, D.H., and Brinson, H. F., private communication.

5. Eisenmann, J.R. and Kaminski, B.E., ENG. FRAC. MECH., Vol 4, 1972, p 907.

6. Takeda, N., NIPPON FUKUGOU ZAIRYO-GAKKAI-SHI, Vol 12 No 2, 1986, p 80.

7. Starnes, J.H., Jr., and Williams, J.G., "Mechanics of Composite Materials-Recent Advances," Pergamon Press, New York, 1982, p 283.

8. Reifsnider, K.L., Henneke, E.G., Stinchcomb, W.W., and Duke, J.C., Ibid., p 399.

9. Ootani, N., Kobayashi, A., and Hagihara, S., Collection of Lectures at the 19th Aerospace Industry Material Symposium, 1989, p 14.

10. Takeda, N., Tohdoh, M., and Takahashi, K., Proc. 4th Japan-U.S. Conf. Comp. Mater., Technomic Publishing Co., 1989, p 331.

11. Takeda, N., H. Komatsu, K. Takahashi, Kyushu U. Research paper, 65 (1987), 307.

12. Takeda, N., Proc. 4th Tech. Conf. Am. Soc. Comp., 1989.

13. Takeda, N., "CAE OF Composite Materials and Examples of Programs and Applications," Compiled by Fukuda and Ishikawa, Ouyou-Gijitsu-Shuppan Co., Ltd., 1985, p 230.

Improving Laminated Composite Materials' Fracture Toughness

906C3829D Tokyo HIKOKI SHINPOJIUMU in Japanese Oct 89 pp 426-429

[Article by Hizuru Yamashita, Mitsubishi Electric Corp.]

[Text] 1. Introduction

The major shortcoming of laminated composite materials, as is well known, is their poor interlayer strength and toughness. When they are used to form objects with complex shapes or as structural materials that are very thick, in particular, the possibility that they will develop stresses in the directions of the three axes normal to each other (interlayer fracture) limits the range of their application in large measure.

With a view to developing a simple technology for interlayer reinforcement of composites, the author is investigating a hybrid molding technology—a technology for molding composite materials wherein whiskers or short fibers are mixed between continuous fibers and the orientation of the whiskers or short fibers is controlled by a magnetic field, as shown in Figure 1. This paper reports on the technology for controlling the orientation of the whiskers in the hybrid molding method and the results of testing of the interlayer fracture toughness on molds.
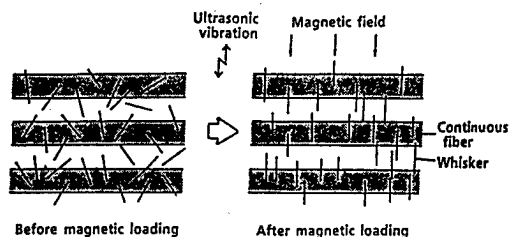

Figure 1. Diagram of the Concept of Hybrid Molding

2. Control of Whisker Orientation

The hybrid molding method is characterized by control of the orientation of the whiskers, which are not just mixed in among the continuous fibers. A simple mixing in of the whiskers results in mere random and two-dimensional

orientations, and the three-dimensional orientation of the whiskers, which is needed to increase the toughness and strength of the composite, is not achieved. Control of the orientation of the whiskers may be accomplished either by the application of electric polarization or by using the fluidity of the matrix resin. However, the application of magnetic moment was favored because of its accuracy, because of the ease with which it is possible to control the whisker orientation, and because of the magnitude of the acting moment involved. In this connection, the whiskers, which are generally diamagnetic, were nickel coated in order to increase their susceptibility to magnetic attraction.

In order to elucidate the parameters involved in the control of whisker orientation by magnetic moment, we conducted a number of experimental and analytical investigations, as shown in Figures 2 and 3. Figure 2(a) presents a plot of the time required to orient the whiskers vs. the magnetic field intensity. Figure 2(b) shows the time vs. aspect ratio of the whiskers.
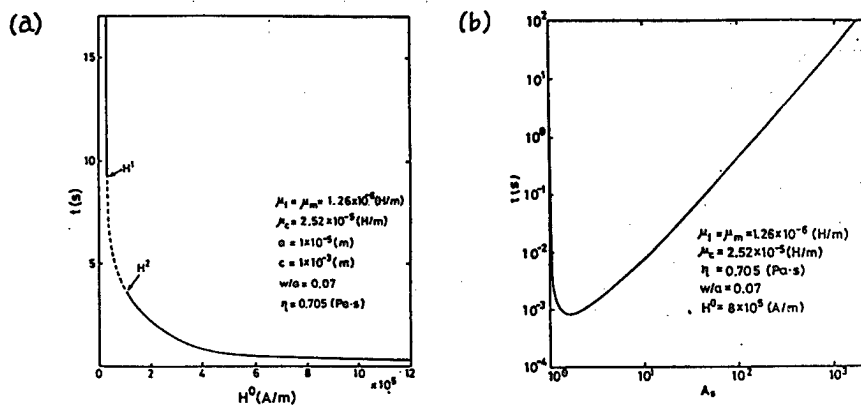

Figure 2. Analysis of Whisker Orientation Control
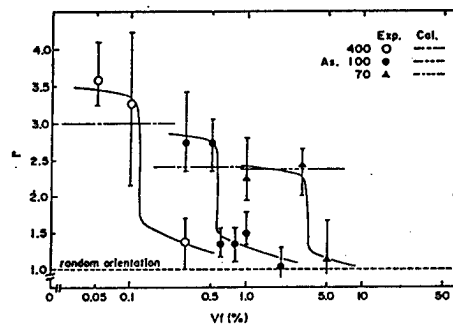
Figure 3. Experiments on Whisker Orientation Control

The time required for the orientation of the whiskers can be considered to be the period of time in which the whisker turns from an angle of 89° to 1° with respect to the direction of the magnetic field. The results indicate that the whisker is capable of orienting itself within 1 second in a magnetic field intensity that can be produced by an ordinary magnetic press, i.e., around 8.0×10^5 A/m. They also show that the relevant time increases rapidly with an

142

increase of the aspect ratio of the whiskers. Thus, whiskers with a low aspect ratio are favored for orientation control, but those with a high aspect ratio display a high reinforcement effect. Thus, a balance needs to be struck between the two factors.

Figure 3 shows the result of an experiment wherein an unsaturated polyester was molded while the nickel-plated short carbon fibers were orienting themselves in a magnetic field. These short fibers were used because the analytical results of orientation control by magnetic moment suggested that the orienting time, t, is not dependent on the absolute dimension of the fiber and because carbon fibers allow direct visual observation. The abscissa of the plot represents the volume content of the fiber and the ordinate represents the ratio of magnetization, r—a ratio of the quantity of the specimen aligned in the direction of the magnetic field to a normal orientation. The r value grows larger as the short fibers become increasingly oriented in the direction of the magnetic field; it is zero in cases where the fibers do not orient themselves and exhibit a random orientation distribution because of the mutual entanglement of the fibers, etc. The values indicated by broken lines in the figure represent the r values analytically obtained in cases where short fibers of different aspect ratios are aligned completely in the direction of the magnetic field.

The results have demonstrated that the volume content of the fiber, V_f, amenable to orientation control grows with decreasing aspect ratio. As in the case of the foregoing analysis, it is necessary to strike a balance between the aspect ratio and the orientation efficiency of the reinforcement material (short fiber or whisker) to obtain an optimal design.

3. Hybrid Molding

We conducted an investigation of the hybrid molding method wherein whisker orientation in actual laminated composites was controlled on the basis of the above experiments.

3.1 Molding Procedure

Figure 4 illustrates the molding procedure used for the hybrid molding. The procedure involves, in order, unfolding the long fibers and introducing and dispersing the whiskers, preparing unidirectional prepregs by the F/W method, laminating the prepregs and press molding in a magnetic field with a magnetic press. The dispersion medium used for unfolding the long fibers and for introducing and dispersing the whiskers was low boiling methanol, which is easy to evaporate. An agent for interface treatment that is effective on both the long fibers and the whiskers was dissolved in the methanol so that the two materials could be subjected to coupling treatment.
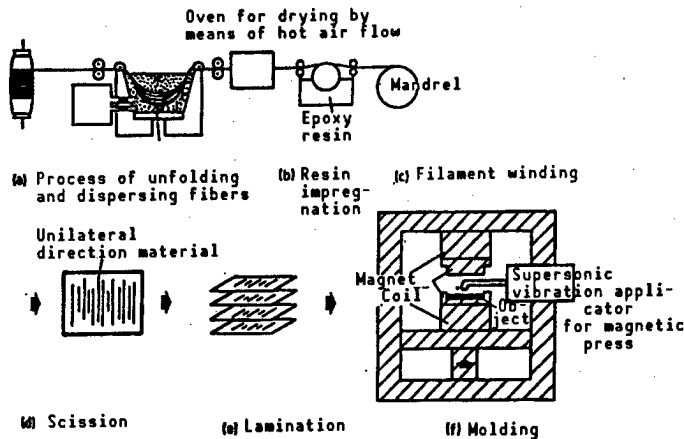
Figure 4. Procedure for Hybrid Molding

3.2 Materials Used in the Specimen

The specimen material was produced using the molding materials shown in Table 1. Short fibers were used in order to investigate the effects of the aspect ratio. The conditions involved for molding were: Cure cycle: 353 K x 0.67 h + 393 K x 3 h; molding pressure: 10 MPa; impressed magnetic field: 1.6×10^6 A/m x 30 min.

Table 1. Molding Materials

Continuous fiber		Made by Toray Co., T300—6k filament
Interlayer reinforcement material	Whiskers	Made by Tateho Chemical Industry Co., SiC, average length: 23 μm, average diameter: 0.4 μm, nickel coated to a thickness of 0.04 μm by electrolysis plating
	Short fibers	Made by Toray, T300—3k filament, average length: 500 μm, average diameter: 7 μm, nickel coated to a thickness of 0.1 μm by electrolysis plating

4. Fracture Toughness Test

4.1 Test Specimen

Double cantilever beam (DCB) test specimens with the dimensions given in Figure 5 were produced from the above specimen material. The part shadowed with slant lines in the figure represents an aluminum tab through which the tensile stresses are to be applied. At an intermediary plane between the upper and the bottom levels is provided with an initial rack with a length a_0 produced by introducing a model film with a thickness of 30 μm at the time the specimen material was prepared.

144
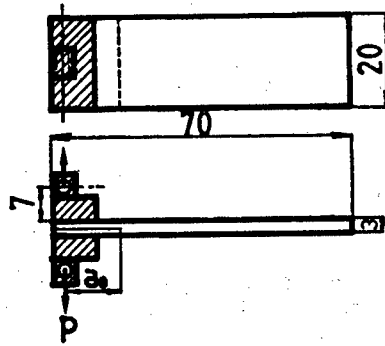
Figure 5. DCB Specimen

4.2 Testing Method

In order to estimate interlayer fracture toughness, the critical strain energy liberation rate GIc was determined by a Mode I test (deformation with opening of layers). The test was carried out with a 1185 Universal Material Tester made by Instron, Inc. at a crosshead speed of 0.5 mm/minute with the movement under control. The crack length was measured by use of a read-out microscope.

4.3 Test Results

Figure 6 presents the results of the test. The abscissa indicates the volume content of the fibers, V_f, and the ordinate represents the fracture toughness, G_{Ic}. The symbol o denotes the relevant values for carbon fiber-reinforced carbon materials (CFRP) with no whiskers involved; the symbol • denotes the values for composites with whiskers magnetically oriented by the hybrid molding; and the mark ■ denotes the values for composites with short fibers magnetically aligned. The value G_{Ic} was approximately doubled by the mixture of whiskers and was raised 3-5 times by the addition of short fibers. In addition, those composites where the whiskers were dispersed but not subjected to magnetic orientation were also tested. The whiskers, however, were aligned two-dimensionally and within layers as described at the beginning of this article. The G_{Ic} values were equivalent to that of conventional CFRP.
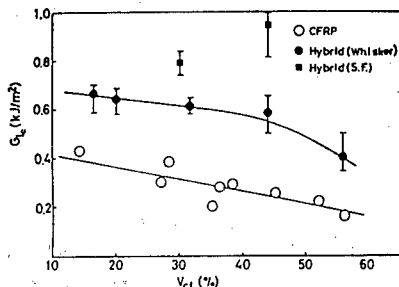

Figure 6. Results of Measurement of Interlayer Fracture Toughness Values G_{Ic}
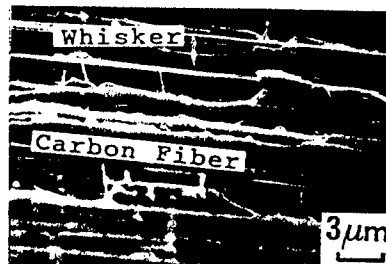
Figure 7. SEM Picture of Fractured Surfaces

145

Figure 7 presents a scanning electron microscope (SEM) picture of a fractured surface. This picture demonstrates that the concept of hybrid molding can be actualized as the whiskers were observed to be aligned normal to the direction of continuous fibers or oriented in the direction of the thickness of the laminates. Further detailed observation of the picture has revealed that whiskers were "pulled out" in many locations. One mechanism for improving fracture toughness by the addition of whiskers is an increased shear-friction effect due to this "pull-out" and the other the so-called crack deflection effect resulting from an increased unevenness of the fractured surfaces.
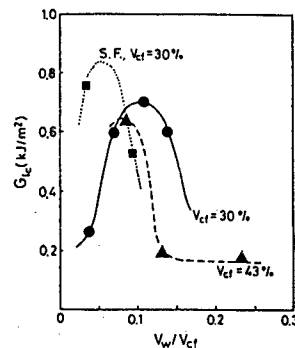

Figure 8. Effects of the Amount of Mixed Whiskers on G_{Ic}

Figure 8 presents the results of an examination of the extent to which the amount of dispersed whiskers serves to improve toughness. The abscissa represents the ratio of the volume content of the whiskers, V_w, to the corresponding figure for carbon fibers, V_{cf}. It can be seen from Figure 8 that the optimum value for V_w is when the V_w to V_{cf} ratio is about 0.08 to 1.0 [as published] while that for short fibers is at a lower level. The appearance of such maximal values for the reinforcement effect can conceivably be ascribed to the presence of some negative effects together with the positive effect of the pull-out referred to above. Such negative factors include molding defects (voids that increase as V_w increases) and greater brittleness of the matrix as a result of the dispersion of short fibers or whiskers.

5. Conclusion

A hybrid molding technology has been developed in an effort to improve the interlayer strength and toughness of laminated composite materials. By orienting whiskers in a direction normal to that of running long fibers through the use of magnetic fields, a value of interlayer fracture toughness, G_{Ic}, about twice that for conventional composite materials has been achieved. it is expected that the research on eliminating molding defects, e.g., voids, occurring as a result of whisker mixing, and on introduction of whiskers with a high aspect ratio are to be tackled henceforth.

146

Molding Technology for Three-Dimensional Fabrics

[Article by Yasuhiro Yamaguchi, Tetsuya Yamamoto, and Shigeruu Nishiyama]

[Text] 1. Introduction

Composite molding technology for three-dimensional fabrics involves weaving a three-dimensional fabric into a shape very similar to the finished product, which is then impregnated with a matrix resin and consolidated. The authors have investigated two types of molding technologies: 1) resin injection and consolidation; and 2) resin film impregnation and consolidation. This article discusses the results of this investigation.

2. Specimen Materials

The three-dimensional fabrics used as the reinforcement materials are depicted in Figures 1 and 2. The resins used for impregnation were heat-resistant epoxy resins (Table 1) that were processed into liquid or film form.

Unit (mm)
11.3
63.3
11.3
9.0
10.10 Fabric density 37.4 volume %
65.1
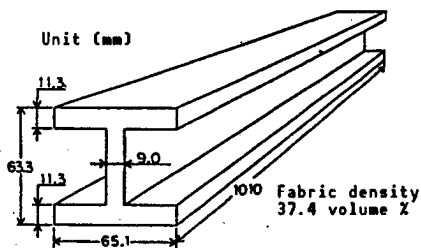
Figure 1. Shape and Dimensions of a Three-Dimensional Carbon Fiber Fabric Molded To Form an I-Beam

X thread   Y thread   Z thread

Dimensions:300 ^{W} X1000 ^{L} X4.5 ^{t} (Unit mm)
Fabric density :35%
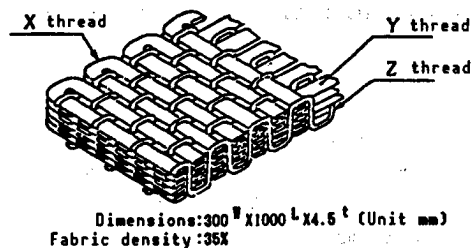
Figure 2. Microscopic Structure of a Three-Dimensional Fabric Made of Carbon Fiber (Flat-plate type)

Table 1. Physical Properties of Four-Functional Heat-Resistant Epoxy Resin Used for Impregnation

Physical property	Type	Resin A	Resin B
Density (kg/m^3)	Unhardened	1233	1247
	Hardened	1259	1264
Rate of shrinkage during hardening (%)		2.1	1.3
Bending fracture elongation of hardened specimens (%)		8.4	10.5
Temperatures for glass transition (K)		483	415

3. Molding Apparatus

3.1 Resin Injection and Consolidation Apparatus

The resin injection and consolidation apparatus was designed and produced for the purpose of molding a long, three-dimensional high V_f, high-quality fabric into the shape of an I-beam (Figure 3 [not reproduced]). A predetermined quantity of heated and fused resin is injected into the three-dimensional fabric, which has been set in a die within the apparatus, and is then consolidated under high pressure.

3.2 Resin Film Impregnation Apparatus

The resin film impregnation apparatus was designed and produced in order to mold three-dimensional fabrics into the form of flat board (Figure 4 [not reproduced]). In the apparatus, a resin film is allowed to fuse and to impregnate the three-dimensional fabrics under vacuum conditions by the capillary phenomenon. This is followed by consolidation under increased pressure.

4. Experiments for Molding Three-Dimensional I-Shaped Fabrics by the Resin Injection and Consolidation Method

4.1 Experiments Method

The I-beam-shaped three-dimensional fabric was set in the die. It was then impregnated with resin at a temperature of 393 K. This was done to allow for the minimal viscosity of the resin and to increase the viscosity of the resin while being introduced. The impregnation speed was 30 mm/minutes, a speed that does not have an adverse affect on the alignment of the fibers of the fabric. Following the completion of resin impregnation, the resin was subjected to an increased pressure of 12.5 MPa and the temperature was raised further to consolidate it. To better consolidate the resin, the temperature was raised at different times for the top, middle, and bottom parts in the die. This made it possible to ensure that the pressure was applied effectively and that the
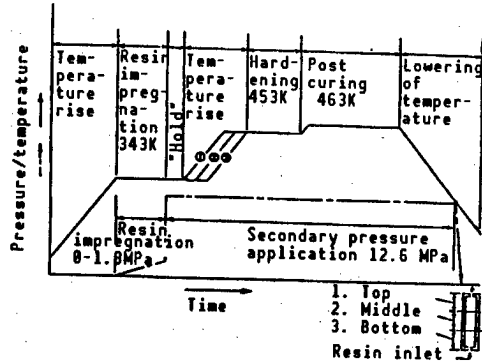
Figure 5. Basic Process

resin turned into a gel in order from the top to the bottom. The basic molding process is presented in Figure 5.

4.2 Results and Discussion

A finished I-beam-shaped product is shown in Figure 6, which indicates its external appearance, shape, dimensions, and cross sectional conditions. The basic molding process was demonstrated to be correct, since there was no part where the resin was not impregnated, in terms of external appearance. Further microscopic cross sectional observation confirmed satisfactory impregnation of the resin into the spaces between the filaments.

Shape and dimensions of the molded products

Condition of a cross sectional surface of the molded product
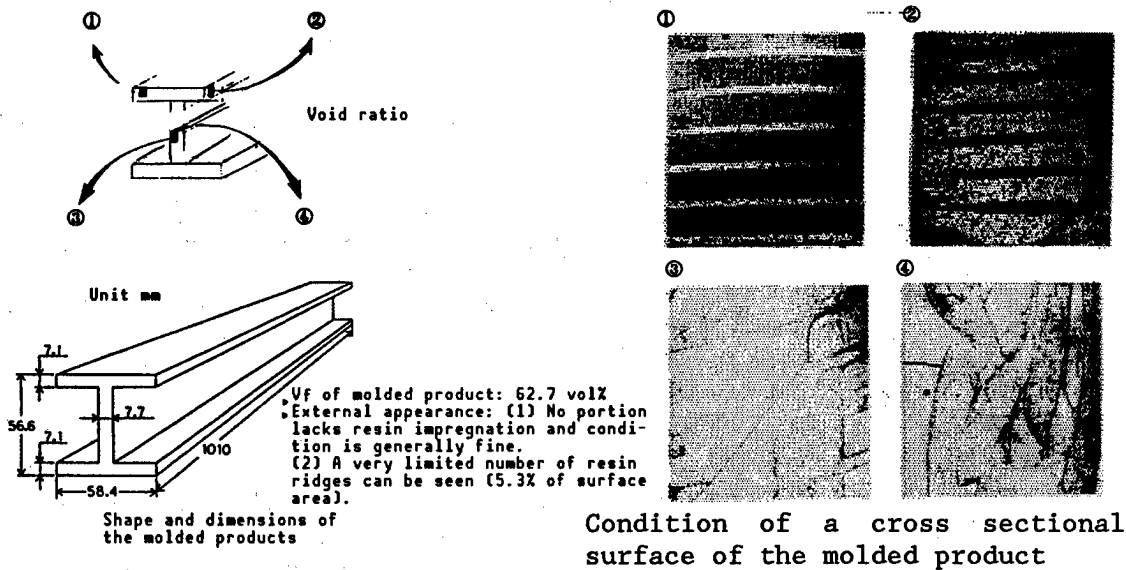
Figure 6. Quality of the Molded Product

It is important in this connection that the density of the fabric be uniform, since the presence of some cracks was noted where the resin had pooled because of an uneven distribution of the fabric density.

149

5. Experiments for Molding Flat Three-Dimensional Fabrics by the Resin Film Impregnation and Consolidation Method

5.1 Experimental Method

The first step was to carry out a series of preliminary experiments to investigate the possibility of resin impregnation of three-dimensional fabrics through the capillary phenomenon and to explore the effects of a vacuum and of the rate of temperature increase on the resin impregnation process. These were followed by an experiment in which a composite was molded in a flat shape, based on the results of the preliminary experiments.

5.2.1 Preliminary Experiments

Figure 7 illustrates the dependence on V_f of the depth of resin impregnation into carbon fibers, with the temperature of the resin kept constant. The results prove that a flat three-dimensional fabric, with a V_f as high as 35 percent, allows resin impregnation by the capillary phenomenon alone without the application of pressure at the time of impregnation.
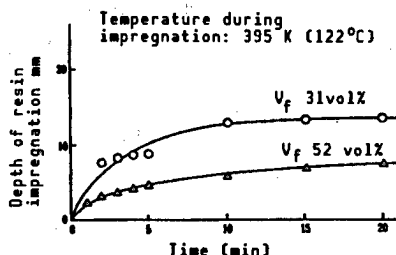

Figure 7. Dependence of the Depth of Resin Impregnation on V_f

Table 2 summarizes the effects of vacuum conditions and the rate of temperature increase on the quality of the composite product. These results indicate that impregnation in a vacuum is necessary as is the application of pressure after impregnation.

5.2.2 Molding of Flat Three-Dimensional Fabric

According to the basic molding process worked out on the basis of results of the preliminary experiments (Figure 8), resin films were applied to the bottom surface of the fabric and molding was allowed to proceed on a horizontal plane. The product proved to be free of any warping, twisting, etc., and the inside was fully impregnated with resin. Nevertheless, some fine cracks were noted in the resin at sites where the resin had pooled. Some resin defects were also visible on the surface. In an effort to improve the quality of the molded product, therefore, resin films were prepared wherein the shrinkage resin at the time of consolidation was reduced, the fracture elongation value was raised, and the number of internal bubbles was reduced. These films were applied to the top and bottom surfaces of the flat fabric. After molding, the product proved to be almost free from fine cracks where the resin had pooled and was also free from resin defects on the surface (Figure 9 [not reproduced]).

150

Table 2. Assessment of the Qualities of the Molded Product

Molded pro- duct	Molding conditions		Qualities of molded product			
	Rate of tem- per- ature in- crease	Resin impreg- nation in a vacuum	Vf (vol %)	Surface condition	Voids	Cracks at sites of resin pooling
#1	1	Afforded	35	Unevenness on top surface Sites of resin pooling on bottom surface	Not visible	Notable
#2	1	Not afforded	35	Unevenness on top surface Sites of resin pooling (with bubbles involved) on bottom surface	Scattered among fiber bundles and at sites of resin pooling	Notable
#3	3	Afforded	35	Unevenness on top surface Sites of resin pooling on bottom surface	Not visible	Notable
#4	3	Not afforded	35	Unevenness on top surface Sites of resin pooling (with bubbles involved) on bottom surface	Scattered among fiber bundles and at sites of resin pooling	Notable
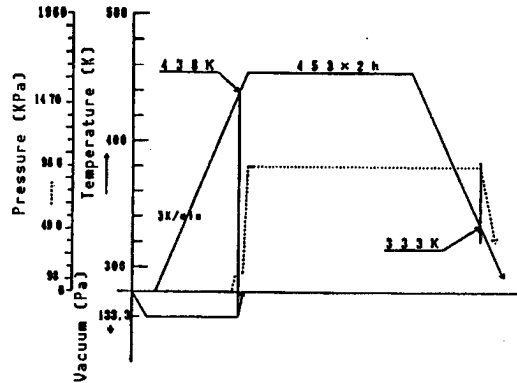
Figure 8. Heat Cycle for Molding

6. Conclusion

We examined two types of technologies—a resin injection consolidation method and a resin impregnation consolidation method—as potential composite molding technologies involving the consolidation of a matrix resin after it had been impregnated into a three-dimensional fabric. Such fabrics are promising as reinforcement materials for high-performance composite materials. The former method is best suited for molding comparatively small three-dimensional fabrics into complex shapes, while the latter is better for molding fabrics into comparatively simple albeit large shapes. It is conceivable that, through the ingenious application of these two molding methods, composite-molding technology for three-dimensional fabrics can be made available for a wide range of structural materials.

Research on Future FRM Composite Materials

[Article by Tetsu Hanano, Polymer Laboratory, Toray Co.]

[Test] 1. Introduction

Among fiber-reinforced metals (FRMs), carbon fiber-reinforced aluminum (C/Al) has a particularly high specific strength and specific modulus. It also displays thermal conductance and a thermal expansion coefficient superior to those of carbon fiber-reinforced plastics. Thus it serves as a valuable structural material in the aerospace industry. As the properties of the C/Al are dictated by those of wire preform, an intermediate material, the development of a high-strength wire preform is a major problem toward achieving a high-strength C/Al. In general, the principal elements in obtaining a high-strength C/Al are first, to promote wetting between the carbon fiber and the aluminum, and, second, to minimize any reaction between them to prevent deterioration of the fiber. With regard to such reactions, pitch-type carbon fibers have generally been held to be superior to the PAN-type fibers.[1] However, considerable progress has been made in PAN-type carbon fibers over the last few years. We are now close to producing PAN-type fibers with a modulus of elasticity equivalent to those of the pitch type, but with a tensile strength far surpassing the latter. In this context, the author and others have been working to develop high-strength wire preforms that take advantage of the fine mechanical properties of the PAN-type carbon fiber.

This paper deals with the compatibility between a PAN-type fiber known as TOREKA and aluminum—a factor that influences the strength of the wire preform.

2. Research Method and Results

With a view to improving the comparability between carbon fibers and aluminum, the author and his colleagues investigated each type of carbon fiber and the corresponding matrix compositions that will facilitate the efficient manufacture of the wire preform. A discussion of the results follows.

2.1 Investigation of Carbon Fibers

2.1.1 Research Method

Previous research has indicated that, among PAN-type carbon fibers, the so-called high-modulus group is less reactive to aluminum than the high-strength group.[1,2] Thus the author and his colleagues examined the reactivity between carbon fibers and aluminum quantitatively in terms of the degree of graphitization of the carbon fibers.

The manufacture of the wire preform was carried out by coating the carbon fibers with a mixture of Ti and B using the CVD method and immersing the resulting product in fused aluminum. This is what is called the CVD impregnation method.

We used nine types of carbon fibers with different degrees of graphitization. Of these, five were produced at different sintering temperatures and four were produced by varying the degree of surface oxidation treatment of the carbon fiber TOREKA-M40, which had the highest sintering temperature. The matrix, in turn, was of the JIS A5056 type.

The index used for denoting the degree of graphitization was the value of the bandwidth at a strength two-thirds that of the peak of a Raman band in the vicinity of 1,600 cm^{-1}. A Raman spectrum was obtained by subjecting the carbon fibers prepared as described above to a laser Raman analysis (the two-thirds value).[3]

The strength of the wire preform was estimated by cutting an "as-fabricated" wire preform into pieces 290 mm long, subjecting the resulting specimens to a tensile test, and dividing the fracture stress applied by the cross section area of the preform. The cross section area of the preform and the volume content of the fibers (V_f) were calculated from the per unit length mass of the preform, the specific gravities of the carbon fiber and the matrix, and the denier value of the fiber.

The reactivity between the carbon fibers and the aluminum was calculated from the ratio by weight of Al_4C_3/C or the ratio by weight of the Al_3C_4 was estimated from the amount of methane liberated during the dissolution of the preform in a 6N hydrochloric acid solution.[4]

The efficiency of manufacturing a wire preform was specified by the value obtained by dividing the manufacture rate of preforms involving any of the carbon fibers noted above by that for the preform using the carbon fiber TOREKA T400, whose rate of manufacture was the highest of all preform types involved.

2.1.2 Results and Discussion

Figure 1 shows a plot of the degree of graphitization of the carbon fibers vs. the fiber-strength utilization rate and the amount of Al_4C_3 produced, where the letter U in the term M40-U indicates the absence of surface treatment and
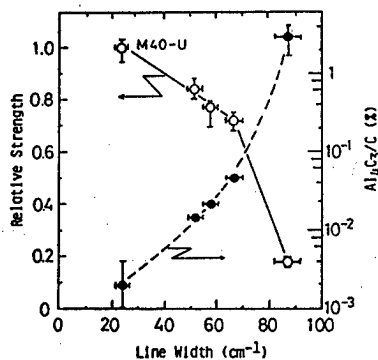
Figure 1. Dependence of Degree of Graphitization on Relative Strength
(Strength utilization rate) and the Al_4C_3/C Ratio

where the strength utilization rate represents the value of tensile strength
of the preform divided by the strength of a single fiber and by V_f. It is
evident from the figure that, with an increase beyond the two-thirds width
value, the value of the Al_4C_3 ratio rises and the strength-utilization rate or
the relative strength falls. This implies in quantitative terms that, with an
increasing degree of graphitization of the carbon fibers, the fibers become
more reluctant to react with the aluminum and the preform becomes stronger.

Figure 2 shows plots of the degree of graphitization against the efficiency of
preform manufacture and relative strength or strength utilization rate. The
figure indicates that the manufacturing efficiency falls with an increasing
degree of graphitization. Thus the manufacturing efficiency and the strength
utilization rate are in opposition, which suggests that it will be extremely
difficult to enhance both factors at the same time.
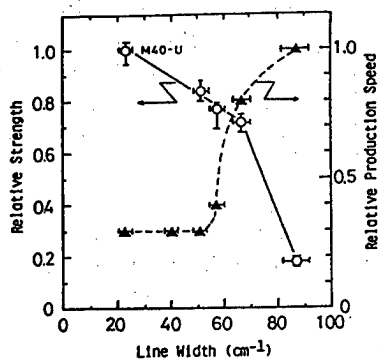
Figure 2. Dependence of Degree of
Graphitization on Relative
Strength and on Relative
Production Speed
(Production efficiency)
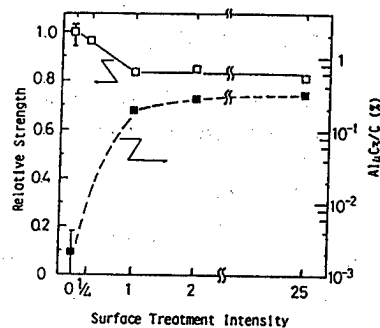
Figure 3. Dependence of Surface Treat-
ment Intensity (Degree of
surface treatment) on the
Relative Strength and on the
Al_4C_3 Ratio

The effects of the degree of surface treatment on the strength utilization
rate and on manufacturing efficiency are as follows: Figure 3 shows plots of
the surface treatment intensity vs. the strength utilization rate and the
amount of Al_4C_3. It can be seen from the figure that the amount to function
rises rapidly with increasing surface treatment intensity up to a final value

155

of one. The reason for this is that, for a constant sintering temperature, the degree of graphitization falls as the degree of surface treatment increases.[3] It can be seen, however, that the amount of Al_4C_3 stays almost constant for values of surface treatment intensity above one. It can also be seen that the strength utilization rate or relative strength tends to fall as the amount of Al_4C_3 grows, but the effect of surface treatment intensity on the strength utilization rate does not seem to be as pronounced as that of sintering temperature, as shown in Figure 1.

Figure 4 is a plot of the degree of carbon fiber graphitization vs. the manufacturing efficiency or relative production speed. The broken line indicates the effect of sintering temperatures and the continuous line represents the effect of surface treatment intensity, with the figures in brackets indicting the degree of intensity. The figure proves that surface treatments applied to only a limited extent result in a pronounced improvement in manufacturing efficiency. One possible reason for this is that the surface treatment renders the fiber surface chemically active and enhances the adhesive bond between the CVD coating and the base material of the carbon fiber so that the coating becomes more reluctant to detach from the fiber when the fiber is immersed in fused aluminum,and thus the wetting property of the fiber is stabilized.
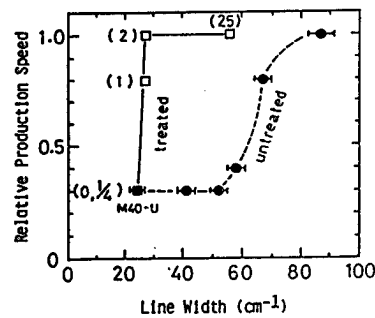
Figure 4. Dependence of Degree of Graphitization
on Relative Production Speed

This result implies that even such carbon fibers as M40, which has a high degree of graphitization and is reluctant to wet aluminum, can have the manufacturing efficiency of its preforms raised by undergoing a small amount of surface treatment itself, which has little effect on its strength utilization rate (relative strength).

Thus we concluded that if a wire preform with a high strength utilization rate or relative strength is to be produced efficiently, carbon fibers with a high level of strength and a high degree of graphitization that have undergone a limited surface treatment are to be favored.

2.2 Investigation of the Composition of the Matrix

2.2.1 Method of Investigation

This section deals with the effects of the matrix composition of the composite on the strength of the wire preform[5] using TOREKA M40J, a carbon fiber with a

high level of strength and a high modulus of elasticity. TOREKA M40J is representative of the PAN-type of fibers on the basis of results obtained in Section 2.1 above. The wire preform was produced by the CVD impregnation method. The reactivity between the carbon fiber and the matrix was estimated on the basis of the strength of extracted fibers. The amount of Al_4C_3 produced was measured as was the product's tensile strength. Six types of aluminum alloys were examined: JISA1080, A6061, A5058, A1080, as well as some with small amounts of Si, Cu, and Mg added. The manufacturing conditions were identical for all the alloys. To facilitate a quantitative determination of the composition of the matrix, the wire preform was subjected to ICP emission spectrometry after it had undergone tensile tests. To elucidate the distribution of alloy elements, the cross sections of the alloys were analyzed by EPMA.

2.2.2 Results and Discussion

Table 1 presents the results of an analysis of the composition of each matrix. Table 2 lists the effects of matrix compositions on the strength and reactivity of the wire preforms (represented by the strength of extracted fibers or residual fiber strength and by Al_4C_3/C, respectively). it is evident from these tables that adding the elements Si, Mg, and Cu to matrixes causes the strength of the wire preforms to decline. By contrast, the tables show that no effects of matrix compositions on the strength of extracted fibers and function/C can be seen. This suggests that the effect of these elements in relevant amounts on the reactivity between the carbon fibers and the aluminum was almost negligible, i.e., the adverse effect of these elements on the tensile strength of the wire preforms is independent of the interface reactivity.

Table 1. Alloy Compositions of Wire Preforms (Percent by weight of the matrix)

Matrix	Ti	B	Si	Fe	Cu	Mn	Mg	Cr	Zn
1080	0.39	0.13	0.072	0.17	0.009	0.003	0.004	<0.001	0.031
5056	0.56	0.15	0.10	0.16	0.005	0.072	4.67	0.088	0.059
6061	0.51	0.14	0.42	0.41	0.28	0.052	1.18	0.20	0.042
1080-Si	0.43	0.16	0.26	0.20	0.0007	0.002	0.0054	0.0009	0.017
1080-Mg	0.41	0.16	0.059	0.13	<0.001	<0.007	2.97	<0.007	0.037
1080-Cu	0.42	0.15	0.085	0.14	0.94	<0.008	<0.002	<0.008	0.041

Table 3 shows the results of an EPMA analysis of a cross section of the preforms. It can be seen from the table that Si concentrations in the matrix are higher in the vicinity of the interface, which suggests that the position of final hardening of the matrix during manufacturing took place in the vicinity of the interface and that a brittle phase with a high concentration of Si was precipitated largely in the vicinity of the fiber, allowing the preform to become more susceptible to notch.

To date, there is no comparable evidence for the elements Cu and Mg, but a similar phenomenon was observed for Cu in the investigations conducted by Fukunaga[6] and Mortensen.[7] As for Mg, the element makes eutectic crystals with aluminum, as do Si and Cu, which suggests it would react in a similar manner.

Table 2. Effects of Matrix Composition on the Strength of Wire Preform

Matrix	Wire tensile strength (GPa)	Fiber residual strength (Gpa)	Al_4C_3/C (%)
1080	1.28(1.24~1.34)	3.29	0.70
5056	0.78(0.73~0.84)	3.34	0.36
6061	0.81(0.73~0.85)	3.69	0.49
1080-Si	0.98(0.92~1.02)	3.27	0.97
1080-Mg	0.78(0.75~0.86)	3.13	0.23
1080-Cu	0.89(0.85~0.94)	3.68	0.54

Table 3. Concentration of Si, Cu, and Mg at the Interface and in the Matrix as Determined by EPMA Analysis

Alloy	Element	Matrix	Interface
1080	Si	5	15
	Cu	ND	ND
	Mg	ND	3
5056	Si	ND	16
	Cu	ND	ND
	Mg	618	1262
6061	Si	27	67
	Cu	15	56
	Mg	208	215
1080-Si	Si	12	55
	Cu	ND	ND
	Mg	ND	ND
1080-Cu	Si	7	17
	Cu	38	160
	Mg	2	ND
1080-Mg	Si	10	71
	Cu	ND	ND
	Mg	549	769

ND : Not Detected

Where the M40J carbon fiber is used, the 1080 matrix alloys afford the wire preform the highest strength in the "as-fabricated" state, as seen in the above.

3. Summary

The results described above can be summarized as follows:

(1) PAN-type carbon fibers, which are strong and have a high degree of graphitization, are favored for the manufacture of high-strength wire preforms.

(2) The application of surface treatment to the carbon fibers is the favored method for improving the manufacturing efficiency of the preform, but should be limited as much as possible in order to retain material strength.

(3) Where wire preforms are produced using carbon fibers that have been subjected to surface treatment, the matrixes of aluminum alloys with relatively less Si, Cu, and Mg are favored because of their strength.

4. Conclusion

Our research was conducted as part of the "Research and Development of Composite Materials" project commissioned to the Institute for Research and Investigation of Next-Generation Metals and Composite Materials as part of the Research and Development Project for Basic Technologies for Future Industries sponsored by MITI's Industrial Science and Technology Agency.

References

1.   Amateau, M. F., JOURNAL OF COMPOSITE MATERIALS, Vol 10, 1976, pp 279–296.

2.   Ounishi, S., Collection of Preliminary Manuscripts for the Second Future Industry Symposium: Technologies for the Materials of Metal Composite Materials, 1984, pp 113–120.

3.   Hanano, T. and Kyouno, T., Collection of Articles for the Third Symposium on Advanced Material Technologies, 1987, pp 31–35.

4.   Padilla, F., Harrigan, W.C., Jr., and Amateau, M.F., TR–0075(5621)–3, 1975.

5.   Kyouno, T. and Hotta, T., Collection of Abstracts of Lectures for the 12th Symposium on Composite Materials, 1987, pp 153–156.

6.   Fukunaga, H. and Aida, K., Collection of Articles of the Japan Machinery Society, A50, 453, 1984, pp 1054–1059.

7.   Mortensen, A., Gunger, M.N., Cornie, J.A., and Flemings, M.C., JOURNAL OF METALS, Vol 38 No 5, 1986, pp 30–36.

Development of Ti-Based FRM Produced by HIP-Molding

[Article by Ken-ichi Aota and Takashi Motoda, Material Laboratory, Kobe Steel Co.]

[Text] 1. Introduction

An apparatus for hot isostatic pressing (HIP), which makes it possible to apply pressure to materials under a gas atmosphere at high pressures and temperatures, has become commercially available for the consolidation ad molding of metal powders and ceramics. Since it also works effectively for bonding consolidation between ceramic fibers and metals, the apparatus has begun finding applications in the molding of FRMs, which have attracted attention as potentially valuable new materials because of their light weight, superior specific strength, superior specific modulus of elasticity, and higher resistance to heat. The apparatus is particularly useful for molding hollow cylinders, objects with curved surfaces and other complex shapes because the application of pressure to such objects is isotropic.

It is important to select a combination of fibers and matrix that will not deteriorate because of an interface reaction at the time of molding. Ti has good prospects for application as a matrix for FRMs because of its light weight and because it is more resistant to heat than aluminum. However, Ti is not only an active metal but also suffers from the drawback that it requires high temperatures for molding, which can have adverse effects on the interface reaction with fibers and on the strength of the product. The authors have investigated these problems in the course of their developmental research, a description of which follows.

2. Interface Reaction Between Fibers and a Ti Alloy

Figure 1 presents a scanning electron microscope (SEM) picture of the fiber interface of an object made by consolidating a mixture of Ti-6Al-4V powder and one of a variety of reinforcement fibers chopped into pieces. In almost every combination of materials, a layer of interface reaction is notable and, in particular, whiskers are almost completely absent because of their fine fiber diameters, which are less than 1 μm. Apart from the nearly complete
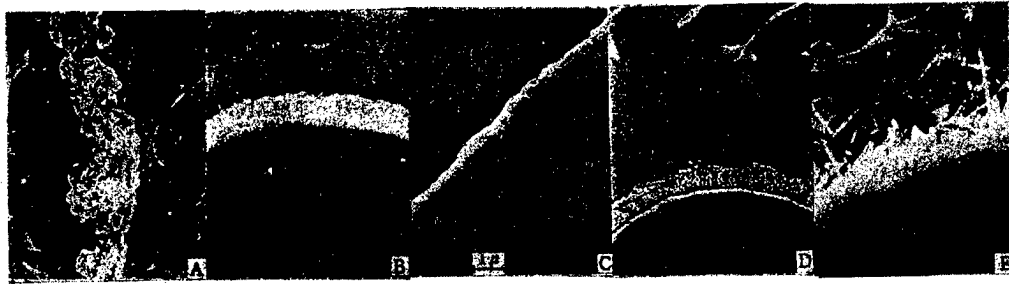
A) SiC(カイス) B) SiC(pcs) C) SiC(CVD) D) Al₂O₃ E) B(CVD)

Figure 1. Microscopic Structure of Composites Involving Ti-6Al-4V
Alloys and Various Fibers (900°C, 98 MPa, 1 Hr)

elimination of the whiskers because of the reaction, the thickness of the
reaction layer declines according to the following order: B(CVD), Al₂O₃,
SiC(PCS), and SiC(CVD). The thickness of the layer is about 3 μm for B, 1 μm
for Al₂O₃ and SiC(PCS), and about 0.5 μm for SiC(CVD) in the neighborhood of
900°C as shown in Figure 2. The diameters of the fibers, in turn, are 140 μm
for those produced by CVD and 15 μm for Al₂O₃ and SiC(PCS). The fibers produced
by CVD, therefore, are favored, and particularly SiC(CVD), in terms of the
ratio of the diameter of the fiber to the thickness of the reaction layer. The
thickness of interface reaction layers for composites made up of SiC(PCS)
fibers and some representative Ti alloys are presented in Figure 3. The thick-
ness declines according to the following order: pure Ti, Ti-6Al-4V, Ti-6Al-
2Sn-4Zr-2Mo and Ti-6Al-2Sn-4Zr-6Mo, suggesting that alloys involving Zr and Mo
are more effective in reducing the formation of the reaction layer.
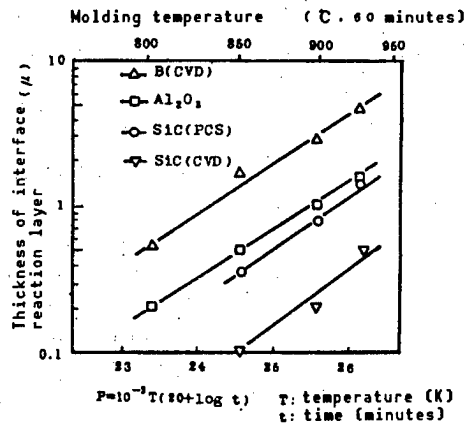
Figure 2. Thickness of the Interface Reaction Layer for Composites
Consisting of Various Specific Fibers and Ti-6Al-4V Alloy

3. Effect of Fibers and Matrices on the Strength of FRMs Involving CVD-Fibers

As seen above, CVD fibers may possibly be the most practical reinforcement
fibers. The authors produced HIP molds shaped like flat boards from these
materials in order to estimate their strength. Over a foil or powder sheet of
each of these alloys we placed a matte of the fibers, which were previously
aligned, fixed with resin, and wound with a spool for an identical length to

161

Thickness of interface reaction layer (μ)
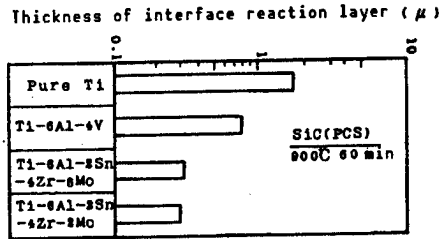
Figure 3. Thickness of the Interface Reaction Layer for Composites
Involving SiC(PCS) and a Ti Alloy

form a pre-sheet. This sheet was then cut into a predetermined shape and laminated in five plies to form the flat boards. The resultant laminates were sealed in a vacuum capsule and subjected to HIP treatment to achieve the desired product.

Figure 4 is a diagram of the tensile strength values for HIPed products where the matrix was Ti-6Al-4V and the fibers were SiC(CVD), B/B$_4$C(CVD) or B(CVD). The tensile strength at room temperature was the highest for SiC(CVD), followed by B/B$_4$C(CVD) and B(CVD) in that order. The order for a temperature of 450°C was identical. The value for B(CVD) is even lower than that for Ti-6Al-4V alloy HIPed uncoupled. Thus, it is unlikely that the tensile strength of this composite can be improved.
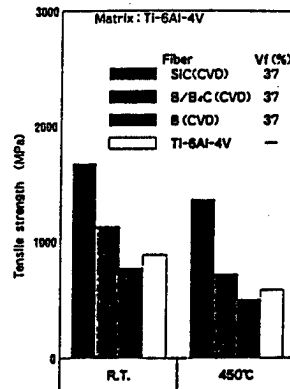

Figure 4. Effects of CVD Fibers on the Strength of FRMs
Involving a CVD Fiber and Ti-6Al-4V Alloy

Figure 5 shows SEM pictures of the fractured surfaces produced by a tensile strength test. It can be seen that a separation occurred between the fiber itself and the interface reaction layer, or the layer of carbon coating over the fiber surface in the case of the SiC(CVD) fiber, as did the B/B$_4$C(CVD) fiber. The B(CVD) fiber, by contrast, suffered no such interface separation, but a sharp crack appeared in the interface layer, which grew up to the fiber itself. This could lead to a fracture.

In this connection Ochiai and his colleagues invested the relationship between the interface reaction layers and strength using a single fiber model. They concluded that where the bonding strength between the reaction layer and the

162

A) SiC(CVD)   B) B/B₄C(CVD)   C) B(CVD)
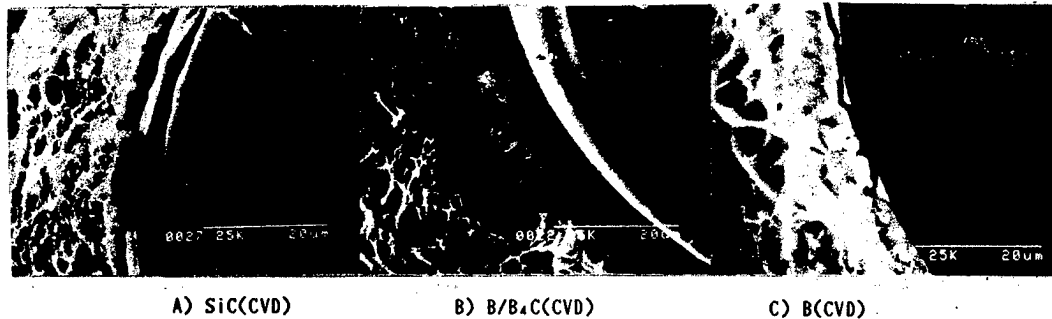
Figure 5. SEM Picture Showing the Structure of FRMs Involving a CVD
          Fiber and Ti-6Al-4V Alloy Following a Tensile Strength
          Testing of the FRM

fiber was high, the cracks produced on the layer grew readily to the fiber
itself and reduced the strength of the fiber. By contrast, where the bonding
strength was low, the crack was prevented from reaching the fiber by the
separation of the interface and hence there was no deterioration of fiber
strength. They also concluded that the larger the thickness of the reaction
layer, the smaller the stress required for the crack to grow.

The composite reinforced with SiC(CVD) fibers conceivably enjoyed high
strength because it had a better interface condition in terms of the thickness
of the reaction layer as shown in the microscopic picture of the fracture.

Figure 6 shows the tensile strength values for the FRMs using SiC(CVD) as the
fiber and the alloys Ti-6Al-4V, Ti-6Al-2Sn-4Zr-2Mo, Ti-6Al-2Sn-4Zr-6Mo, and
Ti-15Mo-5Zr-3Al as the matrix. The tensile strength at room temperature is the
highest for the FRM made of the Ti-15Mo-5Zr-3Al alloy, followed by those of
the alloys Ti-6Al-2Sn-4Zr-2Mo, Ti-6Al-4V and Ti-6Al-2Sn-4Zr-2Mo, in that
order. This order is identical to that of the tensile strength of the matrix
alloys. The tensile strength of these FRMs are all above 1,470 MPa
(150 kg/mm²). The strength of the FRMs produced at 300°C and 450°C follows the
same pattern as those produced at room temperature.

The FRM with the Ti-15Mo-5Zr-3Al alloy stayed above the level of 1470 MPa
(150 kg/mm²), even at a temperature of 450°C. Thus it enjoys good prospects for
high-temperature applications. Further, the composite can be turned into foil
with comparative ease because it is a β-type alloy, which renders it more
adaptable as an FRM material.

Table 1 compares the modulus of elasticity of molds with different matrixes
and those based on the compounding rule. All values are above the 200 GPa
level and are nearly double those of the Ti alloys. Molding efficiency for the
compounding rule was about 90 percent for all the different matrixes with no
appreciable differences among them. The same was true for molding efficiency
in terms of strength. We assume, therefore, that the high level of strength of
the matrixes used were introduced unmodified into the FRMs.
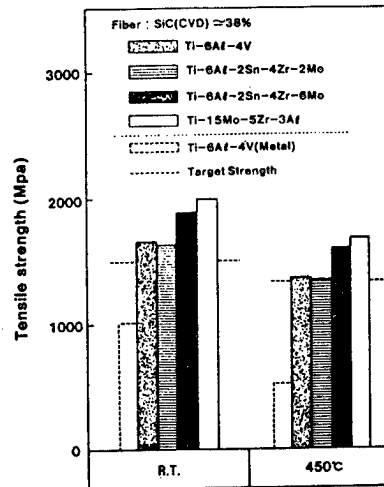
Figure 6. Dependence of Strength of Ti-Based FRMs on
Composition of Different Ti-Based Matrixes

Table 1. Modulus of Elasticity and Mold Efficiency for Ti-Based FRMs

	SiC(CVD)		
	Ti-6Al-4V	Ti-6Al-2Sn-4Zr-2Mo	Ti-6Al-2Sn-4Zr-6Mo
Volume ratio V_f (%)	37	37	37
Modulus of elasticity (GPa)	205	203	218
Compound rule (GPa)	225	228	231
Molding efficiency (%)	91	89	94

4. Features of SiC(CVD)/Ti-15Mo-5Zr-3Al FRM

Raising the V_f value to 42 percent together with a rise in temperature, caused the strength of the composite to diminish somewhat in the direction of fiber alignment and yielded values as high as 1750 MPa at 450°C and 1430 MPa at 600°C. But the strength in the direction normal to the fiber alignment fell notably, as shown in Figure 7. investigation of properties of the composite was therefore carried out largely with one with the V_f level of 37 percent.

The modulus of elasticity in the direction of fiber alignment at room temperature, recorded at some 200 GPa, was roughly equivalent to that obtained by the compounding rule and twice that of the matrix of Ti alloy. For m values, which indicate reliability, a comparatively better figure of 50 for the modulus of elasticity and from 20-30 for tensile strength were obtained.

Hollow cylinders, shown in Figure 8, also exhibited a tensile strength approximately equivalent to that of flat boards and the effectiveness of the
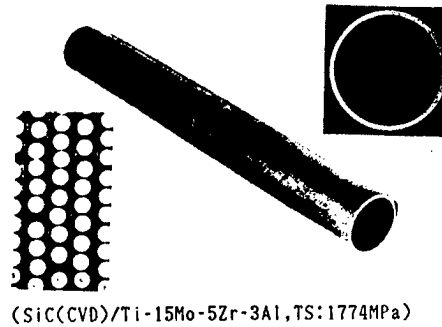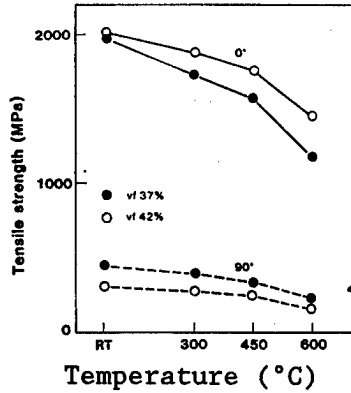
Figure 7. Tensile Strength of SiC/
Ti-15Mo-5Zr-3Al

(SiC(CVD)/Ti-15Mo-5Zr-3Al,TS:1774MPa)

Figure 8. Tube-Shaped Product Made From
a Ti-Based FRM by HIP Molding

Table 2. Compression and Shear Strength of SiC(CVD)/Ti-15Mo-5ZR-3Al

		SiC/CVD)/Ti		SiC(CVD)/Al*
			m	
Compression	Strength (MPa)	3256	13	2980
	Modulus (GPa)	202	25	216
Shear	Strength (MPa)	180	6	48

*AVCO Data

HIP method in molding tube-shaped objects—which are important basic structural elements—was thereby proved.

Compression strength, measured at levels above 3,000 MPa, was 1.5 times greater than the relevant tensile strength and thus affirmed the feature of a large-diameter fiber. The modulus of elasticity, measured at about 200 GPa, was equivalent to that of the tensile test and represents a justifiable value. The m value was 25 for the modulus of elasticity, but a somewhat lower figure of 13 was recorded for strength; both are appreciably lower than the comparable tensile figures.

Shear strength was measured with a stretch interlayer shearing tester and was determined to be about 180 MPa, which was higher than that for SiC(CVD)/Al FRM, which was measured in the same manner. The m value is still as low as under 10, allowing for further scrutiny (Table 2).

The creep fracture strength at 450°C was far above the Ti-6Al-4V and, at 600°C, was superior to Incoloy 800 and approximately equivalent to the Fe-based superalloy A286. Its usefulness in this temperature range was confirmed because its specific creep fracture strength, which allows for the specific gravity of the material, proved to be 1.5 times that of Ni-based Incone 1718, although its actual creep fracture strength was lower (Figure 9).
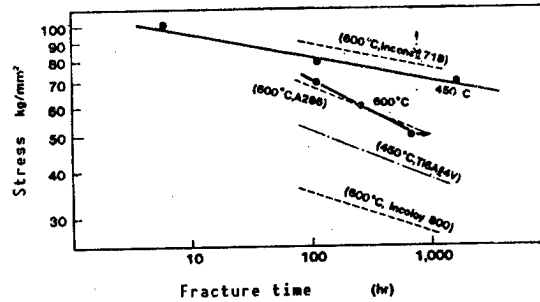
Figure 9. Creep Fracture Strength of SiC(CVD)/Ti–15Mo–5Zr–3Al
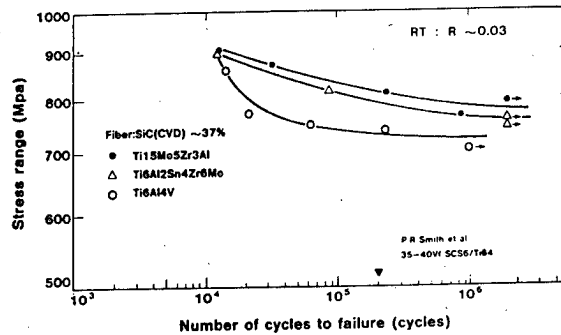
Figure 10. Fatigue Strength of SiC(CVD)/Ti–15Mo–5Zr–3Al

Its fatigue strength, in turn, far surpasses that of Ti–6al–4V with its 10^6–cycle strength, which could conceivably be above the 700 MPa level. Also to be noted is that the values derived from this experiment on HIP molding were much higher than those obtained by Smith, et al. (Figure 10).

5. Conclusion

The FRM strength values derived from our experiments, when examined in terms of specific strength in a high temperature range of 450°C to 600°C, are twice those for Ti alloys and superalloys, which are the currently available engine materials (Table 3). Thus it appears that FRMs have good prospects for applications in this area. It will therefore be necessary to accumulate relevant data adapted for individual practical applications. It will also be to pursue the further development of technologies for the precision molding of component shapes.

166

Table 3. Specific Strength of Ti Alloys, Ti-Based FRMs and Superalloys

		Specific gravity (pg/cm^3)	Strength (upper range σ_{TS}kg/mm^2) Specific strength (lower range σ_{TS}/ρ)				
			RT	300°C	450°C	500°C	600°C
Ti–6Al–4V	α–β	4.47	100 22.4	78 17.4	65 15.4	55 12.3	—
Ti–6Al–2Si–4Zr–2Mo	Near–α	4.54	95 20.9	76 16.7	67 14.8	60 13.2	50 11.0
Ti–6Al–2Si–4Zr–6Mo	α–β	4.68	125 26.7	105 22.4	97 20.7	92 19.7	—
Ti–10V–2Fe–3Al	Near–β	4.65	128 27.5	110 23.7	100 21.5	—	—
Ti–15V–3Cr–3Sn–3Al	β	4.76	140 24.2	115 24.2	—	—	—
Ti–15mo–5Zr–3Al	β	4.9	148 29.9	125 25.2	117 23.6	107 21.6	—
SiC(CVD)/Ti FRM	FRM	4.24	200 47	176 41	160 38	– –	115 27
Incoloy 901	Super-alloy	8.20	121	—	118 14.3	105 12.8	100 12.2
Inconel 718	Super-alloy	8.19	127	—	125 15.3	120 14.7	110 13.4
Waspaloy	Super-alloy	8.19	130	—	128 15.6	120 14.7	115 14.0

Development of Aluminum-Based FRM Composite Materials

[Article by Kouji Itoo, Hirotoshi Nakayama, Mamoru Imuda, and Hiroshi Nakaya, Aerospace Technology Headquarters, Kawasaki Heavy Industries]

[Text] 1. Introduction

Since metal-based composite materials with continuous fibers and fiber-reinforced metals (FRMs) are generally not amenable to extrusion, rolling, forging, and other forms of plastic processing, we are working to create what we call near net shape molding (NNS molding), where composite formation and shape formation can be carried out simultaneously. Among all FRM molding methods developed to date, the melt-impregnation method and the method of powder molding by HIP appear to offer the best prospects for NNS molding.

Of these two, the melt-impregnation method is more likely to allow melted metals at high temperatures to react chemically with the fibers on contact nd thus cause deterioration in the fibers. By contrast, powder molding by HIP may make it possible to avoid fiber deterioration since the material is in a solid phase or in the region where the solid and the liquid phases coexist when subjected to consolidation by high pressure.

This article presents the results of an investment of several varieties of materials reinforced with pitch-type carbon fibers. Our aim as to assess the mechanical properties of flat-shaped FRMs produced by HIP molding of powder. We also attempted the trial manufacture of tube-shaped FRMs forged out as the first step in the NNS molding.

2. Mechanical Properties of Flat-Shaped FRMs

2.1 Raw Materials for Specimens and Testing Methods

The specimens we used were produced by HIP molding using either powder slurry preforms or infiltration wire preforms that had been made by different methods. The slurry preforms produced by Kawasaki Heavy Industries used high-modulus carbon fibers of the PAN and pitch types as the reinforcement fibers.

An Al-12%Si (4032) alloy powder, which has a low-melting point, and an Al-Ni alloy powder, which displays excellent amenability to fibers was used as the matrixes, which were produced by the powder slurry method. The properties of the reinforcement fibers and the aluminum alloy powders are presented in Tables 1 and 2, while those of the wire preforms, which had been produced by the infiltration method by the Toray Co., are shown in Table 3.

Table 1. Properties of Reinforcement Fibers

Property	High modulus carbon fibers of the PAN type	High modulus carbon fibers of the pitch type
Density $(10^3kg/m^2)$	1.83	2.17
Tensile strength (GPa)	3.57	3.43
Tensile modulus of elasticity (GPa)	419	715
Number of filaments (in lines)	6,000	3,000

Table 2. Properties of Aluminum Alloy Powders

Alloy system	Chemical composition (wt%)							Particle size distribution (wt%)	
	Si	Fe	Cu	Zn	Mg	Ni	Al	+250	-325
Al-Si (4032)	11.78	0.26	0.11	0.01	1.11	1.07	Bal.	0.2	85.6
Al-Ni	0.60	0.44	0.10	0.03	0.04	5.74	Bal.	0	92.5

Table 3. Properties of Wire Preform Made by Toray Co.

Property	M40J/1080
Reinforcing fiber	PAN-type carbon fibers with a high-modulus of elasticity (M40J-S)
Matrix metal	Al alloy 1080
Volume ratio of the fiber V_f(%)	40-45
Tensile strength (GPa)	1.18-1.48

Figure 1 is a diagram of the basic procedure of FRM molding by HIP. The HIP can, which was made of pure aluminum (1050), was designed to direct the transmission of pressure and residual strain left after the HIP treatment. A preform was packed into the can and subjected to HIP molding at a set

temperature and in such a way that an FRM in the shape of a plate with a thickness of some 2 mm was produced. The assessment of its properties focused primarily on tensile strength and compression strength at room and high temperatures.
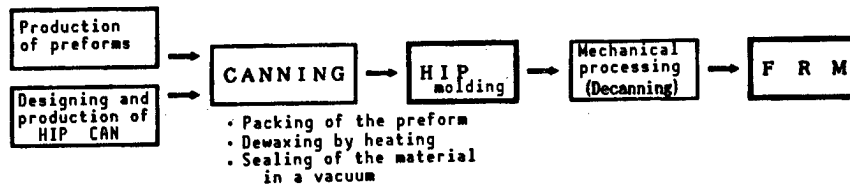

Figure 1. Basic Molding Process of FRMs by HIP

2.2 Test Results

Figure 2 presents the tensile characteristics at high temperatures for the composites M40J/1080, CF(PAN)/4032, and CF(pitch)/4032 and the alloy Ti-6Al-4V. In any composite system, declines in strength and modulus of elasticity, which accompany a rise in temperature, were smaller than those of the alloy and the rates of strength retention at 300° and 450°C were above 90 percent and 80 percent, respectively. This demonstrates that the resistance of these materials to heat is superior to that of the Ti-6Al-4V alloy, even though the matrixes of these FRMs were aluminum alloys.
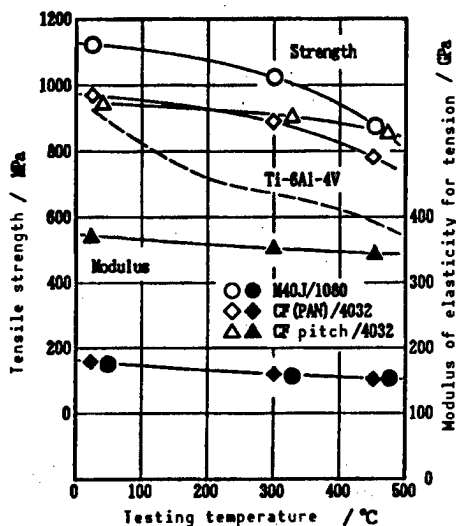

Figure 2. High–Temperature Tensile Characteristics of Various Series of Materials
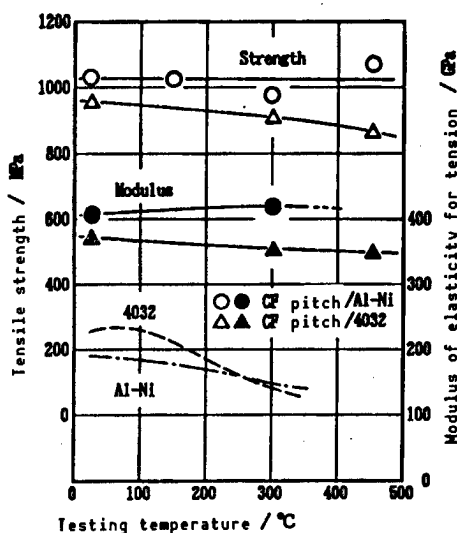
Figure 3. High–Temperature Tensile Characteristics of CF (pitch) /4032 and CF (pitch)/Al-Ni

Figure 3 shows the tensile characteristics at high temperatures of the composite CF(pitch)/4032 and CF(pitch)/Al-Ni, and for the sintered compacts of the matrix alloy powders. It can be seen that there are large differences in the relevant properties between the two composites which have different matrix alloys even though identical reinforcement fibers were used. An examination of

the strength of the fibers extracted from the two FRMs revealed that the strength of the fiber coupled with the 4032 alloy fell to about 70 percent of that for the original raw material fiber. By contrast, the fiber coupled with the Al-Ni alloy retained over 85 percent of its strength. This suggests the possible dependence of the room-temperature strength of FRMs on the compatibility of the reinforcement fibers and the matrix of the composites.

A microscopic picture of a cross section of an FRM, CF(pitch)/Al-Ni, is shown in Figure 4. The Al_3Ni phase, as can be seen, causes spherical particles to disperse among the fibers. This may possibly prevent the matrix from softening at high temperatures thereby endowing the composite with superior high-temperature characteristics.
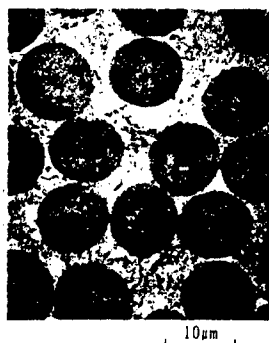
Figure 4. Microscopic Picture of the Cross
Section of CF(pitch)/Al-Ni

The compression strength of FRM material systems at room temperature and at a high temperature of 300°C are presented in Figure 5. Compression strength, on contrast to the tensile strength, varies notably at high temperatures. With regard to PAN-type carbon fibers of equivalent quality, M40J/1080 and CF(PAN)/4032 exhibit a compression strength about equal to tensile strength at room temperature, but this value falls in a large measure as the temperature rises, suggesting the influence of the softening matrix. In the case of material systems using pitch-type carbon fibers, the two materials exhibit similar behavior despite the difference in the matrix alloys involved. There is no decline in their compression strength at 300°C, but this strength is only about 40 percent that of the tensile strength. The difference between FRM materials using PAN-type and pitch-type carbon fibers may conceivably be the result of differences in fiber characteristics. This is suggested by the fact that the fracture shapes of the test specimens and the surface conditions of the broken fibers of the two materials, and by the fact that compression strength is more heavily influenced by fiber characteristics than is tensile strength.

3. Trial Manufacture of a Tube-Shaped FRM

A tube was adopted as the model shape for NNS molding of FRMs using the powder HIP molding method and an experiment to gauge its trial manufacture was carried out.

171
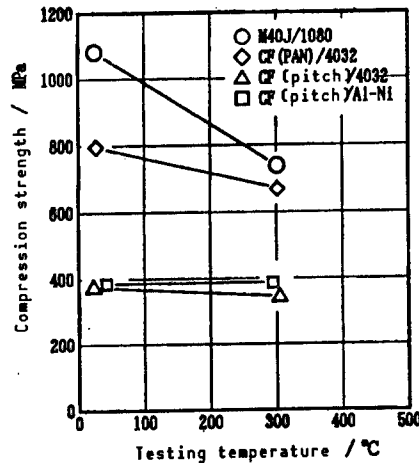
Figure 5. Compression Strength at Room Temperature and at
High Temperatures for Various Material Series

3.1 Test Specimen and Experimental Method

Two kinds of materials were used for the trial manufacture. One was the powder slurry preform, CF(PAN)/4032, produced by Kawasaki Heavy Industries and the other was a wire preform, the PCS type of SiCf/1050, produced with the infiltration method by Nippon Carbon Co.

The process for the trial manufacture of the tube-shaped FRM was largely identical with that used for the HIP molding of plate-shaped FRMs shown in Figure 1. The HIP can, however, was provided with a double shell to insure precise dimensions and the correct orientation of the fibers in the laminates. The can was designed with a fixed external shell and so that internal pressure applied exclusively was available for molding. Among the factors influencing the precision of the dimensions of the mold were the uniform density and the high density of the packed preform as it was introduced into the can.

3.2 Results of Trial Manufacture

The external appearance of the trial manufactured tube-shaped FRMs can be seen in Figure 6. No faults resulting from unsatisfactory molding process were detected in any of the molded products both in terms of their external appearance and after a microscopic examination. By modifying some elements of the HIP molding conditions, the product was made identical in quality and performance to the flat-shaped specimens produced in the basic research phase.

4. Summary

We investigated the technology of powder HIP molding of continuous fiber-reinforced, aluminum-based composites. We produced different types of FRMs and tested their mechanical properties. We have concluded that the molded products exhibited tensile properties at high temperatures that surpass those of Ti alloys, despite the fact that the composites we used involved matrixes
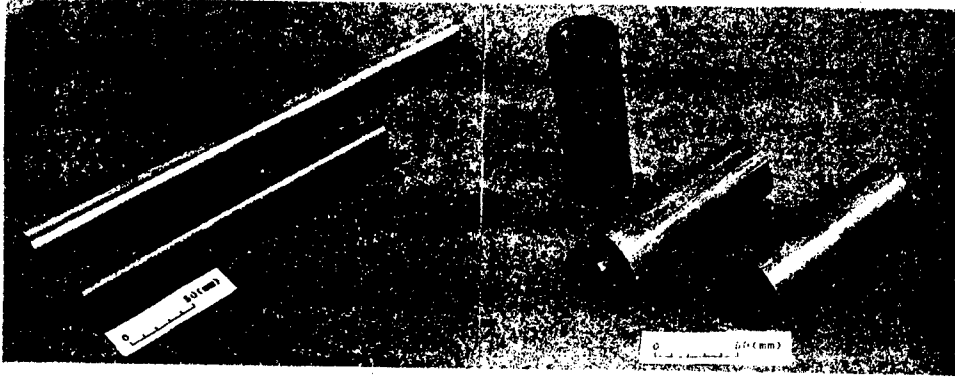
Figure 6. External Appearance of Samples of
Trial Manufactured Tube-Shaped FRMs

consisting of aluminum alloys. We also discovered that the relevant high-temperature properties were further improved by the proper choice of alloy systems for the matrix and that the FRMs involving Al-Ni alloys were capable of sustaining their strength at temperatures ranging from room temperature up to 450°C. The trial manufacture of tube-shaped composites as a three-dimensional model shape, in turn, proved that the product has performance levels equivalent to those of flat molds of the same composites and thus confirmed the possibility of NNS molding of FRMs by the powder HIP molding method.

It must be noted that a large part of the research and development effort presented here was conducted by the Institute for Research and Investigation of Next-Generation Metals and Composite Materials through a commission from NEDO as part of MITI's Research and Development Project for Basic Technologies for Future Industries.

References

1.   Itoo, Nakayama, Imuda, and Nakaya, Anthology of Lectures From the 24th Airplane Symposium, 1986, p 516.

2.   Imuda, A Collection of Preliminary Manuscripts for the Sixth Symposium on Basic Technologies for Future Industries—Metal Composite Material Technologies, 1989, p 405.

3.   Itoo, Imuda, and Nakaya, METAL, Vol 59 No 8, 1989, p 99.

Effects of Processing, Aging on Aluminum-Lithium Alloys

906C3829I Tokyo HIKOKI SHINPOJIUMU in Japanese Oct 89 pp 446-449

[Article by Wataru Asai, Hitoshi Shirai, and Isao Mitoda, Japan Aircraft Co., and Mikio Sasajima, Japan Aircraft Development Institute]

[Text] 1. Introduction

The material property data currently being used in Japan and in the United States as basic data for designing aircraft are contained in the MIL-HDBK-5. This, however, deals predominantly with data on raw materials (or unprocessed materials) and focuses only to a limited extent on data describing how material properties can be changed by plastic processing, despite the fact that most aircraft components are assembled and used after they have been subjected to plastic processing.

Using material data in designing instead of using design data generally does not affect safety because metal materials are generally hardened and improved in strength after having been subjected to plastic processing. It would be more economical, nevertheless, if one could allow for excess safety, or the degree of safety exceeding that required by design specifications, and curtail it. In other cases where materials tend to become softer after processing and hence less safe, as one sometimes encounters, the data naturally need to be corrected and the potential risks eliminated.

One needs to be especially careful in using Al-Li alloys, at this juncture, since they experience greater property changes after plastic processing and subsequent aging. The paper deals with data associated with the safety of Al-Li alloys together with a comparison of these alloys with conventional 2024-T3 and 7075-T6 alloys obtained during the research conducted by the authors.

2. Test Materials

The Al-Li alloy used in this experiment was 8090-T3 made by ALCAN Inc. of Britain. This alloy has a rated size of 1 x 2 m with a plate thickness of 0.8 mm. The surface of the unprocessed, unclad material is a light brown color with many white stains or discolored spots scattered over it.

The alloys used for comparison with the Al–Li alloy were the clad 2024–T3 alloy (204C–T3) with a plate–thickness of 0.8 mm, and the clad 7075–T6 (7075C–T6) alloy with a plate thickness of 0.8 mm. Both are produced in the United States.

The results of an analysis of the elements involved and measurements of the specific gravity of the test specimens are presented in Table 1.

Table 1. Materials for Test Specimens

Material		Al–Li alloy 8090–T3	2024C–T3	7075C–T6
Plate thickness (mm)		0.8	0.8	0.8
Cladding		Applied	Not applied	Not applied
Specific gravity		2.55	2.79 * 2.78**	2.81 * 2.80**
Element analysis values	Si	0.06	0.07	0.03
	Mn	0.001	0.60	0.035
	Cu	1.12	4.36	1.49
	Cr	0.002	0.035	0.19
	Ti	0.025	0.027	0.030
	V	0.001	0.008	0.005
	Fe	0.046	0.20	0.27
	Zr	0.12	0.020	0.002
	Mg	0.65	1.32	2.33
	Zn	<0.01	0.018	5.30
	Li	2.34	—	—

* Cladding eliminated; ** Cladding attached and included

The analysis of the elements was conducted on unclad core materials; the measurement of specific gravities was made on clad materials as well as unclad ones. The Al–Li alloy, which was unclad, was subjected to analysis and measurement without any modifications.

3. Processing and Aging

Two types of processing methods were applied to the specimens. One was stretch processing, which is frequently used in the sheet metal processing of aircraft components. The other was spin processing. In both types of processing, the T3 and T6 were directly subjected to cold working.

Stretch processing involves a uniform elongation induced by stretching plastic deformation and free shrinkage in the direction of width. In this process the behavior of the metal particles is similar to that in simple tensile tests.

Spin processing, in turn, represents a form of continuous processing in which the feed is supplied either on small rollers like the beads of an abacus or with "spatulas" by local pressing. This second technique is different from simple rolling. The basic kinds of processing are drawing, in which the diameter of the specimen shrinks, and stroke or hazing, in which the thickness of the material diminishes. Actual processing usually involves a mixture of these two types. The behavior of the material during the deformation process is complicated and metal particles seem to undergo deformation under rigorous repeating stresses. Changes in material properties after the processing, therefore, have been a matter of concern.

The stretch processing was carried out without using a die as a simple stretching of plates with the extent of processing being set at 3 percent elongation, while the spin processing was effected manually using a die in the shape of a cone with a diameter of about 1 mϕ and an angle of about 20°. The extent of processing was also set at 3 percent.

The aging treatments, which were carried out after the processing treatments, consisted of the T81 aging treatment for the alloys 8090 and 2024, and a process similar to T73 for the 7075 material. Since it aims partly at a relaxation of the residual stresses involved, the aging treatment used here was somewhat different from the original one for crystal deposition. In the spin process, in particular, the deformation of materials resulting from the residual stress was pronounced at the time of cleaving after they had been processed. The residual stresses, therefore, need to be reduced if the materials are to be subjected to cleaving after processing. In our experiments, the residual stress value was reduced by about one-half.

The test materials were subjected to the processing and aging treatments described above to produce test objects. The resulting objects were cleaved, processed as test specimens, and, finally, subjected to various property tests. The combinations of processing and aging and the symbols denoting the test objects are presented in Table 2.

4. Property Tests and Results

The test objects listed in Table 2 were cleaved, processed as test specimens, and subjected to static tensile tests, fatigue tests and fracture toughness tests. The axis of the test specimen was made identical to the lengthwise direction of the test materials. The static tensile test, conducted according to the ASTM E8, was carried out on three test specimens and the average value calculated. The fatigue test, in turn, was conducted under the conditions of stretching-stretching, R=0, smooth, room temperature, and ambient atmosphere. Any S-N curve was drawn from the values of tests performed on some 10 test specimens, and a strength value for the repeating stresses of 10^7 times was obtained from the curve. Next, in fracture toughness tests, carried out according to ASTM E399, E561, etc., a test specimen with a notch at the center

was subjected to the test after it had been given a preliminary fatigue crack. The stresses applied and the crack lengths produced were measured. The K_{IC} values were obtained from an average of these measurements made on two specimens. The results of these tests are given in Table 3.

Table 2. Combinations of Processing and Aging and Symbols for Test Specimens

Test material (raw material)	Processing and aging	Symbol for test specimen
Al-Li alloy 8090-T3	Untreated raw material (T3)	B
	Raw material (T3) subjected to stretch processing	T
	Raw material (T3) subjected to spin processing	P
	Raw material (T3) subjected to stretch processing and T81 treatment	TT
	Raw material (T3) subjected to spin processing and T81 treatment	PT
2024C-T3	Untreated raw material (T3)	B
	Raw material (T3) subjected to stretch processing	T
	Raw material (T3) subjected to spin processing	P
	Raw material (T3) subjected to stretch processing and T81 treatment	TT
	Raw material (T3) subjected to spin processing and T81 treatment	PT
7075C-T6	Untreated raw material (T6)	B
	Raw material (T6) subjected to stretch processing	T
	Raw material (T6) subjected to spin processing	P
	Raw material (T6) subjected to stretch processing and T7X treatment	TT
	Raw material (T6) subjected to spin processing and T7X treatment	PT

Table 3. Results of Testing for Mechanical Properties

Raw test material	Symbol of test specimen	Proof strength kgf/mm^2	Tensile strength kgf/mm^2	Fatigue strength (10^7-cycle time) kgf/mm^2	Fracture toughness K_R kgf/mm$^{3/2}$
Al–Li alloy 8090–T3	B	28.7	35.9	14.8	222
	T	35.4	37.7	17.5	194
	P	35.7	37.2	16.9	151
	TT	50.4	54.4	19.6	102
	PT	48.2	52.4	18.1	95
2024C–T3	B	34.1	45.7	12.4	251
	T	44.3	48.4	16.5	220
	P	38.1	46.9	13.3	176
	TT	43.8	47.7	14.8	153
	PT	42.3	46.3	14.4	128
7075C–T6	B	46.4	53.8	15.6	237
	T	54.4	55.1	15.1	202
	P	49.5	55.9	14.5	183
	TT	42.0	48.1	18.2	245
	PT	41.0	48.0	18.8	222

5. Calculation of Specific Strength and Representation by Indexes

Based on test data shown in Table 3, each of the values for proof strength, tensile strength, and fatigue strength were divided by the relevant specific gravities to give specific strengths. The resultant values were then turned into indexes where the respective raw testing materials are given a value of 100. These specific strength values and indexes are presented in Table 4.

6. Changes in Properties of Test Materials After Processing and Aging

Figure 1 consists of plots for the different properties vs. different test materials based on the indexes given in Table 4. The figure visually represents the rates of property change resulting from different processing and aging treatments for individual test materials. It also presents the differences in the extent of property change among different test objects so that these data will be variable for estimating their effect on design data.

178

Table 4. Conversion of Experimental Results Into Specific Strength Values[*]
and Representation of the Values by an Index
[*]Except for the value of fracture toughness

| Raw material test	Specimen symbol	Specific proof strength		Specific tensile strength		Specific fatigue strength 10⁷ cycle time		Fracture toughness	
		kgf/mm²	Index	kgf/mm²	Index	kgf/mm²	Index	kgf/mm^{3/2}	Index
Al-Li alloy 8090-T3	B	11.3	100	14.1	100	5.8	100	222	100
	T	13.9	123	14.8	105	6.9	119	194	88
	P	14.0	124	14.6	104	6.6	114	151	68
	T T	19.8	175	21.3	151	7.7	133	102	46
	P T	18.9	167	20.5	145	7.1	122	95	43
2024C-T3	B	12.3	100	16.4	100	4.5	100	251	100
	T	15.9	129	17.4	106	5.9	131	220	88
	P	13.7	111	16.9	103	4.8	107	176	70
	T T	15.8	128	17.2	105	5.3	118	153	61
	P T	15.2	124	16.7	102	5.2	116	128	51
7075C-T6	B	16.6	100	19.2	100	5.6	100	237	100
	T	19.4	117	19.7	103	5.4	96	202	85
	P	17.7	107	20.0	104	5.2	93	183	77
	T T	15.0	90	17.2	90	6.5	116	245	103
	P T	14.6	88	17.1	89	6.7	120	222	94
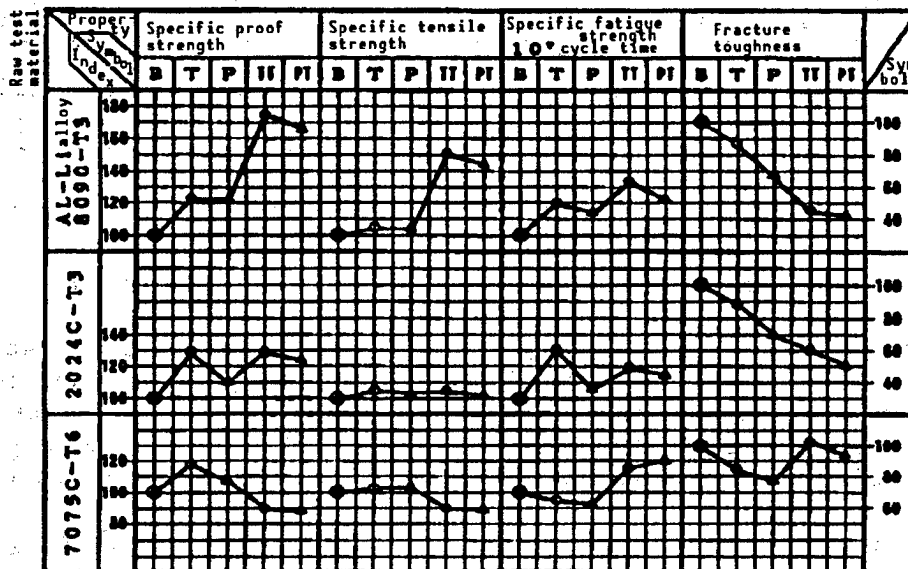
Figure 1. Property Changes Caused by Processing and Aging
(Index representation)

Since the indexes in the figure are indexes based on untreated test materials that are given the value of 100, the values for specific strength given in Table 4 need to be applied if one is to compare the absolute values of properties among different test objects.

179

7. Discussion and Assessment

The data presented in Figure 1 and Table 4 lead to the following conclusions:

(1) Changes in material properties induced by processing without aging: Proof stress and fatigue strength rise (enhancement) in 8090 and 2024. The tensile strength also increases for the three materials, but only to a very slight degree. Processing causes the fatigue strength of 7075 to fall. This suggests that processing tends to cause softening. This stands in marked contrast to proof stress and tensile strength, which are enhanced. All three test objects suffered a decline in fracture toughness after processing. The extent of this decline was nearly identical among the three materials.

(2) Property changes caused both by processing and aging are involved: The proof stress, tensile strength, and fatigue strength of alloy 8090 were increased. The extent of the increases was also pronounced. Proof stress increased by as much as 70 percent, tensile strength by 50 percent, and fatigue strength by 30 percent.

The 2024 alloy experienced a major increase in proof strength and fatigue strength, but only a limited one in tensile strength.

The 7075 alloy exhibited unique changes in that its stress and the tensile strength were reduced by some 10 percent, but its fatigue strength rose by 10-20 percent—changes that are the reverse of those seen in the treatment involving processing alone.

The fracture toughness for alloy 8090 suffered a large decline as does that for alloy 2024. By contrast, the comparable value for alloy 7075 remained approximately the same as that of the raw test material. A fall by up to 60 percent in the value for fracture toughness along with the minimum absolute value for alloy 8090, proved to be the worst result.

(3) Summary. The changes resulting from treatment involving processing alone generally were in the range of common sense, but those produced by treatments involving both processing and aging were pronounced. Differences in the extent of changes among different test objects were also very notable.

The Al-Li alloy, after a combined treatment of processing and aging, exhibits maximum strength but minimum fracture toughness. Thus from these data it is difficult to assess if it will be viable for practical application. Alloy 7075 experienced a small decline in its static strength. However, its fatigue strength was enhanced and its fracture strength remained the same as that of raw material B after it has been subjected to a combined processing and aging treatment. These can be considered good results in terms of properties obtained after processing. Finally, alloy 2024 exhibited property levels between those of the previous two alloys.

8. Summary

The experiment presented in this article was aimed at confirming the proper-
ties of sheet-metal structural elements for aircraft after the materials have
been subjected to plastic processing. It demonstrated that the changes in the
properties involved were greater than expected in spite of the limited extent
of processing performed in the experiment. Changes in the relevant data
resulting from increased processing or varying aging conditions are important
and intriguing, but cannot be predicted on the basis of the limited results of
this experiment.

We hope that data for Al-Li alloys other than that of 8090, which was the
subject of our experiment will be forthcoming. The question of how to apply
Al-Li alloys to maximum advantage may become critical in the future—balancing
its potential drawback of poor resistance to corrosion and its high price with
its advantages of low specific gravity and high modulus of elasticity. We hope
that the question of whether or not a conventional material applied in an
ingenious manner may afford more advantages than this alloy—surely a probable
question—will be answered in coming years.

Finally, our experiment was part of a broader framework of experiments aimed
at improving technologies for YXX processing conducted in FY 1987 and FY 1988
on the basis of a contract involving the commission of research from the Japan
Aircraft Development Association.

Evaluation of Experiment on Composite Graphite Polyimide

[Article by Ei-ichi Endou and Motohiro Atsumi, National Space Development Agency of Japan, and Shigeo Sanbongi and Toshiyuki Shimokawa, National Aerospace Laboratory of the Science and Technology Agency]

[Text] 1. Introduction

Graphite/polyimide (Gr/Pi) is a material with excellent prospects for use in the main structures of the space shuttle HOPE. In current research, a temperature of 300°C has been set as the target for resistance against heat. The National Space Development Agency (NASA), in conjunction with the National Aerospace Laboratory (NAL), has been pushing ahead with research and development on Gr/Pi composites and has carried out basic research.[1-4] In order to assess the mechanical properties of this material, which will provide a basis for designing the main structural elements, a number of test specimens were produced and subjected to systematic tests to obtain basic data on this composite. These data were subjected to further statistical analysis. This article presents the results of that analysis.

2. Test Specimens and Items Used in the Basic Experiment

Three material manufacturers were allotted, by commission, the production of some 570 test specimens of the Gr/Pi composite for use in testing. The basic experiment was carried out by these individual manufacturers. In order to assess variances in the relevant values reported by the different testing organizations, about 130 of the test specimens were offered to the NAL, where the basic experiment was repeated to obtain corroborating data. Two types of specimens, T800H/PMR-15 and Celion 6K/PMR-15 were tested, but the present report deals primarily with the results obtained from the latter.

To account for the environmental conditions under which HOPE is to be used, the experiments were conducted at temperatures of -100, -50, +23, and 300°C. These experiments were made exclusively under the dry condition, which is a humidity condition. Tests were also conducted and relevant data obtained for a wide range of items, such as single-layer plates, laminates, nonperforated

plates, perforated plates, interlayer shearing, impact damage, heat cycles, and fabric materials.

Among all the data obtained, the values for the mechanical properties—Young's modulus E, Poisson ratio v, fracture stress (σ_{max}), maximum strain (ϵ_{max}), shearing modulus G, shearing fracture stress (τ_{max}), and maximum shearing strain (r_{max})—are of particular importance. These values, therefore, were singled out for special statistical analysis, in which the average, standard deviation, and B tolerance were calculated for each test temperature.

3. Kolmogorv-Smirnov Test

The question of how or in what shape a set of sample data are distributed is important for statistical analysis of the data. In or analysis a normal distribution was assumed because of the ease with which the data can be handled. The accuracy of this assumption was tested by a modified Kolmogorv–Smirnov test.[5-6] Whether the assumption was correct or not was estimated by confirming whether or not the cumulative step function derived from the samples was contained within the two tolerance–limit curves at a 95 percent confidence level with respect to the cumulative distribution function for normal distribution.

$$Dn = \max_{1 \le i \le n} [Fo(Xi) - (i-1)/n, \; i/n - Fo(Xi)] < \hat{D}n \tag{1}$$

where n: denotes the sample size ,
   Xi: represents the measured values (i = 1,2,$\cdots$n),
   Fo(X): the cumulative function estimated from the sample, and
   $\hat{D}n$: the bilateral tolerance limit value.

This analysis was conducted for n ≥ 3. Figures 1 and 2 present examples of the results of the Kolmogorv–Smirnov test for normal distribution applied to mechanical property data of laminates. The abscissa uses the value of the standard deviation as the unit. Figure 1 is a plot for the tensile strength σ_{max} of laminates with n = 44 and Figure 2 for compression strength σ_{max} of laminates with n = 18. The data are contained within the two tolerance–limit curves (broken lines) in the figures, which indicates that the statistical assumption of a normal distribution of the data was correct.
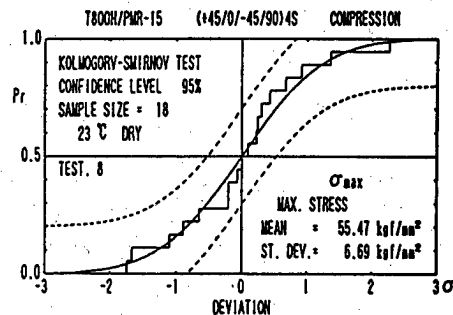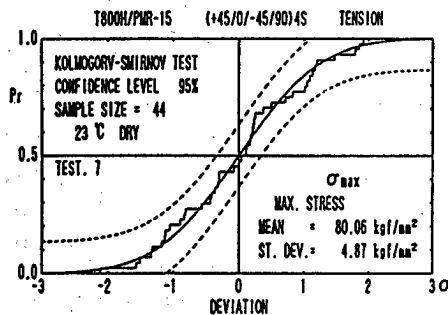

Figure 1. Results of Kolmogorv–
   Smirnov Goodness–of–Fit
   Test (Tensile fracture
   stress for laminates)

Figure 2. Results of Kolmogorv–Smirnov
   Goodness–of–Fit Test
   (Compression stress for
   laminates)

4. Average Values, Standard Deviations, and B Tolerance Values

For the statistical analysis, a sample was selected for each of the mechanical properties and the relevant average value and standard deviation were calculated:

$$X_{mean} = \Sigma \; Xi/n \qquad (2)$$

$$s = \sqrt{\{\Sigma \; (Xi - X_{mean})^2/(n-1)\}} \qquad (3)$$

where X_{mean}: denotes the sample average, and
s: the standard deviation of the sample.

The tolerance value B for an individual mechanical property, which is necessary as a criterion for design work, was derived by direct calculation for samples with a normal distribution.[7,8]

$$X_B = X_{mean} - k_B \cdot s \qquad (4)$$

where X_B: denotes the B tolerance, and
kB: the unilateral tolerance limit coefficient
(confidence level = 95 percent confidence = 90 percent).

For the value of the shearing modulus of elasticity, G, which was estimated by measurements in the ±45° tensile test on a single-layer plate, the shearing stress vs. shearing strain curve or $\tau(\gamma)$ was approximated using the third power formula for γ below while the coefficients a, b, and c were calculated by the least square method. Subsequently, the value of G, the incline of the curve, was calculated by $G = d \; \tau/d \; \gamma$ at $\gamma = 4000 \; \mu$.

$$\tau(\gamma) = a \cdot \gamma + b \cdot \gamma^2 + c \cdot \gamma^3 \qquad (5)$$

To compensate for the possibility of skewed data because of a limited number of measurements, our analysis calculated a discount coefficient ($f_B = X_B/X_{mean}$) from relevant data produced at normal temperature (=+23°C), which have a large n value. These were compiled from the data provided by each of the corporations involved. The average values at the other levels of temperature were multiplied by the coefficient such that the tolerance values Bs for them could be estimated.

5. Results of Statistical Analysis

Statistically produced mechanical property values for E, v, Σ_{max}, G, τ_{max}, and γ_{max} were plotted in graphs with the abscissa indicating temperature. The dependence on temperature of each of the mechanical properties was then examined. Some of the results are shown below. Figures 3-6 present values for σ_{max} at 0° and 90° stretching/compression for single-layer plates. The mark o in the graphs denotes the averages. The vertical lines connect the maximums and the minimums, and the broken lines represent the B values for tolerances. For tensile strength in the direction of 0° where the strength of the fiber involved predominates, the decline in strength with a rise in temperature is

184
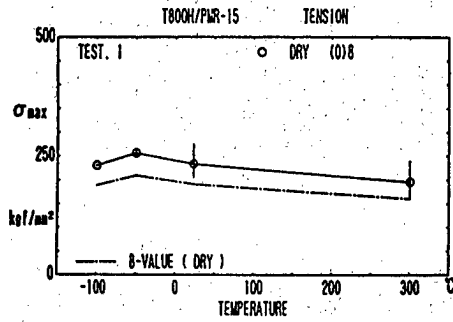
Figure 3. Dependence on Temperature
of Tensile Fracture Stress
σ_{max} for a Single−Layer
Plate in the 0° Direction
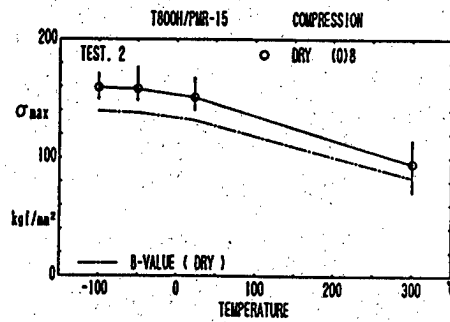
Figure 4. Dependence on Temperature of
Compression Fracture Stress
σ_{max} for a Single−Layer
Plate in the 0° Direction
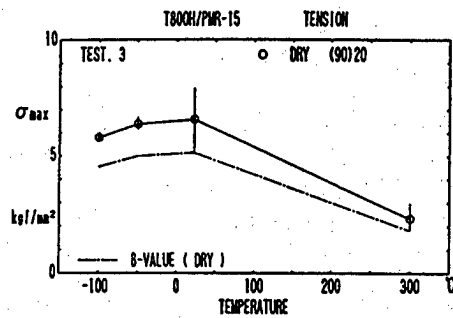
Figure 5. Dependence on Temperature
of Tensile Fracture Stress
σ_{max} for a Single−Layer
Plate in the 90° Direction
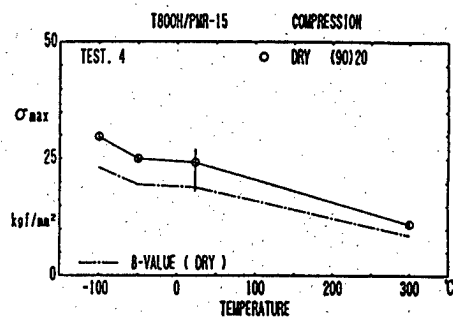
Figure 6. Dependence on Temperature of
Compression Fracture Stress
σ_{max} for a Single−Layer
Plate in the 90° Direction
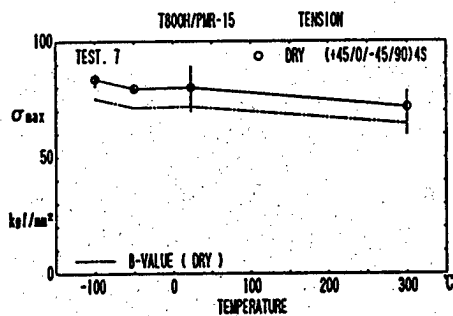
Figure 7. Dependence on Temperature
of Tensile Fracture Stress
σ_{max} for a Laminate
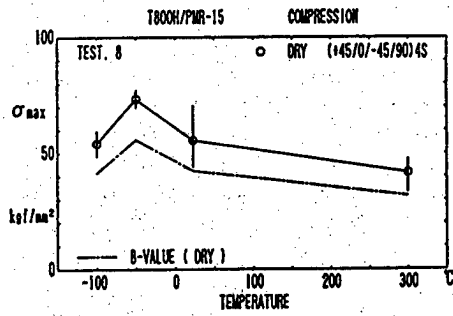
Figure 8. Dependence on Temperature of
Compression Fracture Stress
σ_{max} for a Laminate

no more than 16 percent. By contrast, for compression strength and for 90°
tensile strength where the strength of the resin is predominate, there is a
pronounced decline in strength on the order of 37–65 percent. Figures 7 and 8
present changes in tensile and compression strength with increasing
temperature for laminates. Tensile strength falls by 11 percent with a rise in
temperature, while compression strength declines by 25 percent. Figure 9 shows

185

changes in the G value for a ±45°-direction stretch test of single-layer plates and Figure 10 shows the changes in the value of τ_{max} for the same test. A decline up to 71 percent of the G value can be seen, indicating that the shearing modulus of the material at high temperature is a mere one-fourth of what it is at normal temperatures. The τ_{max} value suffers a decline of 38 percent.
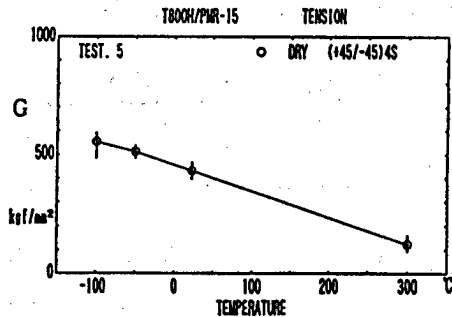

Figure 9. Dependence on Temperature of Stretching (Shearing modulus of elasticity) Value G for a Single-Layer Plate in the Direction of ±45°
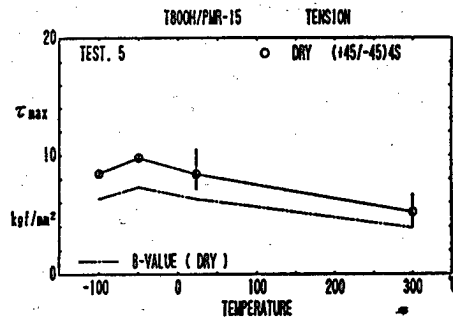
Figure 10. Dependence on Temperature of Stretching (Shearing fracture stress) σ_{max} for a Single-Layer Plate in the Direction of ±45°
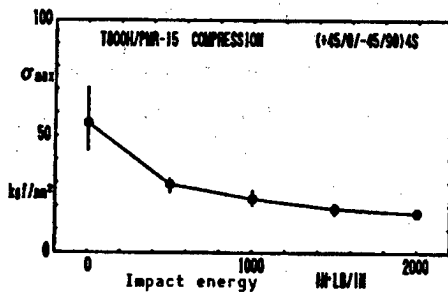

Figure 11. Compression Strength After Impact Damage (Laminate)
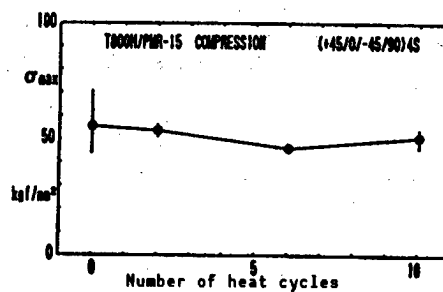
Figure 12. Compression Strength After the Application of Heat Cycles (Laminate)

The mechanical properties (tolerance B) for T800H/PMR-15 at normal temperature and at 300°C are presented in Table 1.

Because composite materials are often susceptible to the force of impact, the relevant properties were also investigated. Figure 11 presents changes in the compression strength for laminates following damage caused by impact. Compression strength can be reduced as much as 59 percent following an impact with a force of 1000 IN·LB/IN. The effect of heat cycles was also examined, since the space shuttle HOPE will be required to resist the stress of launching and reentry 10 times. Changes in compression strength of laminates following heat cycles are presented in Figure 12. When the specimen was subjected to the stress of a heat cycle with no additional mechanical stress, the decline in compression strength, as can be seen, is 17 percent.

Table 1. Mechanical Properties of T800H/PMR-15 (B tolerance)

Test item	Temper-ature	Young's modulus kgf/mm^2	Poisson ratio	Frac-ture stress kgf/mm^2	Maximum strain x10^{-6}
Single-layer plate 0° Tensile test	23°C	16200	0.33	191.3	11600
	300°C	17000	0.30	160.5	8950
Single-layer plate 0° Compression test	23°C	14700	0.34	131.7	—'—
	300°C	14400	0.31	82.9	
Single-layer plate 90° Tensile test	23°C	845	0.02	5.1	5890
	300°C	625	0.01	1.8	3060
Single-layer plate 90° Compression test	23°C	1090	0.02	18.8	23600
	300°C	707	0.02	8.6	13300
Single-layer plate ±45° Tensile test	23°C	429[*1]	—	6.3[*2]	18000[*3]
	300°C	124[*1]	—	3.9[*2]	14200[*3]
Laminate Nonperforated Tensile test	23°C	5590	0.30	71.9	12800
	300°C	5600	0.34	64.3	10800
Laminate Nonperforated Compression test	23°C	5280	0.30	42.3	8600
	300°C	5040	0.30	31.6	6880

Humidity condition: Dry; [*1]: Shearing modulus of elasticity (kgf/mm^2); [*2]: Fracture shear stress (kgf/mm^2); [*3]: Maximum shear strain (x10^{-6}); Young's modulus: Poisson ratio; and maximum shear strain represented as average values

Finally, the thicknesses of the plates subjected to these tests were all the rated ones. The rated thickness of T800H/PMR-15 is 0.134 mm/ply. The rated fiber content is 60 percent and the laminate has a 32-ply lamination structure at (+45/0/-45/90)4S.

5. Summary

The results of our statistical analysis, summarized primarily for the features of T800H/PMR-15, are as follows.

For laminates:

   (1) The decline in tensile strength is limited.
   (2) Changes in Young's modulus values are slight.
   (3) Compression strength drops about one-fourth.

For single-layer plates:

   (4) The decline in tensile strength and modulus of elasticity in the direction of fiber alignment is limited.

(5) The compression strength in the direction of the fiber drops is reduced by about one-third.

(6) The compression strength in the direction normal to that of fiber falls by about one-half.

(7) The shearing modulus of elasticity plummets by about three-fourths.

(8) The interlayer (fracture) shearing strength (σ_{max}) drops by about two-thirds.

NASDA is currently pushing ahead with tests of Gr/Pi composites in wet conditions and with relevant fatigue tests. The results of these tests will contribute to a scheduled assessment of the application of these composites in the space shuttle HOPE.

References

1.   Atsumi, M., et al., "Basic Experiments on Structural Materials for Main Structures of the Space Shuttle HOPE," Collection of Lectures at the 32nd Joint Lecture Meeting on Space Science and Technology, October 1988, pp 52-53.

2.   Kakuta, Y., et al., "Basic Property Experiments on Carbon/Polyimide Composites," Collection of Lectures at the 31st Lecture Meeting on Structural Strength, July 1989, pp 56-59.

3.   Hamaguchi, Y., et al., "On the Variance of the Values Obtained From Basic Property Experiments on Carbon/Polyimide Composites," Ibid., pp 60-63.

4.   Shimokawa, T., et al., "Reliability Analysis of Data for Static Tensile Tests Made on a Large Number of Carbon/Polyimide Laminate Specimens," Ibid., pp 64-67.

5.   Ibid., "Limiting Values for the Modified Kolmogorv-Smirnov Goodness-of-Fit Test on the Extremum Value Distribution and Two-Parameter Weibull Distribution," Collection of Preliminary Printed Manuscripts for the Eighth Symposium on Reliability Engineering in Design, Japan Material Society, December 1988, pp 12-15.

6.   Mann, N.R., Schafer, R.E., and Singpurwalla, N.D., "Methods for Statistical Analysis of Reliability and Life Data," John Wiley & Sons, 1974, pp 349-350.

7.   Yamauchi, J., et al., TABLES FOR STATISTICAL VALUES, JSA-1972, Japan Standard Association, 1972, pp 75-76.

8.   METALLIC MATERIALS AND ELEMENTS FOR AEROSPACE VEHICLE STRUCTURES, MIL-HDBK-5D, Vol 2, June 1983, pp 9.12-9.13.

Molding, Processing Technologies for Composite Materials

[Article by Haruyoshi Nishikuni, Kiyoshi Tsuchiya, and Takashi Nagumo, fuji Heavy Industries, and Takashi Ishikawa, National Aerospace Laboratory]

[Text] 1. Introduction

In recent years there has been a growing concern among researchers on thermo-plastic resins regarding the need to enhance the performance of composite structural materials for aerospace machines and equipment on the ground that such materials have better properties than conventional epoxy resins in terms of resistance to impact and fracture toughness. Efforts to develop these material and the relevant processing technologies are underway both at home and abroad. Research on composite materials using PEEK as the matrix resin, in particular, have been pushed energetically, though molding and processing technologies for these materials have yet to be established. Other nations have set out to develop methods for molding more than one component as one body without subsequent fabrication through the use of fasteners or by secondary adhesive processing.

The authors have been engaged in research and development of thermoplastic resins aimed at finding applications for these materials in appropriate main structures. In this paper, we deal with the results of a trial manufacture, using PEEK matrix resin composites, of a panel that is reinforced with a blade-type stiffener and molded as one body (co-curing).

2. Molding and Processing Experiments

In order to use this material in structural elements of wings, etc., we trial manufactured a reinforced panel in which T-shaped stiffeners and the skin were molded as one body from a CF/PEEK prepreg oriented in one direction (AJPC-2 material; manufactured by ICI Inc.). We obtained relevant molding and processing data.

2.1 Shape of the Specimen

The specimen shown in Figure 1, was a 280 mm by 360 mm reinforced panel in which the skin and the four T-shaped stiffeners fixed thereon were molded as one body. Two L-shaped structural elements were attached back to back to make the T-shaped stiffeners. The number of plies or layers of the laminates was 10 ($\pm45/\pm45/90$) sym for the skin and 24 ($\pm45/\pm45/0_4/90/0_3$) sym for the stiffeners arranged in the mirror image symmetry.
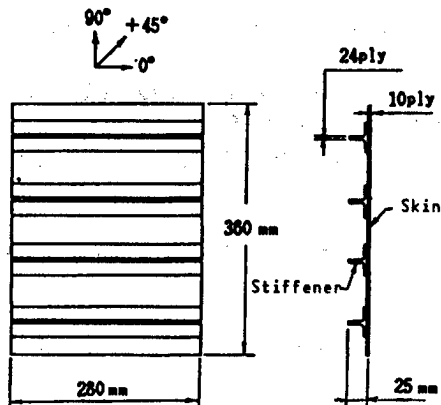

Figure 1. Shape of Trial Manufactured Specimen
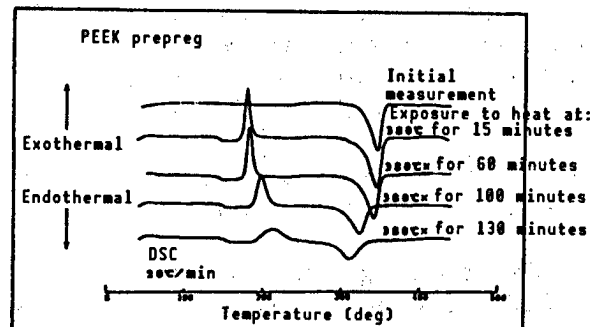
Figure 2. Results of DSC Analysis of APC-2 Prepreg After Exposure to Heat

2.2 Thermal Properties of the Material

Since the raw materials were exposed to heat several times in the process of manufacturing the specimen, the behavior of the resin after being heated to 380°C, the molding temperature, was investigated before the trial manufacture started. As can be seen in Figure 2, the longer it was exposed to heat, the more the endothermic peak of the resin tended to decrease, a sign of thermal deterioration. The results indicated that the endothermic peak of the resin began to fall after it had been exposed to a temperature of 380°C for over 100 minutes. Since any deterioration of the resin could result in poor flow and unreliable quality, it became necessary to devise an efficient molding method and efficient tools and machines for molding so that the time required for molding could be shortened.

2.3 Trial Manufacture of the Specimen

In order to shorten the total time the resin is exposed to heat in the process of molding of a specimen to less than 100 minutes, we devised the following molding procedure (Figure 3).

(1) Laminates (flat), which are used as parts of the skin and stiffeners, were produced by hot pressing.

190
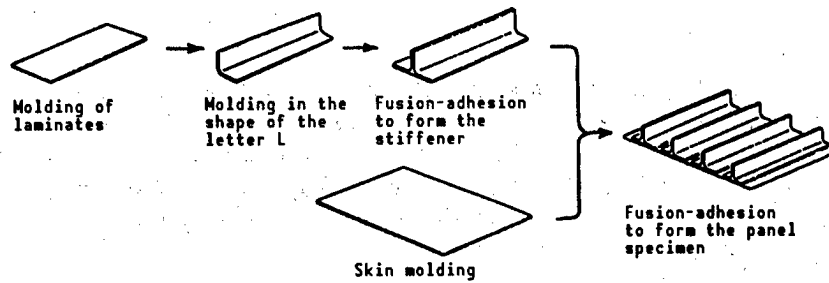
Figure 3. Panels Reinforced by Stiffeners and Made as One Body

(2) The laminates, which were molded by pressing, were molded again by heating them into L-shapes, and each of two L pairs were assembled back to back (in a T-shape). They were then subjected to heat and fusion bonding with a pressing machine to form the stiffener.

(3) The skin and four stiffeners were subjected to bending by heating and fusion with a pressing machine to make a panel.

(4) The molding and bonding by fusion were carried out at temperatures 380~400°C and under pressures 15~20 kg/cm^2.

(5) The molding machine, which is made of steel, has a matched die structure. Before beginning to mold the specimen, test measurements of the temperature at various sites of the die were conducted in order to insure that the temperature distribution was uniform at all sites of the die and that the molding process formulated above was satisfied by the die.

3. Test Results

The specimen we trial manufactured is shown in Photograph 1 [not reproduced]. The specimen had a fine external appearance; neither resin defects nor resin pooling were visible. It also resulted in very little variance in the thickness of the plate, as shown in Figure 4, thus producing fine overall results.

Nevertheless, there was some warping in the plate but this was amenable to correction, even by such a simple method as pressure applied by the fingers. The warping was assumed to have occurred because of a difference between the thermal expansion coefficient of the die and that of the raw material, since the die was made of steel (Figure 5).

3.2 Internal Quality

The internal quality of the specimen was investigated by ultrasonic waves and X-rays for the plate parts and the corner parts, respectively. The results were fine with no indications of defects. The cross sectional areas of cut-out pieces, in turn, did not reveal the presence of any voids, delaminations or fiber curvings (Photograph 2 [not reproduced]), thereby confirming the fine overall results. Based on the results, we determined that the molding dies, molding process, etc., devised for the trial manufacture of a CF/PEEK reinforced panel molded as one body were generally appropriate. The authors

191
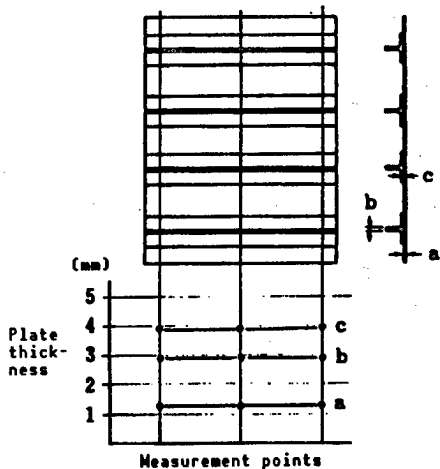
Figure 4. Thickness of Skin Plate
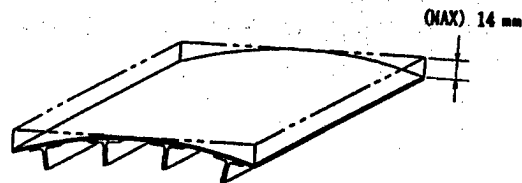
Figure 5. Warping of the Specimen

will press forward with their search for a die material that differs less from the resin material in terms of its thermal expansion coefficient to solve the problem of product warping, with their efforts to improve the molding process to reduce the time the material is exposed to heat, and with their work to find materials that will bond at temperatures below their melting point.

4. Future Problems

Assembly by fusion and bonding is an effective bonding method that takes advantage of the ability of thermoplastic resins to form the thermoplastic composites with a unified structure. There is still a number of technological problems related to processing and molding that need to be resolved in order to be able to apply thermoplastic composites in practical structures. These problems include:

(1) Development of die structures with high resistance to heat and with low thermal expansion coefficients.

(2) Development of materials more amenable to molding; this involves such properties as lower molding temperatures, etc.

(3) Optimization of the molding process and bonding materials.

(4) Development of molding methods other than press molding that will be more appropriate for the shape of a given component.

(5) Development of automated technologies, e.g., an automated lamination process and an automated filament winding process.

In solving these problems it will be necessary to push ahead with developmental research in intimate association with raw material makers with the target clearly defined.

5. Conclusion

In addition to their fine physical properties, thermoplastic resins have the potential for cutting production costs because their molding cycle needs less time. As a matter of fact, however, their advantages have not been used as well as possible because, among other things they require higher temperatures for molding than do thermosetting materials. The authors intend to push forward with the development of materials more amenable to molding and with the development of technologies for molding and processing based on the features of thermoplastic resins, thereby enhancing the application of these materials in the main structures of aerospace machines and equipment.

References

1.   Ishikawa, R., et al., "High Fatigue Strength Characteristics of the Thermoplastic Composite CF/PEEK and Present State of Its Application in Structures," Collection of Lectures From the 31st Lecture Meeting on the Strength of Structures, 1989, pp 6–9.

2.   Ostem, R.B., et al., "Thermoplastic Composite Fighter Forward Fuselage," 34th International SAMPE Symposium, 8–10 May 1989, p 300.

3.   Nagumo, T., et al., "Evaluation of PEEK Matrix Composites," 32nd International SAMPE Symposium, 6–9 April 1987, p 396.

– END –

For Official Use Only

> This is a U.S. Government publication. Its contents in no way represent the policies, views, or attitudes of the U.S. Government. Users of this publication may cite FBIS or JPRS provided they do so in a manner clearly identifying them as the secondary source.

Foreign Broadcast Information Service (FBIS) and Joint Publications Research Service (JPRS) publications contain political, military, economic, environmental, and sociological news, commentary, and other information, as well as scientific and technical data and reports. All information has been obtained from foreign radio and television broadcasts, news agency transmissions, newspapers, books, and periodicals. Items generally are processed from the first or best available sources. It should not be inferred that they have been disseminated only in the medium, in the language, or to the area indicated. Items from foreign language sources are translated; those from English-language sources are transcribed. Except for excluding certain diacritics, FBIS renders personal names and place-names in accordance with the romanization systems approved for U.S. Government publications by the U.S. Board of Geographic Names.

Headlines, editorial reports, and material enclosed in brackets [ ] are supplied by FBIS/JPRS. Processing indicators such as [Text] or [Excerpts] in the first line of each item indicate how the information was processed from the original. Unfamiliar names rendered phonetically are enclosed in parentheses. Words or names preceded by a question mark and enclosed in parentheses were not clear from the original source but have been supplied as appropriate to the context. Other unattributed parenthetical notes within the body of an item originate with the source. Times within items are as given by the source. Passages in boldface or italics are as published.

SUBSCRIPTION/PROCUREMENT INFORMATION

The FBIS DAILY REPORT contains current news and information and is published Monday through Friday in eight volumes: China, East Europe, Soviet Union, East Asia, Near East & South Asia, Sub-Saharan Africa, Latin America, and West Europe. Supplements to the DAILY REPORTs may also be available periodically and will be distributed to regular DAILY REPORT subscribers. JPRS publications, which include approximately 50 regional, worldwide, and topical reports, generally contain less time-sensitive information and are published periodically.

Current DAILY REPORTs and JPRS publications are listed in *Government Reports Announcements* issued semimonthly by the National Technical Information Service (NTIS), 5285 Port Royal Road, Springfield, Virginia 22161 and the *Monthly Catalog of U.S. Government Publications* issued by the Superintendent of Documents, U.S. Government Printing Office, Washington, D.C. 20402.

The public may subscribe to either hardcover or microfiche versions of the DAILY REPORTs and JPRS publications through NTIS at the above address or by calling (703) 487-4630. Subscription rates will be provided by NTIS upon request. Subscriptions are available outside the United States from NTIS or appointed foreign dealers. New subscribers should expect a 30-day delay in receipt of the first issue.

U.S. Government offices may obtain subscriptions to the DAILY REPORTs or JPRS publications (hardcover or microfiche) at no charge through their sponsoring organizations. For additional information or assistance, call FBIS, (202) 338-6735,or write to P.O. Box 2604, Washington, D.C. 20013. Department of Defense consumers are required to submit requests through appropriate command validation channels to DIA, RTS-2C, Washington, D.C. 20301. (Telephone: (202) 373-3771, Autovon: 243-3771.)

Back issues or single copies of the DAILY REPORTs and JPRS publications are not available. Both the DAILY REPORTs and the JPRS publications are on file for public reference at the Library of Congress and at many Federal Depository Libraries. Reference copies may also be seen at many public and university libraries throughout the United States.

For Official Use Only